UNIVERSITÉ CATHOLIQUE DE LOUVAIN
ÉCOLE POLYTECHNIQUE DE LOUVAIN
INSTITUTE OF MECHANICS, MATERIALS AND CIVIL ENGINEERING

NUMERICAL SIMULATION OF AEROTHERMAL FLOWS THROUGH ABLATIVE THERMAL PROTECTION SYSTEMS.

DOCTORAL DISSERTATION PRESENTED BY

PIERRE SCHROOYEN

IN PARTIAL FULFILLMENT OF THE REQUIREMENTS
FOR THE DEGREE OF DOCTOR IN ENGINEERING SCIENCES

THESIS COMMITTEE:

Prof. Philippe Chatelain, Université catholique de Louvain (Advisor)
Prof. Miltiadis Papalexandris, Université catholique de Louvain (Advisor)
Prof. Thierry Magin, von Karman Intitute for Fluid Dynamics
Dr. Koen Hillewaert, Cenaero
Dr. Nagi Mansour, NASA Ames Research Center
Prof. Juray de Wilde, Université catholique de Louvain
Prof. Grégoire Winckelmans, Université catholique de Louvain (President)

Louvain-la-Neuve, November 2015

ACKNOWLEDGEMENTS

Je ne pourrais pas commencer ce document sans remercier toutes les personnes qui m'ont aidé, guidé et soutenu durant ce projet.

Tout d'abord, je tiens à remercier mes promoteurs et mon comité d' accompagnement qui m'ont guidé durant toute cette thèse. Je voudrais exprimer toute ma gratitude envers mon promoteur, Philippe, pour m'avoir donné l'opportunité de réaliser cette thèse et de travailler dans un domaine qui me passionne. Je le remercie de m'avoir soutenu que ce soit scientifiquement ou moralement et de m'avoir accordé sa confiance même quand, moi, je doutais. Merci également pour toutes les relectures et corrections des rapports et papiers durant ces quatres ans.

J'aimerais également remercier Thierry qui m'a toujours conseillé tout en me laissant l'autonomie nécessaire à mon épanouissement personnel. Sa porte était toujours ouverte même quand je débarquais sans prévenir à l'institut et nos discussions m'ont toujours été d'une grande aide. Enfin, je le remercie pour les nombreuses suggestions et corrections sur ce texte qui me rendent fier du travail accompli.

Sans oublier Koen, pour m'avoir accueilli dans son équipe et pour son encadrement, son enthousiasme et ses explications toujours détaillées sur les méthodes numériques. Sans lui, les méthodes DG et Argo seraient restés des mystères pour moi.

Je remercie également Miltiadis pour ces remarques durant les réunions d'avancement qui m'ont aidé à me poser les bonnes questions ainsi que les membres du jury de ma thèse pour leur lecture attentive du texte et leur précieuses corrections. Enfin, je remercie le FRIA pour le soutien financier durant mon doctorat.

J'ai eu la chance de pouvoir faire ce travail en collaboration avec trois instituts (l'UCL, le Cenaero et l'Institut von Karman) ce qui a été très enrichissant pour moi d'un point de vue scientifique mais également humain. Cette expérience m'a permis d'avoir des avis complémentaires sur les divers aspects de mon travail mais également de rencontrer d'autres collègues avec qui partager les moments de cette thèse. Je remercie encore Philippe, Koen et Thierry pour avoir mis sur pied cette collaboration. Bien sûr, cela me donne un rien plus de travail dans cette section afin de remercier comme il se doit mes collègues au sein de ces trois institutions.

A l'UCL, j'aimerais tout d'abord remercier mes collègues qui ont partagé mon bureau, Stéphane et Olivier L., pour avoir contribué à rendre ce petit bureau un endroit où il fait bon travailler et pour les innombrables discussions qui m'ont, je suis sûr, permis de terminer ce travail. Je remercie également Yves, Olivier T. et Philippe P. qui étaient toujours disponibles pour discuter des problèmes que j'ai rencontrés dans mon travail mais aussi Benjamin, François, Nicolas (dit Nini) ou Haddy sans qui l'ambiance en TFL n'aurait pas été la même. J'aimerais également citer les discussions avec Panos et Christos sur certains aspects de ma thèse ainsi que Julien B. pour m'avoir introduit à la modélisation de matériau pyrolysable et Véronique pour les discussions éclairées sur la chimie. Enfin, je remercie Isabelle pour le support administratif durant ces quatres années.

For VKI, I would like to thank particularly Alessandro T. from whom I learned a lot about ablation as well as Bernd and JB for the uncountable interesting discussions on this topic. I would like also to thank them and Eric for welcoming and hosting me in their office when I was coming to VKI. I would like also to acknowledge people from NASA ARC for interesting discussions and advices they provided me. In particular, I would like to thank Nagi Mansour for hosting me at NASA during several summers of my Ph.D. and Francesco Panerai for his help and discussions on the experiments as well as the interest he showed for my thesis which motivated me more than he can imagine. Finally, I would like to thank Jean Lachaud for suggesting the topic of this thesis and for all the interesting discussions we had.

At Cenaero, I would like to acknowledge all the members of the Argo team for continuous support and especially J.-S. who helped me a lot with the numerical aspects of my thesis as well as Corentin and Guillaume.

Je ne pourrais finir ces remerciements sans citer mes amis qui m'ont soutenu moralement et ont toujours montré de l'intérêt pour mon doctorat. En particulier, je remercie les trois mousquetaires Seb, Pierre et Max mais aussi les anciens du SCJ, Guillaume, Thomas, Oli, Antoine, Cédric, Dams, Thibaut et Ben ainsi que le groupe des ingés.

Je tiens également à remercier ma famille, mes frères et soeurs, mes parents et grand-parents pour leur soutien depuis toujours.

Enfin, je garde le meilleur pour la fin, je voudrais remercier de tout mon coeur Aurélie qui a partagé avec moi, depuis le début, mes doutes et mes craintes mais aussi mon bonheur quand la simulation de crashait pas. Elle a su me rendre le sourire et me redonner le courage pour avancer quand mes recherches piétinaient. J'espère que cette thèse la rend fière de moi autant que je lui en suis reconnaissant.

Dès lors, je souhaite à tous ceux qui s'aventurent au delà de ces remerciements... bonne lecture!

"If I have seen further, it is by standing on the shoulders of giants."
Isaac Newton

CONTENTS

NOMENCLATURE

Abbreviations

ARD	Atmospheric Reentry Demonstrator
AUSM	Advection Upstream Splitting Method
BE	Backward Euler
BJ	Beaver and Joseph jump condition
CFD	Computational Fluid Dynamics
CGFEM	Continuous Galerkin Finite Element Method
CPG	Calorically Perfect Gas
CSF	Continuum Surface Force
DGM	Discontinuous Galerkin Method
DNS	Direct Numerical Simulation
DOF	Degrees Of Freedom
EXPERT	eXPErimental Re-entry Testbed
FEM	Finite Element Method
FIRE	Flight Investigation of Re-Entry
FVM	Finite Volume Method
GMRES	Generalized Minimal RESidual method
ICP	Inductively Coupled Plasma
IFEM	Immersed Finite Element Method
IIP	Incomplete Interior Penalty
LED	Local Extrema Diminishing
LTE	Local Thermal Equilibrium
MAE	Matched Asymptotic Expansions

MPI	Message Passing Interface
MSL	Mars Science Laboratory
NASA	National Aeronautics and Space Administration
NCPG	Non-Calorically Perfect Gas
NIP	Non symmetric Interior Penalty
NN	Neale and Nader jump condition
NR	Newton Raphson
NSCBC	Navier-Stokes Characteristic Boundary Conditions
ODE	Ordinary Differential Equation
OpenMP	Open Multi-Processing
OTW	Ochoa-Tapia Whitaker jump condition
PI	Proportional Integral controler
PICA	Phenolic Impregnated Carbon Ablator
PML	Perfectly Matched Layer
REV	Representative Elementary Volume
SEM	Scanning Electron Microscope
SIP	Symmetric Interior Penalty
SLAU	Simple Low dissipation AUSM
SRC	Stardust Return Capsule
STS	Super Time Stepping
TACOT	Theoretical Ablative Composite for Open Testing
TPS	Thermal Protection System
TWCP	Tape Wrapped Carbon Phenolic
VANS	Volume Averaged Navier-Stokes
VKI	von Karman Institute
VOF	Volume Of Fluid
XFEM	eXtended Finite Element Method

Alpha numeric symbols

$\dot{m}$	Mass flux	$\left[\mathrm{kg/m^2}\right]$

c	Sound speed	$[\mathrm{m/s}]$
c_p	Heat capacity at constant pressure	$[\mathrm{J/(K\,kg)}]$
c_v	Heat capacity at constant volume	$[\mathrm{J/(K\,kg)}]$
$D_{i,m}$	Average diffusivity coefficient	$\left[\mathrm{m^2/s}\right]$
E	Total energy	$[\mathrm{J/kg}]$
e	Thermal energy	$[\mathrm{J/kg}]$
E_a	Activation energy	$[\mathrm{J/mol}]$
g	Gibbs energy	$[\mathrm{J/kg}]$
H	Total enthalpy	$[\mathrm{J/kg}]$
h	Enthalpy	$[\mathrm{J/kg}]$
h_f^0	Formation enthalpy	$[\mathrm{J/kg}]$
J_i	Diffusive flux	$\left[\mathrm{kg/(m^2\,s)}\right]$
k_B	Boltzmann's constant	$[\mathrm{J/K}]$
k_b	Backward reaction rate	$[*]$
k_f	Forward reaction rate	$[*]$
L	Characteristic length	$[\mathrm{m}]$
N_s	Number of species	$[-]$
P	Pressure	$[\mathrm{Pa}]$
p	Polynomial order	$[-]$
q	Heat flux	$\left[\mathrm{J^2/(m\,s)}\right]$
R	Universal gas constant	$[\mathrm{J/(mol\,K)}]$
r	Fiber radius	$[\mathrm{m}]$
s	Entropy	$[\mathrm{J/(kg\,K)}]$
S_f	Specific surface	$[\mathrm{1/m}]$
T	Temperature	$[\mathrm{K}]$
v	Velocity	$[\mathrm{m/s}]$
V_i	Diffusion velocity	$[\mathrm{m/s}]$
W	Molecular weight	$[\mathrm{kg/mol}]$
X_i	Mol fraction	$[-]$

Y_i	Mass fraction	$[-]$

Greek letters

α	Penalty parameter	$[-]$
$\bar{\lambda}$	Mean free path	$[\mathrm{m}]$
$\dot{\omega}$	Production rate	$\left[\mathrm{kg/(m^3\,s)}\right]$
ϵ	Volume fraction	$[-]$
η	Tortuosity	$[-]$
γ	Tuning factor sinusoidal model	$[-]$
ι	Blowing correction coefficient	$[-]$
κ	Permeability	$\left[\mathrm{m^2}\right]$
λ	Thermal conductivity	$[\mathrm{W/(m\,K)}]$
μ	Viscosity	$[\mathrm{Pa\,s}]$
ν_i	Stoichiometric coefficient	$[-]$
ρ	Density	$\left[\mathrm{kg/m^3}\right]$
τ	Viscous stress tensor	$[\mathrm{Pa}]$
ξ	emissivity	$[-]$
ζ_i	Basis functions	$[-]$

Non dimensional numbers

Ch	Stanton number
Da	Darcy number
Dam	Damköhler number
Kn	Knudsen number
Le	Lewis number
Ma	Mach number
Pe	Peclet number
Pr	Prandtl number
Re	Reynolds number
Sc	Schmidt number
Th	Thiele number

CHAPTER 1

INTRODUCTION

1.1 Context

The exploration programs of our solar system involve the design of manned or unmanned spacecraft that enter a planet atmosphere at hypersonic velocity. After the successful manned missions to the Moon in the 1960's and many probe entries into the atmosphere of outer planets, the next challenges for space agencies include bringing back samples to Earth by means of robotic missions and continuing the manned exploration program, which aims to send human beings to Mars and bring them home safely. Atmospheric entry is generally the most challenging phase during a space mission. The vehicle is strongly affected by aerodynamic heating due to the dissipation of a huge amount of kinetic energy into thermal energy. To ensure the integrity of the spacecraft, the vehicle is protected by a thermal heat shield. The heat load is evaluated during the design phase to estimate the required properties and thickness of the thermal protection material to withstand the high heating environment. Many achievements in rocket science have been made since the Apollo missions, but prediction of the heat exchange at the surface of the spacecraft remains a challenging task. Inaccuracies in these predictions can be fatal for the crew or the success of robotic missions. The evaluation of the heat flux is challenging because of the interaction between complex phenomena such as surface chemistry, radiation, material decomposition or flow transition from laminar to turbulent. These difficulties are enhanced at higher entry velocities, typical of new missions. The design of the Galileo probe heat shield is a famous example of our current limit to understand and predict the phenomena during atmospheric entry. The Galileo probe was designed to enter Jupiter's atmosphere and is the most challenging entry ever achieved with a entry velocity estimated to be $47.4\ [km/s]$. Figure 1.1 shows the configurations of the heat shield before and after atmospheric entry. It can be observed that the degradation of the thermal protection heat shield at the nose was clearly overestimated while the protection material at the shoulder was barely enough for the spacecraft to survive.

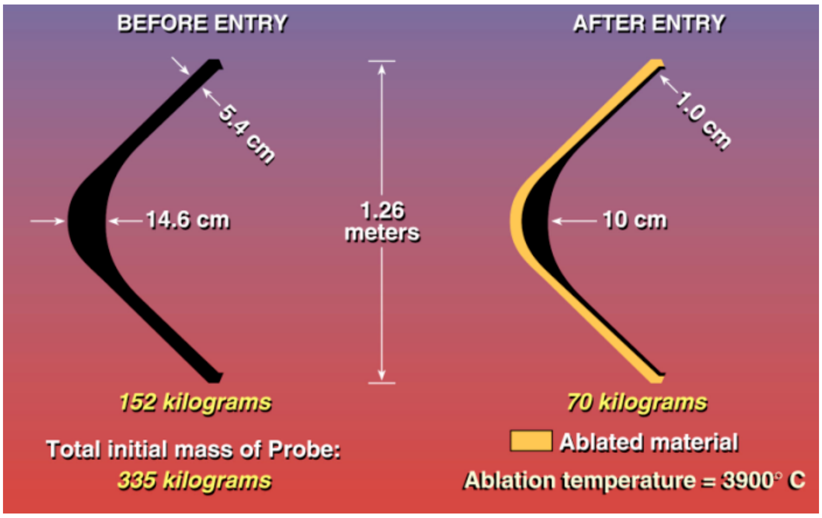

Figure 1.1: Design of the Galileo probe heatshield. Figure taken from [125].

In order to cope with these uncertainties and lack of understanding, excessive safety factors are used nowadays leading to increased mass of the Thermal Protection System (TPS). The TPS mass budget can be quite important (up to 50% for the Galileo probe see Fig. 1.1) and penalizes the onboard maximum payload mass.

Reusable and ablative materials are the two main types of TPS in use today. Reusable materials are designed for low heat flux trajectories and a famous example is the protection shield of the space shuttle which uses radiation reflective ceramic tiles. The space shuttle has been designed for in-orbit servicing at low altitude ($v_{entry} \approx 7.2\ [km/s]$). For the higher entry velocity missions of interest here, ablative material are best suited [68]. The heat shield of the Apollo capsule for example ($v_{entry} \approx 11.1\ [km/s]$) was made of a high density ablative material.

Ablative materials fall in the category of semi-passive thermal protection systems. These material degrade to protect the spacecraft from the large heating load and decompose into a gas which percolates through the material carrying some of the heat outside of the TPS. The use of dense carbon/carbon or carbon/resin composite ablators has been successfully demonstrated during several missions in the past [74]. Requirements concerning mass efficiency for missions with very high entry velocities have led to the development of a new class of light carbon composite ablators. The traits of these new materials are well exemplified by the Phenolic Impregnated Carbon Ablator (PICA), which was successfully demonstrated during the NASA Stardust mission, or ASTERM material developed by Airbus Defence and Space in Europe. These types of composite materials are made of a skeleton of carbon fibers which is partially filled by a phenolic resin. The avenues opened by such TPS materials promise mass efficiency and protection at very high entry velocities, hence their development, study and deployment on new generation vehicles [223].

Experimental investigation of aerothermal entry problems is still an extremely difficult endeavor which makes numerical methods crucial in advancing our understanding of these phenomena and in developing predictive design tools.

1.2 Atmospheric entry: a multi-physics problem

The trajectory during atmospheric entry is characterized by different flow regimes. At high altitudes, the velocity is very high leading to a hypersonic flow regime around the capsule ($Ma > 5$) and, as the spacecraft decelerates, the flow goes through supersonic ($Ma > 1$), transonic ($0.8 < Ma < 1.2$) and subsonic regimes ($Ma < 1$). At Mach number larger than one, a curved detached shock (bow shock) appears in front of a blunt body (low ballistic coefficient), forming a reactive shock layer. The thickness of this layer limited by the shock front and the surface of the probe decreases for higher velocity and is typically of the order of 20 centimeters for an Apollo shape capsule of four meter at peak heating during the reentry trajectory. This shock layer includes a viscous and thermal boundary layers that are developed close to the vehicle. The boundary layer which can be laminar or turbulent has a thickness of micrometers to millimeters. The phenomena in the shock layer and within the boundary layer for a hypersonic atmospheric entry are summarized in Fig. 1.2 and will be described in more details in the following.

The gas particles pass through the shock from a freestream region at relatively low density, low temperature, high velocity, to a dense layer at higher temperature and lower velocity. An example of the values in the freestream and in the shock layer for an Earth atmospheric entry are given in Table 1.1. The kinetic energy of the gas is converted through the shock into translational, rotational, vibrational and electronic energy. The temperature of the gas in the region after the shock can therefore reach really high values of 10^4 $[K]$ typically in the plateau region in the shock layer. Therefore, the shock layer is a region with very fast chemical reactions. Due to the high internal energy, the molecules dissociate and atoms and molecules are ionized. In addition, the excitation and de-excitation of the electronic population in this layer lead to radiation which contributes to the heating load on the thermal heat shield. For instance, the formation of very active molecules like NO for air in this layer plays an important role in the radiative heat flux.

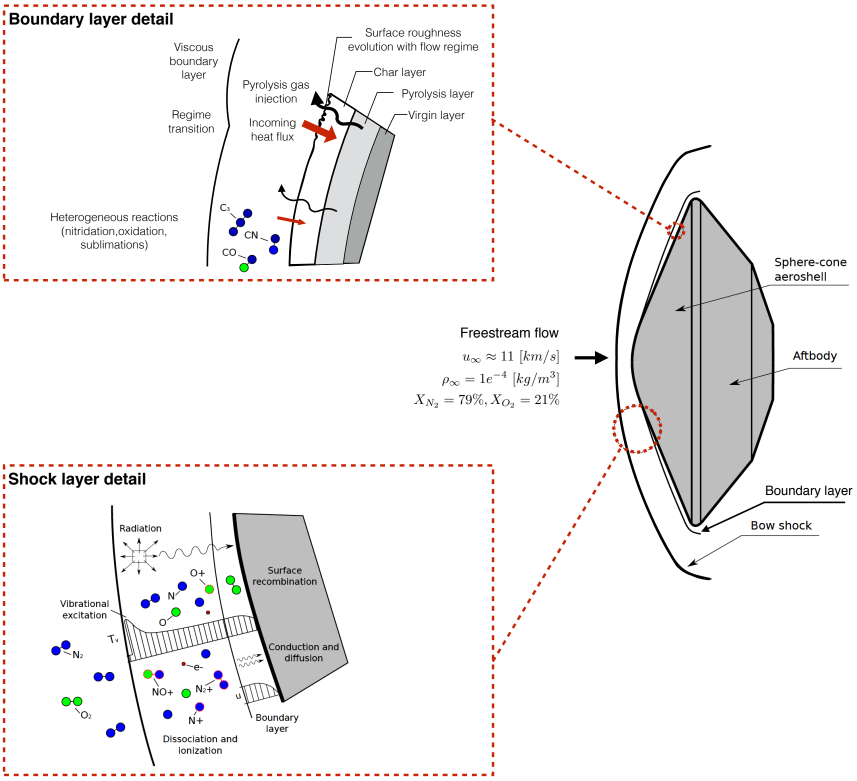

Figure 1.2: Sketch of an atmospheric entry of a space vehicle. Figure modified from Potter [178].

Table 1.1: Shock characteristic quantities for the Flight Investigation of Reentry mission (FIRE II) at a particular moment of the reentry trajectory ($t = 1634\ s$, altitude= $76.4\ km$) [42]. The post-shock conditions are computed with the code shocking^{++} described further.

	$P\ [Pa]$	$T\ [K]$	$\rho\ [kg/m^3]$	$u\ [m/s]$
FreeStream	2.09	195	$3.72e^{-5}$	11360
Post-Shock	$4.53e^3$	$1.04e^4$	$6.51e^{-4}$	649.7

The convection of this high enthalpy flow around the capsule and the radiation will progressively heat up the material. The temperature at the surface of the material can increase approximately to $3000[K]$ for severe entry conditions. The ablative material is designed to absorb this heat by degradation to ensure the integrity of the structure. Low density ablative TPS are generally composite materials made of fibers and a resin matrix. Two different degradation phenomena can be distinguished. First, the material resin is progressively pyrolysed, producing gases which are blown out of the porous material and injected into the boundary layer. The pyrolysis is an endothermic reaction absorbing the heat. The blowing also induces a blockage of the convective heat flux impinging on the surface of the spacecraft hence reducing the heat load. Furthermore, the blowing injects carbon species from the degradation of the material like CO or C_3 into the flow that leads to a more opaque shock layer hence reducing the incoming radiative heat flux [110]. The remaining material is composed of non-pyrolysing matrix and residual carbonaceous material forming the char zone. The second degradation mechanism is the erosion of the remaining char material by the flow. Depending on the material and flow conditions, it can be due to heterogeneous chemical reactions, sublimations or mechanical ablation (spallation) [118]. Detailed information on the gas-solid interactions is given in the next subsection.

The degradation of PICA is illustrated in Fig. 1.3 taken from Ref. [127]. The different states of the material can be observed. First, for the virgin material, the filler resin (phenol in this case) can be observed with the fibers. Progressively, the resin is decomposed leaving the char material and the fibers. Finally, the remaining char material and the fibers are ablated.

Since the material is receding, engineering design tools should be able to predict correctly the total recession of the material as well as the back temperature experienced by the substructure of the vehicle. The development of these tools is challenging since, as described earlier, an atmospheric entry implies a broad range of phenomena involving different scientific fields. The incoming hypersonic flow involves strong shocks, potential non-equilibrium effects, surface and volume chemistry, mass transfer, geometric changes, and radiation. The models of the flow and the material have to take into account distinct regions, the open flow and the wall but also their interaction.

1.2.1 Gas-surface interaction

The solution of the complete multi-physics problem including the shock layer is highly challenging. This work focuses on the interaction between the flow in the boundary layer and the thermal response of the material, hence investigating the region close to the spacecraft. In general, modeling and solving accurately the phenomena in the shock layer is very important since radiative heat flux can play a significant role in the heating of the material (up to 40% of the total heating rate for the FIRE II mission for example [178]). Following Potter [178], the modeling of radiation includes the description of the internal state populations of the chemical species, the electromagnetic spectrum distribution and the transport of the electromagnetic energy which is a non-local phenomenon. The complexity for the modeling of these three domains and the computational methods to reduce the cost associated to treat radiation require a substantial effort not covered in this thesis (see for example [178, 207] and references therein). Within this work, the test cases studied are at rela-

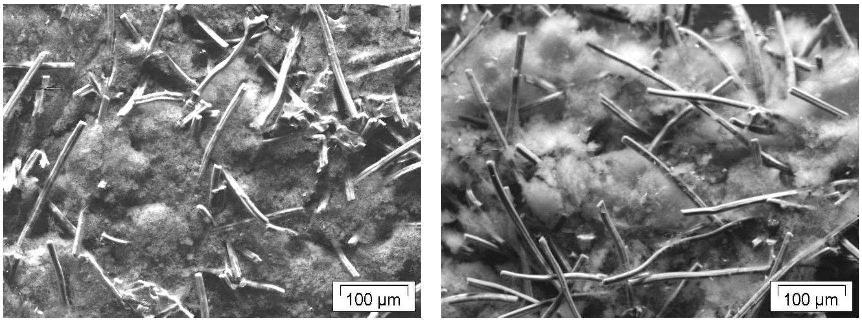

(a) Virgin (b) Partially charred

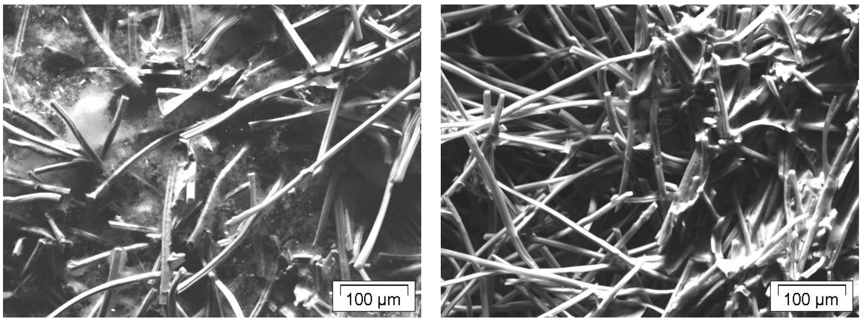

(c) Charred (d) Ablated

Figure 1.3: Scanning Electron Microscope images showing the material response of PICA to a high enthalpy flux. Micrographs are taken at different depths of a sample illustrating the degradation of the material. Figure taken from [127].

tively low velocity and do not involve active radiative species hence radiation in the flow field can be neglected. Nonetheless, this phenomenology is partially included through an energy sink term accounting for the re-radiation at the surface of the material in some of the applications in Chapter 5, 6 and 7.

In the thin region close to an ablative material surface, the remaining char material will be eroded by the high enthalpy flow. Depending on the planets atmospheric composition, nitridation and/or oxidation heterogeneous reactions will occur. If the temperature of the material becomes sufficiently high, sublimation of the carbonaceous matrix can also be significant. In addition, homogeneous reactions occur between the boundary layer gases and the pyrolysis gases produced by the thermal degradation of some components of the material. Finally, due to shear stress, mechanical ablation of the char layer can enhance the recession rate of the material. In addition, the presence of the solid matrix can lead to catalytic reactions and recombination of dissociated species. Note that the temperature in the boundary layer is lower than in the shock layer which might imply recombination. Furthermore, the roughness of the material surface will change with the erosion of the char. This leads to a dynamic interaction between the ablation and the flow regime. A rougher surface will induce transition towards a turbulent flow regime which will enhance the heat and mass exchange leading in turn to higher recession rate [229]. Finally, the shape change due to recession may have an impact on the flow around the vehicle hence its aerodynamic performances.

These phenomena are common for most ablative materials. However, with the development of low density ablative material, another challenge should be considered. Since new low density ablative materials are highly porous, the so-called ”surface” reactions are actually happening in a zone close to the surface [117]. Depending on the flow regime, the species in the boundary layer can penetrate the porous material and react in-depth. This can significantly reduce the mechanical strength of the char layer and imply more spallation. In order to accurately predict the recession rate, this ablation in volume should be accounted for. Figure 1.4 details the interactions between the boundary layer and the material response in the region close to the interface. On top of the TPS, the fibers are eroded in a certain depth of the material by the chemical processes happening with the flow. The pyrolysis gas produced in depth are flowing through this zone.

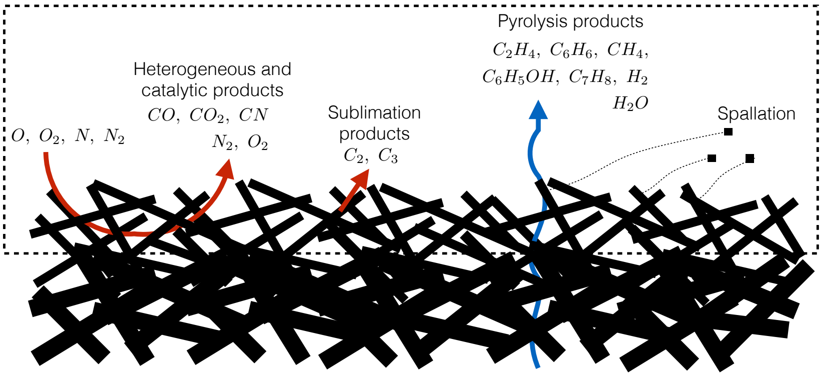

Figure 1.4: Schematic of the gas-surface interaction in the interface region of low density phenolic carbon fibers ablator for an Earth atmospheric entry.

The ablation of the TPS and the flow around the vehicle are strongly coupled. This dynamic interaction is one of the most challenging phenomena in the prediction of heat fluxes during atmospheric entries. Figure 1.5 shows that even recent models do not satisfyingly predict the thermal response of the heat shield. This figure compares predictions and flight data collected in the heat shield of the Mars Science Laboratory (MSL) of NASA. The temperature at the surface of the heat shield is shown and the values for thermocouples at several locations are presented in the plots (solid lines). If we observe the first thermocouple, the temperature prediction (dashed lines) overestimated the flight data in the hot region but it underestimates it in the colder region near the stagnation point. One of the main hypotheses to explain the discrepancy is linked to the transition from laminar to turbulent boundary layer induced by the change in TPS roughness [30]. This particular interaction between the turbulent/laminar regime and the erosion will not be studied in this work.

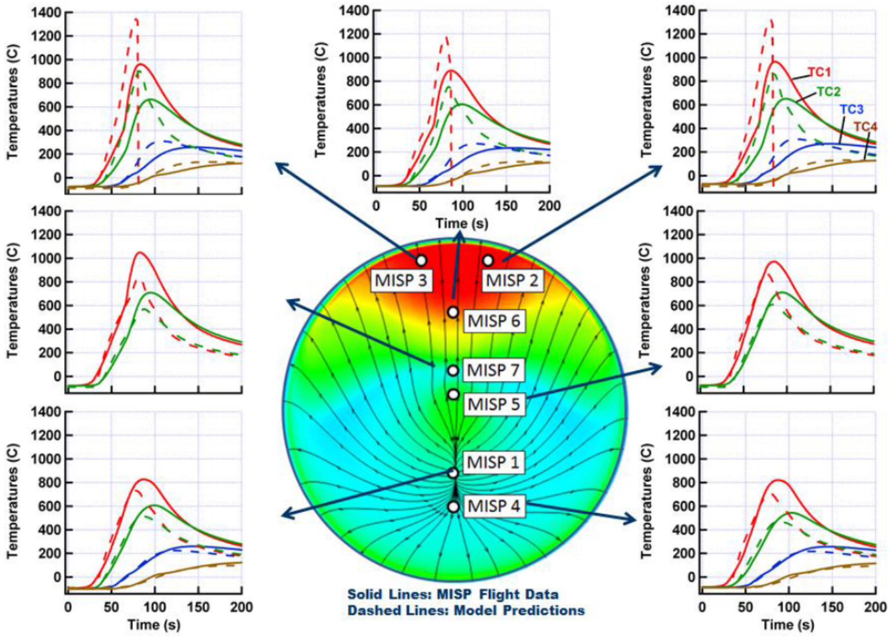

Figure 1.5: Thermal response of the Mars Science Laboratory heat shield during Mars atmospheric entry. Figure taken from [30]. The solid lines are thermocouple flight data, the dashed lines are simulation results.

1.2.2 Scales

The study of atmospheric entry vehicles involves multiple phenomena at different scales. The complexity of solving a multi-scale problem is an additional challenge when dealing with the numerical investigation of atmospheric entry. This section aims to provide to the reader an idea of the orders of magnitude for the phenomena involved as well as the definition and range of main non-dimensional numbers used throughout the text.

First of all, general details on several Space missions involving atmospheric entry are given in Table 1.2. These missions are chosen because they require ablative material for safe atmospheric entry. One can observe that new missions use low density materials (PICA).

Table 1.2: Atmospheric entry missions with their conditions. Values are extracted from Duffa [74] and references therein.

Mission and date	Atm.	Diameter $[m]$	TPS Material	TPS density $[kg/m^3]$	Velo-city $[km/s]$	Integrated heat flux $[MW/m^2]$
Apollo 4 (1967)	Earth	3.91	AVCOAT	530	11.2	300
Galileo (1995)	Jupiter	1.26	TWCP	1450	47.4	2000
Stardust (2006)	Earth	0.81	PICA	250	12.8	360
MSL (2012)	Mars	4.5	PICA	250	5.9	54.8

The atmospheric entry problem spans both several time scales and spatial scales. First, regarding the time scale, the main challenge is the difference between the characteristic time of the flow and the material thermal response time. The variables describing the flow around the capsule are going to change more rapidly than the quantities of interest in the material. However, some phenomena at the interface are tightly coupled. In addition, chemistry is usually very fast when compared to other phenomena. The time scale for the chemical production terms is already very different for strong radicals appearing in the plasma, the time scale for dissociation for example is $\sim \mathcal{O}(1e^{-6})$ and for the heterogeneous reactions for example $\sim \mathcal{O}(1e^{-4})$. Therefore, the homogeneous and heterogeneous chemical reactions introduce stiff terms in the equations. The spatial scales cover the microscopic phenomena inside the porous medium all the way up to scales of the order of the vehicle size. In order to study the evolution of the surface topology with the flow regime proposed in Velghe [228] for instance, one should consider additional scales: Kolmogorov for small scales in turbulent part of the flow ($\approx 10[\mu m]$) and Nikuradse scale for the roughness ($3 - 10\mu m$) to accurately capture the gas-surface interaction.

Non-dimensional numbers are usually used in the text to describe the problem; these are summarized in Table 1.3 and described briefly hereafter. The chemical regime is usually evaluated by the Damköhler number (Dam) described as the ratio between the effective reaction rate and the rate of mass transport (which can be caused either by diffusion or convection). Within this work, both diffusion and reaction limited regimes will be discussed. At low pressure, the diffusive and convective transports can be of the same order of magnitude, this is measured by the Peclet (Pe) number. The external flow is also described by the Reynolds (Re) number which computes the ratio between the convective and the viscous momentum transports. Within this work, the focus is solely on laminar flows involving low Re. The Prandtl (Pr) number characterizes the heat transfer convected versus conducted. In most of the cases studied, Pr is around one. The Mach (Ma) number evaluates the compressibility of the flow. Since the interest here is focused on the phenomena close to the wall, applications targeted in this work are usually at low Ma. The Knudsen (Kn) number determines the validity of the continuum assumption. It depends on the altitude of the flight but within this work, only the continuum regime is considered.

Table 1.3: Main non-dimensional numbers used in the text. The characteristic variables are the length of the problem L, the velocity U, the dynamic viscosity μ, the density ρ, the speed of sound c, the permeability κ, the thermal conductivity λ, the reaction rate k_{eff}, the average diffusion coefficient $\mathcal{D}$ and the mean free path $\bar{\lambda}$.

Non dimensional number	**Name**	**Value**	**Physical description**
Da	Darcy	$\frac{\kappa}{L^2}$	Permeability of the porous medium
Dam	Damköhler	$\frac{Lk_{eff}}{\mathcal{D}}$	Compare diffusive mass transport and reaction rate
Kn	Knudsen	$\frac{\bar{\lambda}}{L}$	Evaluate the continuum approximation
Ma	Mach	$\frac{U}{c}$	Evaluate the compressibility effects
Pe	Peclet	$\frac{LU}{\mathcal{D}}$	Compare convective and diffusive mass transport
Pr	Prandl	$\frac{c_p\mu}{\lambda}$	Compare viscous and thermal diffusion
Re	Reynolds	$\frac{\rho UL}{\mu}$	Compare inertial and viscous momentum transport
Th	Thiele	$\frac{L}{\sqrt{\frac{D_{eff}}{\left(s_f k_f\right)}}}$	Evaluate depth of diffusion allowed by chemical reactions

The internal flow inside the pores should also be characterized (Pe, Re, Kn) to correctly model the phenomena in the porous medium. Low density ablative materials are highly porous (up to 90% void for PICA for instance). However, the Pe number is usually small inside the porous medium as well as the

Reynolds number. The pore size is estimated to be below $100[\mu m]$ for these fibrous materials. The carbon fibers have a diameter of the order $\approx 10\mu m$. The porous medium is also characterized by a permeability measured by the Darcy number (Da). Despite the high porosity of low density ablative materials, their permeability is usually really low. Finally, the Thiele number (Th), which represents the depth of diffusion allowed by heterogeneous chemical reactions, is important because it characterizes if the ablation is a surface or volume phenomenon.

To conclude, the atmospheric entry problem has a strong disparity in the spatiotemporal scale however, dynamic interactions in between the phenomena at these scales implies the need to resolve these accurately.

1.3 State-of-the-art

In order to study atmospheric entry phenomena and, in particular, the response of ablative materials, experiments, modeling efforts and numerical works are conducted in parallel by different institutes and research centers across the globe. This section shortly reviews the current efforts in these three branches and highlights the contribution of this work.

1.3.1 Experiments

In-flight experiments are extremely costly and very rare. For the European efforts, let us cite the Atmospheric Reentry Demonstrator (ARD) which flew back in 1998 and demonstrated the capability of Europe to do Earth atmospheric reentry. Other flight experiments were planned or conducted such as the European eXPErimental Re-entry Testbed (EXPERT) which was supposed to be launched in 2014, but is still waiting for a launcher. Noteworthy is the recent successful flight of the Intermediate eXperimental Vehicle (IXV) that possessed several instruments including one able to measure catalycity at the wall of the thermal protection shield. At a smaller scale, the triple CubeSat Qarman designed at the von Karman institute proposes to study the atmospheric entry on a small platform [192]. Worldwide, several flight tests were conducted to learn about specific phenomena such as the reentry of the FIRE II capsule which was equipped with radiometers and calorimeters to evaluate the radiative heat flux. For ablative thermal protection system, three main space probes were instrumented to analyze material thermal response (Mars Pathfinder, Galileo and MSL). Among these, only MSL's heat shield was made of low density ablative material (PICA). The scientific community also relies on the analysis of degraded heat shields after Earth atmospheric entries which provide valuable data for ablative materials. This includes inheritance from NASA missions like Mercury, Gemini or the Apollo program but also, more recently, data collected on the Stardust capsule [127] and Hayabuza return capsule (JAXA mission) which were protected by a resin impregnated carbon ablators. The interested reader is referred to the book of Launius and Jenkins

[126] for a historical overview of atmospheric reentry capsules.

Flight conditions are very difficult to experimentally reproduce on Earth. However, several facilities across the globe offer the capability of reproducing a subset of realistic flight conditions. The main types of facilities, sorted in descending order for the running time, are continuous cold wind tunnels, blowdown facilities, arc jets, Inductively Coupled Plasma (ICP) wind tunnels and shock tunnels/tubes. Hypersonic cold wind tunnels are especially useful to study the aerodynamics of the vehicle for preliminary design for example. On the contrary, the time duration for shock tube experiments is very short but enables to reproduce very high temperature conditions, hence this type of experiment is used to investigate the chemically reacting gas associated with hypersonic flows. Arc jets and ICP plasma wind tunnel reproduce a high enthalpy environment during few seconds to several minutes which can be used typically to study the material response. Within this last category, the Plasmatron facility [31] installed at the von Karman Institute is an ICP wind tunnel which is extensively used to investigate high enthalpy environments encountered during atmospheric entry. The plasma is generated by an inductive coil and uses a high frequency, high power and high voltage generator ($400kHz$, $1.2MW$, $2kV$) [98]. Figure 1.6(a) shows the Plasmatron installation and Fig. 1.6(b) is a picture taken during the test of an ablative material [98]. Readers are referred to Panerai and Chazot [46] and Lu et al. [136] for a comprehensive overview of the high enthalpy and hypersonic facilities in the world.

1.3.2 Modeling efforts

Currently, design codes for the treatment of the ablative material are based on models developed in the sixties and introduced by Kendall et al. [14]. These models use simplified methods solving mass and heat transfer in the boundary layer. The flow of pyrolysis gases inside the porous medium and the chemical reactions among this gaseous phase are usually neglected. Recently many efforts have been dedicated to increasing the fidelity of these models, which were not always valid when applied to light ablators. For example, in Kendall's model, the ablation or coking phenomena are usually assumed negligible in the volume and considered as surface phenomena. For highly porous materials, this is a strong hypothesis which can lead to an underestimation of the material recession rate.

Based on increasing computational capabilities and specific experiments, development of new models for low density ablative materials have been proposed in the recent literature [118]. These models include physical phenomena neglected until recently. For example, these account for thermal nonequilibrium between the solid and fluid phase [206], radiation in-between fibers in the porous medium [175], finite rate chemistry [119], complex decomposition mechanism [147], mechanical ablation [65]. In addition, the porous

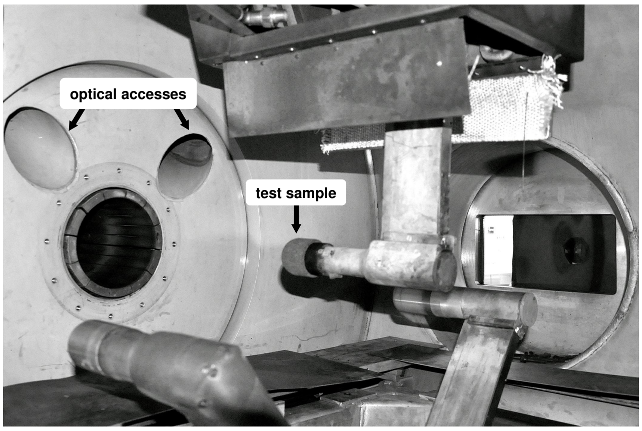

(a) VKI Plasmatron test chamber

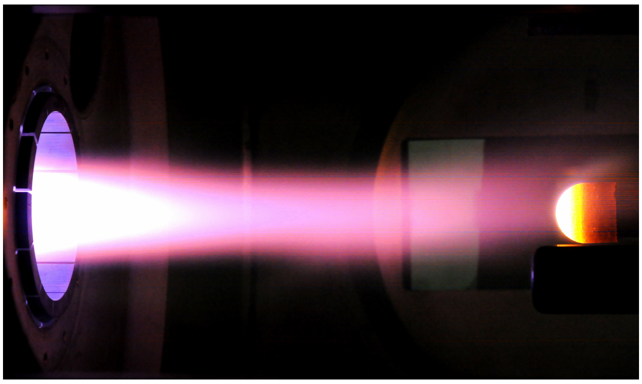

(b) Ablation test

Figure 1.6: VKI plasmatron test chamber overview and picture of subsonic ablative material test. Pictures taken by B. Helber.

medium is described with increased fidelity models including, for example, diffusion of the species inside the pores. More comprehensive literature reviews of modeling are proposed in Chapter 2 for ablative non-pyrolysing materials and in Chapter 6 for pyrolysing materials.

However, increasing model fidelity also demands more accurate description of the material to feed these models. For example, models of Kendall do not account for the presence of several species in pyrolysis gases. Accounting for multi-component flows and finite rate chemistry inside the thermal protection shield requires the development of more accurate decomposition mechanisms. Currently, a substantial effort is also dedicated to better characterize the material properties (tortuosity, permeability, conductivity) [169].

1.3.3 Numerical approaches

Similarly to the physical modeling, the numerical approaches to simulate the response of ablative materials still inherits from the developments in the 1960's. In these computational codes, the flow and the material are solved independently and then coupled using approximate boundary conditions [14, 13, 114]. In general, these methods can be roughly divided into four categories:

1. **Solving the flow**: In the first approach, the surface ablation is treated using a dedicated boundary condition in the flow simulation software. Surface and energy balance at the wall are solved to account for blowing and heat exchange at the surface of the material. This approach has been used extensively in a wide range of applications (i.e., heat shields, solid rocket nozzles) to study both charring and non-charring materials, using either equilibrium or finite-rate surface chemistry, giving satisfactory results [150, 52, 25, 26, 220, 224, 28].

2. **Solving the material**: The second approach is based on the one- or multi-dimensional transient computation of the conduction inside the material [14]. A lot of complexity can be added to the modeling if an accurate resolution of the processes taking place inside the material is sought [117]. However, simplified boundary conditions are usually used for the gas-solid interface in this kind of approach [14]. For instance, inviscid boundary-layer edge conditions are taken from separate simplified flowfield simulations, and the surface conditions (i.e., temperature or convective heat flux) are obtained by means of semi-empirical relations. Several material codes [54, 119, 68, 145] use this approach and Lachaud et al. [118] gives a complete overview of each code capabilities.

3. **Weak coupling**: This approach can be seen as a combination of the previous two. It is performed by coupling together two distinct solvers designed to compute the gas- (first approach) and the solid-side (second approach) of the problem [146, 116, 27, 50, 194]. Two separate tools are developed independently to solve the two sides of the problem and the exchange of the boundary information can be performed only at defined time steps. This strategy takes advantage of the different time scale in the flow and the material. Each code can march in time differently to ensure the most efficient technique. Several update and exchange strategies exist.

4. **Strong coupling**: The last strategy is similar to the previous because both the material and the flow are computed. However this type of approach proposes the use of a unified method in which material and flow are simulated within the same computational tool [91, 145, 202, 64].

The methods of the first type solve the full Navier-Stokes equations with chemical reactions to account for the phenomena in the free fluid region but uses very simplified techniques to consider the presence of a degrading material. On the contrary, the second type of method uses complex models inside the material but is generally based on an inviscid boundary layer approach to identify the conditions needed for the material code from the fluid side. These first two types of approaches have proved their validity in several cases but when the recession rate is high, typically for high velocity atmospheric entry, an accurate analysis of the TPS performances requires a coupled fluid/solid simulation [167]. Indeed, using a decoupling approach, some dynamic interactions cannot be captured accurately because the magnitude and distribution of the heat flux depends on the surface geometry and roughness.

The weak coupling strategy is a first step to increase the model fidelity of the phenomena at the interface. Conti et al.[61] proposed an early attempt to loosely couple Navier-Stokes solutions with material thermal response. The method is based on mass and energy balance at the interface and has been implemented and enhanced by several authors [50, 146, 116]. The main hypotheses usually assumed for weak coupling are (i) one dimensional description inside the material, (ii) chemical equilibrium considered in a control volume close to the surface, (iii) non-receding material, (iv) steady state flow field, (v) interactions between the fluid and the material are happening only at the surface. Keenan and Candler [113] have proposed a coupling solid/fluid which includes the effect of chemical non-equilibrium at the surface for non-charring and non-receding materials. Chen et al. [53] have investigated multi-dimensional shape change simulations for charring materials using a loosely coupled approach. However, developing a coupling strategy, one should take care of how and when the information at the interface is exchanged. For example, the weak coupling approach can lead to instabilities due to the severely non-linear behavior of the ablation process. A small change in the surface temperature could result in a large change of the mass blowing rate and, thence, the heat transfer. Several works have proposed an iterative procedure to remove the spurious oscillations [116, 50]. Nonetheless, the hypothesis (iv) and (v) are always considered.

For the last approach, since both phases are treated in the same domain of computation in a time accurate manner, this implies a better capturing of the interactions. However, even for the latter, the mass and heat exchanges are usually considered as *surface phenomena* while for low density ablative materials, the hypothesis of a mere surface ablation is not accurate enough [117]. Only few works propose to use the last type of approach and usually this goes along with strong assumptions on one side of the problem. In Nompelis et al. [161], the model in the material is restricted to the thermal conduction equation. In Martin [145], the phenomena in the porous domain are computed accurately but only Darcy's law for the momentum equation is solved. Therefore, in the free fluid, the permeability is adapted to mimic a Poiseuille flow hence the numerical strategy is restricted to plug flow in a channel. In Dal Bianco et al. [64], the authors propose to develop a strongly coupled approach but still based on the hypothesis that the ablation process is a surface phenomenon. In 2010, Lachaud et al. [120] introduced volume averaging to solve the concentration of species inside a flow tube reactor with a reactive porous plug accounting for volume ablation. The method is solving only one mass conservation law but the approach is interesting since it allows to have an equation valid in the entire domain. In the porous medium community, the problem of flows around and through porous media has received a lot of attention (see for example [21, 34, 112] but the publications for reactive flows and degrading porous medium [190, 7] are scarce. A detailed literature review for flow in porous medium will be presented in Chapter 2. To the author's knowledge, no paper published has proposed a multidimensional simulation of the flow and the ablative material response in the same domain of computation including finite rate chemistry and which remove the hypothesis of a loosely coupled approach to account for volume ablation. Therefore, the present thesis focuses on a strong coupling method to capture accurately the solid-gas interactions and, in particular, study the volume ablation phenomena. In addition, we investigate two other techniques including the development of a one dimensional material response code and its weak coupling with another CFD tool.

1.4 Objectives

The main objective of this thesis is to develop a numerical analysis tool to better characterize the interactions between the flow and the erosion of the porous medium. To accurately capture this interaction, a fully coupled approach is developed where both the material and the flow are solved in the same domain of computation. A continuum approach is developed to go progressively from a plain fluid region to a receding porous medium. In this case, the porosity of the ablative material will be treated as a variable of the computation to account for volumetric ablation through adequate source terms. The physico-chemical models implemented are accounting for multi-component flows in the porous medium, homogeneous and heterogeneous chemical reactions, variable thermodynamic and transport properties. In addition, physical models for the erosion of carbon fiber materials are discussed and we propose a new model to account for micro scale phenomena during the oxidation of these fibers. The developed tool is used to investigate the competition between surface and volume ablation phenomena.

This thesis is divided in eight chapters. After this introductory chapter, the conservation laws and the constitutive equations to model the problem are presented in Chapter 2. The development of the unique set of equations to model the flow and the porous medium inside the same domain of computation is presented. This chapter describes the physico-chemical models to simulate the non-pyrolysing material response. In the third chapter, the numerical schemes and the tools are presented. The implementation within the computational tool (ARGO) developed at Cenaero is based on a high-order discontinuous Galerkin method (DGM). This discretization method is summarized and specificities of the code to treat multi-component flows and the reactive porous medium are presented. Chapter 4 is dedicated to the test cases used to verify the implemented tool. The different aspects of the code are tested, non-calorically perfect gases, multi-component flows, presence of a porous medium and the heterogeneous reactions. The advantages of a unified method that accounts for volume ablation are shown in Chapter 5. The replication of experiments performed in the NASA Ames side arm facility is presented. In these experiments, a sample of carbon preform is oxidized by a low Reynolds flow at several temperatures. The interactions between the flow and the ablated geometry is studied and especially the competition between surface and volume ablation. The fidelity of the models is discussed and studied through a sensitivity analysis with respect to kinetics and transport properties. The particular case of pyrolysing materials is treated in Chapter 6 in which the one dimensional code developed is described. The chapter demonstrates the capability of DGM for discretizing the highly-nonlinear problem equations, discusses specificities of the numerical scheme to ensure its stability and presents verification and validation results. Chapter 7 presents the development and validation of a weakly coupled approach which is based on the one dimensional code described in Chapter 6 and a stagnation line code. Finally, the last chapter summarizes the achievements of the work and discusses its perspectives.

This work has been presented in several conference proceedings. These are given in the following as references by publication date [200, 201, 202, 203, 197, 196, 195, 194, 199]. In addition, the work has been submitted to one journal

- Schrooyen, P. and Hillewaert, K. and Magin, T.E. and Chatelain, P. , Fully Implicit Discontinuous Galerkin Solver to Study Surface and Volume Ablation Competition in Atmospheric Entry Flows. [submitted for publication].

CHAPTER 2

PHYSICAL MODELING

This chapter reviews the physico-chemical models to simulate atmospheric entry flows through and around a thermal protection heat shield. The thermodynamic and transport models to simulate multi-component atmospheric entry flows are described in the first part of this chapter. The second part deals with the treatment of the ablative material modeled as a reactive porous medium. Finally, the physico-chemical models to treat the interface between a porous medium and a free fluid region are discussed. A summary of the model used and the hypotheses is given at the end of this chapter. This work has been submitted for publication in a paper entitled "Fully implicit method to solve the competition between surface and volume ablation in atmospheric entry flows" [198].

2.1 Introduction

The design and sizing of the thermal protection heat shield of a space vehicle is a challenging task due to the complex physico-chemical processes occurring during the atmospheric entry. Comprehensive models describing the ablation of the TPS must account for a large number of coupled physical phenomena such as diffusion of oxygen from the boundary layer into the porous material and degradation of the material due to ablation and pyrolysis. The phenomena involved during an atmospheric entry are reviewed in Fig. 2.1 including a close-up at the surface of ablative material where chemical reactions occur. Numerical methods will be crucial in improving our predictive capabilities for the material response in high enthalpy flows. As explained in the first chapter, currently, most codes dissociate the modeling of the material response and the flow field. This kind of approach goes along with either (i) simplified hypothesis at the boundaries of the CFD or material solver, or (ii) with a weak coupling procedure between two distinct solvers. Since new low density ablative materials are highly porous, the validity of such approaches is questionable. Therefore, this work aims at simulating both solid and gaseous phases in the same domain of computation. The development of this kind of approach allows to progressively solve the phenomena in the plain fluid region to the one in reactive porous medium.

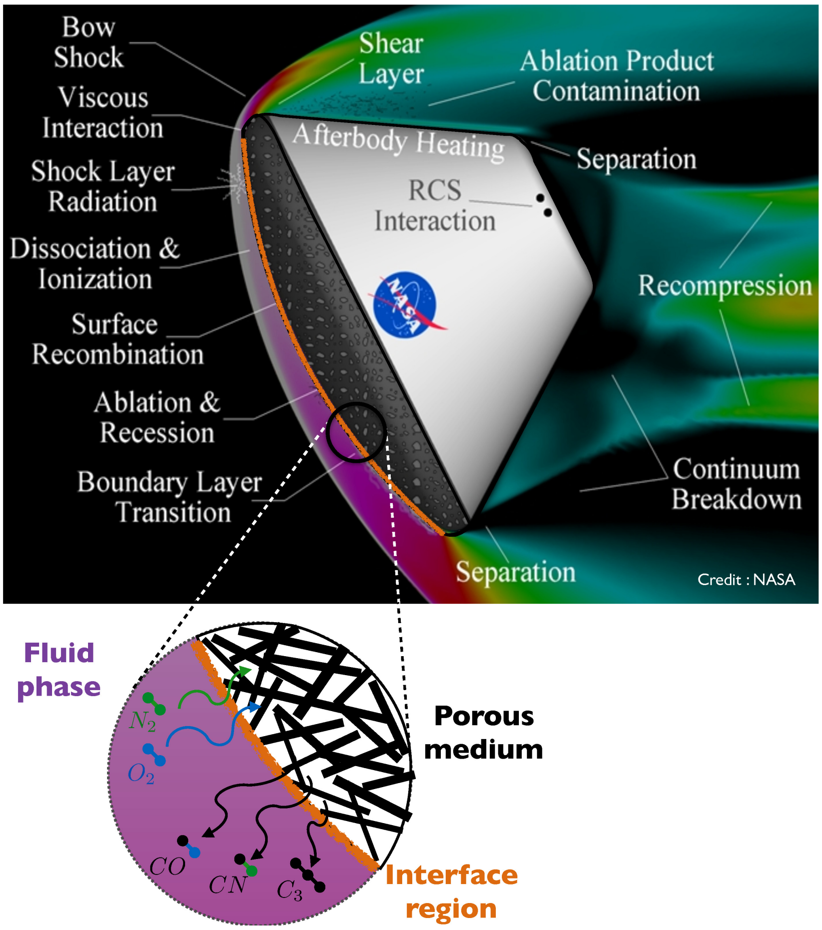

Figure 2.1: Schematic view of the phenomena involved in an atmospheric entry. Image adapted from [1].

The physical background of the phenomena involved during atmospheric entry is briefly summarized for both the flow and material fields. The assumptions and limitations of the models for each phase are described and readers are referred to the first chapter for a more detailed description of the physics of atmospheric entry.

---

[1] http://class.tamu.edu/media/22851/pecos.gif

Flow field

The external flow around a capsule is complex to simulate due the presence of shocks, turbulent phenomena, complex geometries, highly reactive plasma flows, radiation, etc. Capturing accurately the bow shock and the plasma shock layer is beyond the scope of this work. Our focus is on the viscous and chemically reactive layer close to the wall and its interaction with the erosion of the thermal protection material of the vehicle. In order to study properly the gas-surface interaction in such a problem, we use a fluid dynamical description based on multi-component Navier-Stokes equations. We consider the presence of several species, the chemical reactions within the gas phase (homogeneous) or with the heatshield (heterogeneous), and the variation of thermodynamic and transport properties with temperature and mixture composition. The species present in the mixture depend on the atmospheric composition and the products of material ablation. The temperature in the shock layer can reach 10000 $[K]$. Because of the high temperatures encounter in the flow, dissociated and ionized species can be present. The external flow field cannot be entirely dissociated from the material since the thermal protection material is highly porous hence a flow inside the material itself should be considered. For example, depending on the flight conditions, O_2 or N_2 molecules can penetrate the permeable wall and react in depth with the solid matrix of the porous material. In addition, the ablation of the solid part on top of the material leads to a shape change which will influence the external flow. For instance, Vignoles et al. [229] have shown that the erosion of the surface depends on laminar/turbulent regime of the flow on top of the material. The first part of this chapter recalls the governing equations to simulate such multi-component reactive flows without accounting for the presence of the porous material.

Material field

The complex modeling of a pyrolysing material is addressed in details in Chapter 6. Within this chapter, the model assumes that the ablative material is only composed of carbon fibers. The carbon fibers constitute the skeleton of the thermal protection material which might be impregnated by resin in a second step of the manufacturing process. Carbon preform material has been shown to have similar material properties as charred material [214]. Using this assumption, pyrolysis gases can be neglected simplifying considerably the model. Therefore, one should consider the presence of a fibrous medium with a variable microstructure since the fibers are progressively consumed by oxidation, sublimation, and nitridation processes. The second part of this chapter develops the model to treat the fibrous porous medium inside the same computational domain. The local volume averaging theory [234] is applied on the reactive Navier-Stokes equations derived in Section 2.2 in order to extend the validation of this approach to multiphase flows.

2.2 Multi-component reactive flows

This section focuses on the models and governing equations in the flow field without accounting for the presence of the porous medium.

2.2.1 Navier-Stokes equations

During an atmospheric entry trajectory, the flow regime around the capsule will be characterized by decreasing Knudsen number. At an altitude above $100\ km$, the Knudsen number is large (free molecular flow), and statistical mechanics should be used to describe the problem. At altitudes below $60\ km$, the collision frequency is typically $\sim \mathcal{O}(1e^{-6}\ m)$ and continuum mechanics can be used. Our interest is on the interaction between the ablation mechanism and the boundary layer which happens mostly in lower altitude part of the flight where continuum assumptions are valid. The aerothermal equations that have to be considered in this case are the Navier-Stokes equations with additional terms to account for the effects of variable thermodynamics properties, the presence of several species, diffusive transport models as well as complex reactive terms. The system of equations for mass, momentum and energy conservation can be written as

$$\frac{\partial \rho_i}{\partial t} + \nabla \cdot (\rho_i \mathbf{u}) = -\nabla \cdot (\mathbf{J}_i) + \dot{\omega}_i, \ \ \forall\, i \in \{1, N_s\} \tag{2.1}$$

$$\frac{\partial \rho \mathbf{u}}{\partial t} + \nabla \cdot (\rho \mathbf{u}\mathbf{u}) = -\nabla P + \nabla \cdot \boldsymbol{\tau}, \tag{2.2}$$

$$\frac{\partial (\rho E)}{\partial t} + \nabla \cdot (\rho H \mathbf{u}) = -\nabla \cdot \mathbf{q} + \nabla \cdot (\boldsymbol{\tau} \cdot \mathbf{u}) + \dot{\omega}_T, \tag{2.3}$$

where N_s is the number of species in the mixture, ρ_i is the species density ($\rho = \sum_i^{N_s} = 1\rho_i$), $\mathbf{u}$ the velocity vector, $\dot{\omega}_i$ is the chemical production term and $\dot{\omega}_T$ is the energy contribution related to the latter which will be explained in the following. The species diffusion flux is $\mathbf{J}_i$ which can be expressed

$$\mathbf{J_i} = \rho Y_i \mathbf{V}_i = -\rho \sum_{j=1}^{N_s} D_{ij} \mathbf{d}_j. \tag{2.4}$$

The D_{ij} are the multicomponent diffusion coefficients, $\mathbf{V}_i$ is the diffusion velocity, Y_i is the mass fraction of a species i and the driving forces are $\mathbf{d}_j = \nabla X_j$ in which baro and thermal diffusion have been neglected [153]. The latter which is the diffusion of species due to temperature gradient is termed the Soret effect. The X_i are the mole fractions and can directly be linked to the mass fractions using

$$X_i = \frac{W}{W_i} Y_i. \tag{2.5}$$

The viscous stress tensor $\boldsymbol{\tau}$ can be expressed as

$$\boldsymbol{\tau} = \mu \left[\left(\nabla \mathbf{u} + \nabla \mathbf{u}^t \right) - \frac{2}{3} \nabla \cdot \mathbf{u} \mathbf{I} \right], \tag{2.6}$$

assuming Stokes hypothesis for the bulk viscosity. The dynamic mixture viscosity is expressed by μ. The total energy E includes thermal and kinetic energy

$$E = e + \frac{\mathbf{u^2}}{2}. \tag{2.7}$$

The heat flux $\mathbf{q}$ in Eq. (2.3), neglecting the radiative contributions, is given by

$$\mathbf{q} = -\lambda \nabla T + \rho \sum_{i}^{N_s} h_i Y_i \mathbf{V}_i, \tag{2.8}$$

where λ is the translational mixture conductivity and h_i is the enthalpy of a pure species, in this case the Dufour effect which leads to heat diffusion due to concentration gradient is neglected [33] (symmetric term of the Soret effect). For the sake of simplification, we are assuming a single temperature model. The translational, rotational, vibrational and electronic energy modes are described by means of a common temperature. In addition to this system of equations, the perfect gas law linking pressure, density, and temperature is used. For a mixture of N_s perfect gases, Dalton's law applies and the total pressure can be expressed as the sum of the partial pressures

$$P = \sum_{i=1}^{N_s} P_i, \text{ with } P_i = \frac{\rho_i R T}{W_i} \tag{2.9}$$

with the universal gas constant $R = 8.3145\ [J \cdot mol^{-1} \cdot K^{-1}]$ and W_i the species molecular mass. The system (2.1)-(2.3) can be rewritten splitting convective and diffusive part as

$$\frac{\partial \mathbf{U}}{\partial t} + \nabla \cdot \mathbf{F}^c = \nabla \cdot \mathbf{F}^d + \mathbf{S} \tag{2.10}$$

where $\mathbf{U}$ is the vector of conservative variables (ρ_i, $\rho\mathbf{u}$, ρE) and the convective and diffusive flux are

$$\mathbf{F}^c = \begin{pmatrix} \rho_i \mathbf{u} \\ \rho \mathbf{u}\mathbf{u} + P\mathbf{I} \\ \rho \mathbf{u} H \end{pmatrix}, \ \mathbf{F}^d = \begin{pmatrix} -\mathbf{J}_i \\ \boldsymbol{\tau} \\ \boldsymbol{\tau} \cdot \mathbf{u} - \mathbf{q} \end{pmatrix}, \ \mathbf{S} = \begin{pmatrix} \dot{\omega}_i \\ \mathbf{0} \\ \dot{\omega}_T \end{pmatrix}. \tag{2.11}$$

Since most of the geometries studied in this work are 2D axisymmetric, the system of equation (2.10) can be written in cylindrical coordinates and simplified assuming axisymmetric flow and neglecting the azimuthal velocity. Several formulations exist, the most common solution is to write the system as

$$\frac{\partial (r\mathbf{U})}{\partial t} + \left(\frac{\partial (r\mathbf{F}_r^c)}{\partial r} + \frac{\partial (r\mathbf{F}_z^c)}{\partial z} \right) = \left(\frac{\partial \left(r\mathbf{F}_r^d\right)}{\partial r} + \frac{\partial \left(r\mathbf{F}_z^d\right)}{\partial z} \right) + (r\mathbf{S}), \tag{2.12}$$

the fluxes remains almost identical but an additional contribution should be considered in the source term and the diagonal entries of the viscous stress tensor are modified (see Ref. [141] for example). For an alternative option, the set of equations is kept in the conventional way but an additional source term for both the convective and diffusive parts appears in the two dimensional equations to account for components in the circumferential direction

$$\frac{\partial \mathbf{U}}{\partial t} + \left(\frac{\partial \mathbf{F}_x^c}{\partial x} + \frac{\partial \mathbf{F}_y^c}{\partial y} \right) = \left(\frac{\partial \mathbf{F}_x^d}{\partial x} + \frac{\partial \mathbf{F}_y^d}{\partial y} \right) + \mathbf{S} + \mathbf{S}^*, \tag{2.13}$$

where y is the radial and x the axial direction and the component $\mathbf{F}_x$ and $\mathbf{F}_y$ are identical for a 2D or 2D axisymmetric case, the only difference lies in $\mathbf{S}^*$

$$\mathbf{S}^* = \mathbf{S}^c + \mathbf{S}^d = -\frac{1}{r} \begin{pmatrix} \rho_i u \\ \rho u v \\ \rho v^2 \\ \rho v H \end{pmatrix} + \frac{1}{r} \begin{pmatrix} 0 \\ \tau_{yx} \\ \tau_{yy} - \tau_{\theta\theta} \\ \tau_{yx} u - \tau_{yy} v - q_y \end{pmatrix}, \tag{2.14}$$

with $\tau_{\theta\theta}$ expressed by

$$\tau_{\theta\theta} = -\frac{2}{3}\mu \left(\frac{\partial u}{\partial x} + \frac{\partial v}{\partial y} - 2\frac{v}{y} \right). \tag{2.15}$$

This solution to model axisymmetric problem also proposed in [124] was chosen for its ease of implementation since the only difference with a pure 2D case lies in the source term. The singularity of the source term when $r = 0$ renders the scheme not practical for finite volume method but it is not a problem for the numerical method chosen as explained in the next chapter.

Usually, in aerodynamics, the hypothesis of calorically perfect gas is assumed (i.e. constant thermodynamic properties with temperature). This last assumption is no longer valid for the high temperatures encountered in the flow field around the capsule. Indeed, during the atmospheric entry, the shock layer temperature can reach 10000 $[K]$ at the peak heating trajectory part while the material temperature is at 3000 $[K]$. In addition, for reacting flows, the thermodynamic properties are varying with the mixture composition. For example, Fig. 2.3 shows the error made on the specific heat at constant pressure assuming non-reacting calorically perfect gas (c_p^{const}) on this range of temperature. This will be discussed in the following.

To account for the variation of thermodynamic and transport properties in Eqs. (2.1)-(2.3), two options have been implemented within the computational tool Argo. In option one, an internal library featuring thermodynamic and transport properties was implemented in Argo. It is based on the NASA-7 polynomials database [148] for the thermodynamic properties and on simplified models for the transports. In option two, Argo has been coupled with an external library Mutation^{++} developed at the von Karman Institute [205]. Mutation^{++} is a user friendly library based on high accuracy models, updated data (e.g. collision integrals) and low computational cost algorithms. It provides thermodynamic and transport properties as well as reaction rates within the fluid phase for defined mechanisms. The internal library is not as accurate but it will be used to compare for example the mass diffusion models. In addition, it is convenient to run the Argo code without having to link with an external library and the use of the simplified models in the internal library can show a gain up to 20% in the computational time compared to the use of Mutation^{++}. The computation of thermodynamic and transport properties are extensively discussed in Ref. [141, 205] and summarized hereafter.

2.2.2 Thermodynamic properties

The system of equations (2.13) requires the evaluation of the energy and the enthalpy as well as their derivatives with the composition of the mixture and the temperature. Their derivatives are required in order to evaluate the Jacobians needed for implicit time integration. In addition, the Gibbs free energy should be evaluated to compute the equilibrium constant which is needed to calculate the reaction rates for finite rate chemistry. These properties of a pure gas can be computed knowing only its internal energy (e_i) and entropy (s_i). The enthalpy of the pure species is defined as

$$\rho_i h_i(T) = \rho_i e_i(T) + P_i. \tag{2.16}$$

The evaluation of the specific heats at constant pressure and volume can therefore be derived as

$$c_{pi} = \left.\frac{dh_i}{dT}\right|_P \text{, and } c_{vi} = \left.\frac{de_i}{dT}\right|_V, \tag{2.17}$$

where

$$c_{pi}(T) - c_{vi}(T) = \frac{R}{W_i}. \tag{2.18}$$

The Gibbs energy for a pure species can be defined as

$$g_i(P,T) = h_i(T) - s_i(P,T)T. \tag{2.19}$$

For a mixture of ideal gases, the thermodynamic properties are the sum of the quantities for pure species weighted by the composition of the mixture. Therefore, the gas mixture energy (enthalpy) is a linear combination of the species energy (enthalpy)

$$e(T) = \sum_{i=1}^{N_s} Y_i e_i(T) \text{, } h(T) = \sum_{i=1}^{N_s} Y_i h_i(T), \tag{2.20}$$

but the entropy should consider an additional term to account for the entropy of mixing

$$s = \sum_{i=1}^{N_s} Y_i \left(s_i(P,T) - \frac{R}{W_i} \ln\left(X_i\right) \right). \tag{2.21}$$

The internal library uses the NASA-7 [148] database to express the properties of pure species. This database provides accurate curve fits for the thermodynamic properties of pure species using experimental data. The use of polynomial expressions implies a straightforward analytical evaluation of thermodynamic functions of interest using for example Eq. (2.17) and (2.19). In the

NASA-7 database, the expression for the enthalpy of a species i reads

$$h_i(T) = RT\left(a_{i,1} + a_{i,2}\frac{T}{2} + a_{i,3}\frac{T^2}{3} + a_{i,4}\frac{T^3}{4} + a_{i,5}\frac{T^4}{5} + a_{i,6}\frac{1}{T}\right), \tag{2.22}$$

where the coefficient $a_{i,k}$ are tabulated for two ranges of temperature for each species. The enthalpy of a pure species can be separated in sensible and chemical enthalpies

$$h_i(T) = \underbrace{\int_{T_0}^{T} c_{pi} dT}_{\text{sensible}} + \underbrace{h_{f,i}^0}_{\text{chemical}} \tag{2.23}$$

where $h_{f,i}^0$ is the formation enthalpy defined at a chosen temperature T_0. In this implementation, the sensible and chemical enthalpies are separated. This is common for reacting flows [177] and it allows to directly identify the thermal source term due to chemical reactions and simplify the expression of the fluxes. Therefore, in the energy equation, an additional term should consider the formation enthalpy of the species produced

$$\dot{\omega}_T = -\sum_{i=1}^{N_s} \dot{\omega}_i h_{f,i}^0, \tag{2.24}$$

The internal library only uses NASA-7 database which is valid up to $5000\ [K]$ only. For higher temperature, the NASA-9 database implemented within the external library Mutation^{++}, should be used.

The Argo solver considers non-equilibrium flows, hence the evolution of each species is computed. When the chemical relaxation time is very short with respect to the flow characteristic time, chemical equilibrium can be assumed. In this case, only one mass conservation equation is solved and the mixture composition is given by the minimization of the mixture Gibbs energy while ensuring the elemental mass balance conservation [227]. Therefore, the mixture composition depends on pressure, temperature and elemental composition $Y_i = Y_i(P, T, \chi_j)$. The elemental mass fraction is noted χ_j for $j \in \{1, ..., N_e\}$. Chemical equilibrium is not implemented within Argo but the concept of chemical equilibrium is important to be introduced in order to understand the driving mechanisms and the important terms in the thermodynamic and transport properties. Indeed, solving chemical equilibrium flows, some dependancies which are implicit in the formulation presented in Eq. (2.1)-(2.3) should be explicitly stated and therefore can be analyzed. For example, the specific heat at constant pressure for non-equilibrium flow solver is given by

$$c_p^{Frozen} = \sum_{i=1}^{N_s} Y_i \left.\frac{dh_i}{dT}\right|_{P,\chi_j}, \tag{2.25}$$

where the exponent $Frozen$ refers to the non-equilibrium state at a given composition. For equilibrium flow solver, the dependance of the mass fraction with the temperature should be added to the specific heat

$$c_p^{Equil} = \sum_{i=1}^{N_s} \frac{\partial}{\partial T}(Y_i h_i) = c_p^{Frozen} + \sum_{i=1}^{N_s} h_i \left.\frac{dY_i}{dT}\right|_{P,\chi_j}. \qquad (2.26)$$

The comparison of the two specific heats in Fig. 2.3 shows the importance of chemical reactions at high temperature for plasma flows. The specific heats are computed with Mutation^{++} for a mixture of air (N_2, O_2, NO, N, O) and species products of carbon ablation (CO, CO_2, C, C_2, C_3, CN) at atmospheric pressure. The elemental mass fractions are fixed as $\chi_N = 0.75$, $\chi_O = 0.15$ and $\chi_C = 0.1$. The equilibrium composition for the mixture is shown in Fig. 2.2 for the range of temperature encountered in this work. At low temperature, the mixture is mainly composed of N_2, CO_2 and CO. Around 2500 $[K]$, atomic oxygen starts to be present in the flow. At higher temperature (around 5000 $[K]$ the molecular nitrogen starts to dissociate. This is more obvious at the logarithmic scale shown in Fig. 2.2(b). Note that, at the temperature considered, the ionization of species is negligible. The peak in the computation of c_p^{Equil} corresponds to the temperature at which the chemical reactions are occurring. Figure 2.3 shows also the error made by considering calorically perfect gas (c_p^{const}).

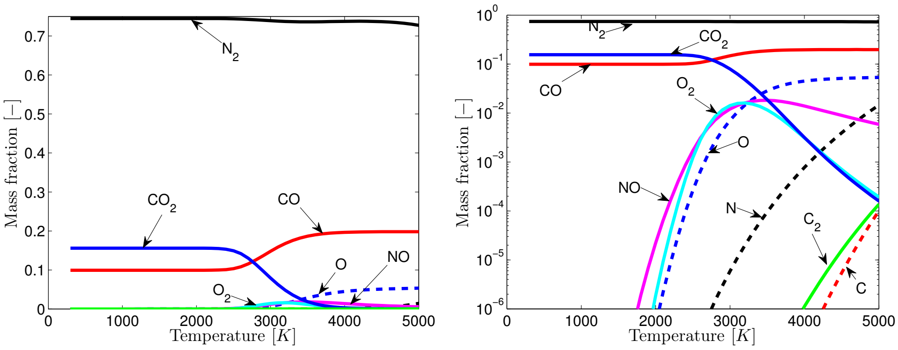

(a) Major components (b) Trace components

Figure 2.2: Chemical equilibrium composition at atmospheric pressure for a mixture of air including ablation components. The elemental composition is imposed as $N : 0.75$, $O : 0.15$, $C : 0.1$. The equilibrium is computed using Mutation^{++}.

For computational fluid dynamics, the speed of sound of the gas mixture should be defined. For non-equilibrium flow solver like Argo, the frozen definition is used

$$c_{Frozen}^2 = \gamma_{fr} \frac{p}{\rho}, \qquad (2.27)$$

where γ_{fr} is the frozen specific heat ratio

$$\gamma_{fr} = \frac{c_p^{Frozen}}{c_v^{Frozen}}. \qquad (2.28)$$

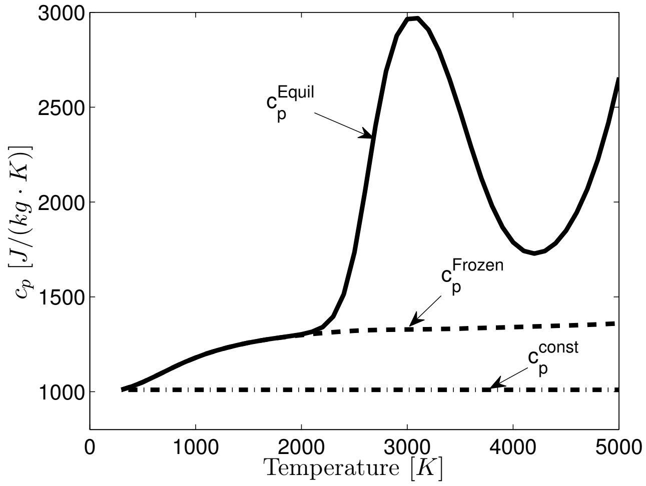

Figure 2.3: Comparison of frozen heat capacity at constant pressure, equilibrium and constant c_p assumption for a mixture of air with ablation species at atmospheric pressure. The thermodynamic variables are computed using Mutation^{++}.

2.2.3 Transport properties

While the thermodynamic properties of a mixture can be computed as the sum of properties of individual species, transport properties reflect the collisions at molecular level hence an interaction between pairs. Rigorously, the evaluation of the transport properties for a mixture should be computed based on kinetic theory. Interested readers are referred to Magin and Degrez [140] and references therein for a complete description of the rigorous computation of transport fluxes.

The dynamic viscosity and thermal conductivity can be obtained by solving linear transport systems which size are proportional to the number of species in the mixture as an approximate result of the Boltzmann equation by the Chapman-Enskog expansion. The result is based on collision integrals which link the macroscopic transport coefficients and the microscopic collision phenomena. Despite the development by Ern and Giovangigli [78] of low cost accurate algorithms to solve these systems, the use of approximate mixture rules is still widely spread. We use accurate computations of the transport properties relying on the solution of the Chapman-Enskog expansion through the use of the external library Mutation^{++} [205]. In addition, several simplified models are implemented in the internal Argo library. For the viscosity and conductivity, the internal library is based on polynomial expressions for each species [217] and Wilke's mixing rule [235] is implemented to compute the mixture properties. Wilke mixing rule has proved its accuracy for simulating low temperature plasma flows [168] and is easy to implement but its computational cost is quite high and exhibits degraded performances at high temperature. Figure 2.4(a) shows the rigorous computation for the viscosity and comparison with Wilke mixing rule for the mixture presented in the thermodynamic section. In Fig. 2.4(a), it can be observed that, at higher temperature, the interactions between neutral species and dissociated species render Wilke's approximation inappropriate.

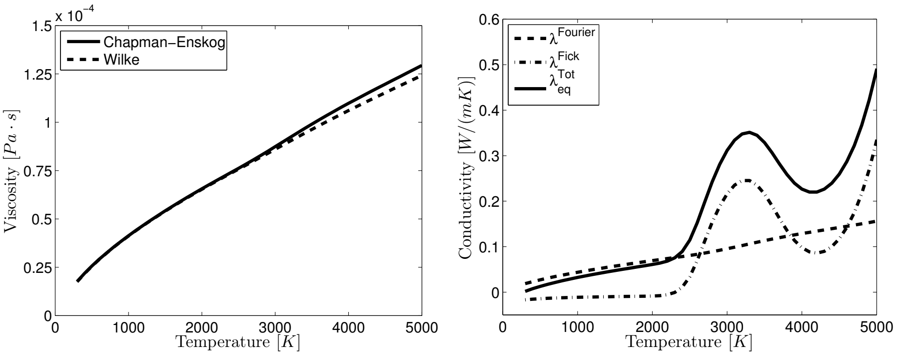

(a) Computation of the viscosity and comparison with approximate mixture rule

(b) Contributions in the evaluation of the conductivity.

Figure 2.4: Transport coefficients (viscosity and thermal conductivity) for a mixture of air with 5 species and carbon ablation species (CO, CO_2, CN, C, $C2$, $C3$) at atmospheric pressure. The data are computed using Mutation^{++}.

Regarding the heat flux, the relation in Eq. (2.8) can be expressed assuming chemical equilibrium as

$$\mathbf{q} = -\lambda^{Tot}\nabla T, \tag{2.29}$$

where λ^{Tot} is the equivalent total thermal conductivity which includes

$$\lambda^{Tot} = \lambda^{Fourier} + \lambda^{Eucken} + \lambda^{Reactive}. \tag{2.30}$$

The $\lambda^{Fourier}$ is the translational thermal conductivity of heavy particles and λ^{Eucken} is the correction to account for rotational, vibrational and electronic thermal conductivities. The $\lambda^{Reactive}$ is the equivalent thermal conductivity due to the diffusion of the species in the mixture with their enthalpy [88]

$$\sum_{i=1}^{N_s} \rho_i h_i \mathbf{V}_i = \underbrace{-\sum_{i=1}^{N_s} \rho_i h_i \left(\sum_{j=0}^{N_s} D_{ij} \frac{\partial X_j}{\partial T} \right)}_{\lambda^{Reactive}} \nabla T. \tag{2.31}$$

The total thermal conductivity, the reactive thermal conductivity and the Fourier conductivity are compared in Fig. 2.4(b). It can be observed that the largest contribution to the heat flux is due to species diffusion arising because of chemical reactions. We also observe that the $\lambda^{Reactive}$ can be negative for low temperature but the total thermal conductivity is always positive. The peak in the total thermal conductivity is identical to the one observed in the specific heat and correspond to the dissociation of major constituents in the mixture.

Finally, in order to compute the mass diffusive flux $\mathbf{J}_i$ (see Eq. (2.1)), the Fick law is used. The species diffusion term is implemented using a Ramshaw projection to ensure that, for any model used, the sum of all diffusive flux is null and therefore the total mass is conserved [216]. The flux can be expressed as

$$\mathbf{J}_i = -\rho D_{i,m} \frac{W_i}{W} \nabla X_i + \rho Y_i \sum_{k=1}^{Ns} D_{k,m} \frac{W_k}{W} \nabla X_k, \tag{2.32}$$

with $D_{i,m}$ the average diffusion coefficient of one species in the mixture defined as

$$D_{i,m} = \frac{(1 - Y_i)}{\sum_{j \neq i} \frac{X_j}{D_{ij}}}. \tag{2.33}$$

To evaluate the diffusion coefficients, four models have been implemented: a constant diffusivity, a constant Lewis number, a constant Schmidt number, or the coefficients can be rigorously obtained using collisional data from Mutation^{++}. For the constant Lewis number, the diffusion coefficients can be expressed as

$$D_{i,m} = D = \frac{\kappa}{Le\ \rho\ c_p^{Frozen}}, \tag{2.34}$$

and, for the constant Schmidt number, as

$$D_{i,m} = D = \frac{\mu}{Sc\ \rho}. \tag{2.35}$$

Comparisons between approximate and more advanced models are available in the literature [74, 4]. It has been shown that the simplest methods assuming a constant Lewis or Schmidt number generally lead to poor results. In addition, the results using approximate methods degrade with increasing temperatures. However, both will be used and compared for the problem investigated within this work.

2.2.4 Chemical kinetic model

As described in the introduction chapter, the shock layer and the region close to the wall is highly reactive. Solving non-equilibrium flows, the production rates due to chemical reactions should be computed and added in the source term of the mass continuity equations (Eq. (2.1)). For a system of N_s species with N_r reactions such as

$$\sum_{i=1}^{N_s} \nu'_{i,k} A_{i,k} \Longleftrightarrow \sum_{i=1}^{N_s} \nu''_{i,k} A_{i,k}, \tag{2.36}$$

where $A_{i,k}$ are the chemical species for the reaction k, $\nu_{i,k}$ the stoichiometric coefficients and the exponents $'$ and $''$ represent respectively the reactants and products. The production rate for a species i is expressed as

$$\dot{\omega}_i = W_i \sum_{k=1}^{N_r} (\nu''_{ik} - \nu'_{ik}) \left(k_{f,k} \prod_{j=1}^{N_s} \tilde{\rho}_j^{\nu'_{j,k}} - k_{b,k} \prod_{j=1}^{N_s} \tilde{\rho}_j^{\nu''_{j,k}} \right). \tag{2.37}$$

In Eq. (2.37), $\tilde{\rho}$ is the molar density, $k_{f,k}$ and $k_{b,k}$ are the forward and backward reaction rates. The forward reaction rates is expressed using an Arrhenius type law

$$k_{f,k}(T) = A_k T^{n_k} \exp\left(\frac{-Ea_k}{RT}\right), \tag{2.38}$$

where the pre-exponential factor (A_k), the temperature exponent (n_k) and the activation energy (Ea_k) are fitted usually to match experimental data. The backward reaction rate should satisfy the equilibrium relation

$$k_{b,k}(T) = \frac{k_{f,k}(T)}{K_{C,k}(T)}, \tag{2.39}$$

where the equilibrium constant is given, considering a reference pressure P_{ref}, by

$$\ln\left(K_{C,k}(T)\right) = -\sum_{i=1}^{N_s} (\nu''_{ik} - \nu'_{ik}) \left[\frac{W_i g_i(P_{ref}, T)}{RT} - \ln\left(\frac{P_{ref}}{RT}\right) \right]. \tag{2.40}$$

The internal Argo library does not contain the evaluation of such terms for homogeneous reactions. Hence to account for reactions among the gaseous phase, the user has to chose Mutation^{++} as the chemical library. The heterogeneous reactions with the solid phase is discussed in the next section.

2.3 Flows in reactive porous media

To understand the interactions between the fluid flow and the thermal protection system, we recall that both media are solved in the same domain of computation. The thermal protection material is treated as a porous medium. To solve both the material and the free flow region at the same time, it is needed to have a set of equations that will be valid in the whole domain. This section describes the development of such set of equations using the volume averaging theory.

2.3.1 Local volume averaging

In order to treat a multiphase system, the volume averaging approach is used to derive continuum equations [234]. Each phase is described by field quantities which are continuous within one specific medium but discontinuous in the whole volume. Solving the equations for each phase separately requires to account for the micro-structure of the porous medium which can be quite complex and computationally expensive. Using volume averaging theory, the equations describing one phase are averaged over a small Representative Elementary Volume (REV) such that the volume averaged quantities are continuous in space. Within this work, the system is composed of two phases, the solid matrix and the fluid phase (see Fig. 2.5).

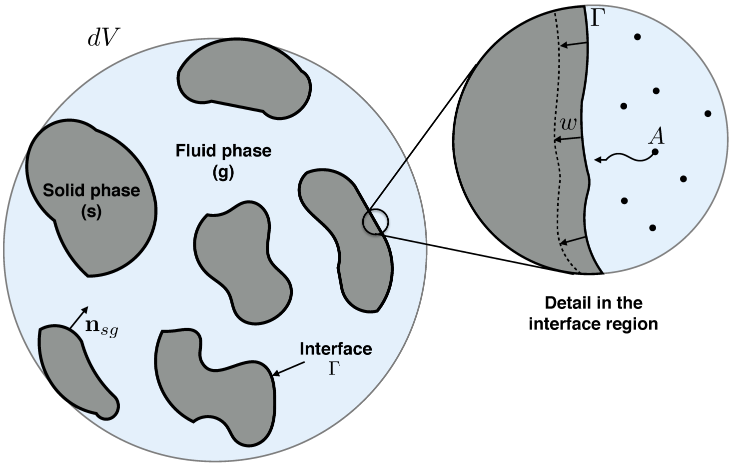

Figure 2.5: Volume averaging for the porous medium and zoom on the reacting solid-gas interface.

The pores of the medium are filled with a fluid phase g; the subscript s denotes quantities related to the solid phase. An averaging volume dV is therefore composed as $dV = dV_g + dV_s$, and the volume fraction of each phase is defined as

$$\epsilon_g = \frac{dV_g}{dV} \text{ , } \epsilon_s = 1 - \epsilon_g = \frac{dV_s}{dV}, \tag{2.41}$$

where the volume fraction of the fluid phase ϵ_g is usually called the porosity or the void fraction. The superficial average of a quantity α

$$\langle \alpha \rangle \;=\; \frac{1}{dV} \int_{dV_\gamma} \alpha \, dv, \tag{2.42}$$

has to be distinguished from the intrinsic average on a general phase $\gamma = g$ or s,

$$\langle \alpha \rangle_\gamma = \frac{1}{dV_\gamma} \int_{dV_\gamma} \alpha \, dv. \tag{2.43}$$

The two averages are linked by the volume fraction

$$\langle \alpha \rangle = \epsilon_\gamma \langle \alpha \rangle_\gamma. \tag{2.44}$$

As explained by Breugem [34], applying the volume averaging theory to a set of conservation laws can be compared to using a filter which will only preserve the large structures. Therefore, using this method, the averaged equations will model the macroscopic behavior of the physical phenomena considered. To apply this method to a set of partial differential equations, the volume average of derivatives has to be related to the derivatives of volume averaged quantities. This relation is given through the use of the theorem of local volume averaging detailed in several works such as [234, 213, 72, 93]. It states that

$$\langle \frac{\partial \alpha}{\partial t} \rangle = \frac{\partial \langle \alpha \rangle}{\partial t} - \frac{1}{dV} \oint_{\partial \Omega_g} (\alpha \mathbf{w}) \cdot \mathbf{n}_{gs} \, dS \; , \tag{2.45}$$

$$\langle \nabla \alpha \rangle = \nabla \left(\langle \alpha \rangle \right) + \frac{1}{dV} \oint_{\partial \Omega_g} \alpha \mathbf{n}_{gs} \, dS \; , \tag{2.46}$$

where $\mathbf{n}_{gs}$ is the unit normal vector directed from the fluid to the solid interface and $\partial \Omega_g$ is the boundary of the fluid phase. For a spatial vector, Eq. (2.46) is written

$$\langle \nabla \cdot \boldsymbol{\alpha} \rangle = \nabla \cdot \left(\langle \boldsymbol{\alpha} \rangle \right) + \frac{1}{V} \oint_{\partial \Omega_g} \boldsymbol{\alpha} \cdot \mathbf{n}_{gs} \, dS. \tag{2.47}$$

The equation (2.45) comes directly from the Reynolds transport theorem and the proof for equation (2.46) can be found in [213]. In addition, every quantity α can be expressed as the sum of a mean value and a deviatory part

$$\alpha = \langle \alpha \rangle_\gamma + \alpha'. \tag{2.48}$$

The elementary volume is defined such that

$$\langle \langle \alpha \rangle \rangle = \langle \alpha \rangle \text{ , and } \langle \alpha' \rangle = 0 \tag{2.49}$$

are satisfied. Hence the mean of the product can be written

$$\langle \alpha \beta \rangle \;=\; \langle \langle \alpha \rangle \langle \beta \rangle \rangle \;+\; \langle \alpha' \langle \beta \rangle \rangle \;+\; \langle \langle \alpha \rangle \beta' \rangle \;+\; \langle \alpha' \beta' \rangle \;=\; \langle \alpha \rangle \langle \beta \rangle \;+\; \langle \alpha' \beta' \rangle. \tag{2.50}$$

Finally, another interesting relation derived by Quintard et al. [184] links these integrals to spatial moments

$$\frac{1}{dV} \int_{\partial \Omega_g} \mathbf{n}_{gs} dS = -\nabla \langle 1 \rangle = -\nabla \epsilon_g, \tag{2.51}$$

Applying the volume averaging theory to the Navier-Stokes equations, the set of equations (mass, momentum and energy conservation laws) describes the macroscopic flow through the porous medium. Detailed development can be found in many publications [234, 34, 84, 66] but often assuming incompressible and non-reactive flows. The following subsections summarize the derivation of the Volume Averaged Navier-Stokes equations (VANS) for a multispecies flow through a reactive porous medium. For a computational domain filled with both a porous and a free fluid region, special care must be applied at the interface, this is treated in the next Section 2.4. Note that while the continuum hypothesis is valid in the external flow (low Knudsen number), it is questionable for the flow inside the pores. Our approach assumes that the continuum equations are still valid.

Mass conservation equation

In order to derive the mass conservation equation inside a porous medium, it is important to clearly separate the domains of the phases and the boundary separating the two (see Fig. 2.5). In order to develop the averaged mass conservation equation for a reactive porous medium, this approach follows two steps. First, the inner boundary condition at the interface is treated and then the volume averaging theory is applied to the mass conservation law inside the fluid phase.

For the inner boundary condition, according to Whitaker [233], the conservation of a component lying on a fluid-fluid interface can be written as

$$\underbrace{\frac{d\rho_{A,\Gamma}}{dt}}_{\text{interface accumulation}} + \underbrace{\nabla_\Gamma \cdot (\rho_{A,\Gamma}\mathbf{u}_{A,\Gamma})}_{\text{transport on the interface}} + \underbrace{\rho_{A,\Gamma}\left(\nabla_\Gamma \cdot \mathbf{n}_{gs}\right)\left(\mathbf{w}\cdot\mathbf{n}_{gs}\right)}_{\text{effect of changing interface area}}$$

$$= \underbrace{\left[\rho_{Ag}\left(\mathbf{u}_{Ag} - \mathbf{w}\right)\cdot\mathbf{n}_{gs} \; + \; \rho_{As}\left(\mathbf{u}_{As} - \mathbf{w}\right)\cdot\mathbf{n}_{sg}\right]}_{\text{interface flux from the bulk phase to the surface}} + \underbrace{\dot{\omega}^{het}}_{\text{heterogeneous reactions}} \tag{2.52}$$

where quantities with the subscript Γ are surface quantities, the operator ∇_Γ is the surface gradient, $\mathbf{w}$ is the velocity of the interface, ρ_A is the density of a component A and $\mathbf{u}_A$ is the component velocity including hydrodynamic velocity and diffusion velocity ($\mathbf{u}_A = \mathbf{u} + \mathbf{V}_A$). The third term of Eq. (2.52) represents the effect of changing the interface area which can be important for growing bubbles in fluid-fluid interfaces. In this particular case of a degrading porous medium, the accumulation at the surface, the transport of the species on the interface and the effect of changing the area of the interface will be neglected. Furthermore, the density of a component A in the s phase is assumed to be zero. Equation (2.52) can be simplified and the jump condition at the $g - s$ interface can be rewritten as

$$\left[\rho_{Ag}\left(\mathbf{u}_{Ag} - \mathbf{w}\right)\cdot\mathbf{n}_{gs}\right] \; = \; -\,\dot{\omega}^{het}. \tag{2.53}$$

Equation (2.53) translates the balance between the production of a species A and the flux of species going towards the surface. This relation at the interface will be used in the second step dealing with the fluid phase.

We move on to the second step of the approach and we consider only the gaseous phase. The mass conservation of a component A can then be obtained within this medium as

$$\frac{\partial\rho_A}{\partial t} + \nabla\cdot\left(\rho_A\mathbf{u}_A\right) = \dot{\omega}^{hom}, \tag{2.54}$$

where $\dot{\omega}^{hom}$ represents the homogeneous production term inside the phase. We recall that this equation does not account for what is happening at the boundaries of the flow domain. The volume average operator is applied to Eq. (2.54) and the volume averaged theorem Eqs. (2.45) and (2.46) is used to express the mass conservation law with respect to averaged quantities

$$\frac{\partial\langle\rho_A\rangle}{\partial t}-\frac{1}{dV}\oint_{\partial\Omega_g}\rho_A\mathbf{w}\cdot\mathbf{n}_{gs}dS+\nabla\cdot\langle\rho_A\mathbf{u}_A\rangle+\frac{1}{dV}\oint_{\partial\Omega_g}\rho_A\mathbf{u}_A\cdot\mathbf{n}_{gs}\,dS=\langle\dot{\omega}^{hom}\rangle, \tag{2.55}$$

The second and fourth term of the left hand side can be replaced using the jump condition (2.53) leading to

$$\frac{\partial\langle\rho_A\rangle}{\partial t}+\nabla\cdot\langle\rho_A\mathbf{u}_A\rangle=\langle\dot{\omega}^{hom}\rangle+\frac{1}{dV}\oint_{\partial\Omega_g}\dot{\omega}^{het}\,dS. \tag{2.56}$$

The second term of the left hand side includes the component velocity which can be divided into multi-species diffusion part and a velocity due to fluid motion. The notation $\mathbf{u}$ will be used for the bulk velocity and $\mathbf{J}_A$ for the diffusive flux of the species A within the mixture. The bulk transport can be rewritten

$$\begin{aligned}\nabla\cdot\langle\rho_A\mathbf{u}_A\rangle &= \nabla\cdot\langle\rho_A\mathbf{u}\rangle+\nabla\cdot\langle\rho_A\left(\mathbf{u}_A-\mathbf{u}\right)\rangle && (2.57)\\ &= \nabla\cdot\langle\rho_A\mathbf{u}\rangle+\nabla\cdot\langle\mathbf{J}_A\rangle. && (2.58)\end{aligned}$$

In the present work, the variables of the system are the intrinsic values (expressed with $\langle\,\rangle_g$). The mass conservation equation can therefore be expressed using Eq. (2.44) and (2.49) :

$$\underbrace{\frac{\partial\left(\epsilon_g\langle\rho_A\rangle_g\right)}{\partial t}}_{\text{Mass accumulation}}+\underbrace{\nabla\cdot\left(\epsilon_g\langle\rho_A\rangle_g\langle\mathbf{u}\rangle_g\right)}_{\text{Convective transport}}+\underbrace{\nabla\cdot\langle\rho_A'\mathbf{u}'\rangle}_{\text{Dispersive transport}}$$

$$=-\underbrace{\nabla\cdot\langle\mathbf{J}_A\rangle}_{\text{Diffusive transport}}+\underbrace{\langle\dot{\omega}^{hom}\rangle+\frac{1}{dV}\oint_{\partial\Omega_g}\dot{\omega}^{het}\,dS.}_{\text{Reaction terms}} \tag{2.59}$$

Depending on how the diffusive flux $\mathbf{J}_A$ is treated, the volume averaged equation will change. Whitaker used the relation

$$\langle\mathbf{J}_A\rangle=-D_{A,m}\nabla\rho_A \tag{2.60}$$

to express the diffusive flux, in which $D_{A,m}$ is the average mixture diffusivity. Equation (2.60) goes along with strong assumptions on the mass fractions and the variation of the total molar concentration. This relation will be used as a first approximation and will be corrected later. Applying volume averaging theory to the diffusive flux, it follows

$$\nabla\cdot\langle\mathbf{J}_A\rangle=\nabla\cdot\left(-D_{A,m}\left(\nabla\langle\rho_A\rangle+\frac{1}{dV}\oint_{A_{gs}}\mathbf{n}_{gs}\rho_A\,dS\right)\right). \tag{2.61}$$

In addition, one can use Eq. (2.48) to develop the term in the integral and split $\nabla\langle\rho_A\rangle$ in $(\nabla\langle\rho_A\rangle_g)\,\epsilon_g + \langle\rho_A\rangle_g\,(\nabla\epsilon_g)$ leading to

$$\nabla\cdot\langle\mathbf{J}_A\rangle = \nabla\cdot\left(-D_{A,m}\left(\epsilon_g\nabla\langle\rho_A\rangle_g + \langle\rho_A\rangle_g\nabla\epsilon_g + \frac{1}{dV}\oint_{A_{gs}}\mathbf{n}_{gs}\langle\rho_A\rangle_g\,dS\right.\right.$$
$$\left.\left.+\frac{1}{dV}\oint_{A_{gs}}\mathbf{n}_{gs}\rho'_A\,dS\right)\right) \qquad (2.62)$$

The theorem (2.51) can be used to simplify the second and third terms of the right hand side in this last equation

$$\nabla\cdot\langle\mathbf{J}_A\rangle = \nabla\cdot\left(-D_{A,m}\epsilon_g\left(\nabla\langle\rho_A\rangle_g + \frac{1}{dV_g}\oint_{A_{gs}}\mathbf{n}_{gs}\rho'_A\,dS\right)\right). \qquad (2.63)$$

The last term in Eq. (2.63) and the dispersive transport terms in Eq. (2.59) include the deviation ρ'_A which should be modeled to close the problem. Whitaker has shown that the deviation is proportional to the gradient of intrinsic density,

$$\rho'_A = \mathbf{b}_g\cdot\nabla\langle\rho_A\rangle_g. \qquad (2.64)$$

where $\mathbf{b}_g$ is a vector of closure variables. Using this closure model, the dispersive and diffusive transport can be expressed

$$-\nabla\cdot\langle\rho'_A\mathbf{u}'\rangle - \nabla\cdot\langle\mathbf{J}_A\rangle = \nabla\cdot\left((D_{eff}+D_{disp})\nabla\langle\rho_A\rangle_g\right), \qquad (2.65)$$

where D_{eff} is the effective diffusion coefficient and D_{disp} is the hydrodynamic dispersion coefficient expressed by

$$D_{disp} = -\langle\mathbf{u}'\mathbf{b}_g\rangle\text{ , and } D_{eff} = D_{A,m}\left(I + \frac{1}{dV_g}\oint_{A_{sg}}\mathbf{n}_{gs}\mathbf{b}_g\,dS\right). \qquad (2.66)$$

To evaluate the effective diffusion coefficient several correlations exist [232, 230, 183] and, in this work, the model used by Tomadakis et al. [222] is chosen where the effective diffusivity depends on the void fraction and the tortuosity (η) of the inner porous medium

$$D_{eff} = \frac{\epsilon_g}{\eta}D_{A,m}. \qquad (2.67)$$

The tortuosity measures the geometric lengths ratio between the real trajectory of a particle between two points in the porous medium and a straight line. The hydrodynamic dispersion coefficient is more complex to model than the effective diffusion coefficient [234]. However, the dispersive effects will only be important if the Peclet number based on the pore size is larger than one [234]. According to Lachaud [120], for the ablation of carbon fibers the Peclet number is smaller than unity leading to a negligible dispersive effects.

Concerning the evaluation of the source terms, we assume here that the deviations of the species density are negligibly small compared to the averaged value ($\langle \rho_i \rangle_g >> \rho_i'$). This leads for the homogeneous production term in the porous medium to

$$\langle \dot{\omega}_i^{hom} \rangle = \epsilon_g \langle \dot{\omega}_i^{hom} \rangle_g = W_i \sum_{k=1}^{N_r} (\nu_{ik}'' - \nu_{ik}') \left(k_{f,k} \prod_{j=1}^{N_s} \frac{1}{dV_g} \int_{dV_g} \left(\frac{\langle \rho_j \rangle_g}{W_j} \right)^{\nu_{j,k}'} dv \right.$$
$$\left. - k_{b,k} \prod_{j=1}^{N_s} \frac{1}{dV_g} \int_{dV_g} \left(\frac{\langle \rho_j \rangle_g}{W_j} \right)^{\nu_{j,k}''} dv \right). \quad (2.68)$$

Note that the forward and backward reaction rates in Eq. (2.68) are computed assuming thermal equilibrium in the porous medium which is an additional hypothesis discussed in the following. When the deviations become important a special treatment is needed [112] and the most accurate solutions are either to perform a DNS in simplified porous medium or Direct Simulation Monte Carlo (DSMC) in real material microstructure obtained by x-ray tomography as proposed for example in Ref. [204].

The heterogeneous reaction term in Eq. (2.59) can be expressed from a kinetics perspective assuming an irreversible first order reaction between the solid phase and the fluid phase

$$\frac{1}{dV} \oint_{\partial \Omega_g} \dot{\omega}^{het} \, dS = \frac{1}{dV} \oint_{\partial \Omega_g} -k_f \langle \rho_A \rangle_{gs} \, dS, \quad (2.69)$$

where k_f is the reaction rate, and $\langle \rho_A \rangle_{gs}$ is the area averaged density on the surface of the solid matrix. The area averaged density $\langle \rho_A \rangle_{gs}$ is assumed constant on the interface and equal to the bulk density, the reaction rate k_f is also supposed constant on the interface leading to

$$\frac{1}{dV} \oint_{\partial \Omega_g} \dot{\omega}^{het} \, dS = -S_f k_f \langle \rho_A \rangle_g. \quad (2.70)$$

where S_f is the volumetric surface occupied by the solid phase. The computation of this volumetric surface for a fibrous porous medium is detailed in Section 2.3.2. As for the homogeneous production term, the deviations of the reacting species density on the surface of the fibers from the bulk value are assumed negligible with respect to the averaged values. Kaviany [112] discusses a case for flames in porous media where the deviations become of the same order of magnitude as the averaged density but this is beyond the scope of this work. Again, a detailed molecular description of the phenomena in the reacting porous medium can be used to treat this problem accurately [204].

Finally, using these assumptions, the mass conservation equation for a component A in the fluid phase g is

$$\frac{\partial\left(\epsilon_g\langle\rho_A\rangle_g\right)}{\partial t}+\nabla\cdot\left(\epsilon_g\langle\rho_A\rangle_g\langle\mathbf{u}\rangle_g\right)$$
$$=\nabla\cdot\left(D_{eff}\nabla\langle\rho_A\rangle_g\right)+\langle\dot{\omega}^{hom}\rangle-S_f k_f\langle\rho_A\rangle_g. \quad (2.71)$$

In the case of material recession, a mass balance for the solid phase is added to the system of equations to track the evolution of the porosity. Inside the solid matrix, the medium is assumed continuous and therefore the mass conservation law becomes

$$\frac{\partial\rho_s}{\partial t}+\nabla\cdot\left(\rho_s\mathbf{v}_s\right)=0, \quad (2.72)$$

where ρ_s is the solid density and $\mathbf{v}_s$ is the solid velocity. In this case, the solid matrix is stationary. The solid domain is considered non-elastic, the recession will occur only at the boundary of the solid medium. Applying volume averaging theory, the mass conservation is written

$$\frac{\partial\langle\rho_s\rangle}{\partial t}+\frac{1}{dV}\oint_{\partial\Omega_s}-\left(\rho_s\mathbf{w}\right)\cdot\mathbf{n}_{sg}\,dS=0 \quad (2.73)$$

Notice that the mass lost by the solid will be gained by the fluid phase, the sum of the mass conservation laws for the considered volume will be zero. The jump condition at the boundary can therefore be expressed as

$$\begin{aligned}\left[\rho\left(\mathbf{u}_\gamma-\mathbf{w}\right)\cdot\mathbf{n}\right] &= 0 \quad (2.74)\\ \rho_g\left(\mathbf{u}_g-\mathbf{w}\right)\cdot\mathbf{n}_{gs} &= \rho_s\left(\mathbf{u}_s-\mathbf{w}\right)\cdot\mathbf{n}_{sg}. \quad (2.75)\end{aligned}$$

Using Eq. (2.75), the solid mass conservation equation becomes

$$\frac{\partial\left(\epsilon_s\langle\rho_s\rangle_s\right)}{\partial t}=\sum_{i=1}^{N_{sr}}S_f k_f\langle\rho_i\rangle_g, \quad (2.76)$$

where the sum is applied on every species reacting with the solid part.

Momentum conservation law

We now move on to the derivation of the momentum conservation law for the fluid phase. The general momentum equation for a compressible flow is given by

$$\frac{\partial(\rho\boldsymbol{u})}{\partial t}+\nabla\cdot\left(\rho\boldsymbol{u}\mathbf{u}\right)=\nabla\cdot\boldsymbol{\sigma}, \quad (2.77)$$

where $\boldsymbol{\sigma}$ is the stress tensor including, for a Newtonian fluid, the pressure and viscous terms (see Eq. (2.6))

$$\boldsymbol{\sigma}=-P\boldsymbol{I}+\boldsymbol{\tau}. \quad (2.78)$$

Applying volume averaging on both side of equation (2.77) and expressing it in terms of intrinsic averages, the transient and inertial terms become

$$\begin{aligned}\langle\frac{\partial(\rho\boldsymbol{u})}{\partial t}\rangle + \langle\nabla\cdot(\rho\boldsymbol{u}\boldsymbol{u})\rangle = {} & \frac{\partial(\epsilon_g\langle\rho\rangle_g\langle\boldsymbol{u}\rangle_g)}{\partial t} + \nabla\cdot(\epsilon_g\langle\rho\boldsymbol{u}\rangle_g\langle\boldsymbol{u}\rangle_g) \\ & + \nabla\cdot(\langle(\rho\boldsymbol{u})'\boldsymbol{u}'\rangle) + \frac{1}{dV}\oint_{\partial dV}\langle\rho\boldsymbol{u}\rangle_g(\mathbf{u}-\mathbf{w})\cdot\mathbf{n}\,dS. \qquad (2.79)\end{aligned}$$

and the right hand side can be expressed as

$$\begin{aligned}\langle\nabla\cdot\boldsymbol{\sigma}\rangle & = & -\nabla\left(\epsilon_g\langle P\rangle_g\right) - \frac{1}{dV}\oint_{\partial dV} P\cdot\mathbf{n}\,dS \qquad (2.80)\\ & + & \nabla\cdot\langle\boldsymbol{\tau}\rangle + \frac{1}{dV}\oint_{\partial dV}\boldsymbol{\tau}\cdot\mathbf{n}\,dS \qquad (2.81)\end{aligned}$$

The pressure term can be developed using equation (2.48) leading to

$$\begin{aligned}& -\nabla\left(\epsilon_g\langle P\rangle_g\right) - \frac{1}{dV}\oint_{\partial dV} P\mathbf{n}\,dS \\ & = -\epsilon_g\nabla\langle P\rangle_g - \langle P\rangle_g\nabla\epsilon_g - \frac{1}{dV}\oint_{\partial dV}\langle P\rangle_g\mathbf{n}\,dS - \frac{1}{dV}\oint_{\partial dV} P'\mathbf{I}\cdot\mathbf{n}\,dS. \qquad (2.82)\end{aligned}$$

The second and third term cancel each other due Eq. (2.51). The last term in equation (2.82) is the form drag and has to be modeled. Following the development for the viscous term in [84], the averaged stress tensor can be expressed as

$$\langle\tau\rangle = \nabla\cdot\left(\mu\left(\nabla\left(\epsilon_g\langle\mathbf{u}\rangle_g\right) + \nabla\left(\epsilon_g\langle\mathbf{u}\rangle_g\right)^t\right) - \frac{2}{3}\nabla\cdot\left(\epsilon_g\langle\mathbf{u}\rangle_g\right)\right) \qquad (2.83)$$

The stress tensor becomes

$$\langle\nabla\cdot\boldsymbol{\sigma}\rangle = -\epsilon_g\nabla\langle P\rangle_g + \nabla\cdot\langle\boldsymbol{\tau}\rangle + \frac{1}{dV}\oint_{\partial dV}\left(-P'\mathbf{I}+\boldsymbol{\tau}\right)\cdot\mathbf{n}\,dS. \qquad (2.84)$$

The surface integrals terms in equation (2.79) and (2.84) as well as the dispersive term in equation (2.79) have to be modeled to close the system of equations. In equation (2.79), the last term represents the exchange of momentum due to the heterogeneous reaction with the solid phase. The last term in equation (2.84) is a drag term imposed by the presence of the solid phase in the porous medium. In Whitaker [234], the closure model for the drag term is solved assuming a proportionality between the spatial deviation (P' and $\mathbf{u}'$) and the intrinsic velocity ($\langle\mathbf{u}\rangle_g$). Comparing the developed expression (see [234]) to the empirical Darcy's law, Whitaker [234] proposes to model the drag term using

$$F_{drag} = \frac{1}{dV}\oint_{\partial dV}\left(-P'\mathbf{I}+\boldsymbol{\tau}\right)\mathbf{n}\,dS = \frac{-\mu}{\kappa}\epsilon_g^2\langle\boldsymbol{u}\rangle_g. \qquad (2.85)$$

where μ is the dynamic viscosity already introduced and κ is the permeability of the medium. The permeability is a parameter depending on the microstructure which measures the ability of a fluid to flow through the porous material.

This model is only valid if the Reynolds number based on the length of a pore is small enough for the inertial term to be negligible. Assuming incompressible and Stokes flow, Darcy's law can be retrieved at steady state

$$\nabla P = -\frac{\mu}{\kappa}\epsilon_g \langle \boldsymbol{u} \rangle_g = -\frac{\mu}{\kappa}\langle \boldsymbol{u} \rangle. \tag{2.86}$$

Breugem [34] has shown that the correlation between the deviations in Eq. (2.79) is often negligible with respect to the drag force term if the Reynolds number in the pores is small. Note that, since we neglect the product of deviations, the average involving a multiplication of three quantities can be simplified to

$$\langle \rho \boldsymbol{u} \rangle_g \langle \boldsymbol{u} \rangle_g \approx \langle \rho \rangle_g \langle \boldsymbol{u} \rangle_g \langle \boldsymbol{u} \rangle_g. \tag{2.87}$$

The exchange of momentum due to volume change will also be neglected in the case of fiber ablation because it can be shown that Darcy's term will be predominant. This leads to

$$\frac{\partial(\epsilon_g \langle \rho \boldsymbol{u} \rangle_g)}{\partial t} + \nabla \cdot (\epsilon_g \langle \rho \rangle_g \langle \boldsymbol{u} \rangle_g \langle \boldsymbol{u} \rangle_g) = -\epsilon_g \nabla \langle P \rangle_g + \nabla \cdot \langle \boldsymbol{\tau} \rangle + \frac{\mu}{\kappa}\epsilon_g^2 \langle u \rangle_g. \tag{2.88}$$

The classical momentum equation is readily obtained if ϵ tends to one (free fluid region). To treat this equation in the DG framework, a conservative form should be retrieved. In this work, we simplify the left and right hand side by the volume fraction to obtain

$$\frac{\partial(\langle \rho \boldsymbol{u} \rangle_g)}{\partial t} + \nabla \cdot (\langle \rho \rangle_g \langle \boldsymbol{u} \rangle_g \langle \boldsymbol{u} \rangle_g) = -\nabla \langle P \rangle_g + \nabla \cdot \langle \boldsymbol{\tau} \rangle_g + \frac{\mu}{\kappa}\epsilon_g \langle u \rangle_g \tag{2.89}$$

in which we have considered that the terms

$$F_1 = \rho u u \frac{1}{\epsilon}\frac{\partial \epsilon}{\partial x} \tag{2.90}$$

$$F_2 = \rho u \frac{1}{\epsilon}\frac{\partial \epsilon}{\partial t} \tag{2.91}$$

are negligible with respect to the drag force. Note that the second term is exactly zero for non-reactive porous medium. In order to show the validity of these assumptions, consider a 1D problem of a flow through a porous plug. Using nominal values for low density ablative material, these terms can be computed and are shown in Fig. 2.6. We observe that these additional terms are at least 5 orders of magnitude lower than the drag force. Therefore, we will neglect these and consider Eq. (2.89) in the system of equations. This is further verified in Chapter 4 which shows good agreement with other methodologies in several configurations.

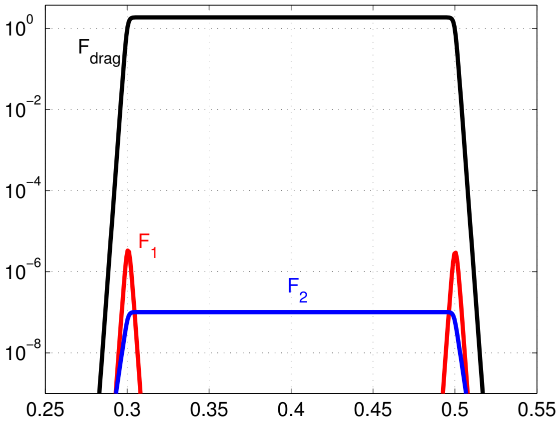

Figure 2.6: Comparison of the additional terms F_{drag}, F_1, F_2. The limit of the porous medium are set at $x = 0.3$ and $x = 0.5$.

Energy conservation law

For the energy equation, thermal equilibrium between the two phases is assumed

$$\langle T \rangle = \langle T_s \rangle_s = \langle T_g \rangle_g . \tag{2.92}$$

The assumption of thermal equilibrium is the most common approach in material response codes [155, 118, 24, 67] and it will be used here. Only few work have been dedicated to the investigation of two temperature models for ablative materials [80, 181, 206]. Removing the assumption of local thermal equilibrium implies the resolution of an additional energy equation and the modeling of the exchange between the two phases. Developing a two temperature model is even more complex for reactive porous medium where the heat release by heterogeneous chemical reactions should be distributed between the two phases [181]. According to Puiroux et al. [181], thermal equilibrium can be assumed if the Peclet number for the heat transfer in the pores is small

$$Pe = RePr = \frac{\epsilon_g \rho_g c_{p,g} L_p \langle u \rangle_g}{\lambda_g} . \tag{2.93}$$

In the cases studied, the gas flow velocity in the porous medium is generally small $\langle u \rangle_g \sim \mathcal{O}(1\ m/s)$ and the characteristic length of the pores is $L_p \sim \mathcal{O}(100\ \mu m)$ ensuring a small Peclet number [123]. Therefore, thermal equilibrium will be assumed and only one energy equation is solved.

Applying the volume averaging theory to the energy equation for the solid and fluid phase respectively, the equations for each phase is written

$$\frac{\partial \langle \rho E_s \rangle}{\partial t} = \nabla \cdot \left(\lambda_s \left(\epsilon_s \nabla \langle T_s \rangle_s + \frac{1}{dV} \oint_{\partial dV_s} \mathbf{n}_{s,g} T'_s \, dS \right) \right) + \frac{1}{dV} \oint_{\partial dV_s} \mathbf{n}_{s,g} \lambda_s \nabla T_s \, dS \quad (2.94)$$

$$\frac{\partial \langle \rho E_g \rangle}{\partial t} + \nabla \cdot (\epsilon_g \langle \rho \rangle_g \langle H \rangle_g \langle \mathbf{u} \rangle_g) = \nabla \cdot (\langle \boldsymbol{\tau} \cdot \mathbf{u} \rangle) - \nabla \cdot \left(\langle \sum_i^{N_s} J_i h_i \rangle \right) + \nabla \cdot \left(\lambda_g \left(\epsilon_g \nabla \langle T_g \rangle_g + \frac{1}{dV} \oint_{\partial dV_g} \mathbf{n}_{g,s} T'_g \, dS \right) \right) + \frac{1}{dV} \oint_{\partial dV_g} \mathbf{n}_{g,s} \lambda_g \nabla T_g \, dS. \quad (2.95)$$

The same methodology as presented in previous sections is used to develop Eq. (2.94) and (2.95) and the full derivation can be found in Whitaker [234]. Again, the product of deviations as for the momentum equation are neglected in this case. Using Eq. (2.92) and summing the two previous equations, the exchange terms at the interface vanish leading to

$$\frac{\partial \langle \rho E_{tot} \rangle}{\partial t} + \nabla \cdot (\epsilon_g \langle \rho \rangle_g \langle H \rangle_g \langle \mathbf{u} \rangle_g) = \nabla \cdot (\lambda_{eff} \nabla T) + \nabla \cdot (\langle \boldsymbol{\tau} \cdot \mathbf{u} \rangle) - \nabla \cdot \left(\langle \sum_i^{N_s} J_i h_i \rangle \right), \quad (2.96)$$

with H being the total enthalpy of the gaseous phase, and ρE_{tot} the total energy which is composed of the energy of the static solid phase and the energy of the fluid phases

$$\langle \rho E_{tot} \rangle = \epsilon_g \left[\langle \rho \rangle_g \left(\langle e \rangle_g + \frac{\langle \mathbf{u} \rangle_g^2}{2} \right) \right] + \epsilon_s \langle \rho \rangle_s \langle e \rangle_s. \quad (2.97)$$

The λ_{eff} in Eq. (2.96) is an effective conductivity inside the porous medium defined as

$$(\epsilon_g \lambda_g + \epsilon_s \lambda_s) \nabla \langle T \rangle + \frac{\lambda_g}{dV} \oint_{\partial dV_g} \mathbf{n}_{g,s} T'_g \, dS + \frac{\lambda_s}{dV} \oint_{\partial dV_s} \mathbf{n}_{s,g} T'_s \, dS = \lambda_{eff} \nabla \langle T \rangle. \quad (2.98)$$

To ensure the closure of the problem, the effective conduction requires in turn a model. Several correlations exist which will depend on the microstructure of the porous medium (connections within the solid phase). For a solid matrix composed of two dimensional array of non-touching cylinders, Ochoa-Tapia et al. [163] have proposed the use of

$$\frac{\lambda_{eff}}{\lambda_g} = \frac{2\kappa^r - \epsilon_g (\kappa^r - 1)}{2 + \epsilon_g (\kappa^r - 1)}, \quad (2.99)$$

where κ^r is the ratio between the solid and fluid conductivity. However, Fig. 2.7 shows that for really high porosity typical of new low density ablative materials, the effective conductivity is almost independent of the ratio between phase conductivities. Therefore, as a first approximation, the deviation in Eq. (2.98) are neglected and the effective conductivity is assumed to be

$$\lambda_{eff} = \epsilon_s \lambda_s + \epsilon_g \lambda_g. \tag{2.100}$$

Equation (2.100) is the upper Wiener's bound [181] for the conductivity of two-phases material. This expression can be corrected by solving the closure problem (Eq. (2.98)) if sufficient microstructure information is known. In general, the effective conductivity also includes the contribution for radiation between fibers which is difficult to characterize otherwise. This will be further discussed in Section 2.5.2.

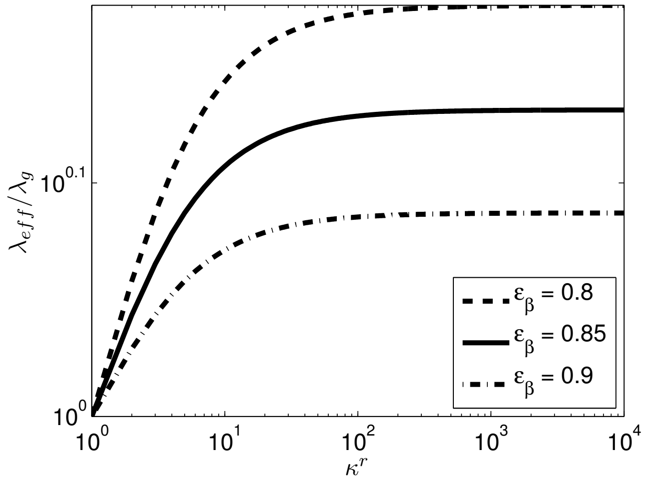

Figure 2.7: Effective conductivity and dependence with respect to intrinsic phase conductivities

2.3.2 Fiber scale oxidation

In order to compute properly the reaction term in Eq. (2.59) and (2.76), one should look at the microstructure of the porous medium. For low density material like PICA, the porous medium is made of several solid phases (phenol and carbon fibers). As explained in the introduction, the effort is focused on the preform material made only of carbon fibers. In order to have an idea of the microstructure, Fig. 2.8 shows the 3D reconstruction of Fiberform using synchrotron X-rays micro tomography; figure is taken from Panerai et al. [169]. The Fiberform is made of carbon fibers and is the skeleton of PICA. The carbon fibers of these highly porous materials can be clearly observed.

As shown in Eq. (2.70), assuming an irreversible first order reaction between the solid phase and the fluid phase, the heterogeneous production term

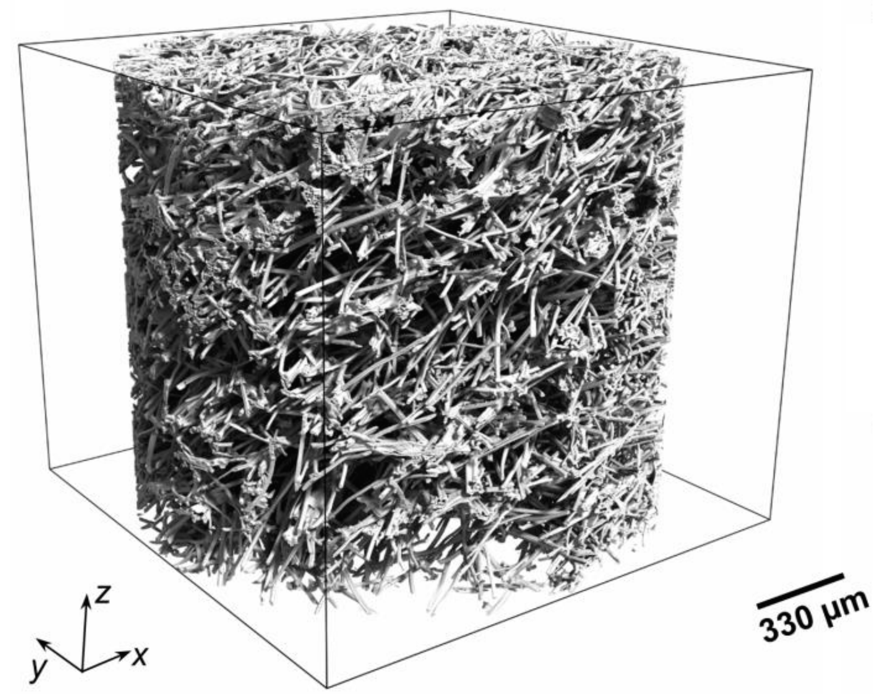

Figure 2.8: 3D reconstruction of microtomography measurements for Fiberform. Figure taken from Panerai et al. [169].

is

$$\dot{\omega}_{het} = -S_f k_f \langle \rho_A \rangle_g, \tag{2.101}$$

where k_f is the forward reaction rate which is assumed constant on the surface of the fibers, and $\langle \rho_A \rangle_g$ is the intrinsic density of a reactant A. The specific surface (S_f) is defined as

$$S_f = \frac{A_w}{dV}, \tag{2.102}$$

where A_w and dV are respectively the contact surface of the solid matrix with the fluid phase and the control volume. The control volume can be expressed using the relation (2.41) as the volume occupied by the fibers divided by the solid volume fraction. Therefore, the computation of the specific surface requires to model the change in the microstructure to compute A_w and ϵ_s during the ablation process. First, two macroscopic models are proposed and described in the following. Finally, the hypothesis of assuming first order heterogeneous reactions is discussed.

Cylindrical model

The model for the oxidation at the scale of the fibers was proposed originally by Lachaud et al. [120], it assumes that the fibers are randomly distributed as well as a uniform and radial recession of these. In addition, the fibers are assumed to be cylindrical. Figure 2.9 shows the Scanning Electron Micrographs (SEM) [120] of oxidized carbon fibers together with the associated model. A close-up of the thinning of the fibers at the gas-material interface is shown. The model is further referred as the cylindrical model.

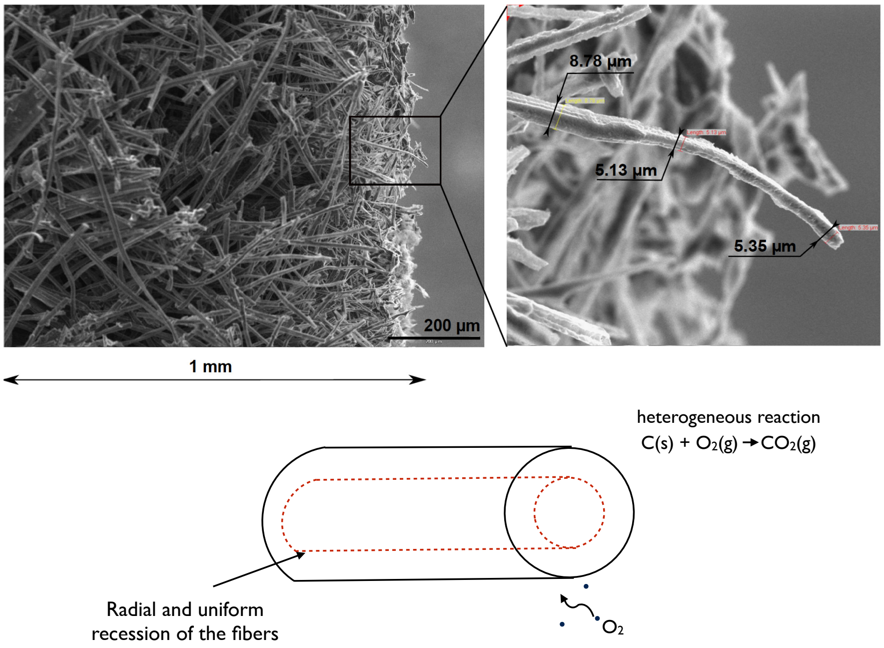

Figure 2.9: SEM of oxidized carbon preform fibers with a zoom on fibers near the facing flow (Figure taken from Lachaud et al. [120]) and the associated cylindrical model.

The fibers (solid phase) are assumed rigid, stationary and the mass loss will occur only at the surface of the solid matrix, the solid mass conservation is

$$\frac{\partial\left(\epsilon_s\langle\rho_s\rangle_s\right)}{\partial t}=\dot{\omega}_{het}, \tag{2.103}$$

where $\langle\rho_s\rangle_s$ is the intrinsic solid density which is not changing. Equation (2.103) is therefore used to track the change in porosity. The idea of Lachaud et al. [120] is to link the radius of the fibers with the porosity of the medium. For a radial and uniform recession of the fibers, the solid volume fraction at any decomposition state is

$$\epsilon_s=\frac{N_f\pi r^2 L_f}{dV}. \tag{2.104}$$

where N_f is the number of fibers in the averaging volume dV, L_f is their length and r the radius. Therefore, the average radius can be computed based on the local solid volume fraction and initial configuration (r_0, $\epsilon_{s,0}$)

$$\frac{r_0^2}{\epsilon_{s,0}} = \frac{r^2}{\epsilon_s}. \tag{2.105}$$

This comes directly from geometric considerations and allows to express the volumetric surface parameter needed in the heterogeneous production term (see Eq. (2.59) and (2.73)). For a porous medium composed of N_f fibers with a related porosity described by Eq. (2.104), the specific surface can be expressed as

$$S_f = \frac{N_f 2\pi r L_f \epsilon_s}{N_f \pi r^2 L_f} = \frac{2}{r_0}\sqrt{\epsilon_{s,0}\,\epsilon_s}. \tag{2.106}$$

Simplified sinusoidal model

Depending on the flow conditions, the hypothesis of a uniform and radial recession of the fibers at the micro scale can be a strong assumption. Figure 2.10 shows that, for particular conditions, the fibers are presenting a pitting phenomenon [170]. Another model, referred as the sinusoidal model, is proposed in this work to relax these hypothesis. The model is detailed here and the motivation of this choice will appear clearly in Chapter 5.

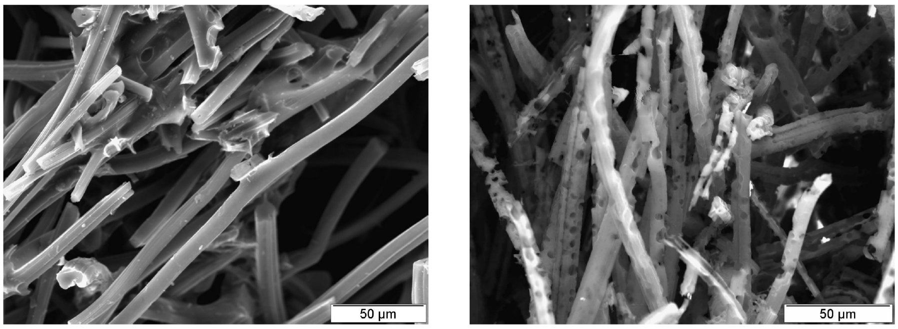

Figure 2.10: Micrographs of virgin carbon fibers (left) and ablated carbon fibers (right). The erosion of the fibers leads to a pitting phenomena for particular conditions. Figure taken from Ferguson et al. [79]

This model assumes that during the ablation of the fibers, these will be composed of sinusoidal holes of a given depth and length. The length and depth are determined based on SEM micrographs or tomography data. The holes on the fibers are modeled as circular ridges which seems to be a good approximation nonetheless. The erosion of the fibers is therefore composed of two steps, during the first phase, the holes are formed and after, the erosion of the fibers is assumed uniform (see Fig. 2.11). During the first phase, the radius of the fibers remains constant (see Fig. 2.11(a)), but the depth of the pits is progressively increasing to its maximum value. Then, the length of the holes and the maximum depth are kept fixed during the second phase of the erosion process but the radius is decreasing (see Fig. 2.11(b)).

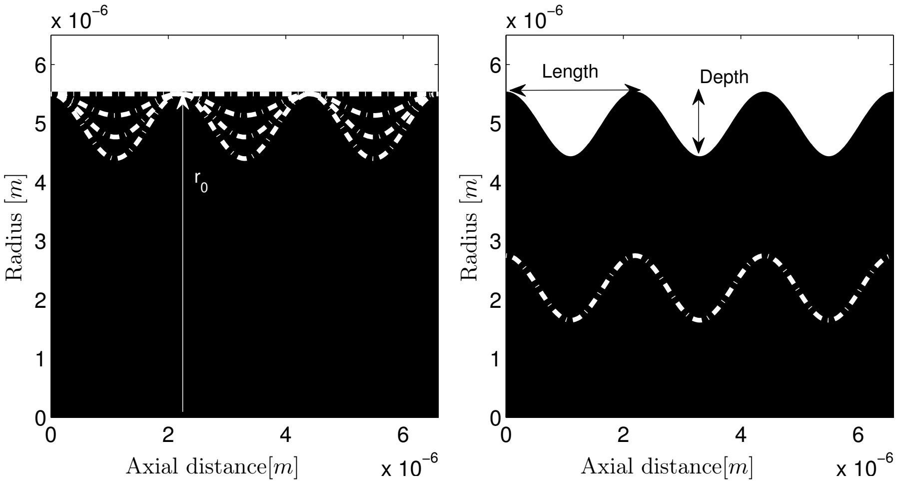

(a) Phase I : formation of the holes (b) Phase II : uniform recession

Figure 2.11: Sinusoidal model to account for pitting of the fibers. The profile is assumed axisymmetric and this pattern is repeated periodically along the fibers. The dashed lines correspond to profiles of an eroded fibers.

For this simple models, an axisymmetric and periodic shape of the fibers is assumed and the profile is parametrized using a cosine function

$$f(x,t) = dp(t)\left(\cos\left(\frac{2\pi x}{L}\right) - 1\right) + r(t), \tag{2.107}$$

where, $r(t)$ is the radius of the fibers, $dp(t)$ and L are respectively the depth and the length of the holes. The length of the hole is kept constant while r and dp are varying with time. In addition to the geometric effect, eroded fibers can be more reactive because of the roughness of the surface [172] or due to the release of gaseous oxidation products which leaves atomic vacancies that enhances the production rate [95, 129]. To account for this increase of reactivity, it is proposed to use the following expression of the specific surface

$$S_f = \gamma \frac{A_w}{dV}, \tag{2.108}$$

where the surface A_w and the volume dV are computed analytically using the revolution integral of $f(x,t)$. In Eq. (2.108), γ is a tuning parameter to account for an increase of reactivity for eroded fibers. This parameter is increasing linearly to its maximum value during the first phase (formation of the holes) and then remains constant. In addition, we assume that for very small solid volume fraction, the specific surface is monotonically decreasing to zero when the fibers are completely depleted. It is suggested for future work, to enhance that model to account for mechanical erosion. Indeed, for very thin fibers, the presence of holes will reduce the mechanical resistance of the fibers.

Therefore, the evolution of S_f with the solid volume fraction is computed knowing the initial radius of the fibers, the length and maximum depth of the holes and the tuning parameter. This evolution is computed beforehand and a polynomial function is then used to fit the evolution of the effective reactive surface with the porosity

$$S_f = \sum_i a_i \epsilon_s^i, \tag{2.109}$$

where a_i are the polynomial coefficients computed beforehand. The effective reactive surface for several γ is shown in Fig. 2.12. The values for the parameters of this model (radius of the fibers, size of the pits, tuning parameters) are discussed in Chapter 5. The specific surface for the virgin material ($\epsilon_s = 0.15$ in Fig. 2.12) is identical for every γ and equal to the one computed with the cylindrical model. Progressively, with decreasing solid volume fraction (i.e. increasing porosity), the specific surface is determined based on an evolving shape of the fibers (described by $f(x,t)$) and the tuning parameter. This leads to an increase of specific surface for decreasing solid volume fraction at the beginning of the fibers oxidation. This is the main difference with the cylindrical model for which the S_f is monotonically decreasing for increasing porosity. Finally, we ensure that the specific surface is zero when the material is completely ablated ($\epsilon_s = 0$).

To conclude, two physical phenomena are modeled, on one hand, this sinusoidal model accounts for the increase of reactive surface due to geometric change and on the other hand γ accounts for a catalytic effects due to an increased roughness of the fibers.

Microscopic analysis

Heterogeneous reactions with the solid matrix are modeled assuming first order reactions and the specific surface accounts for the geometry of the microstructure. Obviously, at the micro scale level, the reactions between gas and solid occur at specific locations called sites. Several mechanisms (adsorption, desorption, Eley-Rideal, Langmuir-Hinshelwood, etc) describe at higher fidelity level these chemical interactions. We use a simplified one-step mechanism for the heterogeneous reactions. Therefore, in our case, the oxidation of the carbon fibers is described as

$$C_{(s)} + O \longrightarrow CO \tag{2.110}$$

$$C_{(s)} + O_2 \longrightarrow CO_2 \tag{2.111}$$

$$2C_{(s)} + O_2 \longrightarrow 2CO. \tag{2.112}$$

For reference, a more complex mechanism for the oxidation reactions [74] is given in Table 2.1.

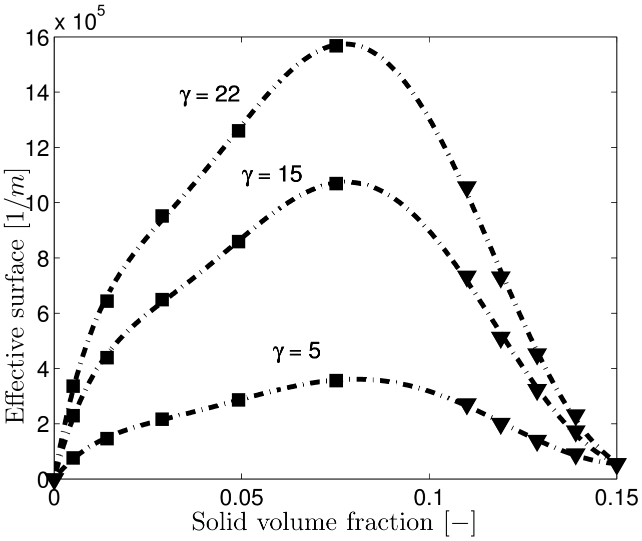

Figure 2.12: Evolution of the effective reactive surface with the solid volume fraction for several tuning parameters. The points used for the polynomial fit in the first phase are represented by triangle symbols and in the second phase by squares.

Table 2.1: Carbon oxidation reactions

Reaction 1	$2Site + O_2 \rightleftharpoons 2Site - O$
Reaction 2	$Site - O \rightleftharpoons Site + O$
Reaction 3	$Site - O + O \rightleftharpoons Site + O_2$
Reaction 4	$Site - O + CO \rightleftharpoons Site + CO_2$
Reaction 5	$Site - O\ (+C_s) \rightleftharpoons Site + CO$
Reaction 6	$Site - O + O\ (+C_s) \rightleftharpoons Site + CO_2$

Considering the simplified mechanism, an error can be made while computing the flux of ablation products. For example, the apparent order of the reaction can be incorrectly predicted. However, the reaction rates and Arrhenius laws given in the literature for this kind of material are usually fitted from experiments and given in the chosen formalism [172]. Finally, in case of catalytic material, the surface can help recombining the dissociated species present in the boundary layer. This mechanism releases reaction energy and increases the heat load at the surface. The catalysis at the wall of an ablative material is still an open question [18], and within this work, the material is assumed inert with respect to atomic recombination.

2.4 Plain fluid-porous media interface modeling

The hypothesis made to derive the VANS equations assumes that the porous medium is homogeneous, i.e. porosity is constant in the small averaging volume. This is no longer valid in the interface region between a porous medium and a plain fluid domain. Since perpendicular and parallel flows to a porous medium are common in today's technological applications (nuclear reactor, wing with a porous tip, biomass problems, etc) or environmental problems (ground water pollution, oil extraction, river flow, etc), numerous studies on the treatment of this transition region exist (see for example [108] and reference therein). In order to correctly describe the modeling problem, Chandesris and Jamet [44] introduce three levels of description for this problem. These scales are illustrated in Fig. 2.13 and correspond to

1. *Microscopic scale*: one should consider only one complex domain accounting for the microstructure of the solid matrix. The flow is described entirely by the Navier-Stokes equations providing that the Knudsen number is sufficiently low. The phenomena are modeled at the scale of the fibers $\mathcal{O}(\mu m)$.
2. *Mesoscopic scale*: the solid and fluid phases are replaced by an equivalent continuous medium. In the vicinity of the interface, there is a transition region where the medium properties vary continuously. The δ is the thickness of the interface layer which is $\mathcal{O}(\sqrt{\kappa})$ that is usually of the order of few pore size diameters ($d = 50\mu m$ for PICA like material) [112].
3. *Macroscopic scale*: one considers as in the mesoscopic scale two homogeneous and continuous region but these are separated by a sharp interface with a discontinuity. In this case, the length scale of the problem is typically $[1e^{-3} - 1e^{0}]\ m$.

The main challenge lies in the correct modeling of the phenomena near the wall. Through this transition layer, depending on the flow conditions (perpendicular or parallel to the permeable surface), pressure, velocity and other variables are changing rapidly. Solving accurately the problem at the microscopic scale is computationally too expensive in most cases and this approach needs detailed information on the internal geometry of the porous medium. Some direct numerical simulations in simplified porous media were performed by Boersma and Breugem [35] and these results are often used in the literature for comparison. Therefore, most approaches solve the problem at the macroscopic level and use appropriate jump conditions at the interface (third level of description). The challenge remains in the correct specification of this boundary conditions especially for unsteady flows.

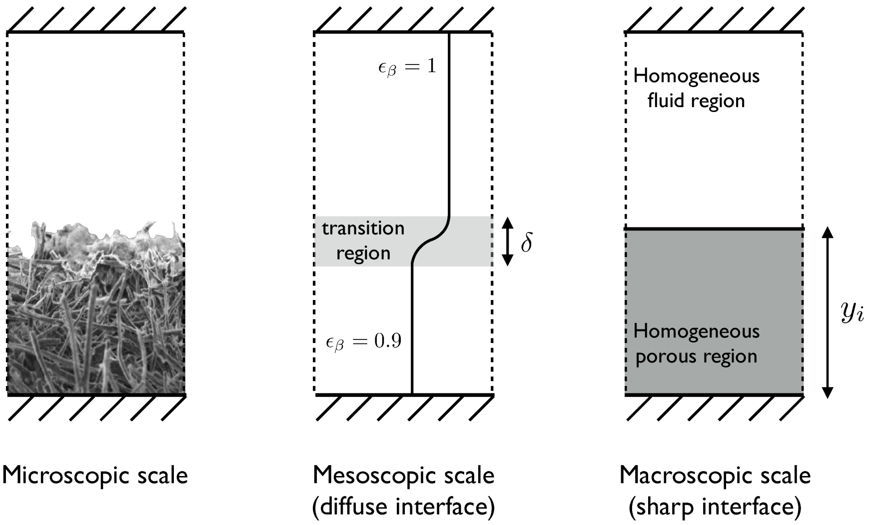

Figure 2.13: Three different levels of modeling for the transition region between a porous medium and a free fluid region. Figure inspired from Chandresis and Jamet [44].

Within this two domain approach, the equations considered are the Navier-Stokes equations for the free-fluid region and inside the porous medium, most publications [112, 21, 62] use the momentum equation derived by Whitaker [234]

$$\frac{\rho}{\epsilon}\left(\frac{\partial\langle u\rangle}{\partial t}+\langle u\rangle\cdot\nabla\left(\langle u\rangle\right)\right)=-\nabla\langle P\rangle_g+\underbrace{\frac{\mu}{\epsilon}\nabla^2\langle u\rangle}_{\text{Brinkman's term}} -\underbrace{\frac{\mu}{\kappa}\langle u\rangle}_{\text{Darcy's term}}-\underbrace{\frac{\rho C}{\sqrt{\kappa}}\left|\langle u\rangle\right|\langle u\rangle}_{\text{Forcheimer's term}}\,. \tag{2.113}$$

This expression is often simplified to keep only the Darcy's term [16]. Note that the Forcheimer's term has been neglected in the derivation of the drag force (see Eq. (2.85)) because it is only important when the Reynolds number within the pores is sufficiently high. For the study of a flow parallel to porous medium, several jump relations to reconcile the solutions in the free fluid domain and in the porous medium can be used. The main jump relations used in the literature are presented briefly here, the comparison of the different models is beyond the scope of this work and interested reader are referred to Ref. [43] which discusses the differences between these interface conditions.

First, Beavers and Joseph [16] have found that the presence of a permeable wall implies a slip velocity at the interface. They have proposed a semi-empirical jump relation (referred as BJ condition) to match Darcy's law in the homogeneous porous medium with the Navier-Stokes equations in the free fluid region. Considering an interface located in $y = 0$, the condition can be written

$$\left.\frac{d\langle u\rangle}{dy}\right|_{y=0} = \frac{\alpha_{BJ}}{\sqrt{\kappa}} \left(u_f - \langle u\rangle\right), \tag{2.114}$$

where the slip coefficient α_{BJ} is an empirical parameter tuned with experimental results, u_f and $\langle u\rangle$ are respectively the velocity at the interface in the free fluid region and the Darcian velocity inside the porous medium. However, it has be shown that the value of α_{BJ} is highly sensitive and depends on microstructure properties (porosity and permeability) but also on the interface position [17, 219, 187]. An alternative approach is the one proposed by Neale and Nader [159] which accounts for the presence of a boundary layer inside the porous medium by using the extended Darcy-Brinkman law. In this case, the jump conditions (referred as NN conditions) are expressed on the average velocity and the tangential shear stress component

$$\langle u\rangle = u_f \text{ , and } \left.\mu\frac{du}{dy}\right|_{y=0^+} = \left.\mu_{NN}\frac{d\langle u\rangle}{dy}\right|_{y=0^-} \tag{2.115}$$

where μ_{NN} is an effective viscosity which can be linked to the slip coefficient $\alpha_{BJ} = \sqrt{\mu_{NN}/\mu}$ [159], the porous medium is located in $y < 0$ and the free fluid region in $y > 0$. However, even though some correlations exist for the effective viscosity [112], the accurate computation of this parameter is a particularly difficult task.

Based on the non-local form of the volume averaged Stokes equations, Ochoa-Tapia and Whitaker [164] have derived a stress jump condition (OTW condition) to be applied at the interface. In addition, they ensure, as for the NN condition, the continuity of the averaged velocity field [165]. In this case, the evaluation of the coefficient is done by an up-scaling method to correct the approximation of the closure model in the interface region:

$$\left.\frac{\mu}{\epsilon}\frac{d\langle u\rangle}{dy}\right|_{y=0^-} - \left.\mu\frac{d\langle u\rangle}{dy}\right|_{y=0^+} = \left.\mu\frac{\beta_{OTW}}{\sqrt{\kappa}}\langle u\rangle\right|_{y=0}, \tag{2.116}$$

where β_{OTW} is a dimensionless coefficient that has to be determined to close the model and is of the order $\mathcal{O}(1)$. Nevertheless, this parameter is less sensitive than the slip coefficient of the Beavers and Joseph model. To only cite a few references, Vafai and Kim [226] as well as Poulikakos et al. [179] are also using this model. Ochoa-Tapia and Whitaker have found good agreement with experimental data [165] and the numerical investigations of Breugem [34] have shown that DNS results agrees well with analytical solutions of the OTW model providing a correct β_{OTW} coefficient.

Several authors use a two steps approach together with the use of DNS results. The DNS results at the micro scale are averaged carefully to be able to solve the closure problem and compute the correct effective coefficient needed [34, 70]. This method is mostly based on semi-empirical relations linking the different variables to the porosity. Despite many research efforts to determine these unknowns (α_{BJ}, μ_{NN}, β_{OTW}) [92], it is still very challenging and remains often an open problem which needs additional microstructure information to be closed. In particular, the dependence of these parameters with the definition of the interface position remains the biggest problem.

Within this two domains approach, Chandesris and Jamet [44, 43] have also proposed recently the use of the Matched Asymptotic Expansions (MAE) to solve analytically the problem in the transition region at the mesoscale level in order to derive appropriate jump conditions at the macroscale level. This analysis provides the explicit relation between the jump parameter and the variation of porosity and permeability. This two steps up-scaling approach has also been used by D'Hueppe [70] to derive correct boundary conditions for the energy equation. Despite very good agreement obtained using these approaches, these imply generally the resolution of a problem at the microscale or mesoscale level to close the models.

For an ablative material, the interface position and the transition layer will change with time. Therefore, the problem to be solved (for the MAE) and the parameters to close the jump conditions (BJ, NN, OTW) should be re-evaluated at every location. The computation of closure parameters using DNS computations thus becomes rapidly prohibitive. In addition, these demand additional microstructure informations at each degradation state that are not always available. Finally, from the computational point of view, the implementation of jump boundary conditions on a moving interface remains a challenging endeavor.

As recalled by Goyeau et al. [92] considering a sharp interface between two homogeneous domains *"is an ideal representation of a region with continuous spatial changes of the macroscopic properties"*. Therefore, another approach consists in using a variable permeability/porosity in the transition region [191, 165]. Rigorously, this is only valid at the mesoscopic scale (second level of description) where the continuity of the phenomena at the interface can be assumed. The averaged equations can be used provided that the thickness of the interface refers to the physical transition layer. In order to be accurate, this assume also that the variations of porosity and permeability are known in the transition region. For this one domain approach, the physical variables encounter strong but continuous variations. The one domain approach with a variable porosity/permeability has been used by several authors, see for example [92, 218, 8, 128] and references therein. It is the approach followed in this work. Figure 2.14 shows the computation of the velocity profile using several approaches presented to evaluate the flow in a channel overlying a porous layer.

Several numerical methods can be used to treat the movement of the interface and are discussed in Chapter 3. The so-called diffuse numerical method selected to treat the moving boundary problem is compatible with the vari-

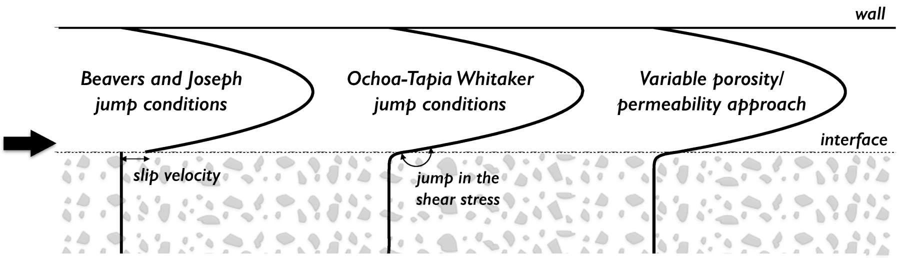

Figure 2.14: Comparison of different approach to solve the flow in a channel on top of a semi-infinite porous layer. The fully developed steady state velocity profiles are computed using the two domains approach with BJ conditions, OTW conditions and using a single domain approach implemented in this work.

able porosity model chosen. These techniques smooth the discontinuity over a transition region. Within this work, a normalized hyperbolic tangent function is used to regularize the initial solid volume fraction on the grid

$$H(\phi) = \tanh\left(\frac{2\pi\phi}{\epsilon_\phi}\right), \tag{2.117}$$

where ϕ is the initial distance function from the porous medium and ϵ_ϕ is the grid distance on which the quantity is smoothed. Non-dimensional porosity and permeability profiles are shown in Fig. 2.15. The porosity will vary from a constant value in the homogeneous porous medium to one in the plain fluid region. The permeability should be infinite in the plain fluid region and a constant value in the homogeneous porous medium. The variation for the inverse of permeability is shown in Fig. 2.15 and its evolution in the interface region will be detailed in the next section.

Note that to preserve the physical meaning of the interface thickness, the mesh and the polynomial order of approximation should be sufficiently fine and high, respectively to capture the transition region at the mesoscale ($\epsilon_\phi \approx \delta$). To decrease the computational cost, we can use a numerical ϵ_ϕ different from the physical thickness if we accept to make an error in the interface region. Numerical test cases are presented in Chapter 4 which investigate how the phenomena in the viscous boundary layer above the permeable wall are captured with the one domain approach and compare with the various approaches.

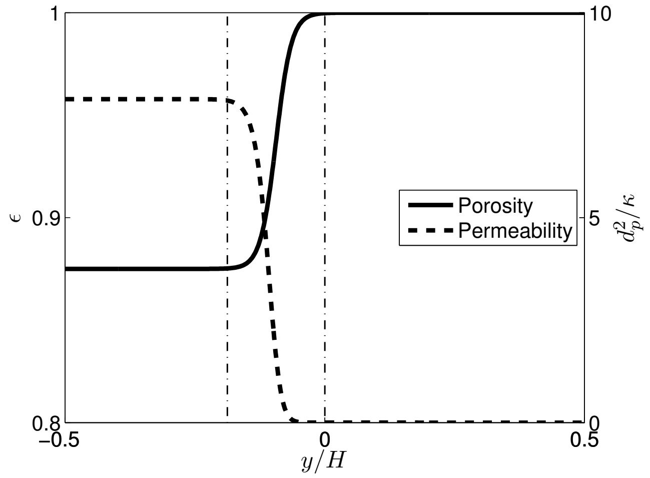

Figure 2.15: Non-dimensional porosity and permeability profile for a simplified porous medium made of cubes with length d_p.

2.5 Summary of the equations and closure models

This section summarizes the set of equations valid the whole domain and developed in Section 2.2 and 2.3. The closure models used are inserted in the conservation laws. The second part of this section describes the material properties needed to feed this model.

2.5.1 Volume averaged Navier-Stokes

The conservative variables used to describe an ablative material made of carbon preform are the averaged mass density of every species i which needs to be tracked ($\epsilon_g\langle\rho_i\rangle_g$), the averaged momentum ($\langle\rho\mathbf{u}\rangle_g$), the total energy ($\langle\rho E_{tot}\rangle$) and the averaged solid density of the fibers ($\langle\rho_s\rangle$). The system of equations written in vectorial form is

$$\frac{\partial\mathbf{U}}{\partial t} + \nabla\cdot\mathbf{F}^c = \nabla\cdot\mathbf{F}^d + \mathbf{S}. \tag{2.118}$$

with U the conservative variables

$$\mathbf{U} = \begin{pmatrix} \epsilon_g\langle\rho_i\rangle_g \\ \langle\rho\mathbf{u}\rangle_g \\ \langle\rho E_{tot}\rangle \\ \langle\rho_s\rangle \end{pmatrix}. \tag{2.119}$$

The expression for the convective fluxes is

$$\mathbf{F}^c = \begin{pmatrix} \epsilon_g\langle\rho_i\rangle_g\langle\mathbf{u}\rangle_g \\ \langle\rho\rangle_g\langle\mathbf{u}\rangle_g\langle\mathbf{u}\rangle_g + P \\ \epsilon_g\langle\rho\rangle_g\langle\mathbf{u}\rangle_g\langle H\rangle_g \\ \mathbf{0} \end{pmatrix}, \tag{2.120}$$

and the diffusive fluxes are expressed

$$\mathbf{F}^d = \begin{pmatrix} -\langle \mathbf{J}_i \rangle \\ \langle \boldsymbol{\tau} \rangle_g \\ \langle \boldsymbol{\tau} \cdot \mathbf{u} \rangle + \lambda_{eff} \nabla \langle T \rangle - \sum_{i=1}^{N_s} h_i \langle \mathbf{J}_i \rangle \\ \mathbf{0} \end{pmatrix}. \tag{2.121}$$

where we recall that the averaged mass diffusive flux is

$$\langle \mathbf{J}_i \rangle = -\epsilon_g \langle \rho_i \rangle_g \frac{D_{i,m}}{\eta} \frac{W_i}{W} \nabla X_i + \epsilon_g \langle \rho_i \rangle_g \sum_{k=1}^{N_s} \frac{D_{k,m}}{\eta} \frac{W_k}{W} \nabla X_k. \tag{2.122}$$

Finally, the source term is

$$\mathbf{S} = \begin{pmatrix} \langle \dot{\omega}_i^{het}(\langle T \rangle, \langle \rho_i \rangle_g, \langle \rho_s \rangle) \rangle + \epsilon_g \dot{\omega}_i^{\mathrm{hom}}(\langle T \rangle, \langle \rho_i \rangle_g) \\ \mathbf{F_{gs}} \\ -\sum_{i=1}^{N_s+1} \left(\langle \dot{\omega}_i^{het}(\langle T \rangle, \langle \rho_i \rangle_g, \langle \rho_s \rangle) \rangle + \epsilon_g \dot{\omega}_i^{\mathrm{hom}}(\langle T \rangle, \langle \rho_i \rangle_g) \right) h_{f,i}^0 \\ \langle \dot{\omega}_i^{het}(\langle T \rangle, \langle \rho_i \rangle_g, \langle \rho_s \rangle) \rangle \end{pmatrix}, \tag{2.123}$$

where $\mathbf{F_{gs}}$ is the momentum exchange term between the two phases. In this work, the closure of this term only includes the first order drag force predicted by Darcy (see Eq. (2.85)). The homogeneous production term ($\dot{\omega}_i^{hom}$) is given by Eq. (2.37) and the averaged heterogeneous production rate for reacting species ($\langle \dot{\omega}_i^{het} \rangle$) is expressed in Eq. (2.70).

It is trivial to observe that if ϵ_g tends to one, additional source terms disappear and this system of equations reduces to the classical Navier-Stokes equations presented in Eq. (2.11).

2.5.2 Medium properties

The intrinsic properties of the gas and solid phase respectively are varying with temperature but for a reactive porous medium, the effective properties are also changing with the porosity. To characterize the porous medium, the model in Eq.(2.120)-(2.123) needs several closure parameters. The value of these properties will be specified for each test case but this section aims to provide enlightenment to the reader about order of magnitude for these and main measurement techniques. Additionally, it presents the model for the evolution with the porosity.

Initial porosity

The initial porosity of the material can be inferred from micro tomography data which capture the microstructure of the material [144, 169]. For carbon preform material, the initial porosity is comprised between 0.85 and 0.9. The intrinsic solid density of the fibers ($\langle \rho_s \rangle_s$) is assumed invariant therefore the local porosity can be computed using

$$\epsilon_g = 1 - \epsilon_s = 1 - \frac{\langle \rho_s \rangle}{\langle \rho_s \rangle_s}. \tag{2.124}$$

The averaged density of the virgin carbon preform material should be measured experimentally.

Fiber radius

The fiber radius has to be evaluated to define the reactive surface needed in Eq. (2.70). The initial fiber diameter can be computed based on scanning electron microscopy images [171] and the average value for carbon preform is $6 - 12$ $[\mu m]$ [171, 98]. We recall that the evolution of this diameter should be computed based on either the cylindrical model (see Eq. (2.105)) either the sinusoidal model.

Effective thermal conductivity

The effective thermal conductivity is modeled in this work using Eq. (2.98). Rigorously, the effective thermal conductivity should include the radiative heat transfer in between the fibers for carbon preform material. The effective conductivity can be computed based on laser flash analysis [149]. When it is specified in the text, the value of the effective thermal conductivity including radiative effects is taken from the TACOT (Theoretical Ablative Composite for Open Testing) database. TACOT is a synthetic material but with properties which should be similar to those of real material.

Fibers reactivity

The heterogeneous production rate requires the knowledge of the fibers reactivity. This reactivity is usually expressed with an Arrhenius law. The definition of the coefficients (A_f, $E_{a,f}$ and n_f) varies greatly in the literature [170] and will be discussed in more detail in Chapter 5.

Tortuosity

The tortuosity is a material parameter depending on the architecture of the porous medium and the mean free path. For an anisotropic and non overlapping fiber structure which is typical of carbon preform, the tortuosity is extracted from numerical simulations done by Lachaud et al. [117] using a random walk algorithm in the fibrous medium. For the reactive porous medium, a linear interpolation is used between the freestream tortuosity ($\eta = 1$) and the constant bulk tortuosity. Typically, for PICA like material, the tortuosity is comprised between $[1.0 - 1.5]$ [117].

Permeability

The permeability is also dependent on the microstructure of the material. There is no general function of the porosity and the existing relations assume homogeneous porous medium. For example, it can be computed for simplified porous media made of spheres or squares and several correlations are proposed by Kaviany [112]. Breugem [34] has shown that it is possible to extract the permeability profile in the heterogeneous region by using the volume averaging theory on microscopic scale numerical simulations. However, in the absence of accurate data on the microstructure of the porous medium, the semi-empirical model of Carman-Kozeny [76] will be used to link the local porosity and the permeability. This semi-heuristic model is based on the concept of hydraulic radius and leads to a permeability, κ, which depends on the porosity, the tortuosity and the specific surface area

$$\kappa^{-1} = \frac{S_{f,0}^2 (1-\epsilon_g)^2 k_k}{\epsilon_g^3}, \tag{2.125}$$

where $S_{f,0}$ is the initial specific surface, k_k is directly proportional to the tortuosity and the proportional constant depends on the shape of the solid matrix. The definition of the constant is not trivial [48], in this work, the constant is adapted by measuring the initial permeability (using the pressure drop across a sample for example [170]) and computing $S_{f,0}$. Using this model, even in the heterogeneous interface region, the permeability will be adapted implicitly in case of recession. Two other models have been implemented to compare with the Carman-Kozeny model; a linear relation based on the porosity and an exponential function proposed by Martin [145],

$$\kappa^{-1} = \frac{1}{\kappa_0} \frac{(1-\epsilon_g)}{\epsilon_{s,0}} \text{, and } \kappa^{-1} = \frac{1}{\kappa_0} \left(1 - \exp\left(1-\epsilon_g\right)\right), \tag{2.126}$$

where κ_0 is the virgin permeability. Figure 2.16 shows the permeability with respect to the porosity for the models implemented. One can observe that the permeability computed with the Carman-Kozeny model decreases faster at low porosity than the other two models which present similar behavior. The behavior of the flow in the transition layer will of course be influenced by the type of model chosen. These will be compared in Chapter 4 and 5 to evaluate the best model to be used. Every model presented is directly dependent on the porosity, therefore the transition layer for the porosity determines the thickness on which the permeability is varying. However, as shown by Chandesris [44], the transition region for the permeability and the porosity can be different but this is not modeled in the present approach. Carbon preform materials are highly porous but the permeability is really low ($\kappa \approx [1e^{-8} - 1e^{-11} m^2]$).

Finally, note that, in general, the carbon preform material is not-isotropic since the fibers exhibit a preferential orientation. Therefore, properties of the material should be considered as second order tensors; the conductivity for example will be higher in the direction of the fibers [169]. Within this work, we will restrict ourselves to isotropic material.

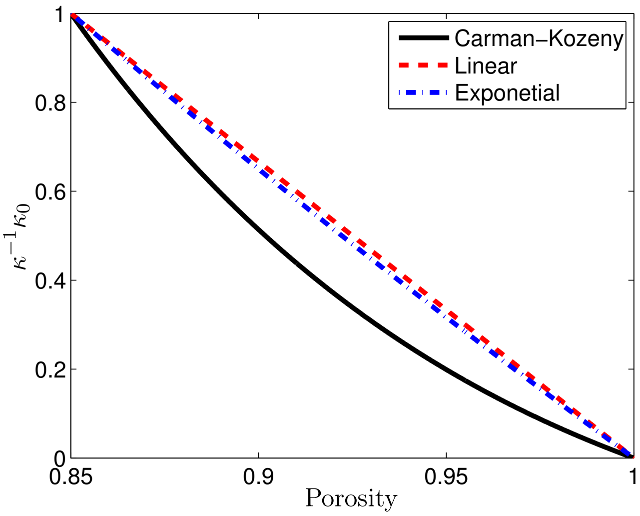

Figure 2.16: Evolution of the permeability for several models

2.6 Conclusions

The volume averaging theory applied to the reactive Navier-Stokes equations allows to derive a system of equations valid in the whole domain. In deriving such a system of equations, closure terms need to be modeled. Simplified models have been proposed and Chapter 5 will verify the models implemented. The treatment of the transition layer between the homogeneous fluid region and the homogeneous porous domain is done by using a variable porosity/ permeability approach. The one domain approach is computationally simple to treat without having to account for boundary conditions at the interface. The analysis of the different scales of the problem has shown that to capture accurately the phenomena in the transition layer, the numerical thickness of the interface should correspond to the physical thickness of transition at the mesoscale level. In addition, this approach proposes to treat the reactions with the solid matrix inside the porous medium to account for volume ablation. Finally, adding an equation for the evolution of the solid density eliminates the need to develop a method to track the position of the interface.

CHAPTER 3

NUMERICAL METHODS

This chapter gathers the numerical techniques used to simulate the gas-surface interactions between eroding flows and eroded materials. First, existing numerical tools are presented by highlighting the contributions of this work. Then, the spatial and temporal discretization used to solve the system of partial differential equations presented in Chapter 2 are detailed. Finally, a particular care is dedicated to treat the moving interface problem arising from the ablation of the reactive porous medium.

3.1 High order numerical tools

Within this work, two codes have been developed separately. First, a one-dimensional code Echion was developed to get familiar with the discretization method and investigate several approaches to treat the reactive porous medium. The 1D code is a material response code only using a simplified form of the system (Eq. (2.118)). Secondly, the solution of the full system is computed with the multidimensional tool Argo developed at Cenaero. This section reviews briefly the features of the codes.

3.1.1 Echion

The one-dimensional tool was initially developed at Cenaero by Gorissen [90]. The numerical code has been improved and modified to simulate the thermal response of an ablative material. The code possesses a structure similar to the multidimensional platform Argo. The numerical code written in C^{++} is able to solve systems of partial differential equations in 1D using a Discontinuous Galerkin Method (DGM). The enhanced tool is able to treat convection, diffusion and reaction problems. Several time integration schemes have been implemented, both explicit and implicit. A substantial effort has been dedicated to treat variable diffusion problems using the work proposed by Proft and Riviere [180]. In addition, a moving mesh algorithm was implemented to deal with recession of an ablative material. Specifications of the code developed to treat the in-depth thermal response of ablative material are presented further in details in Chapter 6. This code was also used to study the approach developed to consider multiphase systems in the same computational domain. This will be discussed in the last part of this chapter.

3.1.2 Argo

The Argo platform is a multi-physics code based on a discontinuous Galerkin method. The solver has been verified and validated to simulate compressible and incompressible flows [100, 40]. Its parallel implementation renders it very efficient and scalable for industrial use. Argo is developed at Cenaero by a multi-disciplinary team involving currently five full-time researchers and three PhD students. The platform is also written in C^{++} benefitting from the flexibility and polymorphism of this language. Several conservation laws can be solved and the polymorphism of the language allows to easily add an additional one. The solver uses an hybrid parallelization relying on the Message Passing Interface (MPI) and Open Multi-Processing (OpenMP) [40] to deal with costly simulations. The code has already been exploited for two main applications up to now. The treatment of scale resolving simulations of turbulent flows [40] and complex modeling of multiphase flows [176, 39].

Figure 3.1 shows an overview of the building blocks of Argo with the main contributions of this work highlighted in red. The contributions will be detailed in this chapter. Several modules are implemented to treat different kind of problems. The module developed during this work is benefitting from the architecture of the platform and the various developments made by each researcher of the team. The experience of simulating multiphase flows has for example been useful to develop the approach which handles the reactive porous medium. The numerical development of this work have been grouped in a module of Argo referred in the following as *DGAblation*. This module is based on the existing compressible module (named *DGFluid*) but works with primitive variables. The reasons are explained in Section 3.3. This module aims at modeling the high enthalpy flows of several species and the presence of a reactive porous medium. Inside the Argo platform, little work was done on the discretization scheme but the effort focuses on increasing the fidelity of the physico-chemical models. The conservation law implemented in *DGAblation* represent the most important part of the work. The conservation laws implemented account for several species, non-calorically perfect gas, and complex reaction terms. In addition, if needed, the presence of an inert or reactive porous medium is handled in the code. These imply numerical challenges handled by the implemented module.

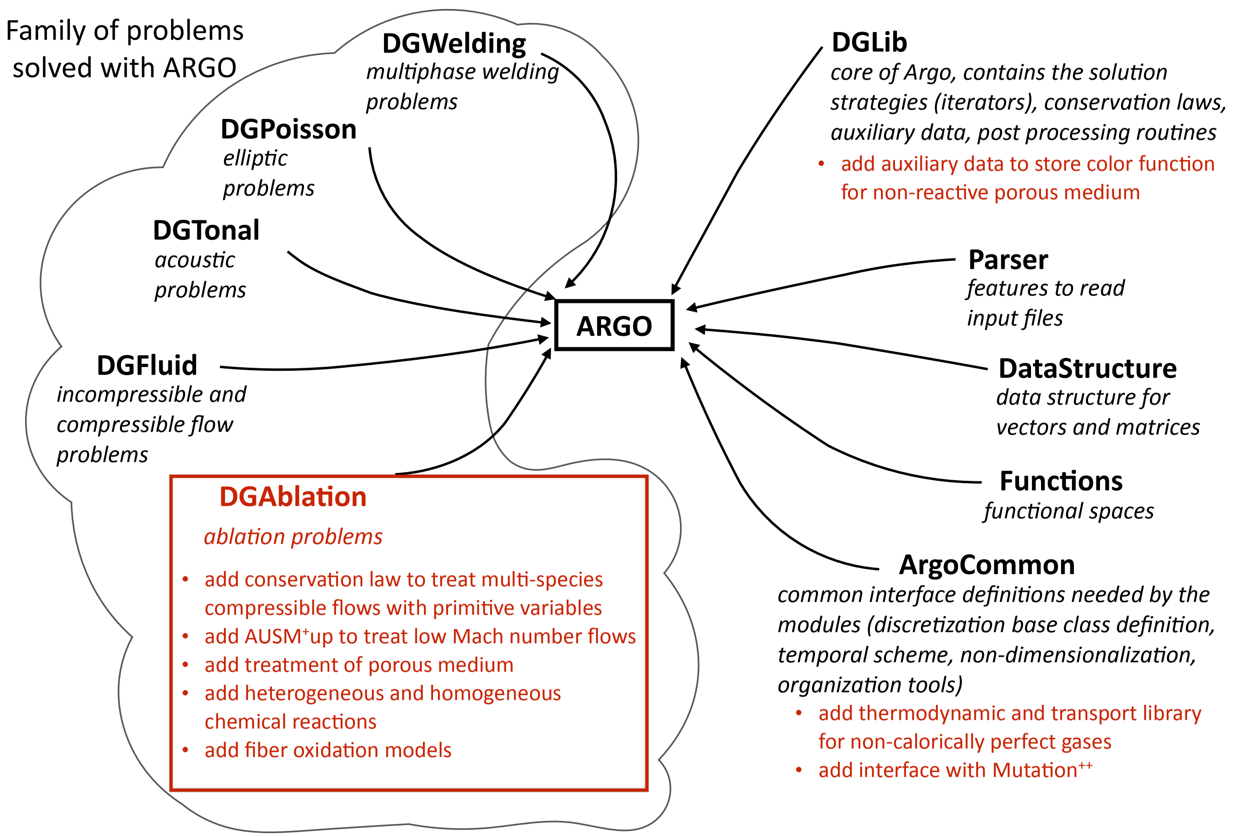

Figure 3.1: Summary of the architecture of Argo with the main contributions of this work highlighted in red.

3.2 Spatial discretization

The non-linear system of partial differential equations to solve (see Eq. (2.118)) is a convection-diffusion-reaction problem. The *Discontinuous Galerkin Method* (DGM) is proposed in this work to discretize this system. This section reviews the basics of the scheme and discusses advantages and disadvantages of this type of method.

3.2.1 Discontinuous Galerkin method

This type of discretization was introduced back in 1973 by Reed and Hill [185] to solve neutron transport problems. DGM cumulates the advantages of finite volume and finite element methods. The advantage lies in their accuracy on unstructured meshes, computational efficiency and scalability due to the locality of data and operations [59]. This type of discretization is a particular class of *Finite Element Methods (FEM)*.

The system of equations (Eq. (2.118)) can be written in a general form for a component m of the solution state vector $\tilde{\boldsymbol{u}}$

$$\begin{aligned}\mathcal{L}_m(\tilde{\mathbf{u}}) &= 0\ ,\ \forall m \in \{1, N_v\}\\ &= \frac{\partial \tilde{u}_m}{\partial t} + \frac{\partial}{\partial x^k} F_m^{c,k}(\tilde{\boldsymbol{u}}) - \frac{\partial}{\partial x^k} F_m^{d,k}(\tilde{\boldsymbol{u}}, \nabla \tilde{\boldsymbol{u}}) - S(\tilde{\boldsymbol{u}},\ \nabla \tilde{\boldsymbol{u}}),\end{aligned} \tag{3.1}$$

where N_v is the number of variables in the system and the negative sign in Eq. (3.1) for the diffusive and source parts is used to be consistent with the definition of the problem (see Eq. (2.118)). The diffusive term in Eq. (3.1) can be expressed using the Jacobian of the diffusive flux with respect to the solution gradients defined as

$$F_m^{d,k} \approx -D_{m,n}^{k,l}(\boldsymbol{u}) \frac{\partial \tilde{\boldsymbol{u}}_n}{\partial x^l} \tag{3.2}$$

where $D_{m,n}^{k,l}$ is a fourth order tensor relating the diffusive flux for variable m and in direction k, to the solution gradients.

In theory, solving Eq. (3.1) requires an infinite number of values to describe the solution $\tilde{\boldsymbol{u}}$ which is impossible computationally. In practice, for any type of FEM, the solution state vector is then approximated by a finite set of functions in the test space $\mathcal{V}$.

In order to form the functional space $\mathcal{V}$, the domain (Ω) is decomposed in a finite number of elements (Ω_e). The mesh or grid is composed of these elements which cover the entire domain without overlapping. Based on these elements a "broken" functional space $\mathcal{V}$ is then defined, which consists of functions that are regular polynomials of order p when restricted to any given element, but are not necessarily continuous across element boundaries. Background information on functional analysis can be found in Hillewaert [100] and references therein.

Therefore, the approximate solution is expressed as a linear combination of the *shape functions* ζ_i, which form a basis for $\mathcal{V}$

$$\tilde{u}_m \approx u_m = \sum_{i=1}^{N} U_{i,m}\zeta_i, \tag{3.3}$$

where the notation $U_{i,m}$ is used for the coefficients of the approximation which are the DOF of the problem. The functions (ζ_i) in the test space are then continuous in the interior of each element but without any imposed continuity across element boundaries. Therefore, the approximate solution (see Eq. (3.3)) can be discontinuous at the internal boundary between two cells. This is the major difference between DGM and Classical Galerkin Finite Element Method (CGFEM). For simplicity, the shape functions ζ_i will be chosen to have a support that is limited to a single element, such that in practice we can associate each shape function to an element and rewrite Eq. (3.3) as

$$u_m = \sum_{e}\sum_{i=1}^{N^e} U^e_{i,m}\zeta^e_i \tag{3.4}$$

From then on, several options for the definition of the shape functions ζ^e_i exist. Within Argo, Lagrange interpolants of order p are used, defined with respect to equidistant control points in the element. Figure 3.2 represents the one dimensional discretization of a discontinuous function using DGM with a third order polynomial interpolation. We can observe that, since no continuity is imposed at the boundary of each cell, the interface nodes are duplicated increasing the total number of DOF.

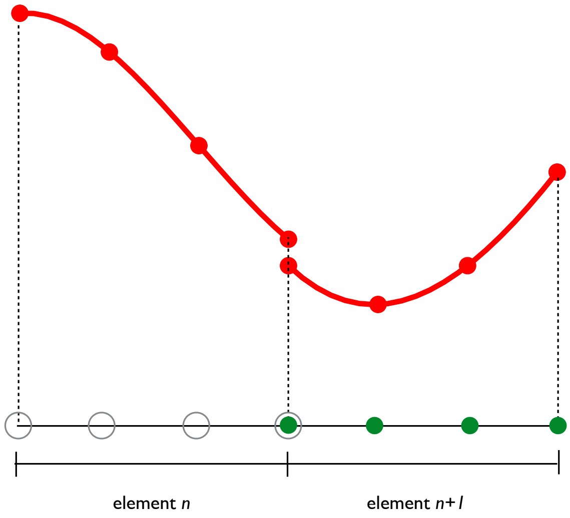

Figure 3.2: Discontinuous Galerkin representation of a discontinuous function on two elements using a third order Lagrangian polynomial interpolation in 1D.

The Lagrange polynomials are defined usually in a parametric coordinates system on a reference element. Therefore, a mapping is needed to transform the physical coordinates ($x_1,\ x_2$) into the parametric space ($\xi_1,\ \xi_2$). The reference element (parent) is identical for each type of element for a given interpolation order and Fig. 3.3 shows the transformation for a random triangle to a reference element.

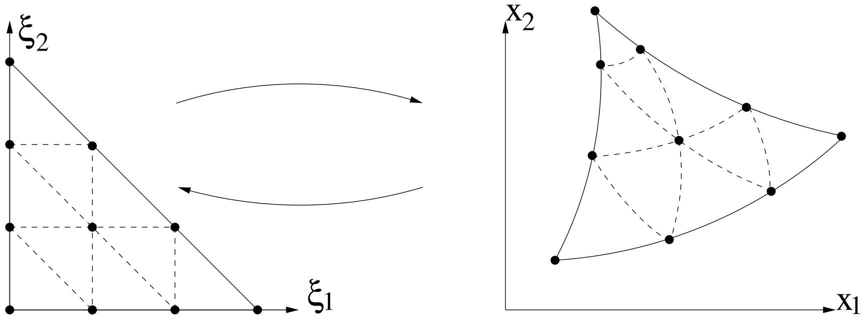

Figure 3.3: Third order mapping of a triangle with second order interpolation from a random element to the reference space. Figure taken from [100].

Since $\mathcal{L}_m(\tilde{u}_m) = 0$ cannot be verified everywhere in the domain, the orthogonality of the residual of Eq. (3.1), computed using the approximate solution (u_m), to every function in the test space is required instead. Therefore, the expansion weights U_{im} are found by the Galerkin variational formulation

$$\int_{\Omega} v\mathcal{L}_m(\mathbf{u}) = 0,\ \forall\ v\ \in\ \mathcal{V}. \tag{3.5}$$

As usual in FEM the required regularity of the functions v is decreased by applying partial integration to the variational formulation (3.5). Due to the discontinuity of the interpolatory and test functions, element interface contributions need to be added to the residual of the variational problem, which are absent for CGFEM. Replacing $\mathcal{L}_m(\tilde{\boldsymbol{u}})$ from Eq. (3.1) in Eq. (3.5) and using partial integration, the complete weak formulation for the convection-diffusion-reaction problem is then

$$
\begin{aligned}
\int_{\Omega} v\mathcal{L}_m(u) &= 0,\ \forall v \in \mathcal{V},\ \forall m \in N_v \\
&= \underbrace{\sum_{\Omega_e \in \Omega} \int_{\Omega_e} v \frac{\partial u_m}{\partial t}\, d\Omega_e}_{\text{Tv}} \\
&- \underbrace{\sum_{\Omega_e \in \Omega} \int_{\Omega_e} \frac{\partial v}{\partial x^k} F_m^{c,k}(\mathbf{u})\, d\Omega_e}_{Cv} + \underbrace{\sum_{I_i \in I} \oint_{I_i} [v]^k n^k \mathcal{H}_m(\mathbf{u}^+, \mathbf{u}^-, \mathbf{n})\, dS}_{Ci} \\
&+ \underbrace{\sum_{\Omega_e \in \Omega} \int_{\Omega_e} \frac{\partial v}{\partial x^k} (F_m^{d,k}(\mathbf{u}))\, d\Omega_e}_{Dv} - \underbrace{\sum_{I_i \in I} \oint_{I_i} \langle D_{mn}^{kl} \frac{\partial \mathbf{u}_n}{\partial x^l} \rangle [v]^k\, dS}_{Di} \\
&- \underbrace{\theta \sum_{I_i \in I} \oint_{I_i} \langle D_{mn}^{kl} \frac{\partial v}{\partial x^l} \rangle [u_m]^k\, dS}_{Dt} + \underbrace{\alpha \sum_{I_i \in I} \oint_{I_i} [v]^k [u_m]^k\, dS}_{Dp} \\
&- \underbrace{\sum_{\Omega_e \in \Omega} \int_{\Omega_e} v S(\mathbf{u}, \nabla \mathbf{u})\, d\Omega_e}_{Sv}
\end{aligned}
\tag{3.6}
$$

In Eq. (3.6), Ω_e are the elements, I_i are interfaces between adjacent elements and $\mathcal{H}$ is the interface flux which will be defined in the following. The jump and average *trace operators* in Eq. (3.6) are defined respectively by

$$[a] = a^- n^- + a^+ n^+ \tag{3.7}$$

$$\langle a \rangle = \frac{1}{2}(a^- + a^+). \tag{3.8}$$

The temporal term is noted T_v, and the terms Cv, Dv and Sv of Eq.(3.6) are the volume contributions for the convective, diffusive and source terms respectively which are shared with CGFEM. The remaining terms (C_i, D_i, D_t, D_p), absent in CGFEM, can be considered as internal boundary conditions that couple an element with its neighbors. The treatment of the convective and diffusive interface terms is different and will be detailed hereafter. For the simplicity of notation, the general form of Eq. (3.6) will be simplified for the case of a single variable in one dimension.

Using the parametric space previously defined allows to easily integrate the weak formulation. Indeed, in order to compute the integrals in the variational formulation (Eq. (3.6)), a Gauss-Legendre quadrature is used. The points and the weights are defined on the reference element and the transformation matrix is used to integrate on the physical element. Note that the Gauss-Legendre quadrature are defined inside the element hence the integration of the source term does not imply any evaluation on the boundary. This is convenient for the axisymmetric approach chosen (see Section 2.2.1) since it avoids the singularity along the axis of symmetry.

Main advantages of DGM

The main advantage of discontinuous Galerkin methods is their high-order accuracy on unstructured meshes. DGM handles a wide variety of element types and it is well suited for local adaptation in mesh size and interpolation order p (hp adaptivity)[57]. Furthermore, DGM ensures the local conservation of physical quantities. Despite the additional DOF due to the discontinuous character of the scheme, the compactness renders the method highly scalable [40]. The benefits of DGM have already been proven by several authors for a large variety of applications such as compressible and incompressible fluid dynamics [15, 57], multiphase flows [176], plasma-dynamical applications [58] or transport in porous medium [189]. Therefore, DGM is a suitable discretization method to simulate reactive flows of interest here thanks to its high-order accuracy, compactness of the scheme and local mass conservation properties [137].

The low numerical dissipation and dispersion of DGM are also an asset to simulate the transport of chemically reacting flows [137]. Figure 3.4 shows the dispersion and dissipation properties for high-order DGM. These are computed by Gassner and Kopriva [86] by studying a scalar linear advection problem in a one dimensional periodic domain and using an upwind flux. The complex dispersion relation for the discretized equation is written $\Omega^*(K^*)$; the real part is the dispersion relation while the imaginary part is the dissipation. It can be observed in Fig. 3.4(a) that the dispersion error and the dissipation are very low for wave number $K^* < \pi/2$ and decreasing for higher polynomial degrees used. When the dispersion becomes higher for larger wave numbers, the dissipation is also higher (see Fig. 3.4(b)). Finally, the high dissipation property at high wave number dissipates the under-resolved scales without altering the largest ones. This can be exploited for under-resolved turbulence computations as proposed for example in the work of Carton de Wiart et al. [41].

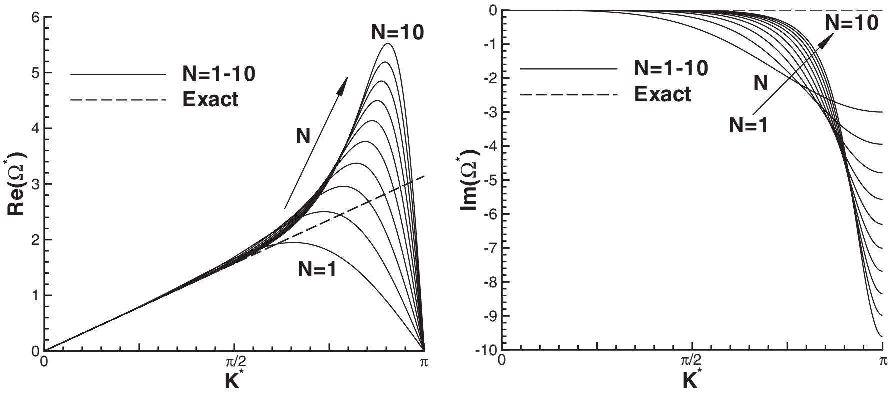

(a) Dispersion (b) Dissipation

Figure 3.4: Numerical dispersion and dissipation errors of the 1-D DGM scheme from polynomial degree $N = 1$ to $N = 10$ using a purely upwind flux. Figures taken from Gassner and Kopriva [86].

Convective variational form

Reducing the system Eq. (3.1) to its hyperbolic part in 1D, the variational form for a scalar quantity can be written

$$\begin{aligned}\int_{\Omega} v\mathcal{L}^h(u) &= 0,\ \forall v \in \mathcal{V}\\ &= \underbrace{\sum_{\Omega_e \in \Omega} \int_{\Omega_e} v\frac{\partial u}{\partial t}\, d\Omega_e}_{\text{Tv}}\\ &\quad \underbrace{- \sum_{\Omega_e \in \Omega} \int_{\Omega_e} \frac{\partial v}{\partial x} F^c(u)\, d\Omega_e}_{Cv} + \underbrace{\sum_{I_i \in I} \oint_{I_i} [v]\mathcal{H}(u^+, u^-, \mathbf{n})\, dS}_{Ci},\end{aligned} \tag{3.9}$$

where the interface flux $\mathcal{H}$ is required to be an E-flux which is function of the internal u^+ and external u^- states at the boundary. The E-flux was defined by Osher [166] as a numerical flux satisfying

$$\left(\mathcal{H}(u^-, u^+, \mathbf{n}) - f(u)\right)\left(u^+ - u^-\right) \leq 0, \tag{3.10}$$

where u belongs to $[u^-, u^+]$. The discretization of the convective part takes its inspiration from classical upwind *Finite Volume Method* (FVM) [100] of which it is a high order extension. Indeed, it is trivial to see that, if one considers piecewise constant functions for the functional space, the Cv term disappears and the formulation for semi-discrete form on an element e is reduced to

$$\int_{V_{\Omega_e}} v\frac{\partial u}{\partial t}\, d\Omega_e = -\sum_{I_i \in I} \oint_{I_i} [v]\mathcal{H}(u^+, u^-, \mathbf{n})\, dS, \tag{3.11}$$

which effectively reduces to a first order FVM, which computes the time evolution of the cell average based upon the flux balance at the boundary of the cell

$$\frac{du}{dt} = -\frac{1}{V_{\Omega_e}} \sum_i \mathcal{H}(u^+, u^-, \mathbf{n}) \ , \ \forall e. \tag{3.12}$$

If the numerical flux $\mathcal{H}$ is an E-flux (see Eq. (3.10)), it can be shown that the Godunov scheme is positive which ensures energy stability and a discrete entropy inequality but also prevents the local solution extrema to be increased (*Local Extrema Diminishing*). The solution at an ulterior time step is a convex combination of its previous value and the neighbours. This last feature is essential to capture sharp discontinuities such as shocks. The demonstration can be found in Ref. [131].

Therefore, DGM at order zero inherits these properties from the FVM [100]. Extension to high order implies that the scheme is not positive anymore hence requiring a specific treatment to capture the shocks. However, Jiang and Shu [109] have shown that the energy stability is still conserved at high order by choosing E-fluxes. Therefore, this interface contribution (Ci) ensures energy stability of the Galerkin formulation, unlike in continous FEM for which the same formulation is not stable. The numerical flux $\mathcal{H}$ provides a Dirichlet boundary condition, by exchanging the correct characteristics between the cells adjacent to the interface. The choice of the flux is also dictated by the type of applications targeted as explained in a dedicated Section 3.2.2.

Diffusive variational form

In contrast to the discretization of the convective terms, many alternatives exist for the discretization of the diffusion terms, an overview and comparison can be found in Arnold et al. [9]. Within Argo and Echion, the Interior Penalty (IP) method is chosen. We consider again a scalar problem and the elliptic part of the weak formulation is then

$$\begin{aligned}\int_\Omega v\mathcal{L}^e(u) = & \underbrace{\sum_{\Omega_e \in \Omega} \int_{\Omega_e} \frac{\partial v}{\partial x}\left(D(u)\frac{\partial u}{\partial x}\right) d\Omega_e}_{Dv} - \underbrace{\sum_{I_i \in I} \oint_{I_i} \langle D(u)\frac{\partial u}{\partial x}\rangle [v] \ dS}_{Di} \\ & \underbrace{- \ \theta \sum_{I_i \in I} \oint_{I_i} \langle D(u)\nabla v\rangle [u] \ dS}_{Dt} + \underbrace{\alpha \sum_{I_i \in I} \oint_{I_i} [v][u] \ dS}_{Dp},\end{aligned} \tag{3.13}$$

where D becomes the diffusion coefficient of the scalar equation, θ defines if the form is symmetric $\theta = 1$ (SIP), non-symmetric $\theta = -1$ (NIP) or incomplete $\theta = 0$ (IIP) and α is the penalty parameter.

The diffusive interface terms Di, Dt and Dp are associated to the interior penalty formulation. They implement a Nitsche-type weak Dirichlet condition. The term Di arises directly from the partial integration of the diffusive term while Dt and Dp are the symmetric and penalty terms which are added to ensure the coercivity of the bilinear form hence the stability of the scheme.

The parameter θ can in principle be chosen freely without affecting consistency, while the interior penalty parameter α needs to be bounded to ensure stability while not degrading the conditioning of the matrix representing Eq. (3.13). The critical value for α depends in general on the mesh size, the polynomial approximation chosen and the diffusivity coefficient. The derivation of the sharp stability bounds for NIP can be found in Ref. [9], whereas Shahbazi [209] provided those for SIP and IIP on simplical elements and the generalization for generic elements is elaborated by Hillewaert [100]. In practice, the symmetric interior penalty with $\theta = 1$ is chosen due to superior convergence. Another useful variant is the NIP due to the relaxed requirements on α, since in this case only positivity of α is required [9]. In this work, a symmetric interior penalty method is used unless specified otherwise. However, for cases where the diffusion coefficient is highly variable in space (in case of large temperature gradient for example), the non-symmetric interior penalty method is preferred to ensure the stability of the computation [188].

Boundary conditions

The discretization scheme at the limit of the domain is treated by implementing weak boundary conditions. Typically, for the convective part, the ghost cell values are specified and the Riemann problem is solved on the physical boundary of the domain as in classical FVM. For the hyperbolic Euler equations, the ghost values to be specified should be in agreement with the number of entering characteristics of the hyperbolic system. The outer values for each type of boundary conditions are given in Table 3.1 for inviscid and viscous flows. For each particular test case, the conditions will be specified.

For the diffusive part, either Dirichlet, Neumann or Robin boundary conditions are implemented. For the Dirichlet type, the interface terms of the variational formulation reduces to

$$-\theta \sum_{I_i \in I} \oint_{I_i} \langle D \frac{\partial v}{\partial x} \rangle (u^+ - u^-) \, dS + \alpha \sum_{I_i \in I} \oint_{I_i} [v](u^+ - u^-) \, dS \qquad (3.14)$$

where u^- is the ghost value. For Neumann type boundary conditions the right and left values are set identical, hence the jump in the interface terms becomes zero and the flux $(\mathbf{F}^d \cdot n)$ is directly specified. Note that for highly reacting flows, if the domain is truncated, imposing a reflective boundary condition will induce errors due to the interactions between the acoustic waves and the chemistry in the flow. Non reflective boundary conditions such as the Navier-Stokes Characteristic Boundary Conditions NSCBC [221, 177] or Perfectly Matched Layer (PML) [10, 105] can be used to avoid non physical reflexions at the outlet/inlet. This is not investigated within this work and to reduce the reflection a coarse mesh is usually used to damp the pressure waves at the outlet.

Table 3.1: Main boundary conditions implemented in *DGAblation*. Interior values are indicated with the superscript '$+$' while outer variables are noted with '$-$'. The vector of conservative variables is noted $\mathbf{U}$ and the diffusive flux is $\mathbf{F}^d$.

BC type	Euler conditions	NS conditions
Subsonic inflow	$\mathbf{u}^-$, T^-, Y_i^- are given and $P^+ = P^-$	$\mathbf{F}^{d,+} \cdot \mathbf{n} = 0$
Adiabatic wall	$\mathbf{u}^-$ is given while other variables are taken as $\mathbf{U}^+ = \mathbf{U}^-$	$\mathbf{F}^{d,+}_{energy} \cdot \mathbf{n} = 0$, $\mathbf{F}^{d,+}_{mass} \cdot \mathbf{n} = 0$
Isothermal wall	$\mathbf{u}^-$ and T^- are given while other variables are taken as $\mathbf{U}^+ = \mathbf{U}^-$	$\mathbf{F}^{d,+}_{mass} \cdot \mathbf{n} = 0$
Subsonic outlet	P^- is given while other variables are taken as $\mathbf{U}^+ = \mathbf{U}^-$	$\mathbf{F}^{d,+} \cdot \mathbf{n} = 0$
Symmetry	$\mathbf{U}^+ = \mathbf{U}^-$	$\nabla \mathbf{U}^+ \cdot \mathbf{n} = 0$
Freestream	$\mathbf{u}^-$, T^-, Y_i^-, P^- are given	$\mathbf{F}^{d,+} \cdot \mathbf{n} = 0$

3.2.2 Interface fluxes

The discontinuous Galerkin discretization involves the solution of a Riemann problem at the boundary of each cell as in Finite Volume Method (FVM). Within the compressible module of the Argo code, several Riemann solvers are already available, an exact Riemann solver, the Roe approximate Riemann solver and a Lax-Friedrich scheme are implemented for calorically perfect gas. The treatment of multispecies flows involves to extend these fluxes. The simplest one is the Lax-Friedrich flux. For a conservative system of equations written as

$$\frac{\partial \mathbf{U}}{\partial t} + \nabla \cdot (\mathbf{F}^c(U)) = 0, \tag{3.15}$$

the Lax-Friedrich flux can be expressed

$$\mathcal{H}^{LF} = \frac{\left(\mathbf{F}^{c,L} + \mathbf{F}^{c,R}\right)}{2} - \frac{1}{2}\lambda_{LF}(\mathbf{U}^R - \mathbf{U}^L). \tag{3.16}$$

The superscripts R and L are respectively the right and left state, $\mathbf{F}^c$ is the convective flux and λ is the spectral radius of the flux Jacobian with respect to $\mathbf{U}$. For multicomponent flows, the fluxes $\mathbf{F}^{c,L}$, $\mathbf{F}^{c,R}$ should be defined accounting for the variation of the thermodynamic variables with temperature and composition. The maximum eigenvalue for the transport of multicomponent flows is $\lambda_{LF} = \bar{\mathbf{u}} \cdot \mathbf{n} \pm c^{Frozen}$, in which $\bar{\mathbf{u}}$ is the mean velocity at the interface.

The Lax-Friedrich scheme was chosen for its ease of extension to multispecies flows. However, this scheme is not an appropriate solver for the kind of application targeted here. Indeed, during an atmospheric entry, the temperature is really high implying a large sound speed. Therefore, low speed tests can lead to really low Mach number regime. Additionally, the density is varying because of the strong temperature gradients but does not depends on pressure variations anymore [141]. The treatment of low Mach number flow with a compressible solver leads to numerical issues regarding the convergence and the accuracy of the computation. The slow convergence is directly related to the disparity. This well known problem is strongly related to the difference between the convective and acoustic time scales. To treat this problem, a preconditioning of the time derivative is usually applied to scale the different terms hence avoiding to have a computation driven by acoustic propagation terms. The problem of accuracy is related to the stabilization, which is often not appropriate for low Mach number flows. If the Mach number tends to zero, the flow is dominated by pressure terms, and small perturbation of the pressure field may lead to great change in the velocity field [134].

The AUSM^{+}up scheme developed by Liou [134] tackles this second challenge by splitting the pressure terms and the convective terms. This scheme is valid for all speeds regime, some terms in the numerical flux will be switched off if the Mach number is sufficiently high to ensure the accuracy for subsonic, transonic or supersonic flows. In addition, this scheme is easily adapted for reactive flows [11]. The basic idea of the AUSM family scheme is to write the inviscid numerical flux as

$$\mathcal{H}_I^{AUSM} = \dot{m}_I \boldsymbol{\psi}_{L,R} + \boldsymbol{\mathcal{P}}_I, \tag{3.17}$$

where the subscript I indicates the interface and $\boldsymbol{\psi}$ is used for the vector of quantity convected by the mass flux $\dot{m}$. The challenge remains in defining the appropriate mass scalar flux $\dot{m}_I$ and the pressure flux $\boldsymbol{\mathcal{P}}_I$. The algorithm for a multi-component AUSM^{+}up is summarized hereafter. Note that the AUSM^{+}up scheme is an E-flux [134] which is the condition to ensure stability of the convective part.

AUSM^{+}up algorithm

This scheme relies on the concept of numerical speed of sound to define appropriate scaling for the numerical dissipation depending on the flow speed. A common speed of sound c_I is defined :

$$c_I = \min\left(\tilde{c}^L, \tilde{c}^R\right), \text{ , where } \tilde{c} = (c^*)^2 / \max(c^*, |u|) \tag{3.18}$$

where L and R refers to left and right states respectively and c^* is the critical speed of sound computed when the local Mach number is one

$$c^* = \sqrt{\frac{2(\gamma^{fr}-1)}{(\gamma^{fr}+1)}h}, \tag{3.19}$$

with h the mixture enthalpy and γ^{fr} the heat capacity ratio. These are computed based on Eq. (2.20) and (2.28). The interface Mach number (Ma_I) can be defined using this unique numerical speed of sound

$$Ma_I = \mathcal{M}^+(Ma^L) \; + \; \mathcal{M}^-(Ma^R) \; - \; \frac{\kappa_p}{f_a}\max(0, 1-\sigma\bar{Ma}^2)\frac{P^R - P^L}{\bar{\rho}c_I^2}. \tag{3.20}$$

where the left and right Mach number are evaluated as

$$Ma^{L,R} = \frac{u^{L,R}}{c_I}, \tag{3.21}$$

in which $u^{L,R} = \mathbf{u^{L,R}} \cdot \hat{\mathbf{n}}$. The two first terms of Eq. (3.20) are defined using split Mach numbers which are polynomial functions of the Mach.

$$\mathcal{M}^{\pm}(Ma) = \begin{cases} 0.5\,(Ma \pm |Ma|) & : \text{if } |Ma| \geq 1 \\ \pm 0.25\,(Ma \pm 1)^2 \pm \beta(Ma^2-1)^2 & : \text{else,} \end{cases} \tag{3.22}$$

$$\mathcal{P}^{\pm}(Ma) = \begin{cases} 0.5\,(1 \pm \text{sign}(Ma)) & : \text{if } |Ma| \geq 1 \\ \pm 0.25(Ma \pm 1)^2(2 \mp Ma) \pm \alpha Ma(Ma^2-1)^2 & : \text{else,} \end{cases} \tag{3.23}$$

The intermediate pressure is also defined using these split Mach numbers

$$\begin{aligned} P_I = {} & \mathcal{P}^+(Ma^L)P^L + \mathcal{P}^-(Ma^R)P^R \\ & - 2\kappa_u(\bar{\rho}f_a c_I)(u^R - u^L)\mathcal{P}^+(Ma^L)\mathcal{P}^-(Ma^R) \end{aligned} \tag{3.24}$$

quantities with the superscript "$-$" are mean value at the interface defined as

$$\bar{\rho} = \frac{\rho^L + \rho^R}{2}\text{ , and } \bar{Ma}^2 = \frac{(u^L)^2 + (u^R)^2}{2(c_I)^2} \tag{3.25}$$

The upwinding Mach numbers are defined:

$$Ma_I^{\pm} = 0.5\,(Ma_I \pm |Ma_I|) \tag{3.26}$$

Using this splitting approach, the numerical flux is defined as

$$\mathcal{H}_I^{AUSM} = c_I \left\{ Ma_I^+ \begin{pmatrix} \rho_{\mathbf{i}} \\ \rho\mathbf{u} \\ \rho H \end{pmatrix}^L + Ma_I^- \begin{pmatrix} \rho_{\mathbf{i}} \\ \rho\mathbf{u} \\ \rho H \end{pmatrix}^R \right\} + \begin{pmatrix} \mathbf{0} \\ P_I \\ 0 \end{pmatrix}. \tag{3.27}$$

The different parameters in this formulation are chosen as $\kappa_p = 0.25$, $\kappa_u = 0.75$, $\sigma = 1$, $\beta = 1/8$ and $\alpha = -3/4 + \hat{\alpha}(Ma)$ [29]. Finally, $\hat{\alpha}(Ma) = \frac{15}{16}f_a^2$ is

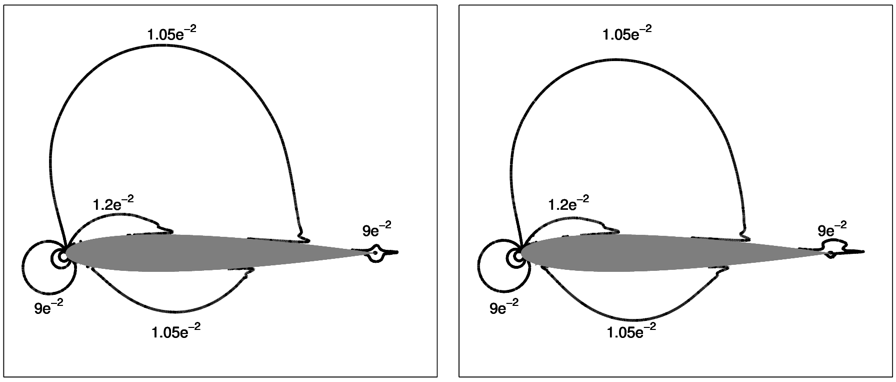

(a) Roe flux formulation $Ma = 10^{-1}$ (b) AUSM^{+}up flux formulation $Ma = 10^{-1}$

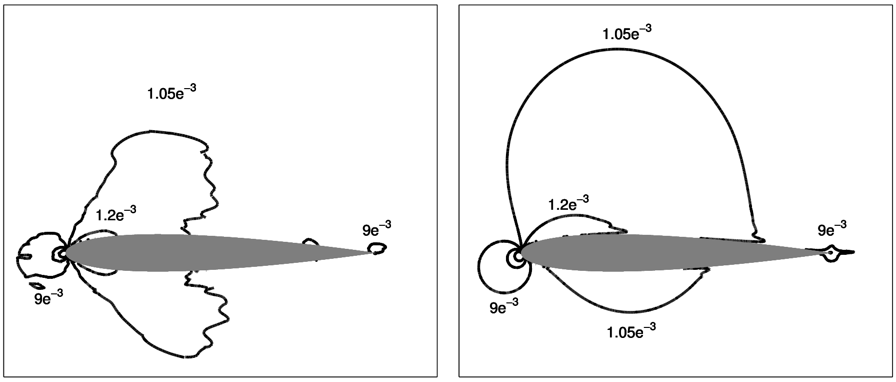

(c) Roe flux formulation $Ma = 10^{-2}$ (d) AUSM^{+}up flux formulation $Ma = 10^{-2}$

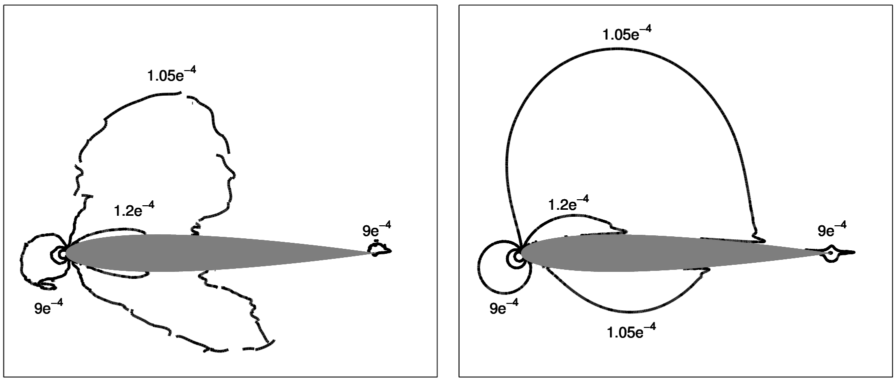

(e) Roe flux formulation $Ma = 10^{-3}$ (f) AUSM^{+}up flux formulation $Ma = 10^{-3}$

Figure 3.5: Iso-Mach contours for inviscid flow around a NACA012 profile for several freestream Mach numbers from top to bottom 10^{-1}, 10^{-2}, 10^{-3}. The isolines are shown for $[0.6 : 0.15 : 1.2] * 1e^{-Ma}$. The steady state results are computed with $p = 4$ and with a maximum number of 200 iterations.

defined using the scaling function $f_a = M_0(2 - M_0)$ with the reference Mach number (M_0) which accounts for a cut-off Mach if the real Mach number tends to zero: $Ma_0^2 = \min(1, \max(\bar{M}a^2, Ma_{co}^2))$.

The advantages of such a numerical flux are demonstrated in Fig. 3.5 for which the inviscid flow at several Mach numbers around a NACA profile is studied. The numerical tests have shown that, as expected, the convergence problem is not resolved using such technique, however, the results obtained using this flux formulation are far more accurate than the ones provided by a regular Roe solver. The same tolerance on the convergence and maximum number of iterations have been applied for both solvers.

In addition, the Simple Low dissipation AUSM (SLAU) Riemann solver [211] implemented by J.S Cagnone in the *DGFluid* module has also been extended to treat multi-species flows. The extension of this scheme to multi-component flows is readily obtained by the same development presented for the AUSM^+up. As for the development of the latter, the convective flux for each partial density is considered, the speed of sound is computed using the frozen specific heat ratio ($\gamma^{fr}(Y_i, T)$) and the mixture enthalpy is computed using Eq. (2.20). SLAU possesses a behavior similar as the AUSM^+up scheme with the advantage of being free from user parameters to define (no cutoff Mach number).

3.3 Time discretization

First, regarding Echion, several time stepping schemes have been implemented in the 1D code including a Backward Euler (BE) integration scheme and the Super Time Stepping scheme (STS). The STS proposed by Alexiades [3] is a method which relaxes the stability constraint to accelerate standard explicit schemes without the cost of solving a linear system. Since these methods have been used only in the one dimensional code, detailed information on the implementation can be found in Section 6.3.2.

Secondly, Argo is able to solve steady or unsteady problems. In this work, the ablation of the material leads to a moving interface problem and no steady state exists. Therefore, this section focuses mainly on the methods to solve unsteady problems. Both explicit and implicit time stepping schemes are available in the Argo platform. However, strong reactive terms as well as the presence of a porous medium put severe stability constraints on the time step for an explicit method. Therefore, a fully implicit time marching method has been selected. Due to the large disparity of scales involved in this kind of problem (see Section 1.2.2), it could be easier to split the system of equations and march in time differently for stiff terms as it is proposed for example in [137]. However, we have chosen a fully implicit method to solve the system of equations and the splitting is proposed as perspective of this work.

Several implicit time discretization schemes are available within the multidimensional tool Argo but the standard scheme used is the multistep Backward Differentiation Formula at second order (BDF2) combined with a Newton-Raphson (NR) algorithm. Consider the system of equation in vectorial form

$$\frac{\partial \mathbf{U}}{\partial t} = \mathcal{R}^{CDS}(\mathbf{U}), \tag{3.28}$$

where $\mathbf{U}$ is the system of conservative variables (see Section 2.5) and $\mathcal{R}^{CDS}(\mathbf{U}) = -\nabla \cdot \mathbf{F}^c + \nabla \cdot \mathbf{F}^d + \mathbf{S}$ groups the convective, diffusive and source terms, the BDF2 scheme is then written

$$\begin{aligned} \mathbf{U}^{n+1} &= \mathbf{U}^n + \Delta t \mathcal{R}^{CDS}(\mathbf{U}^{n+1}), && (3.29) \\ \mathbf{U}^{n+2} &= \frac{4}{3}\mathbf{U}^{n+1} - \frac{1}{3}\mathbf{U}^n - \frac{2}{3}\Delta t \mathcal{R}^{CDS}(\mathbf{U}^{n+2}). && (3.30) \end{aligned}$$

This implicit scheme results in non-linear systems to be solved for which a NR is used. In turn, NR algorithm requires the solution of a linear system at each iteration. In order to solve the linear system associated with the NR, a direct Gauss solver as well as iterative methods are implemented inside Argo. The code features one of the first matrix free GMRES implemented for DG by Hillewaert [101, 102]. This section does not aim to provide detailed information on the implementation of matrix-free Newton-Krylov approach but the main ingredients are summarized to provide the readers some insights of the method. Consider that the linear problem to solve can be written

$$\mathbf{L}^* \Delta \mathbf{U} = -\mathbf{r}^*, \tag{3.31}$$

where $\mathbf{L}^*$ is the Jacobian of the residual ($\mathbf{r}^*$) with respect to the solution state vector $\mathbf{U}$. The solution of this system by a Newton-Krylov method requires the definition of the so-called Krylov subspaces $\mathcal{K}_n$ based on $\mathbf{L}^*$ and $\mathbf{r}^*$

$$\mathcal{K}_n(\mathbf{L}^*, \mathbf{r}^*) = span\{\mathbf{r}^*,\ \mathbf{L}^* \cdot \mathbf{r}^*,\ ...,\ (\mathbf{L}^*)^n \cdot \mathbf{r}^*\}. \tag{3.32}$$

Iterative methods like Generalized Minimum RESidual (GMRES) can be used to approximate the solution based on the Krylov subspaces. Observing the definition of the Krylov space, we only need the matrix-vector product ($\mathbf{L}^* \cdot \mathbf{r}^*$), and not the Jacobian itself which is the basic idea behind the development of a matrix-free method. This matrix vector product can be approximated by a finite difference approximation, hence, -in theory- this method does not require the computation and storage of the Jacobian. In practice, the computation of this Jacobian is still needed for preconditioning because the linear system (Eq. (3.31)) to solve is usually badly conditioned. Block-Jacobi or ILU factorization are implemented within Argo and can then be used as preconditioner for the system. The computation of the Jacobian can be frozen during few iterations of the Newton-Raphson algorithm to save computational time. Unless specified otherwise, we always freeze the Jacobian during three iterations. Detailed information on the method and its implementation can be found in Hillewaert [100] and references therein.

Because of the large disparity in the scales of the problem (gas density can be several orders of magnitude smaller than solid density), a high fill-in for the preconditioner is required and for some cases iterative methods fail and direct solvers should be used to ensure convergence. Unless specified otherwise, the direct Gauss solver is used in this work and this implies computationally expensive simulations.

For implicit time integration, a particular attention has to be paid to the derivation of the Jacobian. In order to simplify the derivation of this matrix, it is desirable to use primitive variables as working quantities instead of conservative one. Indeed, the non-linear dependence of the internal energy with respect to the temperature implies that deriving the energy with respect to the temperature is trivial while the inverse does not exist analytically. Within this work, the set of partial pressures (P_i), the velocity vector ($\mathbf{u}$), and the temperature (T) are chosen as primitive variables. In addition, for multiphase problems, solid density is considered in the list of primitive variables.

Note that using primitive variables does not imply the loss of conservation. In order to show this, we consider the simple BDF1 time integration scheme and the system of conservative variables $\mathbf{U}$ and the primitives $\mathbf{Q}$. BDF1 can be written

$$\frac{\mathbf{U}^{n+1} - \mathbf{U}^{n}}{\Delta t} = \mathcal{R}^{CDS}(\mathbf{U}^{n+1}). \tag{3.33}$$

The conservative and primitive variables are related by $\mathbf{U} = \mathbf{U}(\mathbf{Q})$ and this relation is used to linearize the BDF1 scheme around $\mathbf{Q}^*$, the current estimate of the vector of primitive variables at time t^{n+1},

$$\frac{1}{\Delta t}\left(\frac{\partial \mathbf{U}}{\partial \mathbf{Q}} + \frac{\partial \mathcal{R}^{CDS}}{\partial \mathbf{Q}}\right)\delta\mathbf{Q} + \frac{\mathbf{U}(\mathbf{Q}^*) - \mathbf{U}^{n}}{\Delta t} = \mathcal{R}^{CDS}(\mathbf{U}(\mathbf{Q}^*)). \tag{3.34}$$

Equation (3.34) reduces to the original system of equation at convergence ($\delta\mathbf{Q} = 0$). Therefore, the Jacobian $\frac{\partial \mathcal{R}^{CDS}}{\partial \mathbf{Q}}$ with respect to primitive variables can be used. Using the discretization of convective, diffusive and source term (see Eq. (3.6)), the definition of the Jacobian requires to evaluate

$$\frac{\partial \mathbf{F}^{C}}{\partial \mathbf{Q}}, \ \frac{\partial \mathbf{F}^{D}}{\partial \mathbf{Q}}, \text{ and } \frac{\partial \mathbf{S}}{\partial \mathbf{Q}}. \tag{3.35}$$

The derivation of the conversion matrix to change from primitive to conservative variables and the Jacobian without porous medium is presented in Appendix A. Numerical issues regarding the computation of the Jacobian should be prevented by ensuring existence of the derivative. For example, in the NASA-7 database, the transport and thermodynamic properties are fitted with polynomial expressions on two ranges of temperatures (from 300 to 1000 and 1000 to 5000 [K]). In order to ensure the convergence of the computation, the fitted curve must have a continuous first derivative on the whole temperature range. For instance, the transport coefficients computed in the internal Argo library taken from [148] and not the one in [217], lead a discontinuity at

1000 [K] for the species CO. In turn, this implies a step change of the Jacobian when simulating cases with a temperature around 1000[K]. Figure 3.6 shows the discontinuity of the viscosity for this species at 1000[K] if we use the polynomial fit from [148]. We observe that computing the viscosity using the fit proposed in [217] or with Mutation^{++} leads to a continuous viscosity. For the same reason, the specific surface S_f of the fibers used to compute the heterogeneous reaction rate is approximated by a polynomial fit (see Eq. (2.106)). This remove the singularity of the square root when the solid volume fraction tends to zero. The development of the Jacobian for each term in Eq. (3.35) was verified against a finite-difference Jacobian.

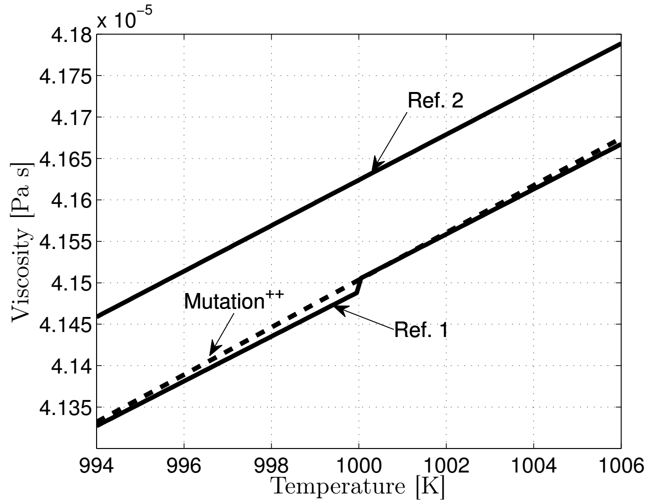

Figure 3.6: Viscosity of a mixture of pure CO with respect to temperature using the polynomial fit of [148] (noted Ref.1), the one of [217] (noted Ref.2) and computing it with Mutation^{++}.

3.4 Multi-phase treatment

To simulate the thermal response of an ablative material to a high enthalpy flux occurring during atmospheric entries, the nowadays widespread strategy proposed by Kendall et al [14] consists in solving the flow field and the material response independently and coupling them using boundary conditions on the mass and heat fluxes. The advantages of such a formulation are its reduced complexity and computational cost. However, using such an approach, some interactions previously discussed cannot be captured. As already mentioned, the originality of this project lies in the treatment of the bulk phase and the material in the same domain of computation. In addition, this porous medium is progressively eroded by the incoming flow. Therefore, using a one domain approach, one has to deal with a moving boundary problem in DGM.

The Volume Averaged Navier-Stokes equation presented in Section 2.3, shows how the validity of the Navier-Stokes equations can be extended to multiphase systems in order to treat a homogeneous porous medium. We use a variable porosity/permeability approach to describe the transition from the fluid flow to a porous medium. Since the variables encounter strong but continuous change, this approach does not need the definition and tracking of an interface. Nonetheless, as explained in the physical modeling chapter, another approach consists in using jump conditions at the interface between the bulk phase and the porous medium. This requires the treatment of a sharp embedded interface. An effort has been dedicated to review and investigate several techniques to treat the high gradients/discontinuities at an interface, this is summarized in Appendix B.

Using the variable porosity/permeability approach discussed in Section 2.4, it is natural to adopt a *diffuse interface approach* which smoothes the discontinuity across the interface. Therefore it is the only one discussed in this chapter. The porosity will vary from a constant value in the homogeneous porous medium to one in the plain fluid region. Within this work, a normalized hyperbolic tangent function is used to regularize the initial solid volume fraction on the grid

$$H(\phi) = \tanh\left(\frac{2\pi\phi}{\epsilon_\phi}\right), \tag{3.36}$$

where ϕ is the initial distance function (level-set) from the porous medium and ϵ_ϕ is the grid distance on which the quantity is smoothed. Note that this is not exactly the thickness of the interface since the hyperbolic tangent function is not a compact function. Pochet [176] has observed for several numerical test cases that, in order to ensure stability of the scheme, the smoothing distance has to satisfy

$$\epsilon_\phi > 3\frac{h}{p}, \tag{3.37}$$

h being the mesh size and p the interpolation order. Figure 3.7 shows the smoothed Heaviside of Eq. (3.36). In this case, ϵ_ϕ is defined to be $0.2L$ to observe clearly the transition region.

Thanks to the smoothing introduced, the porous region does not have to conform with the mesh which is interesting for receding porous problem. Indeed, the mesh movement can seriously degrade mesh quality in cases of non-uniform material recession and remeshing can be time consuming and quite complex depending on the shape of the interface. In this work, the mesh is fixed and we consider an immersed interface. Finally, one can observe that the evolution of the embedded geometry does not have to be tracked because an additional solid mass equation is solved. Assuming that the solid matrix of the porous medium is rigid, the mass is lost at the surface of the carbon fibers, the porosity can be deduced and therefore the interface can be reconstructed during post-processing of the results. The level-set function is only used at the initialization step to define the porous region. Note that, for non reactive porous medium the solid density is not a variable of the system anymore. The structure of Argo allows to account for auxiliary data; in case of an inert porous medium, the color function associated with the porous medium region is therefore saved in this data structure.

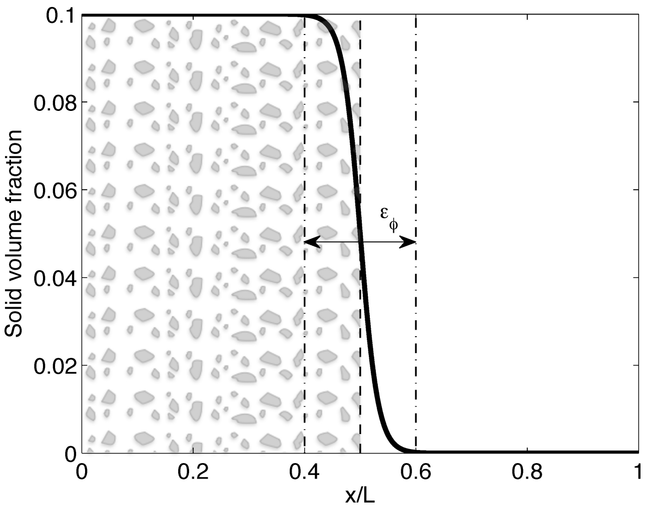

Figure 3.7: Hyperbolic tangent function used to regularize the initial solid volume fraction.

Figure 3.8 shows the evolution of the transition region for a reactive porous plate. The black line at the center of this transition region represents the position of the post-processed interface which does not conform with the mesh. Since the normal recession velocity is not constant everywhere along the interface, the resulting shape is curved hence the benefits of using an unstructured grid in this case. It can also be observed that the interface thickness can vary depending on the kinetics regime, this will be further investigated in Chapter 5. In order to keep a physical meaning of the interface thickness while satisfying the criterium in Eq. (3.37), the mesh is refined in the interface region. Since the limit of the porous medium is changing, the mesh is refined in the zone where the interface is expected to evolve.

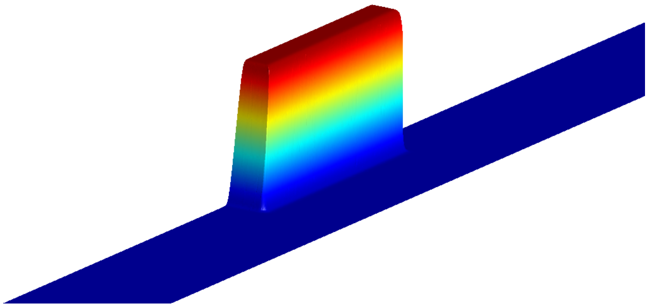

(a) Smoothing of the solid volume fraction

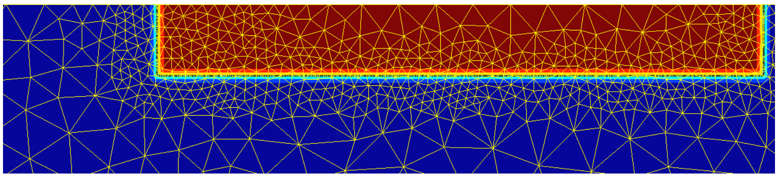

(b) Initial porous medium shape

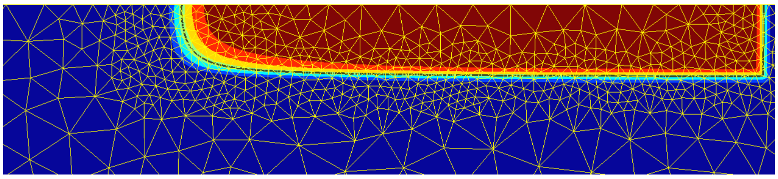

(c) Ablated porous medium shape

Figure 3.8: Diffuse interface method, the evolution of the interface region on an unstructured grid for a reactive porous medium is shown. The 3D plot shows the smoothing of the solid volume fraction on the domain.

3.5 Conclusions

Two different numerical codes using DGM have been developed. On one hand, the development of a one dimensional code Echion was used to simulate in-depth thermal response of the material and to study the approach to treat the moving boundary problem. On the other hand, the *DGAblation* module of Argo developed in this thesis, is able to solve compressible flows with multi-species and potentially low-Mach number flows. In addition, the new module of Argo can simulate problems involving the presence of degrading or non-reactive porous medium. The derivation of the Jacobians for reactive Navier-Stokes equations with variable thermodynamic and transport properties helps for the use of an implicit time integration scheme. This implementation of complex conservation laws inside the Argo code has proved the flexibility and robustness of the platform developed at Cenaero. The verification of the developed module on several cases is proposed in Chapter 4.

CHAPTER 4

VERIFICATION OF THE SIMULATION TOOL

This chapter presents several test cases to verify the development of the numerical tool. The volume averaging approach and the treatment of several species in a reactive flows presented in Chapter 2 have been implemented in a new module of the Argo code described in Chapter 3. The numerical code developed is verified against a series of test cases of increasing physical complexity to test independently the different aspects of the code. First, the implementation of a module solving reactive flows is verified. Subsequently, extensive tests are proposed to verify the presence of an inert porous medium, and finally, the evolution of the material surface submitted to heterogeneous reaction is proposed to verify the treatment of the reactive porous medium.

4.1 Introduction

In order to verify the implementation of the *DGAblation* module implemented within Argo, the different parts of the equations summarized in Section 2.5 are tested. Eight different test cases are proposed. The test cases 1-4 verify the treatment of variable thermodynamic properties (tc_1), the presence of stiff reactive terms (tc_2), the solution of the reactive Euler equations (tc_3) and the diffusion in a multi-component mixture (tc_4). The tests tc_5, tc_6 and tc_7 compare the results of Argo for flow through and around porous medium with results in the literature. Finally, the last case tc_8 analyzes the recession of a porous medium by an oxidizing flow. The Table 4.1 provides to the reader a summary of the hypothesis made for each test case. These will be described in details within each case but the table gives an overview of the capabilities tested.

Table 4.1: Summary of the test cases analyzed with the respective hypothesis on the system of equation Eq. (2.118).

	Supersonic nozzle	Adiabatic reactor	Shock relaxation	Diffusive case	Porous plug	Porous slab	Porous cylinder	Reactive porous
Model used/test cases ($tc_{\#}$)	1	2	3	4	5	6	7	8
Code dimensionality								
Pseudo 0D		✓						
Pseudo 1D			✓	✓	✓			✓
2D	✓					✓	✓	
Gas-phase mass conservation								
Number of species	1	2	11	2	1	1	1	3
Convective term ($\epsilon_g \langle \rho_i \rangle_g \langle \mathbf{u} \rangle_g$)	✓		✓		✓	✓	✓	✓
Multi-component diffusion (J_i)				✓				✓
Homogeneous source term ($\langle \dot{\omega}_i^{hom} \rangle$)		✓	✓					
Heterogeneous source term ($\langle \dot{\omega}_i^{het} \rangle$)								✓
Solid-phase mass conservation								
Porous medium					✓	✓	✓	✓
Heterogeneous reactions								✓
Momentum conservation								
Convective term ($\langle \rho \rangle_g \langle \mathbf{u} \rangle_g \langle \mathbf{u} \rangle_g + P$)	✓	✓	✓		✓	✓	✓	✓
Diffusive viscous term ($\langle \boldsymbol{\tau} \rangle_g$)					✓	✓	✓	✓
Drag force ($\epsilon_g \frac{\mu}{\kappa} \langle u \rangle_g$)					✓	✓	✓	✓
Energy conservation								
Convective term ($\epsilon_g \langle \rho \rangle_g \langle \mathbf{u} \rangle_g \langle H \rangle_g$)	✓	✓	✓		✓	✓	✓	✓
Diffusive viscous term ($\langle \boldsymbol{\tau} \cdot \mathbf{u} \rangle$)					✓	✓	✓	✓
Fourier heat flux ($\lambda_{eff} \nabla \langle T \rangle$)					✓	✓	✓	✓
Multispecies diffusion term ($\sum_{i=1}^{N_s} h_i \langle \mathbf{J}_i \rangle$)								✓
Thermo/transport properties								
Variable thermodynamic properties	✓	✓	✓					✓
Variable transport properties								✓
Internal Argo library	✓			✓	✓	✓	✓	✓
Mutation++ library		✓	✓					
Boundary conditions								
Subsonic inflow	✓		✓		✓	✓	✓	
Adiabatic wall	✓	✓	✓	✓	✓	✓		✓
Isothermal wall								
Subsonic outlet			✓		✓	✓	✓	
Symmetry	✓							
Freestream							✓	✓

4.2 Supersonic nozzle

To verify the implementation of varying thermodynamic properties (non calorically perfect gas), the steady over-expanded inviscid flow in a supersonic nozzle is investigated. The initial pressure ratio is imposed to ensure a supersonic flow in the divergent part of the nozzle. The outlet boundary condition is supersonic hence no information is needed. Only one fake species corresponding to a frozen mixture of O_2 and N_2 is considered in this test case and Table 4.2 summarizes the conditions used.

Table 4.2: Test case conditions for an over-expanded inviscid flow in a supersonic nozzle.

Mixture	Area throat $[m]$	Total pressure $[Pa]$	Total temperature $[K]$
Air	0.25	101325	1500

The throat of the nozzle is defined at $x_t = 1$, and the convergent and divergent geometries are described by

$$y_c = 0.5 - 2.5x^3 + 3.75x^4 - 1.5x^5,\ \forall x < x_t \tag{4.1}$$

$$y_d = \frac{1}{3} - \frac{7}{40}x + \frac{1}{10}x^2 - \frac{1}{120}x^3,\ \forall x > x_t. \tag{4.2}$$

The one dimensional analytical solution is shown for both calorically and non-calorically perfect gases. The discrepancy with the numerical results are due to two dimensional effects not accounted for in the analytical solution. Indeed, for a two dimensional case, there is a propagation delay of information from the wall hence the discrepancy at the center of the nozzle. The offset with respect to the analytical solution is of the same order of magnitude for calorically perfect gases (CPG) and non-calorically perfect gases (NCPG). The code is also verified against another implementation done independently by Cagnone [38] in the *DGFluid* module of the Argo code. Both implementations are based on the internal thermochemical library developed and give exactly the same results.

Figure 4.1 shows the importance of assuming non-calorically perfect gases for this application. After the sonic throat, the temperature in the divergent of the nozzle is significantly different for NCPG and CPG. The nozzle geometry, the mesh used and the pressure field inside are shown in Fig. 4.2. We use a polynomial order of interpolation $p = 2$ and the mesh is composed of 1118 triangles with a characteristic length of $6.25e^{-2}[m]$. The GMRES linear solver algorithm is used in this case. It takes approximatively $25[s]$ on a single core to converge (reducing the initial residual by 12 orders of magnitude).

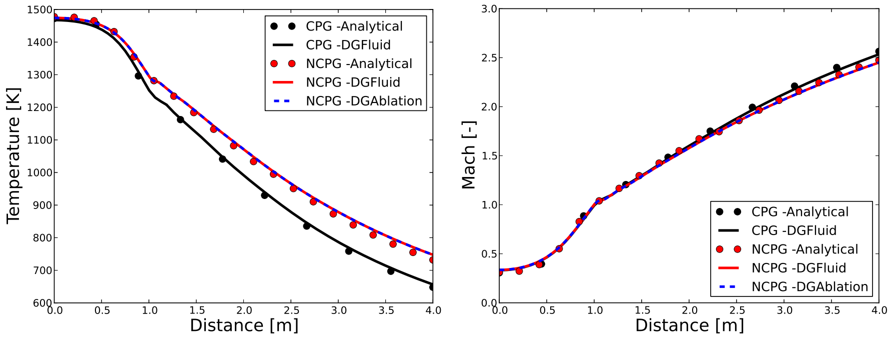

(a) Temperature (b) Mach number

Figure 4.1: Steady supersonic inviscid flow in a nozzle. The profiles at the center of the nozzle are compared for Calorically Perfect Gas (CPG) and Non-Calorically Perfect Gas (NCPG) with the respective analytical solution.

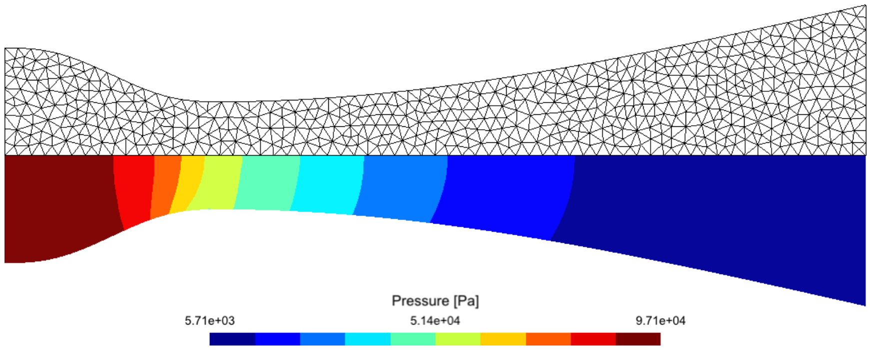

Figure 4.2: Steady state pressure field in the nozzle.

4.3 Adiabatic reactor

In order to verify the implementation of the chemical source term and the implicit temporal integration, the O_2 dissociation at high temperature in a zero dimension perfectly mixed adiabatic reactor is studied. In order to simulate the pseudo 0D case, the numerical domain is a box composed of one element and periodic boundary conditions are imposed on the sides. The results of Argo are compared with a 0D code developed which solves only the evolution of the species density assuming adiabatic conditions, no convection and no diffusion. This 0D code is distributed within the Mutation^{++} suite, it uses a simple forward Euler scheme to integrate the ordinary differential equation.

The initial temperature is set to $5000[K]$ and the gas mixture is only composed of O_2. A simple mechanism for the decomposition of molecular oxygen to atomic oxygen is used and summarized in table 4.3. We use the GMRES algorithm to solve the linear system associated with the implicit time integration scheme. The time step chosen is $1e^{-5}[s]$ to ensure the accuracy of the results. Figure 4.3 shows the excellent agreement between the 0D code and the Argo results.

Table 4.3: Dissociation mechanism of molecular oxygen in atomic oxygen (M is a third body).

Reactions	$A\ [mol\ K/s]$	$T\ [K]$	n
$O_2 + M \rightleftharpoons 2O + M$	$2.75e^{13}$	59500.0	-1

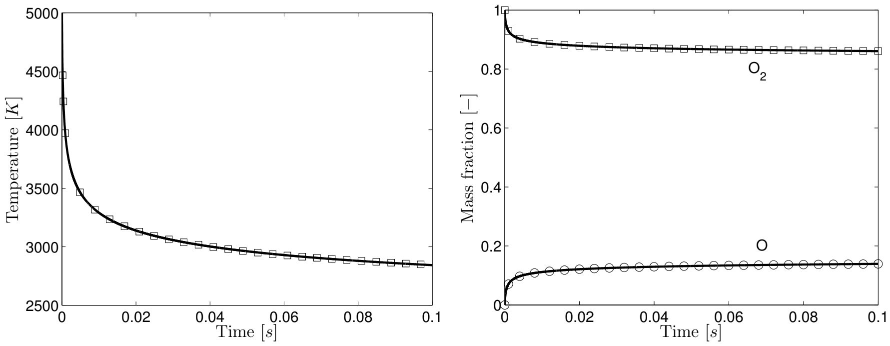

(a) Temperature (b) Mass fractions

Figure 4.3: O_2 dissociation in a $0D$ adiabatic reactor. Solid lines are the Argo results and symbols are the results of the 0D code.

4.4 Shock relaxation

This test case verifies the solution of the multi-species reactive Euler equations. As explained in Chapter 1, during the atmospheric entry of a blunt body, a bow shock appears in front of the vehicle forming a reactive layer. In order to assess the capabilities of the code to solve reactive flows, the chemical relaxation after the shock is studied.

As explained in Chapter 3, special treatments to capture the shock are required for DGM (i.e. in Argo). However, only the relaxation after the shock is interesting in this test case. In order to find the post-shock quantities used as input, one needs to solve the Rankine-Hugoniot relations (Eq. (4.3) to (4.5)). This system is strongly non-linear due to the dependence of the thermodynamic properties with respect to temperature

$$\rho_1 u_1 = \rho_2 u_2 \text{ (continuity)}, \tag{4.3}$$

$$P_1 - P_2 = \rho_2 u_2^2 - \rho_1 u_1^2 \text{ (momentum)}, \tag{4.4}$$

$$h_1 + 0.5u_1^2 = h_2 + 0.5u_2^2 \text{ (energy)}. \tag{4.5}$$

The chemistry is assumed frozen through the shock. In order to solve this system, the jump conditions are first computed assuming constant γ^{fr} (cold gas approximation). These values are then used as initial conditions to solve the non-linear system with a Newton-Raphson algorithm. These post-shock values are the left boundary conditions for the relaxation.

First of all, we have developed a numerical tool to solve steady state reactive Euler equations. Assuming steady state and 1D problem, it is possible to transform the system of partial differential equations into a system of ordinary differential equations which can be solved easily [139]. The solution of this system was implemented in the shocking^{++} code provided in the Mutation^{++} suite. This code computes the post-shock values and solves the steady state Euler equations to simulate the chemical relaxation. The 1D flow solver is based on the model proposed by Magin et al. [139] modified to account for only one temperature. Details on the development of this code can be found in Appendix C. The shocking^{++} code has been verified independently and the results will be compared with Argo.

The particular test case in this section studies the relaxation behind the shock corresponding to a particular moment of the second Flight Investigation of Re-Entry (FIRE II) trajectory [42]. The FIRE capsule is a subscale model of the Apollo vehicle and these flight experiments took place during the Apollo campaign in the sixties. The data used correspond to the $t = 1634[s]$ of the flight; the freestream conditions and post-shock values are given in Table 4.4.

Table 4.4: Shock characteristic quantities for the FIRE II trajectory [42].

t $[s]$	X [-]	P [Pa]	T [K]	v_s [m/s]
1634 (pre-shock)	N_2/O_2 $0.79/0.21$	2.09	195	11360
1634 (post-shock)	N_2/O_2 $0.79/0.21$	4352	38005	1063

The chemical relaxation of air with 11 species; N_2, O_2, NO, N, O, N_2^+, O_2^+, NO^+, N^+, O^+, e^- is considered with the kinetic mechanism of Park [173]. The external library Mutation^{++} providing the thermodynamic, transport properties and reaction rates is used. The comparison between shocking^{++} and the results of Argo are shown in Fig. 4.4 for the velocity, pressure, temperature and composition profile after the shock. Only the main species are shown in Fig. 4.4(d) but the traces of some ions (e^-, N_2^+, O_2^+, NO^+) at high temperature are also well captured by the Argo code (see Fig. 4.4(e)).

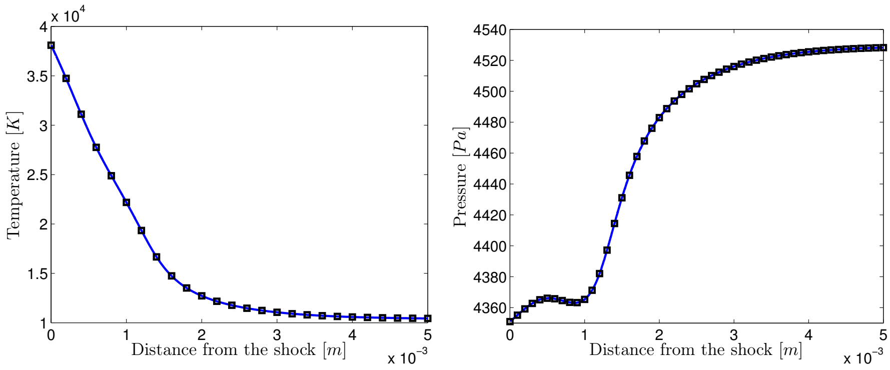

(a) Temperature (b) Pressure

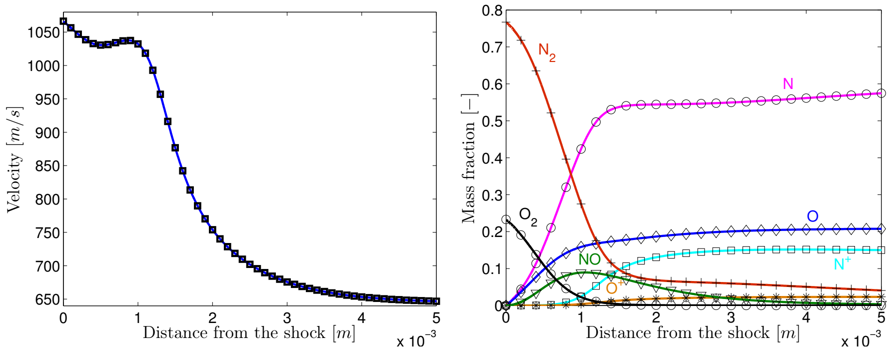

(c) Velocity (d) Mass fractions

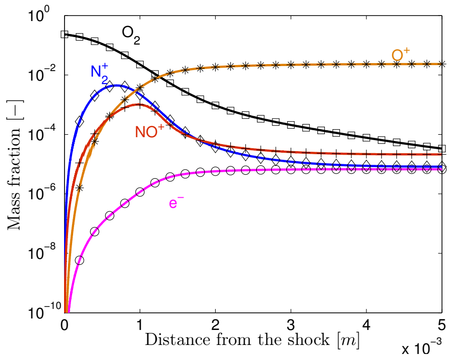

(e) Mass fractions

Figure 4.4: Chemical relaxation behind a strong shock. Symbols are the results of the shocking^{++} code, solid lines are Argo results.

The domain length is ten times bigger than the region plotted in Fig. 4.4 to ensure that the equilibrium is reached before the outlet boundary. It is composed of 400 triangles with a refinement in the region close to $x = 0$. The minimum length for the triangles in this region is $4e^{-6}[m]$. To ensure convergence of the computation, an increasing polynomial interpolation is used. First, the initial guess is computed with $p = 0$ then $p = 1$ and finally the results in Fig. 4.4 are computed with $p = 2$. The excellent agreement between the numerical codes verifies the solution of compressible reactive non-viscous flow in the DG code. The solution at the end of the relaxation should be at equilibrium and the comparison assuming local thermal equilibrium and a very long relaxation is provided in the Appendix C.

4.5 Diffusive transport

Multi-component flows involve the presence of additional diffusion terms in the mass and energy conservation laws. This section analyses the diffusion model implemented. The diffusion of a mixture of N_2, O_2 is investigated in pseudo 1D with imposed diffusivity. For this test case, the system of equations reduces to

$$\frac{\partial \rho_i}{\partial t} = \frac{\partial}{\partial x}\left(\rho D \frac{W_i}{W}\frac{\partial X_i}{\partial x}\right). \tag{4.6}$$

Periodic boundary conditions are imposed on the top and bottom part of the domain while the right and left boundaries are considered as walls. The conditions chosen for this test case are given in Table 4.5. The initial mass fraction is given by

$$Y_{N_2} = 0.5 - 0.13\left(1 - 0.13\cos\left(\frac{2\pi x}{L}\right)\right), \text{ and } Y_{O_2} = 1 - Y_{N_2} \tag{4.7}$$

Table 4.5: Test case conditions for the diffusion in a binary mixture.

Mixture	L $[m]$	P $[Pa]$	T $[K]$	D $[m^2/s]$
N_2/O_2	0.01	$5e^6$	1000.0	$2.6e^{-6}$

The temporal evolution is verified against a simple Matlab code using the *pdepe* solver. The temporal discretization in the Matlab routine *pdepe* is ensured by a variable time step ODE solver [210] and the spatial discretization of this solver is described in Ref. [212]. The number of elements in the Matlab code is chosen to be 5000 equispaced $1D$ elements to provide a reference solution. Figure 4.5 shows the evolution of the N_2 mole fraction. The mesh for Argo is composed of 100 triangle elements and a polynomial order of approximation $p = 3$ is chosen.

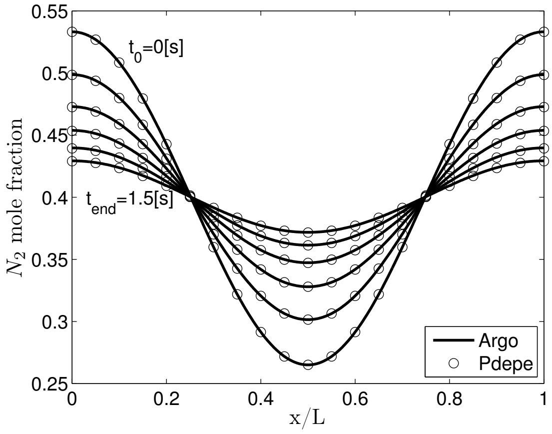

Figure 4.5: Diffusion of a two species mixture with initial gradient composition. The solution is plotted from $t_0 = 0\ [s]$ to $t_{end} = 1.5\ [s]$ every $0.3\ [s]$.

4.6 Channel flow through a porous plug

In order to verify that the code is able to simulate the flow perpendicular to a porous surface, we study several channel flows with different conditions and with a porous plug. The setup is shown in Fig. 4.6. The mesh used is composed of 1250 triangles elements with a refinement in the interface region and the polynomial approximation used for all the configurations is $p = 2$. The interface thickness is defined as $\epsilon_\phi = 3e^{-2}[m]$ while the minimum mesh size in the interface region is fixed to be $6.5e^{-3}[m]$. The direct Gauss solver is used because of the large difference between solid and fluid densities.

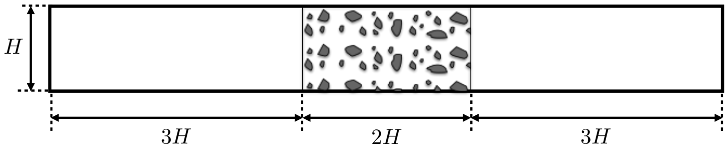

Figure 4.6: Setup for the porous plug test cases.

In this case, the flow is normal to the interface hence the pressure gradient will be substantially higher in the porous region while the averaged velocity is expected to be of the same order of magnitude. Two test cases are investigated on the same geometry but with different boundary conditions. Table 4.6 summarizes the conditions chosen for both test cases.

Table 4.6: Conditions for the flow through a porous plug.

Mixture	H $[m]$	P_{outlet} $[Pa]$	T_{inlet} $[K]$	U_{inlet} $[m/s]$	κ $[m^2]$	μ $[Pa\ s]$
Air	0.1	10132.5	293.15	$1.25e^{-3}$	$1e^{-5}$	$1.5e^{-5}$

First, periodic boundary conditions have been imposed on the top and bottom part of the channel to retrieve one dimensional Darcy law. As expected, the pressure drop in Fig.4.7(a) is linear inside the porous medium and the difference in pressure at steady state matches Darcy law:

$$\Delta P_{Darcy} = L_{plug} \cdot \frac{\mu}{\kappa} \cdot \langle u \rangle = 3.738e^{-4}\ [Pa] \tag{4.8}$$

$$\Delta P_{Argo} = 3.738e^{-4}\ [Pa]. \tag{4.9}$$

The comparison between the superficial velocity ($\langle u \rangle$) and the interstitial velocity ($\langle u \rangle_g$) can be observed in Fig. 4.7(b). As expected, the interstitial velocity will increase to conserve the mass flux through the channel while the superficial velocity remains constant.

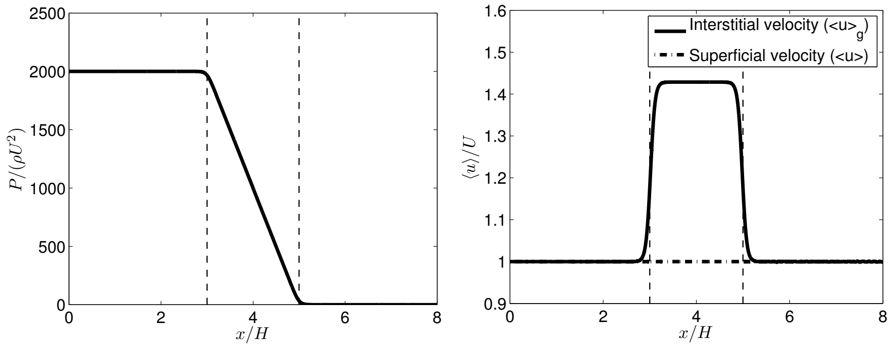

(a) Non-dimensional pressure profile (b) Non-dimensional velocity profile

Figure 4.7: Steady state results of a 1D flow through a porous plug characterized by a Darcy number $Da = 1e^{-3}$.

In a second step, no-slip conditions are enforced on the upper and lower boundaries and the results are compared with respect to the results in the literature [62, 21]. Betchen et al. separate the problem in two regions with appropriate interface conditions between the free fluid region and the porous domain. In their model, the flow is governed by incompressible Navier-Stokes equations in the free fluid region and Darcy-Brinkman in the porous medium. They assume continuity of the averaged velocity, the intrinsic pressure and the shear stresses through the interface. They use a finite volume method with a grid aligned with the porous-fluid interface and a special attention is given to the discretization of the interface conditions.

For this problem, the Poiseuille velocity profile will flatten to become more uniform in the porous region (see Fig. 4.8). The numerical results at steady state for the pressure and velocity along the axis of symmetry of the channel are compared with the results of Betchen [21] in Fig. 4.9. A small discrepancy can be observed in the interface region which can be explained by the smoothing technique used. Decreasing the mesh size in this region will enhance the sharpness of the interface, driving the results towards the ones of Betchen. The influence of the numerical smoothing will be further investigated in Section 4.7.3

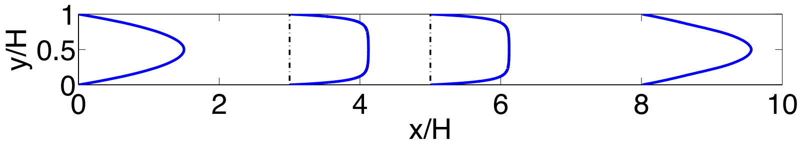

Figure 4.8: Velocity profile through the channel

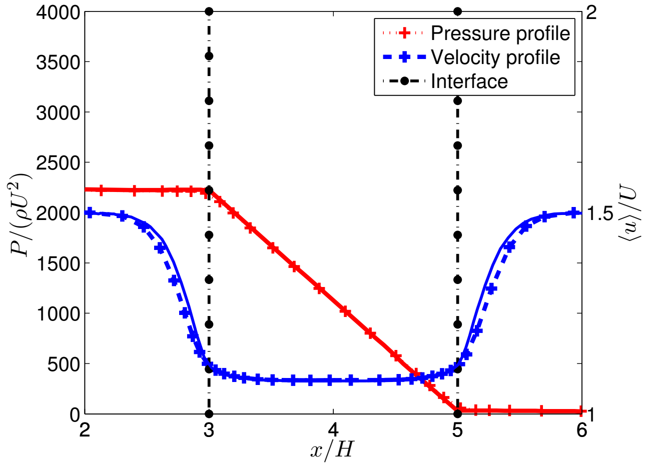

Figure 4.9: Non-dimensional pressure and velocity profile at the center of the channel for a the steady state flow with a porous plug ($Da = 1e^{-3}$). Solid lines are the numerical results of Betchen [21].

4.7 Channel flow above a porous slab

The fully developed flow on top of a semi-infinite porous medium is a well known test case studied originally experimentally by Beavers and Joseph [16]. Whereas the pressure gradient is high and velocity remains mostly the same for perpendicular flows, the velocity is orders of magnitude different in the porous medium and the pressure gradient is negligible for near parallel flows.

In this work, for the sake of simplicity, a finite channel is considered as in Costa et al. [62] and Gartling et al. [85]. The porous medium fills half of the domain as illustrated in Fig. 4.10 and is sufficiently long to ensure a fully developed flow on top of it. It can be shown that to have a fully developed Poiseuille flow, the entrance length in the channel is $x_e/H \approx 0.015 Re_H$ [193]. In this case, the low Reynolds number of the case ensures a short hydrodynamic entrance length. In order to apply proper boundary conditions for the inlet and outlet, pure fluid regions are added at the beginning and the end of the domain. The mesh, shown in Fig. 4.10, is composed of 1956 triangular elements with a minimum resolution of $6e^{-2}H$ in the interface region. The numerical thickness of the interface is defined to be $1.5e^{-1}H$. The following subsections discuss two different test cases involving parallel flows to show the accuracy of the approach implemented and the comparison with existing methods.

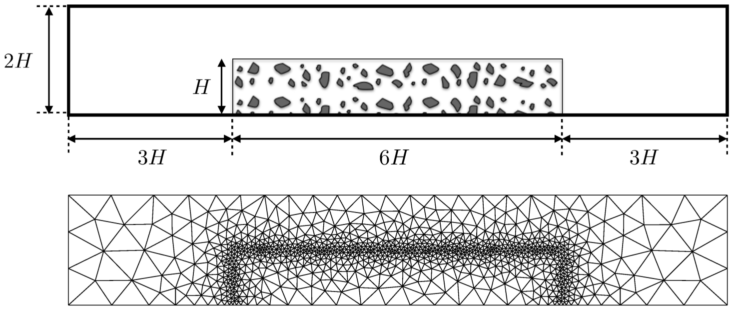

Figure 4.10: Configuration setup to study flows parallel to a porous domain and mesh used for the simulations with Argo.

4.7.1 Beavers and Joseph problem

Within this test case, the flow characteristics are $Re_H = 1$, $\epsilon_g = 0.7$ and two permeabilities are studied, characterized by $Da = 1e^{-2}$ and $1e^{-3}$. The conditions chosen for this case are summarized in Table 4.7. The simulations are performed for a flow composed of one species AIR (frozen mixture of N_2 and O_2) and with calorically perfect gas assumption.

The Argo results are compared with the numerical simulations presented in Betchen et al. [21] but also with an analytical approach. For the original

Table 4.7: Conditions for the flow through a porous plug.

Mixture	H $[m]$	P_{outlet} $[Pa]$	T_{inlet} $[K]$	U_{inlet} $[m/s]$	μ $[Pa\ s]$
Air	0.1	10132.5	293.15	$1.25e^{-3}$	$1.5e^{-5}$

problem, Beavers and Joseph assumed that the porous medium was infinite and in this case, an analytical steady state solution exists using the two domain approach. This method, as explained in Section 2.4, requires the definition of additional parameters (β_{OTW}) to close the inner boundary condition that should be applied at the interface. The analytical development for a two domain approach is presented in Appendix D. Note that this solution requires the definition of an empirical parameter. In this section, we compare the Argo numerical results with the two domain solutions obtained with two values of the jump parameters. First, we assume that $\beta_{OTW} = 0$ and then we use the value proposed by Yu et al. [236] $\beta_{OTW} = 0.7$ to reproduce this experiment. Figure 4.11 shows the velocity profiles compared with these analytical solutions as well as the results of Betchen et al. [21]. The approach used by the latter was described in Section 4.6. The velocity profiles are non-dimensionalized using the mean velocity in the free fluid region.

The velocity profiles are in good agreement with the results of Betchen et al. [21]. A small discrepancy in the interface region can be observed especially at high Darcy number which can be explained by the smoothing technique used and is discussed further in the following subsection. The first analytical solution using the two domain approach with $\beta_{OTW} = 0$ agrees well with the results of Betchen et al. [21] because they are assuming also continuity of the shear stresses at the interface. The solution obtained with the value proposed by Yu et al. [236] differs from these and the Argo results. This comparison shows the sensibility of splitted methodology with this jump condition and in particular the influence of β_{OTW} in the interface region. Finally, we can observe a discrepancy at $y/H = 0$ between the two domain analytical solutions and numerical results. This is the consequence of assuming a semi-infinite porous medium to develop the analytical solution.

We recall that Betchen et al. [21] assume continuity of the shear stresses at the interface while in practice, experiments have shown the need for a jump. Therefore, it would be more accurate to compare with the analytical solution provided that a correct jump parameter is given. Obviously, the method with a variable porosity/permeability adopted in this work, does not converge towards the two domain approach with a jump when the interface thickness tends to zero. The goal is to have a physical meaning of the interface thickness together with the appropriate variation of porosity and permeability.

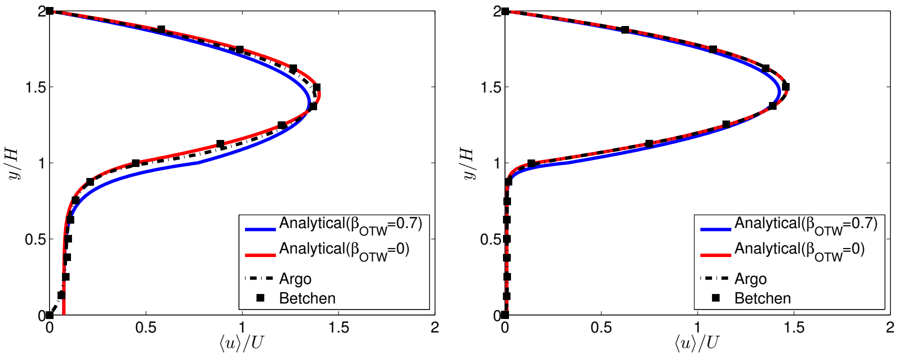

(a) $Da = 1e^{-2}$

(b) $Da = 1e^{-3}$

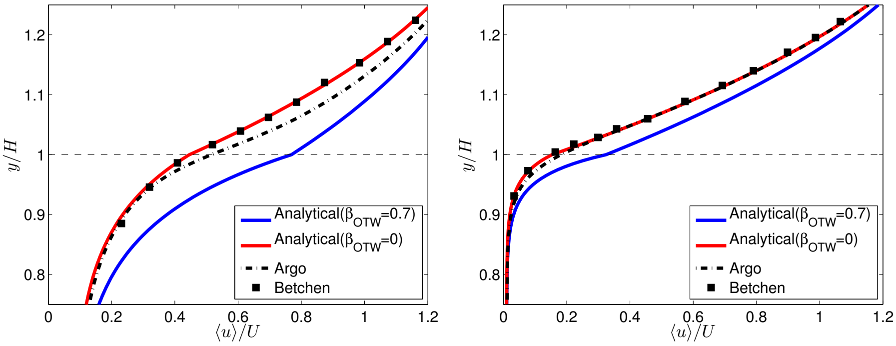

(c) Close-up view $Da = 1e^{-2}$

(d) Close-up view $Da = 1e^{-3}$

Figure 4.11: Velocity profile at the center of the channel (x=6H), comparison between Argo results, solution of Betchen et al. [21] and analytical solution.

Therefore, for the diffuse approach chosen, an appropriate model linking the permeability and the porosity in the transition region should be selected (see Section 2.4). For the results presented, this dependence is modeled by a Carman-Kozeny relation (see Eq. (2.125)). Several other models are considered (see Section 2.5.2) and are compared in Fig. 4.12. The model used will influence the behavior in the transition region but also in the plain fluid zone. It can be observed that a larger velocity at the location of the permeable wall implies a lower peak shifted slightly toward the center of the domain. Indeed, changing the skin friction at the permeable wall will influence the flow in the free fluid region. Subsequently, the mass flow rate is higher than expected in the plain fluid region and the peak is located closer to the center of the free fluid region. The model of Carman-Kozeny gives the closest results compared to the literature hence this model will be used in the rest of this work unless specified differently.

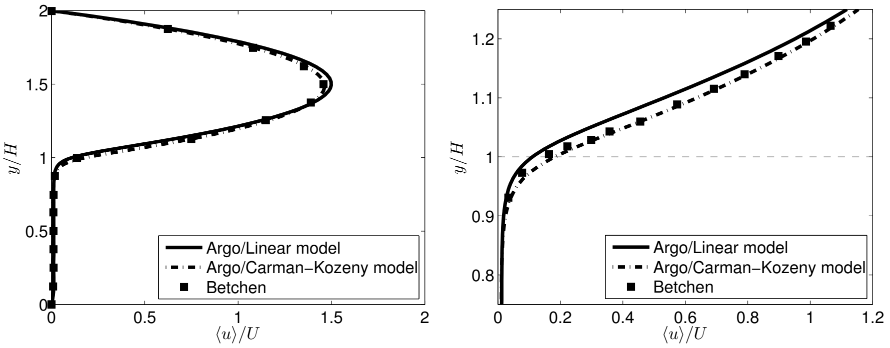

(a) $Da = 1e^{-3}$ (b) Close-up view $Da = 1e^{-3}$

Figure 4.12: Evaluation of different permeability model and their influence on the velocity profile with a close-up view in the interface region.

4.7.2 Comparison with direct numerical simulation

To evaluate how accurately the boundary layers close to the wall inside the porous medium and in the free fluid region are captured, Direct Numerical Simulation (DNS) results from Breugem [34] are compared with the present results. In [34], the microstructure of the porous medium is modeled by a network of cubes of length d_p separated by a distance d_f which fills half of the channel height $2H$ (see Fig. 4.13). For Breugem, the Navier-Stokes equations are solved in the whole domain using an immersed boundary method to account for the obstacles. The DNS uses a ratio $d_p/d_f = 1$ and d_p/H was fixed to 0.0625. To simulate the same configuration with our methodology, the macro-scale parameters for the porous medium can be computed based on the length of the cubes and the inter-distance. Breugem [34] shows that, based on geometrical considerations, the porosity for this case is $\epsilon_g = 0.875$ and the permeability in the porous domain is $\kappa = 0.132 d_p^2$. Furthermore, based on the DNS, Breugem [34] computes the closure parameter (β_{OTW}) required by the two domain analytical model. The DNS of Breugem and the solution using the two domain approach is presented in Fig. 4.14.

It should be noticed that for Breugem, the interface is defined where the porosity is unity. In addition, from his results, the thickness of the transition region can be computed as $3d_p$. On the contrary, in this work, the interface position should be the middle of the transition region. This has been already discussed in Breugem, and Fig. 4.14 shows the influence of the interface definition on the analytical solution. The analytical solution using the two domain approach gives better agreement with the DNS considering the interface position in $z_i = -1.5d_p$. The solution of Argo is therefore compared with the analytical profile assuming this position of the interface.

The results for the channel computation in DNS overlap almost entirely the approximate analytical solution with a small discrepancy in the interface

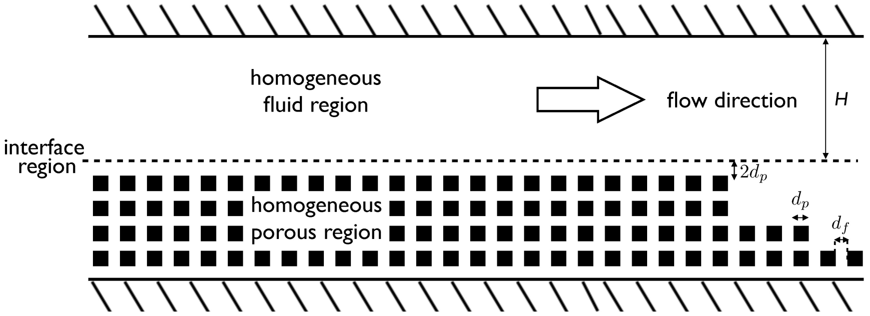

Figure 4.13: Breugem [34] configuration. Permeable wall modeled by a network of cube of length d_p.

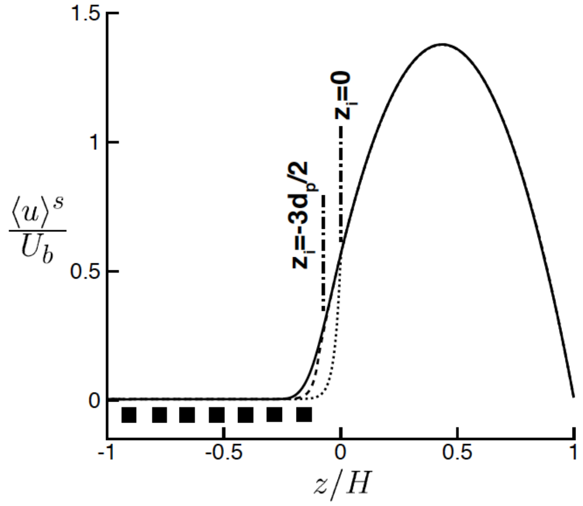

Figure 4.14: Volume averaged velocity profile, solid line is the DNS result of Breugem, dashed lines are the analytical solutions using the two domain approach and considering two positions of the gas-porous interface. The black squares shows the position of the cube. Figure taken from [34].

region [34]. The velocity profile seems to be underestimated in the interface region by the two domain approach. In this work, the numerical solution matches well the analytical profile (see Fig. 4.15) but seems to underestimate slightly the velocity in the transition region located in the porous domain. However, the numerical interface thickness defined can explain this discrepancy and is investigated in the next section.

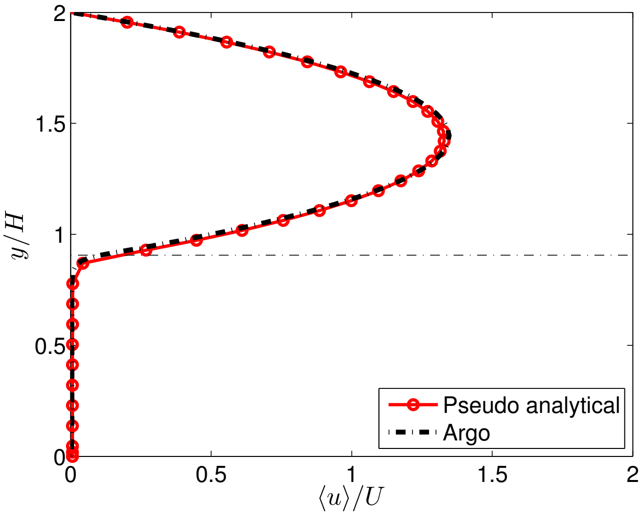

Figure 4.15: Channel flow over a permeable wall. Comparison between the analytical averaged velocity profile (plain dotted line) computed assuming OTW condition with $\beta_{OTW} = 0.91$ given by the DNS of Breugem [34] and the Argo results (dashed line).

4.7.3 Influence of the smoothing distance

The numerical interface thickness (ϵ_ϕ) plays also an important role for an accurate evaluation of the velocity profile in the interface region. Using a smoothing technique, the mesh size in the interface region cannot be determined independently if the boundary layer over the porous domain has to be captured accurately. No internal boundaries are implemented but this comes with a price to pay when meshing the domain. Figure 4.16 shows the effect of decreasing the numerical interface thickness towards the value predicted for the transition region by Breugem [34]. The results are getting closer to the two domain solution using the jump parameter proposed by Breugem. The test case proposed in Fig. 4.16 simulates the same setup as for Section 4.7.2.

Reducing the distance of smoothing too much can lead to spurious non-physical overshoot for the void fraction due to the high-order approximation. This effect does not only depend on ϵ_ϕ but also on the relative position of the interface on the unstructured mesh. This spurious overshoot in the interface region is shown in Fig. 4.16(b) when the interface thickness is $\epsilon_\phi/H = 1e^{-2}$. In practice, the criteria presented in Section 3.4 has to be respected in order to avoid such spurious oscillations at the interface and to ensure the stability of the run.

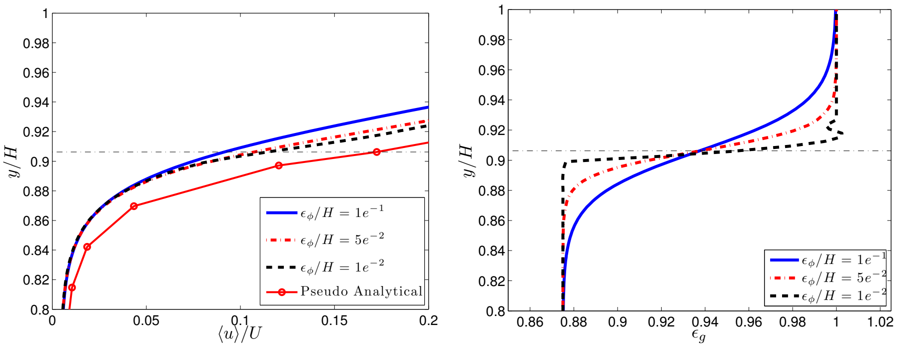

(a) Velocity profile (b) Porosity profile

Figure 4.16: Channel flow over a permeable wall. Comparison of velocity profiles close to the interface for different smoothing distance on the same mesh and the equivalent porosity profile.

4.8 Flow past a porous cylinder

This test case shows the importance of the permeability parameter. For the same porosity, the porous matrix can have several permeability hence let the flow passes through it differently. In order to analyse and show the influence of permeability, the flow around a cylinder is studied. The symmetric rectangular domain of dimensions $40D \times 20D$, with D the diameter of the cylinder is considered. The mesh is composed of 2609 triangles with a refinement in the interface region around the porous cylinder shown in Fig. 4.17. A polynomial approximation of order 3 is chosen for the runs in this section. The mesh should be sufficiently fine to accommodate a small transition region in order to avoid an artificial increase of the diameter size. In this case, the smoothing distance is chosen to be $3e^{-2}D$ while the minimum mesh size in the interface region is $1e^{-2}D$. Finally, regarding the numerical scheme, the iterative solver GMRES is used to solve the steady problem.

The study of steady flow past a solid cylinder at several Reynolds numbers is common in the literature. The flow over a permeable cylinder has also been investigated by several authors [23, 111, 162, 237]. For this test case, the flow is characterized by a low Reynolds number ($Re = 20$) and the permeability (represented by Darcy number) for the material of the cylinder varies. The parameters chosen for the runs are summarized in Table 4.8.

As expected, for the lower Darcy number case, the porous cylinder acts as an obstacle and the flow will mostly avoid it. In this case, the streamlines closely resemble those past a solid obstacle. For a higher permeability, the flow will pass through the sample and finally will prevent the formation of a recirculation zone after the cylinder (see Fig. 4.19). Not only does the presence of the recirculation zone depend on the permeability, but so does the geometry

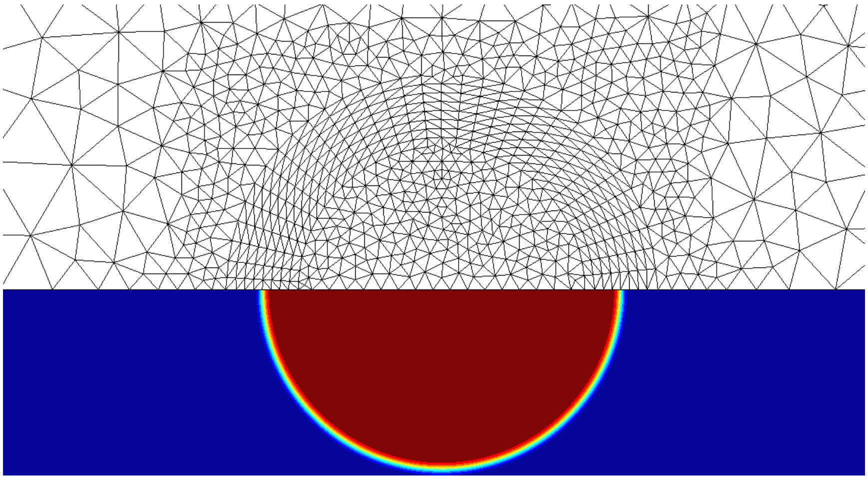

Figure 4.17: Mesh around the cylinder and smoothing region of the solid volume fraction.

Table 4.8: Test case conditions for the flow past a porous cylinder with various permeability.

Mixture	D $[m]$	ϵ $[-]$	u_{inlet} $[m/s]$	T_{inlet} $[K]$	P_{outlet} $[Pa]$
Air	0.1	0.4	$2.49e^{-2}$	293.15	10132.5

of the wake. For instance, for a particular Darcy number, the wake penetrates the rear part of the cylinder as observed in Fig. 4.19(b) and confirmed by the analysis done by Yu et al. [237]. The recirculation length is another parameter that will depend on the Reynolds number for a solid cylinder but also on the Darcy number for a permeable medium. The recirculation length is defined as the first point along the axis to retrieve a positive axial velocity after the back of the cylinder. Figure 4.18 shows the evolution of the recirculation length (L_r) with respect to the Darcy number. For small values of Darcy number, the wake length converges towards the one of a solid cylinder. Table 4.9 compares these results with the literature. It shows good agreement with the results for a porous cylinder computed by Yu et al. [237]. They modeled the free fluid and the porous domain using a two domain approach with a jump in the tangential shear stresses (OTW conditions).

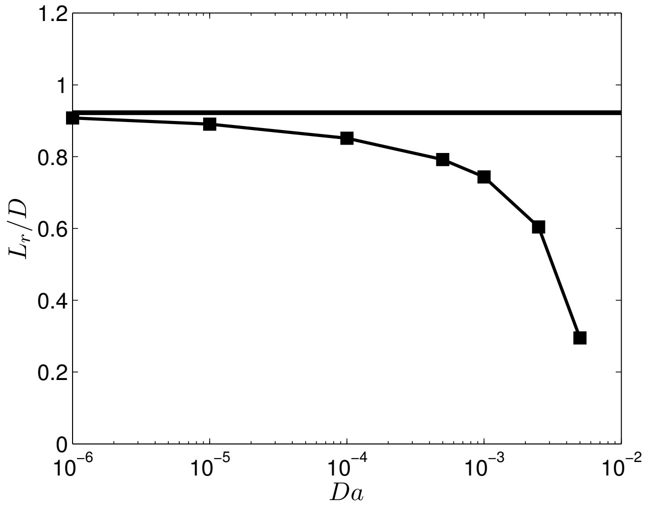

Figure 4.18: Evolution of the non-dimensional recirculation length with Darcy number. The horizontal solid line is the reference wake length for a solid cylinder.

Table 4.9: Non-dimensional recirculation length of flow at Reynolds 20 past a cylinder.

Medium of the cylinder	Present work	Ref. [237]	Ref. [81, 69, 182]
Solid	0.922	0.916	$[0.9 - 0.94]$
Porous at $Da = 1e^{-6}$	0.908	0.906	-

Using such formulation, it is therefore possible to simulate the flow around complex geometries without carefully meshing the domain of computation if the permeability is defined with care. Khadra and Angot [115] have proposed this to account for embedded solid domains, it is the principle of the Brinkman penalization method [135]. This can be very interesting for moving geometries for example, which, without this kind of penalization method would require the heavy procedure of remeshing.

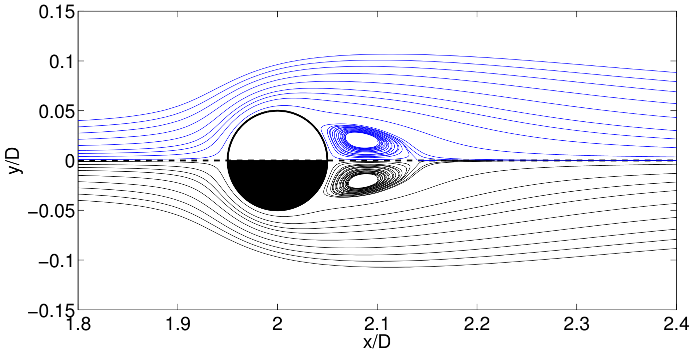

(a) $Da = 1e^{-4}$

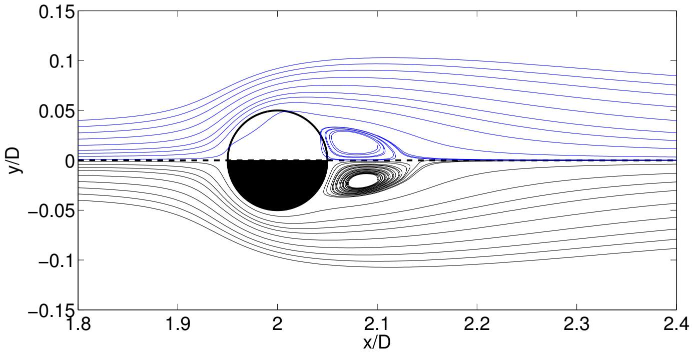

(b) $Da = 1e^{-3}$

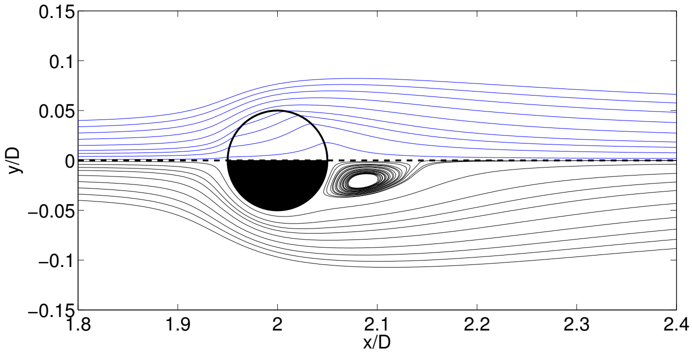

(c) $Da = 1e^{-2}$

Figure 4.19: Streamlines of the low Reynolds flow ($Re = 20$) past a cylinder for several Darcy numbers. The bottom part of each figure shows the comparison with the streamlines past a solid cylinder with a body fitted mesh.

4.9 Reactive porous medium

This section analyzes the movement of the interface in case of a reactive porous medium. The approach implemented does not track the position of the interface but it can be post-processed from the solid density field. Duffa et al. [75] have proposed a 2D analytical model to study the recession of an ablative material under sublimation and oxidation without any flow on top of the material. In this particular case, the convective flux is neglected and the system of equations solved by Duffa et al. is reduced to a diffusion-reaction system. They have shown that the interface shape can have two stationary profiles. The first is the trivial solution, the material surface is flat. The second stationary profile presents circular ridges. An illustration of these solutions is shown in Fig. 4.20

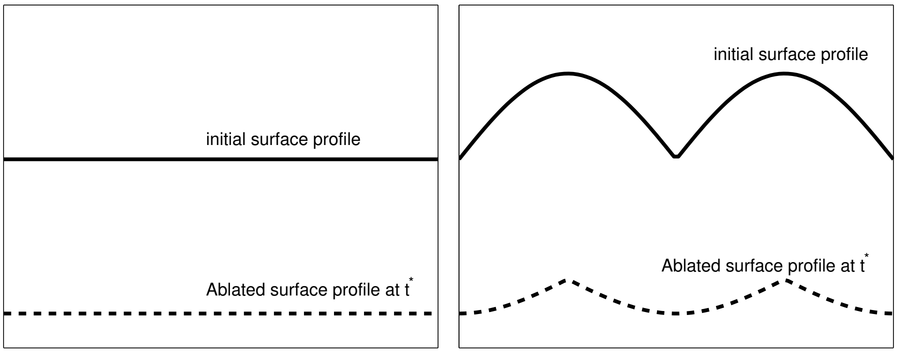

(a) Trivial solution (b) Circular shape solution

Figure 4.20: Steady solution for the evolution of an ablated surface.

Depending on the initial solution, the boundary conditions, and the flow regime one of the two profiles will be developed. Duffa et al. [75] investigate the recession of purely solid material. The methodology followed in this work implies the presence of a porous medium. However, as shown in Section 4.8 the material properties can be modified to approach closely the behavior of a solid. In this particular case of diffusion-reaction, the tortuosity is increased to limit the diffusion of molecules inside the porous material. This test case investigates the recession of a flat surface.

The square domain is periodic in the x direction, the bottom part is assumed to be a rigid adiabatic wall while at the top freestream conditions are applied. The mass fractions at the top are imposed to ensure a positive flux of oxidant species. We consider a mixture of three species N_2, O_2 and CO_2 with an heterogeneous reaction with the fibers given by $C_{(s)} + O_2 \rightarrow CO_2$. The forward reaction rate is fixed as 1.6 $[m/s]$. In addition, we assume that the porous medium is made of fibers of 11 $[\mu m]$ in diameter, the porosity of the porous medium is 0.85 and the tortuosity is set to 20. The other parameters for this test case are given in Table 4.10.

Table 4.10: Conditions for the reactive porous medium.

$Y_{i,freestream}$ $[-]$	L $[m]$	P $[Pa]$	T $[K]$	D_{eff} $[m^2/s]$
$N_2/O_2/CO_2$ $0.767/0.232/0.001$	$2.4e^{-5}$	$5e^6$	4300	$1.1e^{-7}$

The mesh is composed of 328 triangular elements and we used here a polynomial order $p = 1$. The resolution of the grid is increased not only in the initial interface region but in half of the porous domain. Indeed, the interface is moving hence the mesh should be fine enough to capture the smoothed discontinuity with time. The minimum cell size is fixed to $1e^{-7}[m]$ and the initial interface thickness is assumed to be $1e^{-6}[m]$. A direct Gauss solver is used to solve the linear system associated with the Newton-Raphson algorithm. The time step is adapted to ensure the convergence of the NR. At the beginning, we used a time step of $1e^{-7}[s]$ that is progressively increased to $5^{-6}[s]$. At initialization, the oxygen will react with the carbon fibers producing gaseous products. Therefore, the time step is smaller at the beginning to capture the fast changes in the composition of the gas.

The evolution of a straight surface is compared to a simplified one dimensional code developed with Matlab which solves only the mass conservation equations accounting for diffusion and reaction

$$\frac{\partial\left(\epsilon_g\langle\rho_i\rangle_g\right)}{\partial t} = \frac{\partial}{\partial x}\left(\langle\rho\rangle_g D_{eff}\frac{W_i}{W}\frac{\partial X_i}{\partial x}\right) + \dot{\omega}_i^{het} \tag{4.10}$$

$$\frac{\partial\left(\epsilon_s\langle\rho_s\rangle_s\right)}{\partial t} = \dot{\omega}_s^{het}. \tag{4.11}$$

The code uses the *pdepe* solver and is similar to the one presented in Section 4.5 with an additional source term. The position of the interface is compared in Fig. 4.21(a). It can be observed on the Argo results that a slight volume oxidation occurs, the interface thickness is increased meaning that the porosity evolution is smoother after a while. At the beginning of the computation, the O_2 present is oxidized in a thin region close to the wall resulting in volume ablation with negligible recession of the interface. Then, at steady state, the porosity profile remains the same but is shifted due to recession (see Fig. 4.21(b)). The position of the interface based on the porosity profile is shown in Fig. 4.21(b). The two step process leads to a change in the recession rate observed in Fig. 4.21(a). Finally, the recession speed is slightly decreasing with time since the surface moves away from the boundary where the oxygen concentration is imposed. Solving only the O_2 mass conservation and the evolution of the porosity, the steady recession rate is very close to what is computed with Argo. Slight differences can be explained by the numerous approximations made within the simplified Matlab code. For example, the Argo code takes into account the fact that the heterogeneous reaction is exothermic hence due to the temperature gradient, a velocity field will progressively appears reducing the concentration of O_2 at the interface. Therefore, the recession rate is larger for the simplified approach.

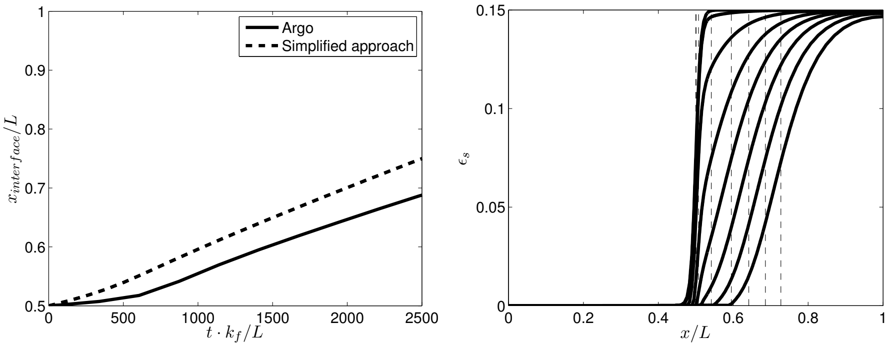

(a) Interface position

(b) Porosity profile (vertical dashed lines are the position of the interface)

Figure 4.21: Evolution of a flat surface under oxidation.

4.10 Conclusions

The development of a numerical tool to simulate multi-species reactive flows with the presence of a porous medium has been verified against several test cases of increasing complexity. Good agreement with other computation codes and other approaches has verified the development and implementation of this methodology. In addition, several cases have shown the limitations of this approach. Indeed, running the code, the thickness of the transition region should be defined adequately with respect to the mesh but sufficiently small if one wants to capture the physical phenomena in this layer accurately. The importance of defining properly the material and fluid properties have been highlighted through several test cases, the permeability of the porous medium seems to be one of the most important parameter to measure in order to capture the interaction between the flow and the porous medium as well as the phenomena in the homogeneous porous medium.

CHAPTER 5

COMPETITION BETWEEN SURFACE AND VOLUME ABLATION

The competition between surface erosion and volume ablation of carbon preform is studied. The reproduction of an experiment allows us to discuss the numerical approach and models used. This chapter is a concatenation of the modified versions of several conference proceedings presented at international symposiums [197, 199, 203] and a journal article submitted for publication. Computational resources have been provided by the supercomputing facilities of the Université catholique de Louvain (CISM/UCL). The authors would like to thank especially J. Lachaud, F. Panerai and N. Mansour for valuable discussions on the experiments and for providing the data used in the comparisons with the numerical results.

5.1 Introduction

Low density ablative materials are highly porous (up to 90% of void), hence the hypothesis of a mere surface used for example in the 1D thermal response code might not be sufficient to capture the phenomena close to the wall and to predict a correct recession of the heat shield. Indeed, Lachaud et al. [117] have shown that, due to the high porosity, oxygen can diffuse inside the thermal protection material and react in depth with the carbon fibers. The weakening of the structure due to the eroded fibers can lead to enhanced mechanical ablation under shear stress and enhance the depletion of the thermal protection layer. Capturing the volume ablation is thus crucial for such a material. The competition between surface and volume ablation depends on the magnitude of the Thiele number defined as the ratio between a reference length and the depth of diffusion inside the material allowed by the chemical reactions

$$Th = \frac{L}{\sqrt{D_{eff}/(S_f k_f)}}, \tag{5.1}$$

in which, we recall that, the D_{eff} is the effective diffusion inside the porous medium, S_f is the specific surface, and k_f is the rate coefficient. For high values of the Thiele number, the diffusion process is not fast enough and the oxygen in this case will be consumed at the surface of the sample (surface ablation). In the case of volume ablation, the flow regime is more reaction-limited leading to a low value of Th.

The Thiele number is influenced by the flow conditions (temperature, pressure, etc). For example, increasing the pressure leads to lower diffusion coefficients and enhance the reactivity by the increased presence of the oxidizer.

We illustrate the importance of including volume ablation through the analysis of the Stardust reentry conditions. Stardust is a NASA mission designed to collect and bring back to Earth dust samples from the trail of a comet [186]. In January 2006, the Stardust Sample Return Capsule (SRC) made its atmospheric reentry which is the fastest ever achieved by a man-made capsule with a velocity of about 12.9 $[km/s]$. The capsule was protected from the severe entry conditions by a lightweight ablative heat shield made of PICA. In Lachaud et al. [117], the oxidation of a Fiberform sample under conditions corresponding to the Stardust peak heating conditions during atmospheric entry is studied through direct numerical simulations. The Fiberform is the carbonaceous matrix of PICA without phenolic content which has been proved to have properties similar to charred PICA [214]. The recession of this material is similar to PICA since the ablation is mainly due to carbon fibers oxidation. Their solver uses a random walk algorithm to compute the mass diffusion inside the material and they consider heterogeneous first order reactions. The motion of the fibers interface is computed using a marching cube algorithm. The results of these micro-scale simulations taken from [117] are shown in Fig 5.1. In these cases, the competition between surface and volume ablation is estimated by considering directly the ratio between diffusion and reaction.

Since the methodology followed in this work does not impose any particular boundary condition in a control volume attached to the surface, the continuous approach allows us to account for volume ablation. To illustrate the capability of the code to simulate such problem from a macro-scale point of view, Fig. 5.2 presents the Argo results for the exposition of a carbon preform in conditions similar to [117]. Two pressure conditions are tested, a low pressure test case at $P = 0.26$ $[atm]$ and a higher pressure at $P = 10$ $[atm]$. The low pressure case is the actual condition for the Stardust entry. The temperature of the material at this trajectory point reaches 3360 $[K]$. The initial radius of the fibers is 5 $[\mu m]$ and the length of the domain considered is 200 $[\mu m]$. The 2D numerical domain is similar to the verification test case presented in Section 4.9 and is composed of carbon preform on half of its length and on top

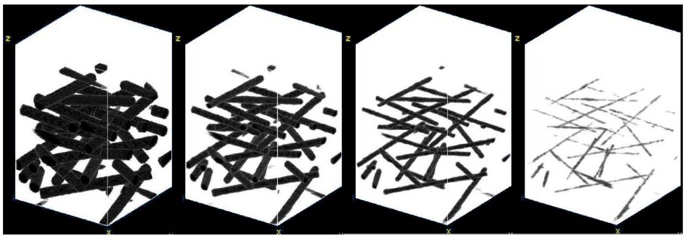

(a) Reaction limited regime, $P = 0.26\ atm$, $D/k = 2mm$

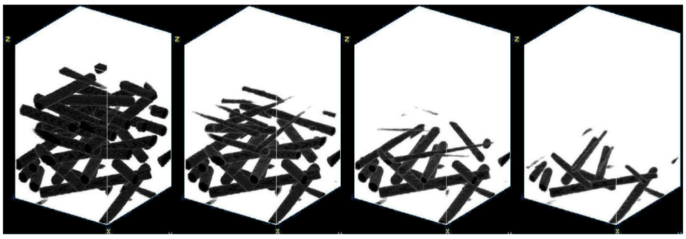

(b) Diffusion limited regime, $P = 10\ atm$, $D/k = 50\mu m$

Figure 5.1: Direct numerical simulations of the erosion of carbon preform at the microscale level under two pressure conditions. Figure taken from [117].

a free fluid region. Periodic conditions are applied on the sides of the domain, freestream boundary conditions are imposed at the top while the bottom of the material is assumed adiabatic and impermeable.

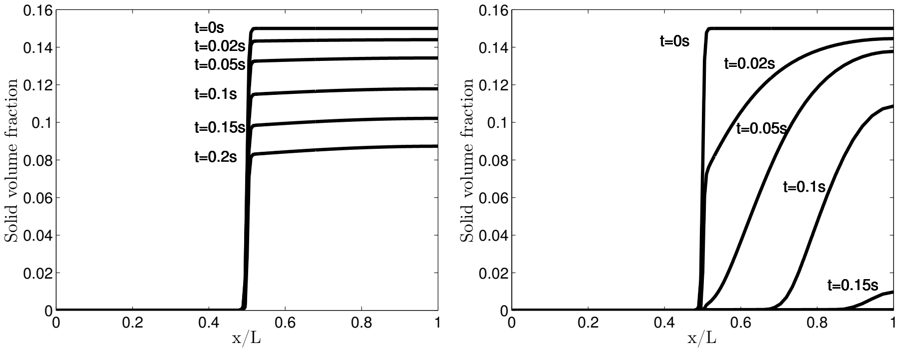

(a) Low pressure, $P = 0.26\ atm$

(b) High pressure, $P = 10.0\ atm$

Figure 5.2: Solid volume fraction of the carbon preform fibers eroded in atmospheric entry conditions corresponding to Stardust peak heating conditions. For each case, the solid volume fraction is plotted at different times from the top curve to the bottom, $t = 0s$, $t = 0.02s$, $t = 0.05s$, $t = 0.1s$, $t = 0.15s$, and $t = 0.2s$.

One-to-one comparison with the results of Lachaud is not possible since here mass, momentum and energy conservation laws are solved while for

Lachaud isothermal conditions are assumed. In addition, in the reference test case, D/k is fixed; here, the Arrhenius law and the dependence of the diffusion coefficient on temperature and mixture composition will cause a variation of this diffusion to reaction ratio. In spite of this, the same conclusions hold. As it can be seen in Lachaud [117], for the low pressure case, the solid volume fraction tends to decrease homogeneously in the whole sample (full volume ablation) while for the higher pressure case (higher Thiele number), the ablation of the fibers is closer to a surface phenomenon. As expected, for the high pressure case, the total mass loss is higher for the same exposition time because the concentration of oxygen is larger in this condition. It can be observed in Fig.5.2(b) that for $t = 0.2$ $[s]$, the fibers are completely depleted. The solid volume fraction can be related directly to fibers radius using Eq. (2.105). These simulation results show immediately the importance of considering volume ablation depending on the flow conditions.

This qualitative agreement shows that the trend is well captured by the model implemented in Argo but this chapter aims at an accurate quantitative capture of the competition between surface and volume ablation. The present chapter analyzes also the current models to treat these in-depth phenomena. These studies are compared with experimental data on ablation of carbon preform in several regimes.

5.2 Validation: NASA plug experiment

The computational tool is used to investigate numerically the oxidation of carbon preform as performed in a set of experiments conducted inside the NASA flow tube reactor by Panerai et al. [170, 171]. First, the experiments is described, then the numerical setup is discussed and finally, the results are compared and analyzed.

5.2.1 Experimental setup

A cylindrical carbon preform sample of 25.4 $[mm]$ in length is inserted inside a 22 $[mm]$ diameter tube enclosed in a furnace. A low Reynolds number flow is forced to pass through the porous sample. The temperature is set by the furnace and remains constant during the experiment while the outlet pressure is not fixed to ensure constant inlet conditions. The experimental setup performed at NASA by Panerai et al. [170] is shown in Fig. 5.3.

Different pressure and temperature conditions have been tested and this work focuses on the replication of three tests. The experimental setup values are summarized in Table 5.1 and the properties of the material are given in Table 5.2 for each test sample.

The gas flowing inside the sidearm reactor is air and therefore the presence of oxygen will progressively ablate the carbon preform sample. The onset of the exothermic oxidation of the carbon fibers will lead to a temperature peak

Table 5.1: Experimental Setup [170].

Test ID	P_1 $[Pa]$	T $[K]$	t_{final} $[s]$	$\dot{m}$ $[mg/s]$
a3	1920	900	3600	2.21
a4	1960	1000	3600	2.21
a6	1973	1200	3600	2.21

Table 5.2: Initial Material Properties [170].

Test ID	$\epsilon_{g,0}$	$\rho_{C,0}$ $[kg/m^3]$	κ_0 $1e^{-9}$ $[m^2]$	r_0 $[\mu m]$	η_0
a3	0.85	1089.99	1.3987	5.5	1.15
a4	0.85	1095.77	1.3720	5.5	1.15
a6	0.85	1038.67	1.3786	5.5	1.15

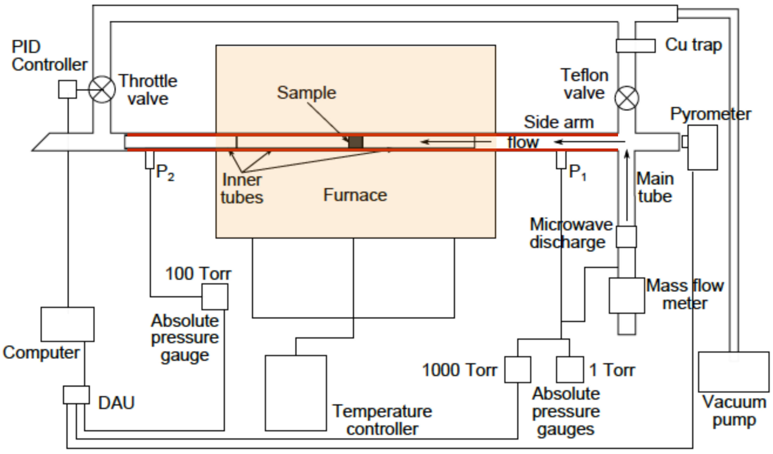

Figure 5.3: Schematic of the experimental setup in the NASA sidearm reactor. Figure taken from [170].

at the surface of the material which is measured in Ref. [170] using a pyrometer. Since the air is flowing through the porous plug, the oxygen can react at the surface of the plug or in depth. The mass loss and the volume loss are measured after 60 $[min]$ of exposure. Finally, the pressure drop across the sample is also measured in the experiment [170] to evaluate how the permeability has changed over time.

5.2.2 Numerical setup

The numerical setup is described in this part. First, the boundary conditions are exposed. Secondly, we discuss the re-radiation at the surface of the plug. Then, the heterogeneous reactions occurring in this experimental conditions are presented. Finally, the definition of the interface for our approach is discussed.

Boundary conditions

The problem is treated as a 2D axisymmetric case. The surfaces of the tube are modeled as non-slip isothermal walls. For the boundary condition at the outlet, the pressure has to be specified hence a Proportional Integral (PI) controller is implemented in order to adjust the outlet pressure to keep the mass flux constant at the inlet. The definition of the constants for the controller is very sensitive and was achieved by trial and error. Increasing the proportional constant decreases the settling time but leads to overshoot of the back pressure which can cause reverse flows and endanger the convergence of the computation. Figure 5.4 shows the numerical setup and the boundary conditions used to simulate this experiment. The mesh of the computational domain is not shown because the geometry is rather simple but note that it has to be sufficiently fine near the plug to capture the smoothing region defined to be 1.5 $[mm]$. In addition, for all the computations in this chapter, a polynomial degree of order 2 has been used. The same triangular mesh is used for every case in this section and Table 5.3 summarizes the number of elements used, the number of DOF and the computational time to run the experiment.

Table 5.3: Summary of the computational performances to simulate the ablation of the porous plug during 60 min of exposure (test a4) using Argo. Run is performed on the zenobe cluster host by Cenaero (Ivybridge 2.7GHz CPU type).

Test ID	Nb of time steps	Nb of elements	Nb of DOF	Nb of threads	CPU time [s]
a4	72000	496	$496 \times 6 \times 7$	6	≈ 50000

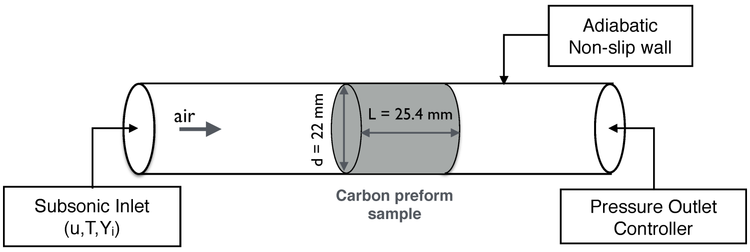

Figure 5.4: Schematic of the numerical setup in the NASA sidearm reactor and the conditions implemented at the boundaries of the computational domain.

Radiation

Following the numerical work of Martin [145], re-radiation from the hot surface has to be accounted for to simulate accurately the experiment. The radiation sink term limits the increase of temperature within the material by modeling the exchange with the colder tube walls. The fluid is considered optically transparent and the material optically thick. The radiation terms inside the material are already taken into account by using an effective conductivity. Radiation at the interface regions at the extremities of the sample is modeled through a sink term

$$q_{rad} = F_{s,t}\xi\left(T_w^4 - T_\infty^4\right), \tag{5.2}$$

where the emissivity (ξ) is taken as 0.9 and the view factor ($F_{s,t}$) is computed *a priori* depending on the geometry. The configuration factor for simple geometries are tabulated in Howell [104]. Considering the geometry of the sidearm and the cylindrical plug, the view factor of surfaces exposed to the flow with respect to the inner wall of the sidearm tube is $F_{s,t} = 0.99$. Therefore, a value of 1 is used and $T_\infty = T_{furnace}$. The sink term in Eq. (5.2) cannot readily be applied within our approach since we do not have a sharp interface. Instead, this term is integrated in the interface region by considering

$$q_{rad} = F_{s,t}\xi\left(T_w^4 - T_\infty^4\right)\delta(x,y), \tag{5.3}$$

where $\delta(x,y)$ is a smoothed Dirac computed based on the porosity. In this implementation, we consider

$$\delta(x,y) = \frac{1}{\epsilon_0}\left|\frac{\partial \epsilon_s}{\partial x} + \frac{\partial \epsilon_s}{\partial y}\right| \tag{5.4}$$

Note that the expression given in Eq. (5.4) is only valid for straight interfaces aligned with the x or y direction (as in the plug experiment). For curved interface, we should use instead

$$\delta(x,y) = \frac{1}{\epsilon_0}\sqrt{\left(\frac{\partial \epsilon_s}{\partial x}\right)^2 + \left(\frac{\partial \epsilon_s}{\partial y}\right)^2}. \tag{5.5}$$

For a one dimensional problem, Eq. (5.4) or (5.5) can be used provided that the ϵ_0 is the maximum value at the end of the transition such that $\delta(x,y)$ integrates to one on the whole domain. Figure 5.5 shows the definition of the interface region based on the regularized Dirac.

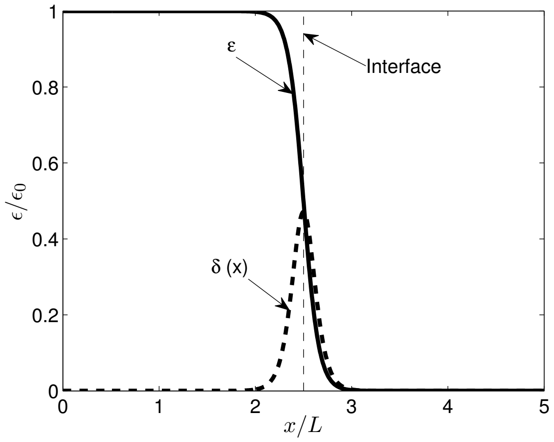

Figure 5.5: Smoothed porosity and interface region described by the smoothed Dirac for a one dimensional problem.

Heterogeneous reactions

Several heterogeneous reactions can be considered, as proposed by Panerai et al. [171], looking at the evolution of the Gibbs free energy with respect to temperature (see Ellingham diagram [77] in Fig. 5.6), the most probable reaction to occur in the range of temperature studied is the forward heterogeneous reaction $C_{(s)} + \frac{1}{2}O_2 \rightarrow CO$ which is the only one considered in here.

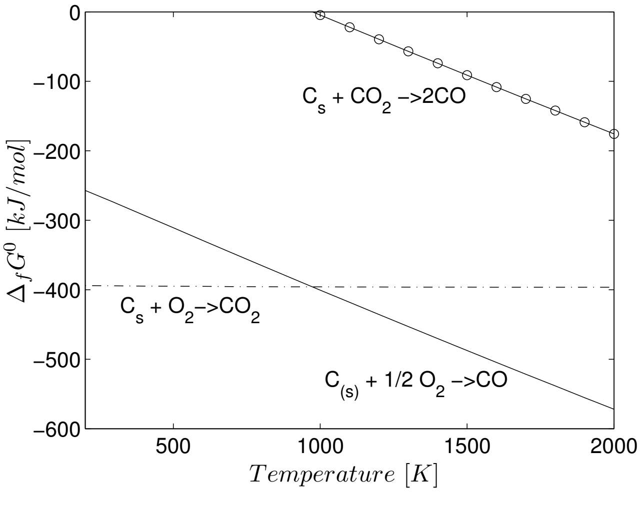

Figure 5.6: Ellingham diagram showing the Gibbs free energies with respect to temperature for several oxidation reactions. The Gibbs free energies are computed with the NIST-JANAF database [45].

The reference forward reaction rate is taken from Panerai et al. [170]

$$k_f = 0.087 \exp\left(\frac{-42400}{RT}\right) [m/s]. \tag{5.6}$$

This reaction rate will be discussed in the following but the Thiele number (see Eq. (5.1)) can already be computed based on it. The parameter to estimate the Thiele number are the reference length $L = 25.4$ $[mm]$, the initial specific surface of the fibers and D_{eff} computed with Mutation^{++}. The Thiele number for the three cases studied is respectively 1.3, 1.5, 2.0. Therefore, at these Thiele numbers, surface and volume phenomena are competing.

Interface definition

In order to compare the competition between surface and volume ablation, the relative mass and volume losses are compared with the experiments after 60 $[min]$ of exposure time. Note that, the position of the interface is needed to compute the volume loss (recession). With the methodology followed in this work, the gas-solid interface is not sharp anymore but is a region with a certain thickness which can evolve during the computation. Several criteria can be used to define the interface position *a posteriori* (inflexion point, definition of a threshold porosity, etc). The definition of the interface position is therefore arbitrary but should be consistent through the study. In this work, the interface position is defined as the location where the porosity is half the maximum value in the transition zone. This criterion is kept in this work because it is readily applicable to complex geometries.

5.2.3 Results

The data in Table 5.4 shows the comparison between our results, the experimental results (E_P) and the numerical replication provided in Ref. [170] (N_P). The reference results for Argo are denoted by N_A for the cylindrical fiber model and by N_A^* for the sinusoidal model developed in this work. The results will be illustrated and discussed in the following for each parameter in the table. The discussion in this section is focused on the comparison between E_p, N_P and the numerical results of the cylindrical model (N_A). This study leads to a sensitivity analysis described in the next section. The insights offered by this sensitivity analysis motivated the development of the more refined fiber sinusoidal model, which is exposed in the fourth section of this chapter.

Table 5.4: Comparison between experimental data (E_P), numerical results of Panerai et al. (N_P) and numerical results of the Argo code (N_A). The N_A^* are the numerical results of Argo considering pitting (see Section 2.3.2).

Test ID	Work	Δx $[mm]$	$\Delta V/V_0$ [%]	$\Delta m/m_0$ [%]	$p_{2,0}$ $[Pa]$	$p_{2,end}$ $[Pa]$	ΔT $[K]$
a3	E_P	0.0	0.0	19.4	1218	1246	7.5
	N_P	–	–	19.6	1212	1790	8.5
	N_A	0.05	0.22	16.0	1220	1360	2.5
	N_{A^*}	0.5	1.88	18.3	1220	1239	12.6
a4	E_P	3.8	14.96	23.3	1084	1125	7.5
	N_P	–	–	23.3	1087	1841	8.5
	N_A	0.4	1.79	23.7	1084	1317	3.6
	N_{A^*}	3.1	12.28	21.9	1084	1131	13.1
a6	E_P	5.8	22.83	28.7	577	787	13
	N_P	–	–	28.5	595	1866	6.25
	N_A	1.2	4.84	37.1	595	1238	15.9
	N_{A^*}	5.9	23.43	29.2	600	1080	35.1

Temperature

First, the temperature in the region of the plug is analyzed. The temperature field is 2D since isothermal conditions are imposed at the boundary of the tube and exothermic reactions are occurring. The axial temperature profile at the final time is plotted in Fig. 5.7 and compared to the 2D field in Fig. 5.8.

The ΔT in Table 5.4 is the jump in the surface temperature due to the exothermic oxidation reaction and is defined as $\Delta T = T_w - T_{furnace}$. It is measured experimentally after switching the gas flow from helium to air. Compared to the experiments, the value computed numerically is lower but remains close to the $9 - 13$ $[K]$ range measured. The maximum temperature is found inside the preform sample and this is also observed numerically by Panerai et al. [170]. The sink radiation term at the surface of the material can explain the location of this peak and its value computed with Argo is in good agreement with their numerical replication ($\approx$ 10 $[K]$ above surface temperature).

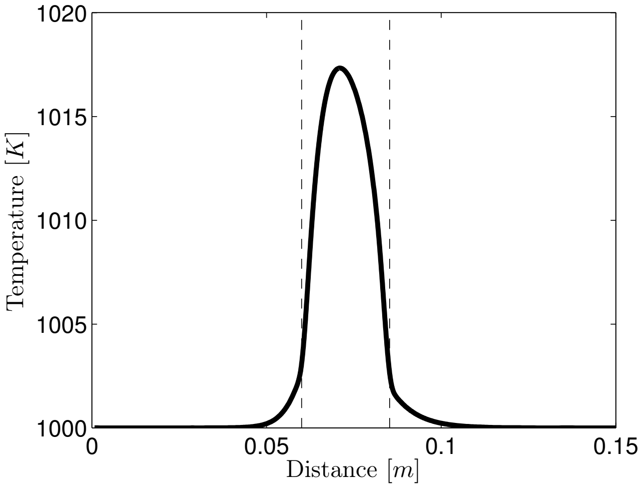

Figure 5.7: Temperature profile along the axis of the tube for test a4 at $t = 3600$ $[s]$. The vertical dashed lines limit the position of the plug.

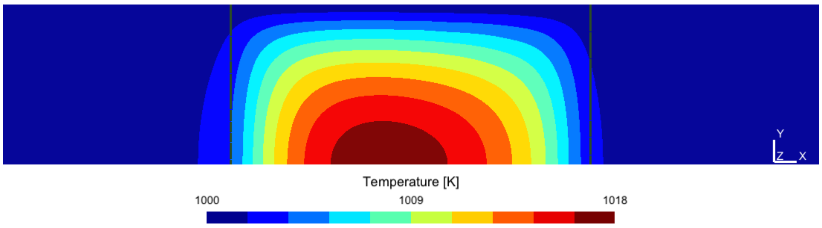

Figure 5.8: Axisymmetric temperature field inside the tube reactor for test a4 at $t = 3600$ $[s]$, the $\vec{Y}$ direction pointed towards increasing radius and the $\vec{X}$ is the axial direction.

Mass fractions

The consumption of the oxygen and formation of the carbon monoxide is shown in Fig. 5.9 at the final time for the a4 test. As expected, the oxygen is consumed in the plug sample, and one can observe that it is not entirely depleted by flowing through the carbon preform. The N_2 is not reacting with the plug but the production of CO is changing the mass fraction as observed in Fig. 5.9. At these conditions, the diffusion of the species upstream is non-negligible as can be observed in the numerical mass fraction profiles. The presence of CO is detected up to 2.5 $[cm]$ in front of the plug. This is consistent with the experiments. Indeed, Panerai et al. [171] observed the deposition of ablation products on the surface of the tube upstream of the sample.

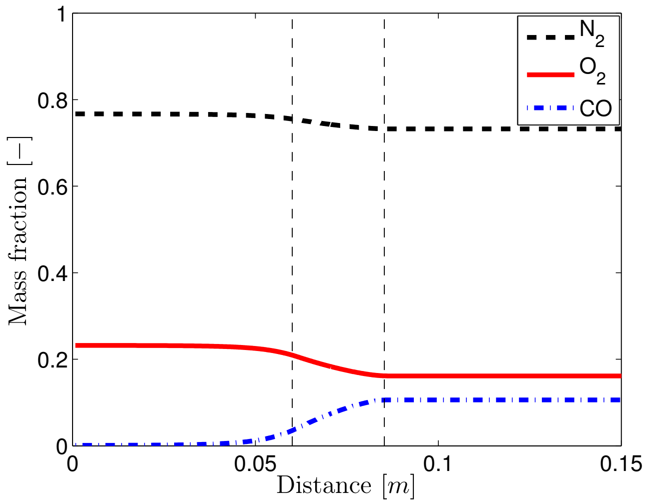

Figure 5.9: Mass fractions inside the tube for test a4 at $t = 3600$ $[s]$. The vertical dashed lines limit the position of the plug.

Pressure

The pressure drop across the sample (see Table 5.4) evolves as expected; for higher mass loss, the permeability is higher leading to a reduced pressure difference. In addition, the model used to link the porosity and permeability (Eq. (2.125)) gives a pressure difference closer to the experimental data than the one computed in the numerical work of [170]. The virgin permeability of the samples are computed based on the pressure difference at time $t = 0$. These values are used in the model and this explains why the initial back pressure matches so well the experimental value.

Mass and volume losses

The mass and volume losses are also analyzed. These are computed based on the evolution of the solid density. The integral of the solid density field on the domain will give the remaining mass of the sample ($\Delta m/m_0$) while the analysis of the recession (Δx) will allow to compute the volume loss ($\Delta V/V_0$).

Figure 5.10 shows the density profiles superimposed with the interface position facing the incoming flow. We can already observe that the solid density has mostly been reduced in the volume.

The numerical values for the mass and volume loss are given in Table 5.4 and plotted in Fig. 5.11. The mass loss for the a4 test is very close to the experimental data and the numerical replication of Panerai et al. while a discrepancy can be observed at lower and higher temperature. It should be noted that their numerical replication gives very good values for the mass loss be-

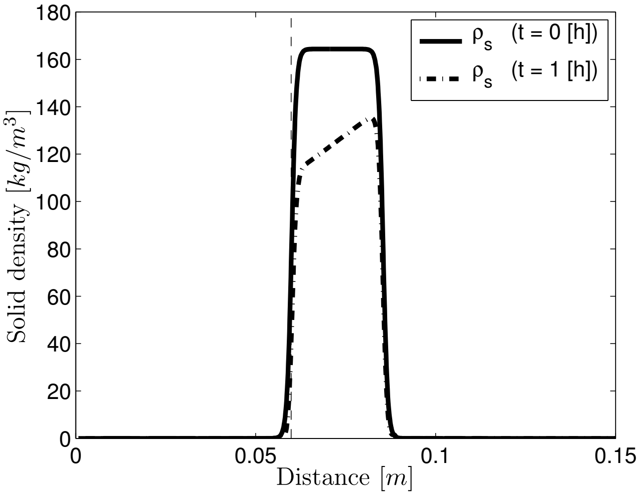

Figure 5.10: Comparison of the averaged solid density profile along the axis of the cylinder for test a4 at $t = 0$ and 3600 $[s]$. The front interface position is shown for the initial time by the vertical line.

cause the Arrhenius law in Eq. (5.6) is tuned on the experimental data using their code. Therefore, this suggests that the Arrhenius law for the oxidation reaction should be adapted from the one proposed by Panerai et al. to fit the results.

It can already be observed that the numerical results with the sinusoidal model (N_A^*) are in better agreement but this discussion is kept for later and detailed in Section 5.4. Finally, as found by Panerai et al. [170], the recession computed numerically is much lower than the one measured in the experiments. The volume loss and recession are directly related by

$$\frac{\Delta V}{V_0} = \frac{\pi R^2 (L - L_0)}{\pi R^2 L_0}. \tag{5.7}$$

with R the cylindrical radius of the sample and L its length. The competition between surface/volume ablation is not well captured with the cylindrical model implemented. Uncertainties on some material properties as well as physical phenomena neglected in the present model can explain this discrepancy. For instance, mechanical erosion (spallation) is not accounted for. The next section analyzes the influence of major parameters of the model on the ablation predictions.

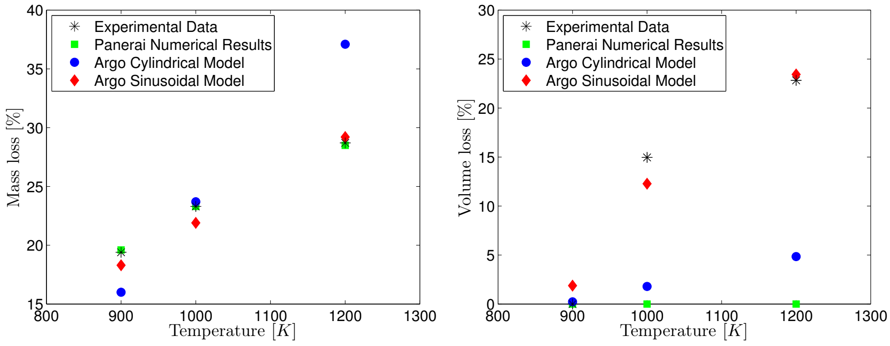

(a) Mass loss (b) Volume loss

Figure 5.11: Comparison between experimental data (E_P), numerical results obtained with Argo without pitting (N_A) and numerical computations with tuning (N_A^*).

5.3 Sensitivity analysis

The sensitivity analysis is mainly based on parameters involved in the Thiele number (see Eq. (5.1)) to investigate the competition between surface and volume ablation. We recall that the competition between diffusion and reaction will drive whether the sample is ablated mainly at the surface or whether the mass is lost in depth. Therefore, uncertainty on these parameters could explain the discrepancy observed between numerical results and experimental data. This sensitivity analysis has lead to the development of the new sinusoidal model discussed in Section 2.3.2. In order to save computational time, the sensitivity analysis studies the effect after 20 $[min]$ of exposure and for the a4 test only.

5.3.1 Diffusion models

To compute the diffusion coefficients, several models are implemented. As explained in Section 2.2.3, it is possible to specify a constant diffusion coefficient, a constant Schmidt number or use the multi-component diffusion coefficients provided by Mutation^{++}. Using this last approach, the coefficients are computed based on collisional data and this will be considered as the reference because it is the most accurate approach. It can be interesting to see the impact of choosing an approximate model or the multi-component diffusion model. The three models are compared here, a constant diffusion model based on the value given by Mutation^{++} at the initialization (D_m = constant), the accurate multi-component model with a varying diffusion ($D_{N_2,m}$, $D_{O_2,m}$, $D_{CO,m}$) and a constant Schmidt number ($D_m = \mu/(Sc\rho)$). The Schmidt number is ranging from 0.6 to 1.0 for air between $300 - 6000$ $[K]$ [74] and for the range of simulated temperatures a $Sc = 0.8$ is taken here. The recession is identical for the three models while the mass loss after 20 $[min]$ of exposure is slightly different (less than 1%). The mass loss is given in Table 5.5 and the diffusion coefficients are plotted in Fig. 5.12(a).

Table 5.5: Study on the impact of the diffusion models. Mass loss is computed after 20 $[min]$ of exposure.

Models	$\Delta m/m_0$ $[\%]$
Constant diffusivity($D_m = 7.9e^{-3}[m^2/s]$)	8.22
Constant Schmidt ($Sc = 0.8$)	8.06
Multi-component diffusion	7.93

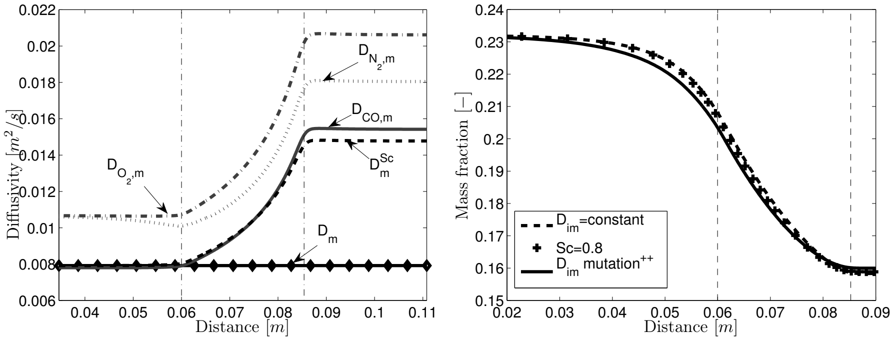

(a) Diffusivity coefficients (b) O_2 mass fraction at t=60 min

Figure 5.12: Diffusivity coefficients and mass fraction of O_2 along the axis of symmetry for several diffusion models. The vertical dashed lines limit the position of the porous plug.

One can observe in Fig. 5.12(a) that the diffusion assuming constant Schmidt number is close to the diffusion obtained for the CO species only. Therefore, it can be interesting to specify a Schmidt number for each species and not a global one. The constant diffusivity model is close to the other models in front of the plug since the conditions are really close to initial conditions. Nevertheless, downstream of the plug, the pressure is much lower leading to an increased diffusivity for each species which cannot be captured by the constant diffusivity model. Finally, it should be noted that Fig. 5.12(a) does not show the effective diffusion coefficients, the plotted values must be corrected to account for the presence of the porous medium. The mass fraction of O_2 after 20 $[min]$ is shown in Fig. 5.12(b) for the different models. The profile of Y_{O_2} is close for every model but a discrepancy can still be observed in front of the plug. Even though the diffusivity is varying in the domain, the model used to treat the diffusion does not seem to influence the mass and volume losses computed in these conditions.

5.3.2 Effective diffusion

Considering the diffusion inside the porous medium, the effective diffusion is also directly dependent of the tortuosity which is a material parameter representing its microstructure (see Eq. (2.67)). The tortuosity is computed by Lachaud [117] using random walk simulations through fibrous preform medium. In reality, the material is orthotropic but, within this work, isotropic properties are assumed in a first attempt. The uncertainty of computing this parameter is analyzed in this section. Two additional tortuosities are considered $\eta = 1.75$ and $\eta = 2.5$. The mass and volume losses are shown in Table 5.6. It can be observed that even doubling the tortuosity leads to the same volume loss and approximatively 0.2% mass loss change.

Table 5.6: Study on the impact of the tortuosity. Mass and volume losses are computed after 20 $[min]$ of exposure.

	$\Delta m/m_0$ $[\%]$	$\Delta V/V_0$ $[\%]$
$\eta_0 = 1.15$	8.22	0.47
$\eta_0 = 1.75$	8.33	0.47
$\eta_0 = 2.50$	8.39	0.47

5.3.3 Reaction rate

The Thiele number is directly dependent on the reaction rate; increasing k_f leads to a higher Thiele number and promotes surface ablation. In addition, as seen in Fig. 5.7, due to the exothermic heterogeneous reaction, there is a temperature gradient inside the sample. Therefore, the dependence of k_f with respect to temperature will also influence the effective rate at different depth. As explained in Section 5.2, the Arrhenius law chosen is the one proposed by Panerai et al. [170]. However, discrepancies in the choice of the Arrhenius law for the oxidation of carbon among the literature show how sensitive the selection of this reaction rate might be. As observed in Fig. 5.13, the rate coefficient found in the literature can be several orders of magnitude different. Both experimental conditions and material properties can explain this large range of reaction rate [145]. The present study does not aim to determine the actual reaction rate but tries to investigate the effect of such a choice on the surface/volume ablation competition. For this analysis, two additional reaction rates found in the literature are investigated and results are specified in Table 5.7.

As expected, a higher reactivity is more favorable to surface ablation. Still, we could not find kinetics such that both the volume/surface ratio and the total mass loss agree with the experiment at several temperatures. The surface ablation is always underestimated when compared to volume ablation.

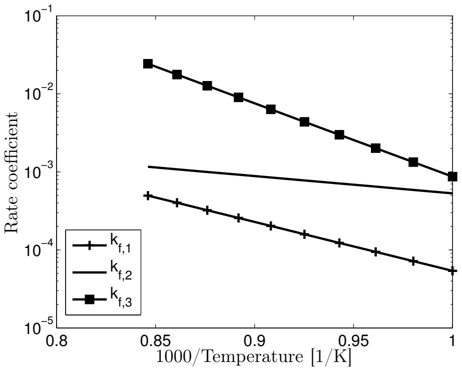

Figure 5.13: Reaction rate for several Arrhenius laws found in the literature. The reaction rates k_{f1}, k_{f2}, k_{f3} are taken respectively from [117, 170, 47].

Table 5.7: Study of the reactivity, the reaction rate is expressed as an Arrhenius law $k_f = AT^n \exp\left(\frac{E_a}{RT}\right)$. Mass and volume changes are computed after 20 $[min]$ of exposure.

A $[m/s/K^n]$	n	E_a [kJ/mol]	Ref.	$\Delta m/m_0$ [%]	$\Delta V/V_0$ [%]
$1e^2$	0.0	120.0	[117]	2.09	0.00
0.087	0.0	42.4	[170]	8.22	0.47
$2.2e^6$	0.0	180.03	[47]	22.1	30.4

5.3.4 Permeability

The permeability appears in the drag term of the momentum equation (2.85) and, depending on the flow conditions, it can have an influence on the pressure gradient and the velocity field inside the porous medium. For the plug case, as shown in the verification test case (see Section 4.6), it affects mostly the pressure gradient. The initial value for this parameter is computed such that the initial back pressure ($p_{2,0}$) is the one measured experimentally. Considering a permeability a hundred times smaller than the one in Table 5.2, the recession length is found to be the same as in the reference case while the mass loss is slightly higher ($\pm 1\%$). Decreasing the permeability leads to a higher pressure in front of the sample hence more oxygen is present which implies this increase of mass loss. However, the small resulting change suggests that the permeability is not a key parameter to explain the discrepancy in the surface and volume ablation balance.

5.3.5 Surface of reaction

The sensitivity analysis conducted on uncertainties of material parameters cannot explain the mismatch between surface and volume ablation observed numerically. Regarding the definition of the Thiele number, another key parameter is the effective reactive surface. We recall that the cylindrical model assumes that recession of the fibers is radial and uniform. This leads to a monotone reactive surface (S_f) decrease with respect to the fiber radius and porosity. However, micrographs of oxidized carbon preform have shown a pitting phenomenon at low pressure [170] which results in a more complex function of S_f. Micrographs in Fig. 5.14 of the virgin and eroded carbon fibers taken from Panerai et al. [170] shows the formation of the holes in the fibers for these experimental conditions. The formation of pits has also been experimentally observed in graphite oxidation by Hahn [95].

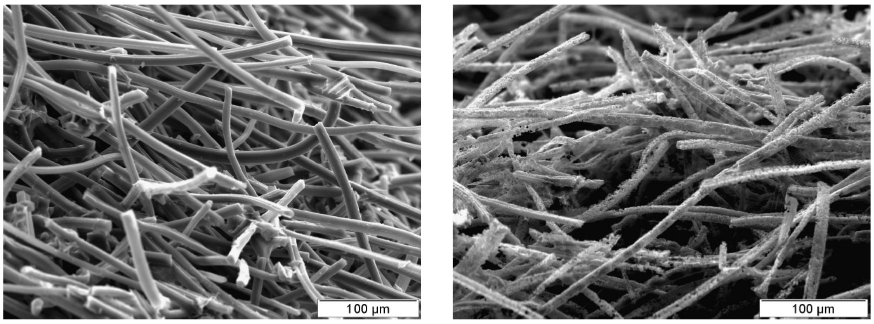

Figure 5.14: Micrographs of carbon fibers preform ablated in the sidearm reactor. Pitting phenomena can be observed on oxidized carbon fibers (right image). Figure taken from [170]

Furthermore, an increase of the oxidation rate where gaseous oxidation products are released [95, 129] can also influence the ratio between surface and volume ablation. Indeed, Hahn et al.[96] have observed that the production of CO molecules leads to atomic vacancy at the surface of graphite which, in turn, leads to an increase of the electronic density and finally to an increase of the oxidation rate. Considering these, the heterogeneous reactions with fibers already eroded will be enhanced. This new model to account for a change in the reactive surface was presented in Section 2.3.2. Therefore, we recall that using the sinusoidal model, the reactive surface function is assumed to be expressed as

$$S_f = \gamma \frac{A_w}{dV}, \tag{5.8}$$

with γ a tuning parameter to account for an increase of reactivity for eroded fibers as suggested in experimental observation of graphite by Lee et al. [129]. The eroded fibers are considered not cylindrical anymore but composed with holes of $1-2$ $[\mu m]$. These values for the pit size are extracted from micrographs and given in Ref. [171]. In order to study the impact of the model chosen for the oxidation of the fibers, we consider as a first guess that eroded fibers (activated) react twice as much as virgin fibers ($\gamma = 2$). Note that impurities found on the tube after the experiments can also contribute to this enhanced reactivity close to the plug surface. This results in a reactive surface evolution depicted in Fig. 5.15. The replication of test a4 with the reference rate and this $S_f(\epsilon_s)$ gives after 20 $[min]$ a mass loss of 14.9 $\%$ while the volume change is 3.6 $\%$. As expected, this has a direct influence on the ratio volume/mass loss. Therefore, a better knowledge of the evolution of fibers reactivity and geometry can help in defining an accurate effective reaction rate in order to match both mass and volume losses.

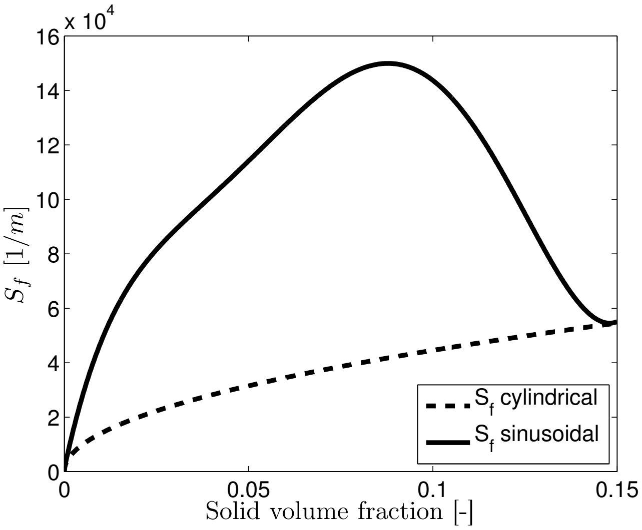

Figure 5.15: Specific surface with respect to solid volume fraction computed with the cylindrical and sinusoidal model.

5.4 Definition of an effective reaction rate

As suggested by the sensitivity analysis conducted before, including the evolution of the roughness of the fibers allows to find an appropriate combination of reaction rate and specific surface to match both mass and volume losses. The present section describes the procedure and the results to determine the parameters needed in the sinusoidal model. Note that to account for enhanced surface reactions, another model based on Park [172] was investigated and is described in Appendix F. Unlike the cylindrical model, the two models proposed give satisfactory results to match both recession and mass loss. Additionally, the sinusoidal model proposed was found to be more flexible and easier to optimize in order to fit with experimental data. It should be noted that these models are only valid when the pitting phenomenon is observed, and hence within a reaction-limited regime.

The numerical experiments have shown that the numerical transition zone from the pure fluid to the porous medium should be handled with care using the sinusoidal model. Indeed, the specific surface for the sinusoidal model highly depends on the porosity of the porous medium. For a lower porosity, we consider that the fibers are already eroded hence are more reactive. However, at initialization, the virgin porosity is varying in the transition zone from the fluid region to the homogeneous porous medium. This leads incorrectly to activated fibers in the transition layer. Therefore, the results are highly dependent on the smoothing distance and the mesh. To avoid such spurious triggering of the chemical reactions, the specific surface is computed using the local porosity with respect to its initial value. This way, in the interface region, we are closer to a matrix of variable porosity but with fibers similar in nature. Figure 5.16 shows the importance of considering this correction in the interface region at initialization. Indeed, we can observe that, without correction, the specific surface computed with the sinusoidal model leads to a spurious overshoot. This correction has proved to yield results independent with respect to the smoothing distance.

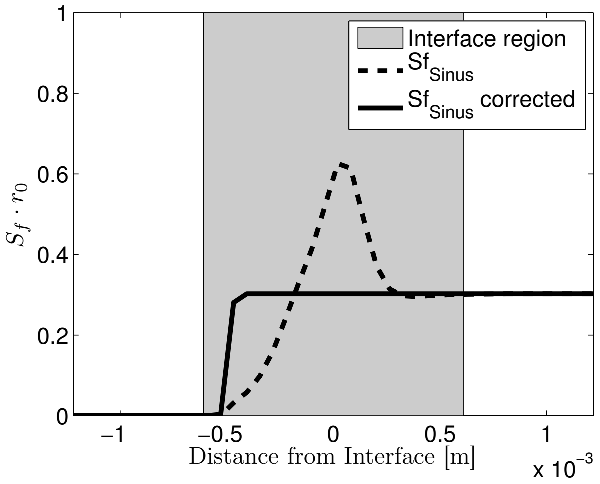

Figure 5.16: Correction of the sinusoidal model in the interface region to avoid an artificial activation of the fibers. The non-dimensionalized specific surfaces with and without correction are plotted in the interface region.

In order to identify the tuning parameter of this corrected sinusoidal model (γ) and the effective reaction rate, we carried out a preliminary analysis by considering mass conservation in 1D using a simple MATLAB code[1]. Although the phenomena cannot be captured accurately because of the simplicity of the model used, this code has shown similar trends as Argo. The sensitivity to define the tuning factor and the reaction rate can easily be observed in

---

[1] The solution of a 1D mass conservation equation using the cylindrical model is proposed in a module COACO of the material response code PATO developed by Lachaud et al. [119], and the implementation inside the MATLAB code follows the same approach.

Fig. 5.17. For a volume loss matching experimental data, the associated mass loss is higher for low γ. Therefore, increasing γ leads to a mass loss closer to the experimental data for a given volume loss.

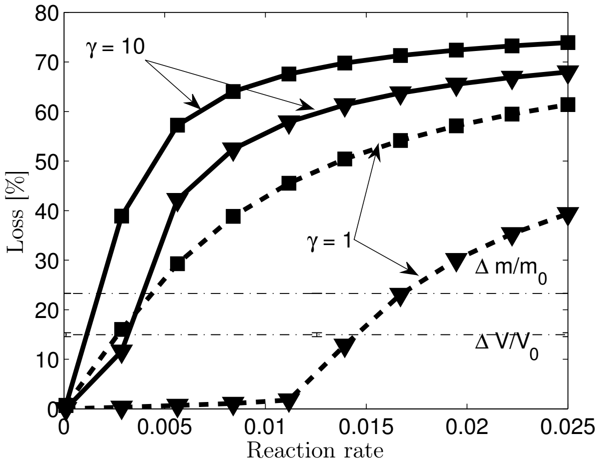

Figure 5.17: Evolution of the mass loss (squares) and the volume loss (triangles), for several tuning factor and reaction rate defined. The horizontal lines define the experimental values for the a4 test.

After this qualitative study, a shooting algorithm is then used to identify the tuning parameter for the a4 test case ($\gamma \approx 50$) using Argo. In addition, the Arrhenius law is adapted from Eq. (5.6) to match the mass loss at different temperatures (see Fig. 5.18). Only the test cases above 900 $[K]$ are considered. Panerai et al. [170] computed the reaction rate (see Eq. (5.6)) based on the whole range of temperature [700-1300 K] while clearly two regimes can be distinguished at low and high temperatures. We consider a limited temperature range [900-1200 K], this leads to a lower activation energy than computed by [170] ($Ea \approx 15500$ $[J/mol]$ instead of $Ea \approx 42400$ $[J/mol]$).

To summarize, the parameters for the sinusoidal model are calibrated using the following scheme

1. Determine the geometrical values (radius of the fibers, size of the pits) based on micrographs of virgin and oxidized fibers.
2. Use one dimensional analysis to have an idea about the range for the tuning parameters (γ) and the rate coefficient (k_f).
3. Use Argo with a fixed k_f and tune γ using a shooting algorithm to fit the volume loss for a given experiment (we use the a_4 experiment in this case).
4. Tune the rate coefficient to fit the mass loss at different temperature.

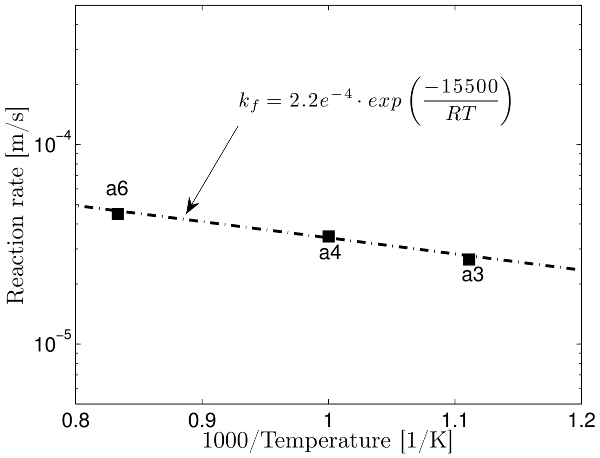

Figure 5.18: Fitting of the Arrhenius law to match the mass loss at different temperatures considering pitting of the fibers.

Since the plug is under volume ablation, the fibers in the whole plug will start to show some pitting and will react exponentially faster. The evolution of the mass and volume loss is shown for test a4 in Fig. 5.19. The first phase where the plug is under volume ablation is clearly shown in Fig. 5.19(b). The comparison of the experimental data with all the numerical replications is presented in Table 5.4 and shown in Fig. 5.11. The numerical results computed with Argo and the sinusoidal model with $\gamma = 50$ and the fitted Arrhenius law is noted N_A^*.

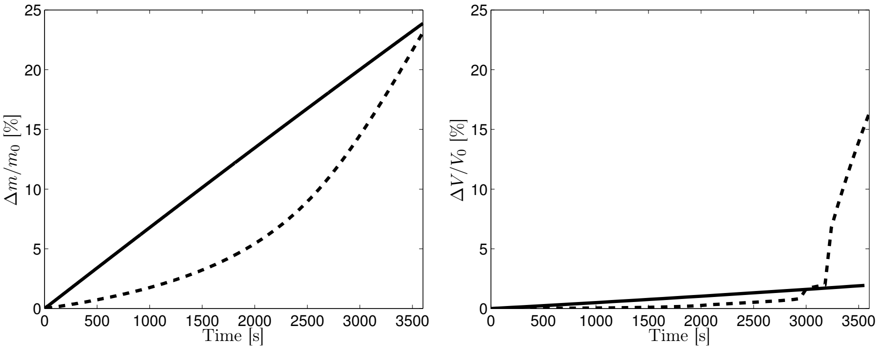

(a) Mass loss

(b) Volume loss

Figure 5.19: Time evolution of the mass and volume loss for test a4. The dashed lines are the results of the computation with the sinusoidal model, a tuned Arrhenius law and a tuning factor $\gamma = 50$ while the solid lines do not account for pitting and the Arrhenius law is the one given in Eq. (5.6).

Before discussing the results, let us first discuss the value of the fitted γ. The value of the tuning parameter is unexpectedly high suggesting that the proposed sinusoidal model or the parameters feeding the latter (i.e. holes, depth) should be adapted. However, the high value highlights again the importance of an enhanced reaction at the fluid-porous interface to match mass and volume loss in these conditions.

Using the sinusoidal model together with a tuned Arrhenius law, a very good matching with the experiments has been demonstrated for both the volume and mass losses. Since the volume loss is closer to the experimental measurement the discrepancy between the measured and computed back pressure has also been reduced. Using this model, the evolution of the recession with time can explain why the volume loss observed experimentally is dropping from test a4 to a3 while the mass loss is not that different (see Fig. 5.11). To the authors' knowledge, this code is the first to possess predictive capability to match mass loss and recession. Therefore, we have shown that the specific surface is an important parameter to study if one wants to investigate the competition between surface and volume ablation.

Based on the numerical analysis performed on this experiment and discussions with the authors of [170, 171], we have several suggestions for the experimental setup which could lead to a better characterization of the phenomena and thence, the development of a more accurate model. First, the exposition time is relatively long ($60[min]$) with experimental measurements only at the end of the test duration. This leads to computationally expensive simulations, it would be better to shorten the duration of the tests or to have time accurate data during these. For example, having experimental data at different times can help confirming the evolution of the mass and recession and hence validate the behavior observed with the sinusoidal model (see Fig. 5.19). Secondly, the tests proposed in Ref. [170, 171] are performed using air, while it could be interesting to isolate the effects of one species on the erosion of the fibers. In addition, running the experiments with pure species decreases also the number of degrees of freedom needed for the numerical simulations. The analysis could also benefits from measurements on the composition of the gas mixture after the plug. This could help identifying the oxidation products and determining the blowing rate. Finally, the analysis of the tomography data can be exploited to increase the fidelity of the model proposed. The effective surface can be directly measured and compared with the predictions. The analysis of ablated samples with this method can also help determine the depth of ablation and the evolution of the porosity inside the sample.

Therefore, this analysis suggests that having more information about the evolution of the micro-structure and kinetics data is crucial to correctly capture the competition between surface and volume ablation. At the same time, our model remains simple enough and is capable of accounting for pitting though the profile function $f(x,t)$, which can be readily adapted to consider more realistic geometries of the fibers.

5.5 Validation: NASA ring experiment

The same facility is used to study the ablation of a ring of Fiberform (see Fig. 5.20). Preliminary cases were run at higher pressure conditions and with the Arrhenius law proposed by Panerai et al. [170]. These runs consider wrongly the formation of CO_2 even at higher temperature while the Ellingham diagram shows that at these temperature the formation of CO is favored. Additionnaly, since there are at different pressure conditions, any comparison with the plug results are not straightforward. This will be discussed at the end of this section. For these reasons, the preliminary results at higher pressure are presented in Appendix G. Nonetheless, the conclusions of these results are still interesting: the same trend as for the porous plug was observed; the surface recession was underestimated for a given mass loss using the cylindrical model.

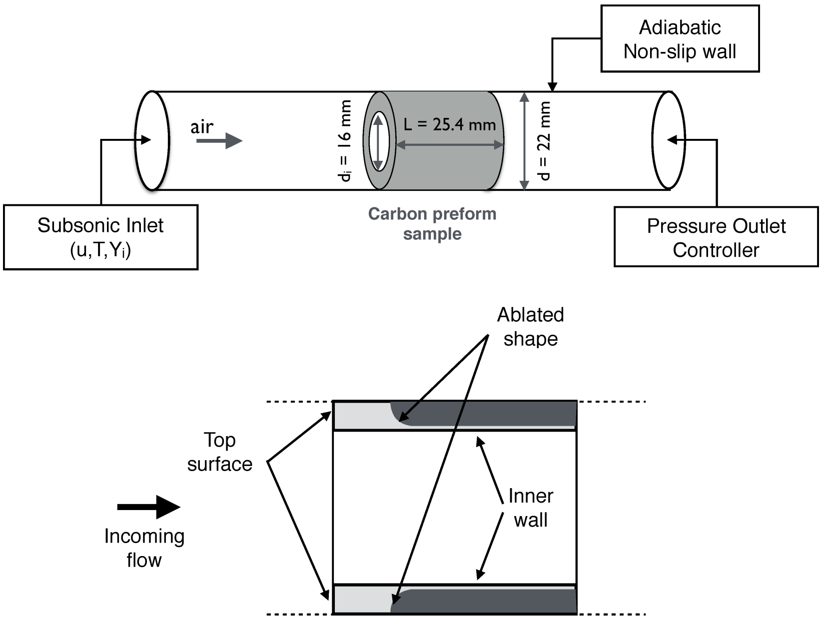

Figure 5.20: Ring experiment in the NASA sidearm reactor. The boundary conditions and geometry of the sample are presented.

In order to verify if the sinusoidal model and the tuned Arrhenius law proposed in Section 5.4 can also explain the discrepancy in the results presented in the Appendix between the experimental data and the numerical results, the following test case is proposed. Table 5.8 summarizes the conditions of the test performed at pressure similar to the one proposed in the previous section. The parameters for the sinusoidal model are the ones defined in Section 5.4 , i.e. we take $\gamma = 50$ and the Arrhenius law as $k_f = 2.2e^{-4} \exp\left(-15500/RT\right)$.

The boundary conditions are similar to the plug test case and summarized in Fig. 5.20. The re-radiation at the surface of the plug is again considered. Note that comparing to the flat surface of the plug, the geometry is more complex and the view factor for each surface should be computed and updated if the shape changes. This is not considered within this work and we are still assuming a view factor $F_{s,t} = 1$ for each surface of the ring exposed to the flow. This is justified by the small temperature rise observed at the surface comparing to the furnace temperature and the uncertainty on the emissivity factor (taken as 0.9).

Table 5.8: Experimental conditions for the ablation of a ring of carbon preform in NASA sidearm facility [171].

Test ID	P $[Pa]$	T $[K]$	$\dot{m}$ $[kg/s]$	$\rho_{s,0}$ $[kg/m^3]$	t $[s]$
a6	1630	1200	$2.21e^{-3}$	167.2	3600

As for the plug experiment presented in Section 5.2, the sample of carbon preform will be progressively eroded by the flow. In this case, the flow can pass freely through the sample. Therefore, the top surface of the ring and the inner wall will be eroded by the incoming flow (see Fig 5.20). This configuration is similar to the verification test case proposed in Section 4.7 which investigates the flow around a forward non-reactive porous step. In this configuration, the velocity of the flow inside the porous medium will be very low compared to the free fluid region since the flow will tend to avoid the obstacle (carbon preform samples have a very low permeability). In comparison with the plug test case, the porous medium is affected by additional shear stresses in the interface between the free fluid region and the carbon preform due to the higher velocity gradient. Therefore, mechanical erosion should be considered but it is beyond the scope of this work and spallation is proposed as a perspective.

The comparisons with experimental results are shown in Fig. 5.21. The mass loss after an hour of exposition, computed with the tuned Arrhenius law (see Fig. 5.18) is underestimated. This leads also to an underestimation of the recession which can be observed in Fig. 5.21(b) which compares the ring profiles. As observed in Fig. 5.19(b) for the plug or in Fig. 5.22, using the sinusoidal model, the recession with time is not linear hence underestimating the mass loss the error on the volume loss is also large. However, the agreement between the numerical results and the experimental data is undoubtedly better with the sinusoidal model than with the cylindrical model. The latter is unable to predict the mass or the volume loss. The final solid density field in Fig. 5.22(d) shows also that the interface region is very large for this test case. We observe that the remaining solid volume fraction is varying from 0 in the flow field to its maximum value on a distance equal to half its final length.

Finally, it should be noted that, using the sinusoidal model, the reactions at the surface are faster implying the need of a more resolved grid in this region to capture the recession of the porous medium.

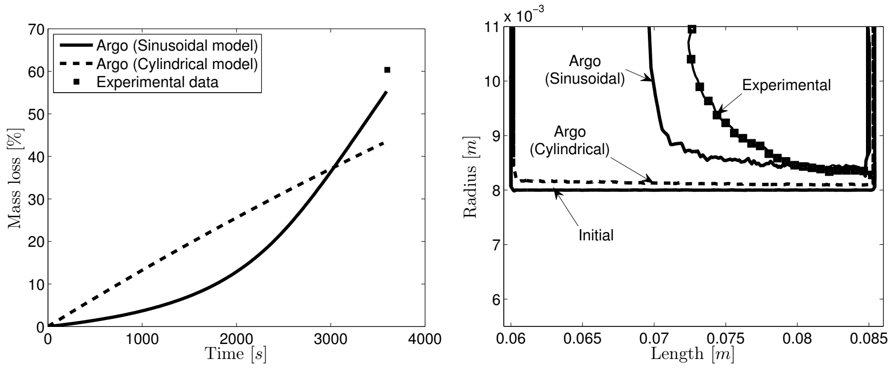

(a) Mass loss (b) Ring profile

Figure 5.21: Ablation of a carbon preform ring by a low Reynolds air flow with conditions given in Table 5.8. Comparison between experimental data [171] and Argo numerical results with the cylindrical and sinusoidal models. The parameters for the sinusoidal model are taken from the calibration conducted in Section 5.4.

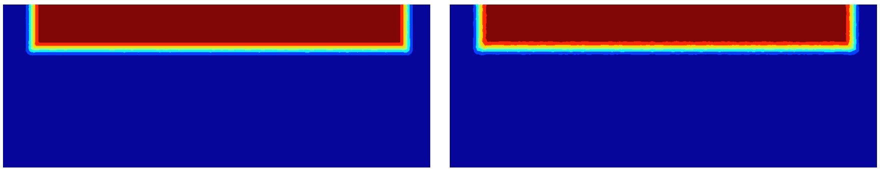

(a) 0 min (b) 20 min

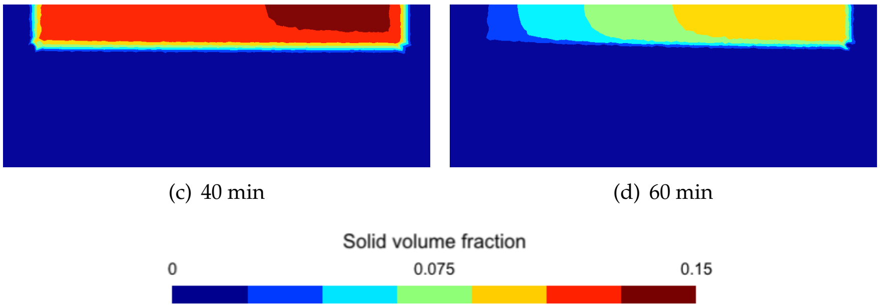

(c) 40 min (d) 60 min

Figure 5.22: Ablation of a carbon preform ring by a low Reynolds air flow with conditions given in Table 5.8. Contours of solid volume fraction with time.

In Ref. [171], the test campaign involves the ablation of a ring at different pressure conditions. The preliminary runs proposed in the Appendix G are investigating pressures higher than the test case summarized in Table 5.8. As explained above, the computational results presented in the Appendix do not consider the correct heterogeneous reaction at the surface with production of CO_2 rather than CO. The evolution of the mass loss with respect to increasing pressure is investigated for the ablation of the ring in conditions summarized in Table 5.9.

Table 5.9: Experimental conditions for the ablation of a ring of carbon preform in NASA sidearm facility [171].

Test ID	P $[Pa]$	T $[K]$	$\dot{m}$ $[kg/s]$	$\rho_{s,0}$ $[kg/m^3]$	t $[s]$
a4	1630	1000	$2.19e^{-3}$	167.3	3600
b4	10000	1000	$2.18e^{-3}$	173.1	3600

The mass loss computed with the cylindrical model and the reference reaction rate is compared with the tuned sinusoidal model and the experimental data. Table 5.10 shows the resulting mass loss after an hour of exposition in the sidearm. First, it can be observed that the mass loss measured experimentally decreases with increasing pressure while the numerical results with the two models give an opposite trend. In opposition to what we observe at low pressure, the sinusoidal model overestimates completely the mass loss at high pressure. At higher pressure, the mass loss computed numerically with the cylindrical model gives better agreement with the experimental data. However, the surface recession is completely underestimated with the cylindrical model as shown in Fig. 5.23 at both pressure test conditions. This has been already observed in the preliminary runs proposed in Appendix G. We can also observe that, while the mass loss measured in the experiment is decreasing for higher pressure, the recession is higher. This trend for the volume loss is captured numerically by the two models implemented. There is no ring profile for the high pressure case using the sinusoidal model because, in that case, the ring is completely ablated.

To fit the experimental observations, this would require another fit at these pressure conditions or, better, including the pressure dependance when computing the reaction rate. As already discussed in Section 2.3.2, we are not taking into account the complex mechanisms for the heterogeneous reaction at the surface. Indeed, we consider that the heterogeneous reaction is the irreversible oxidation reaction given by $C_s + \frac{1}{2}O_2 \rightarrow CO$ and we do not take into account the fact that this reaction is composed of a series of adsorption-desorption processes. This can lead to an incorrect prediction of the apparent order of reaction [74]. For example, in coal gasification, the widely used treatment for the reaction rate of the carbon oxidation is expressed as

$$k_c = k_0 \exp\left(-\frac{E_a}{RT}\right) P_{O_2}^n, \tag{5.9}$$

where P_{O_2} is the partial pressure of oxygen and n is an apparent kinetic order of reaction [107]. This has not been further investigated in this work. Another set of pressures for the ablation of the plug would help to study and understand the pressure influence for the ablation of the carbon fibers.

Table 5.10: Mass loss after 60 [min] of exposure of a ring sample in two pressure conditions (test a4 and b4 summarized in Table 5.9). Comparison between experimental data, numerical results of Argo with the cylindrical model and numerical results with the sinusoidal model.

$\Delta M/M_0$ [%] P $[Pa]$	Experimental data	Argo Cylindrical model	Argo Sinusoidal model
$1.63e^3$	54.51	18.21	44.73
$1.0e^4$	53.16	65.46	99.74

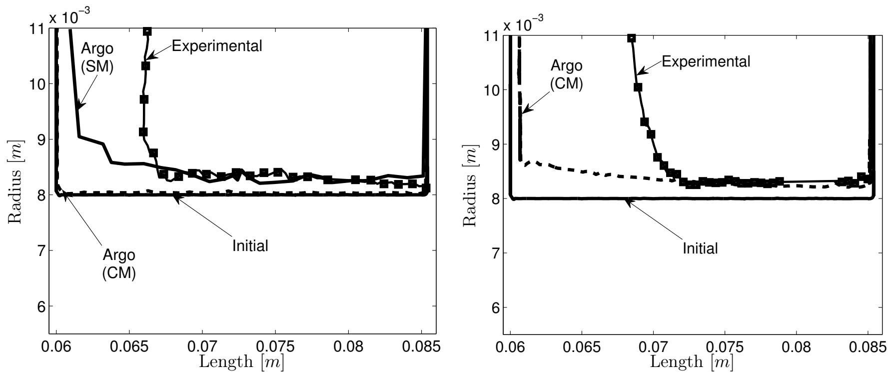

(a) $P = 1.63e^3$

(b) $P = 1.0e^4$

Figure 5.23: Comparison between experimental ring profile [171] and Argo numerical results with the cylindrical (CM) and sinusoidal (SM) models. The parameters for the sinusoidal model are taken from the calibration conducted in Section 5.4.

5.6 Conclusions

The competition between surface and volume ablation is a key parameter to capture in order to correctly predict the recession of the thermal protection material, hence select its adequate thickness. The replication of an experiment conducted in the NASA Ames sidearm facility has shown the limits of this code and current models to capture this competition. The new calibrated model has proved to be more accurate than the cylindrical model proposed in Ref. [120]. Accounting for pitting phenomena in these experimental conditions is very important to correctly capture the competition between volume and surface ablation. Several temperature conditions have been tested successfully with the calibrated sinusoidal model for the ablation of a plug. The numerical tests for the ablation of a ring in the same facility has shown better agreement with the sinusoidal model than with the cylindrical model at low pressure conditions. For higher pressure conditions, the sinusoidal model and the fitted reaction rate proposed overestimate the mass loss. It is proposed to study the apparent order of the oxidation reaction to explain the discrepancy at higher pressure. The need for microstructure information is clear if one wishes to develop an appropriate model depending on the evolution of the fibers. The sinusoidal model is a first step in the right direction toward high fidelity modeling of carbon fibers oxidation at the macro-scale level.

CHAPTER 6

COMPLEX THERMAL RESPONSE OF AN ABLATIVE MATERIAL

This chapter deals with the complex in-depth thermal response of a low density ablative material and the development of a one dimensional code to simulate it. The chapter is a modified version of the article presented in the AIAA conference [195]. The author would like to thank especially J. Lachaud for valuable discussions about the physical modeling and for providing the data used to verify the developed tool.

6.1 Introduction

The material response to a high enthalpy flow is a complex matter. Correctly capturing the in-depth phenomena inside the ablative thermal protection shield is essential to design its thickness. The goal is of course to ensure that the back structure remains at a reasonable temperature to ensure the integrity of the spacecraft. During an atmospheric entry, as explained in Chapter 1, the heat flux penetrates inside the material. For low density ablative material composed of carbon fibers and phenolic resin, the resin will progressively be thermally degraded. The pyrolysis of the phenol content generates gases which will percolate through the remaining carbon fibers and char material. In addition, at the surface of the material, the carbonized material and the carbon skeleton will progressively be eroded by the incoming flow (see Chapter 5). Therefore, a material code has to account for thermal conduction, thermal degradation, erosion, internal flow of pyrolysis gases and chemical reactions. Since the material is thermally decomposed and under a high temperature gradient, the change in material properties should also be accounted for.

To simulate the response of the material, numerous numerical codes exist. However, most of the material response codes used for design still rely on models developed in the 1960's[118]. The recent interest for higher fidelity modeling has raised numerous research studies regarding pyrolysis and ablation problem [118]. The in-depth thermal response codes can be separated in three categories following the complexity of the models used [121]. The first type of code (type I) uses simplified models inherited from the first open literature publication in the 1960's. For these models, three main hypotheses are assumed. Thermal equilibrium between the solid and gaseous phase is supposed, the gas velocity is supposed perpendicular and directed toward the surface and a short residence time inside the control volume is assumed [155]. Removing respectively the second and third hypotheses yields type II and type III codes which implement more complex models to describe the gaseous phase inside the porous media. The second type of code models the gas motion inside the porous media with Darcy's law. The last category is large and includes codes that contains any improvement with respect to type II. For example, these codes can have more complex models for radiation, can include finite rate chemistry or accurate transport models. Figure 6.1 taken from [119] shows the phenomena involved dealing with the material response and summarizes the fidelity associated with each model type.

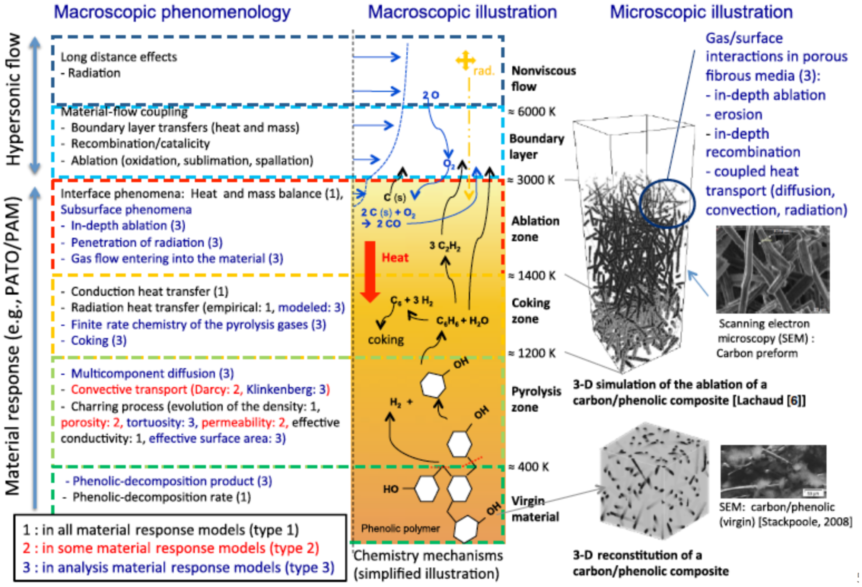

Figure 6.1: Macroscopic and microscopic phenomena of a material response to a high enthalpy flow. Figure taken from [119].

This chapter presents the development of a one dimensional code to simulate complex in-depth thermal response of the material. First, a review of the constitutive equations to model the material response to high enthalpy flow is detailed. The conservation laws derive from Chapter 2, but does not account for the presence of a pure fluid phase while the modeling of the material response is of higher fidelity. Then, the numerical scheme to solve the 1D in-depth thermal response is presented in Section 6.3. Finally, verification results including comparisons with state-of-the-art codes are presented and the reproduction of an experiment conducted inside the Plasmatron of the von Karman Institute for Fluid Dynamics is used as validation.

6.2 Simplified governing equations

The governing equations implemented in 1D are summarized hereafter for type II and III code and the reader is referred to Lachaud et al [118] for more information regarding the development of the models. The current implementation considers type II models and available tools with their respective fidelity are presented in Appendix E.

6.2.1 Mass conservation equation

Depending on the level of fidelity, the approach will track every species in the gaseous phase or only a mixture. Accordingly, a mass conservation equation is solved for each species or an overall pyrolysis gas mass conservation equation is used,

$$\frac{\partial(\rho_i \epsilon_i)}{\partial t} + \frac{\partial(\rho_i \epsilon_i v_g)}{\partial x} + \frac{\partial(J_i)}{\partial x} = \Pi_i + \epsilon_i \omega_i \text{ , i} \in S \tag{6.1}$$

$$\frac{\partial(\rho_g \epsilon_g)}{\partial t} + \frac{\partial(\rho_g \epsilon_g v_g)}{\partial x} = \Pi, \tag{6.2}$$

where ρ_i stands for the mass density of the gaseous species, ϵ_i is the volume fraction, v_g is the interstitial flow velocity within the porous media and J_i is the diffusion flux through the pores. The gas production rate from the decomposition of the solid is Π_i , ω_i is the gas production rate due to reactions among the gaseous phase and S is the set of indices of gaseous species. The solid decomposition by pyrolysis is absent in the physical model described in Chapter 2. The gas production rate is obtained using one or several Arrhenius laws for the decomposition of the solid phase that are usually fitted on thermogravimetry analysis results

$$\frac{\partial \rho_s}{\partial t} = -A_s \cdot \exp\left(-\frac{E_a}{RT}\right) \rho_0 \left(\frac{\rho_s - \rho_r}{\rho_0}\right)^{m_s}, \tag{6.3}$$

where ρ_s is the instantaneous component density of the solid, while ρ_0 and ρ_r are the initial and residual mass density. In this implementation, the three-component decomposition rate law from Goldstein [89] is used. In this case, the material is supposed to be composed of carbon fibers and two phenolic resin components. The current implementation considers type II models and does not track several species, only one mass conservation equation is solved (Eq. (6.2)).

6.2.2 Momentum conservation law

The momentum conservation law described in Section 2.3.1 is simplified and, in the present context, Darcy's law is used

$$v_g = -\frac{\kappa}{\mu_g \epsilon_g} \frac{\partial P}{\partial x}, \tag{6.4}$$

where κ is the permeability, μ_g is the viscosity and P is the pressure field.

6.2.3 Energy conservation law

Assuming thermal equilibrium between the pyrolysis gases and the porous material, the energy conservation equation can be written as

$$\frac{\partial(\rho_a e_a)}{\partial t} + \frac{\partial(\epsilon_g v_g \rho_g h_g)}{\partial x} = \frac{\partial}{\partial x}\left(\lambda \frac{\partial T}{\partial x}\right), \tag{6.5}$$

where λ is the thermal conductivity and the total internal energy includes the contributions of the matrix, fiber and gas phase

$$\rho_a e_a = \epsilon_m \rho_m e_m + \epsilon_f \rho_f e_f + \epsilon_g \rho_g e_g. \tag{6.6}$$

The properties of the solid material such as permeabilities and thermal conductivities are interpolated from the values for pure virgin and char material,

$$X = \xi_v \cdot X_v + (1 - \xi_v) \cdot X_c, \tag{6.7}$$

where X stands for a generic properties, the subscripts v and c refer to the virgin and charred material properties and ξ_v is the fraction of remaining virgin material. For the results presented in Section 6.4, type II models are implemented.

6.2.4 Boundary conditions

The in-depth thermal response of the material is strongly coupled to the interaction and transfer at the gas-solid interface. To correctly model the phenomena at the interface and implement correct boundary conditions, the existing methods can be separated into two main categories. For the first approach, simplified boundary conditions are usually used for the gas-solid interface [14]. For instance, inviscid boundary-layer edge conditions are taken from separate simplified flowfield simulations, and the surface conditions (i.e., temperature or convective heat flux) are obtained by means of semi-empirical relations. For the second method, the material code is coupled to a CFD code and exchange information at the boundary. This can be performed either by coupling together two distinct solvers designed to compute the solid and the gas-side of the problem [27, 50], or by directly developing a unified numerical tool capable of computing the flow through the material accounting also for in-depth ablation of the material fibers [120, 145, 202]. The latter was developed in the previous chapters. Within this chapter, the first method using the transfer coefficients approach will be used. This method is largely used in the aerothermodynamic community and has proven its efficiency [118]. The mass and energy balance based on the transfer coefficients approach are summarized hereafter. The boundary conditions at the back of the material are simpler and the rear wall is often assumed adiabatic and impermeable.

Mass balance

In order to solve the mass balance at the gas-solid interface, the conservation of a chemical element k is considered inside a control volume tied to the receding surface (see Fig. 6.2). If mechanical erosion (spallation) is neglected, the surface mass balance for each element can be expressed as

$$J_{w,k} + (\rho V)\, y_{w,k} = \dot{m}_g y_{g,k} + \dot{m}_c y_{c,k}, \tag{6.8}$$

where subscript $w,\ g$ and c refer respectively to quantity at the wall, pyrolysis gas and char material. The y are the pseudo mass fractions for each chemical element and J represents the diffusive flux towards the surface. Summing Eq. (6.8) for all elements, and recognizing that the pseudo mass fractions sum to one in each phase, the mass balance can simply be rewritten

$$(\rho V)_w = \dot{m}_g + \dot{m}_c. \tag{6.9}$$

The term $\dot{m}_c$ is the mass blowing due to the surface heterogeneous reactions which consume the material. It corresponds to the sum of all the source terms of those species that participate to these reactions. Similarly, $\dot{m}_g$ is the pyrolysis gas mass flow rate generated by the in-depth material decomposition.

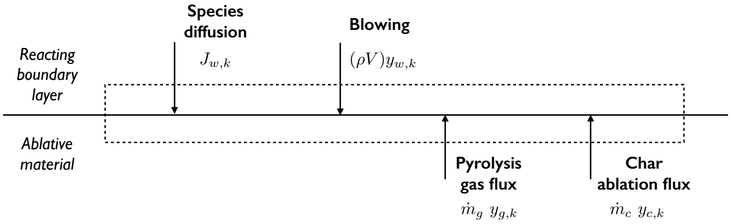

Figure 6.2: Mass balance at the ablative wall for a chemical element k neglecting spallation.

Energy balance

In order to identify the important terms in the heat transfer, we study the laminar steady boundary layer equation for the energy in two dimensions which can be written

$$\rho u \frac{\partial h_0}{\partial x} + \rho v \frac{\partial h_0}{\partial y} = \frac{\partial}{\partial y}\left(\frac{\mu}{Pr}\frac{\partial h_0}{\partial y}\right) + \frac{\partial}{\partial y}\left(\mu\left(1-\frac{1}{Pr}\right)\frac{\partial}{\partial y}\left(\frac{u^2}{2}\right)\right) + \frac{\partial}{\partial y}\left(\rho D\left(1-\frac{1}{Le}\right)\sum_i h_i \frac{\partial y_i}{\partial y}\right), \quad (6.10)$$

where h_0 is the total enthalpy, Pr is the Prandl number and Le the Lewis number. On top of a non-ablating surface, the Stanton number can be used to describe the mass and energy transfer at the wall. The Chilton-Colburn relation can be used to relate the mass and heat Stanton numbers

$$C_m = C_h (Le)^{\frac{2}{3}}, \quad (6.11)$$

where C_m is the mass transfer coefficient (also referred in the literature as St_m) and C_h is the heat transfer coefficient (also called St) The classical definition for the heat Stanton number is

$$St = Ch = \frac{\rho_e u_e \left(h_{0,e} - h_w\right)}{q_{conv}}, \quad (6.12)$$

where the subscript e indicates the terms that belong to the boundary layer edge. Note that the Stanton number can be related to the skin friction coefficient by the Reynolds analogy

$$Ch = Pr^{-\frac{2}{3}} \frac{C_f}{2}, \quad (6.13)$$

where C_f is the skin friction coefficient. The total enthalpy at the edge of the boundary layer, $h_{0,e}$, should be replaced by a recovery enthalpy in case of non-unitary Prandl number [24]. In addition, evaluating the heat flux at the wall using the heat Stanton number in Eq. (6.12) assumes that the Lewis number is unity. If it is not the case, an additional contribution should be accounted for due to the diffusion of the species carrying their enthalpy (last term in Eq. (6.10)) [24].

Considering the control volume attached to the receding surface, the surface energy balance can be written

$$\left(\rho_e u_e C_h\right)\left(h_{0,e} - h_w\right) - \left(\rho V\right) h_w + \dot{m}_g h_g + \dot{m}_c h_c + q_{rad,in} - q_{rad,out} = q_{cond}. \quad (6.14)$$

In the surface energy balance, Eq. (6.14), the terms $\dot{m}_g h_g$ and $\dot{m}_c h_c$ represent the contribution due to the enthalpy (h) carried on by the pyrolysis and ablation product gas, q_{cond} is the solid heat conduction in the material, and the last two terms of the left hand side are the radiative heat flux. The convective heat flux depends directly on the flow and should be provided as well as the incoming radiation flux. Note that, in this work, the radiative heat flux accounts only for the re-radiation from the hot surface. A sketch of the energy balance is shown in Fig. 6.3.

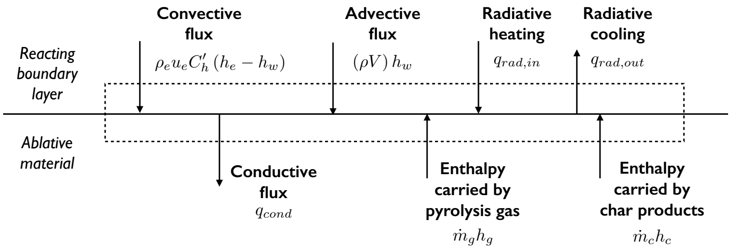

Figure 6.3: Energy balance at the ablative wall neglecting spallation.

The transfer coefficients expressed in Eq. (6.11) and used to model the convective heat flux have to be corrected to account for the blocking effects imposed by the blowing of gas from the material inside the boundary layer. The blowing correction can be expressed as [155]

$$C_h' = C_h \left(\frac{\ln(1 + 2\iota B')}{2\iota B'} \right). \tag{6.15}$$

with ι a coefficient depending on the flow regime (0.5 if laminar), and B', the non-dimensionalized total mass flux which can be expressed as

$$B' = B_g' + B_c', \text{ with } B_g' = \frac{\dot{m}_g}{\rho_e u_e C_m}, \text{ and } B_c' = \frac{\dot{m}_c}{\rho_e u_e C_m}. \tag{6.16}$$

Finally, in order to close the surface balances, the ablation rate ($\dot{m}_c$) has to be defined. This term should account for the thermodynamic conditions in the boundary layer, the gas-surface heterogeneous reactions as well as blowing effects. Usually, thermochemical equilibrium is assumed close to the wall and the value of B_c' and the enthalpy at the wall are pre-computed and tabulated with respect to the temperature, pressure and pyrolysis blowing rate [156].

6.3 Numerical methods

In order to solve the problem described by the constitutive laws, the system of equations is decomposed. First the energy and mass density of the solid media are advanced in time with a Super Time Stepping (STS) scheme [3]. Then, the pressure field is found by solving implicitly the gaseous mass conservation where Darcy's law and the perfect gas equation have been used. Finally, thanks to the pressure field, the velocity field is updated. At the end of one time step, the mesh is updated to account for recession of the material. The different steps and equations solved are summarized in Fig. 6.4 and the paragraphs hereafter describe the specificities of the method.

6.3.1 Spatial discretization

The spatial discretization uses as Argo a DGM and the architecture of Echion is similar to Argo. In the discretization of the convective terms (see Eq. (3.6)),

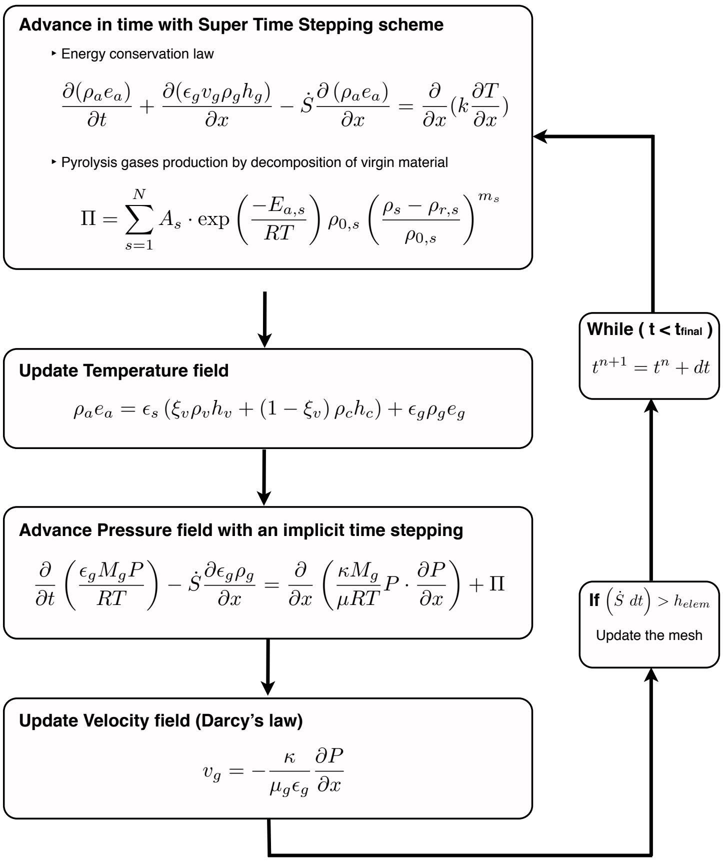

Figure 6.4: Numerical strategy proposed to solve in-depth-thermal response

the interfacial term corresponding to the convective part is treated by a Lax-Friedrich numerical flux. For the diffusive part, the interior penalty method proposed in particular by Riviere [188] to solve parabolic problems in porous media has been chosen. Discontinuous Galerkin methods have also been used for ablation problem by Bathia and Roy [22] which implemented a Bassi Rebay-1 method to compute the viscous fluxes. More details on the spatial discretization can be found in Chapter 3.

6.3.2 Temporal discretization

As shown in Fig. 6.4, the system of equation is split and two types of time integration schemes are used. The in-depth thermal response is dominated mainly by diffusion terms. The computational time associated with diffusion dominated problems solved by explicit scheme is known to be high due to stability constraints on the time step. Since the problem is dominated by diffusion, the stable time step then depends on the inverse square of the mesh size. Using an implicit scheme allows to use an arbitrary time step at the cost of the solution of a linear system at each time step. An alternative to implicit scheme is the *Super Time Stepping (STS)* scheme that uses cheaper explicit procedure while relaxing the stability constraint [3]. The idea is to ensure the stability after N sub-time steps and maximize the duration of the super time step. This super time step is defined as the combination of smaller time steps chosen carefully to ensure the stability

$$\Delta\tau = \sum_{j=1}^{N} \tau_j . \tag{6.17}$$

For example, to discretize a typical time dependent equation

$$\frac{dU}{dt} + AU = 0, \tag{6.18}$$

the STS explicit scheme can be written

$$U^{n+1} = \left(\prod_{j=1}^{N} (I - \tau_j A) \right) U^n \tag{6.19}$$

where the stability constraints is applied on the product. According to Alexiades [3], the optima sub-time steps depend on the regular explicit time step defined for stability purpose and on two parameters N and $\bar{\nu}$ used to control the accuracy

$$\tau_j = \Delta t_{expl} \left((-1+\bar{\nu}) \cdot cos\left(\frac{2j-1}{N}\frac{\pi}{2} \right) + 1 + \bar{\nu} \right). \tag{6.20}$$

Therefore, the super time step can be rewritten

$$\Delta\tau = \sum_{j=1}^{N} \tau_j = \Delta t_{expl} \frac{N}{2\sqrt{\bar{\nu}}} \left(\frac{(1+\bar{\nu})^{2N} - (1-\bar{\nu})^{2N}}{(1+\bar{\nu})^{2N} + (1-\bar{\nu})^{2N}} \right). \tag{6.21}$$

The stability limit corresponds to $\bar{\nu} = 0$ and it can be observed that for this limit the super time step tends to $N^2 \Delta t_{expl}$. Since N regular explicit steps cover a $N\Delta t_{expl}$ time interval, a STS scheme can be up to N times faster than a regular explicit scheme. The gain with respect to regular first order explicit scheme is shown in Fig. 6.5 for several value of N and $\bar{\nu}$.

The advantages with respect to implicit schemes are that it is rather easy to implement, there is no need to derive the Jacobian for non-linear cases and to solve the linear system associated with it. Furthermore, Alexiades [3] has shown that STS can be more advantageous than implicit scheme when one considers the CPU cost-accuracy ratio. These advantages make the method attractive for the first step of our time advancement strategy.

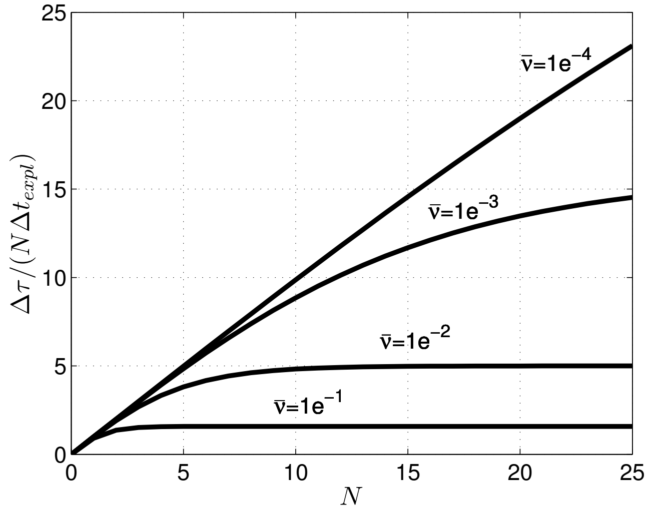

Figure 6.5: Comparison between Super Time Stepping scheme and regular explicit scheme. The ratio between the super time step and N explicit stable time steps is shown with respect to N for several value of $\bar{\nu}$.

The second step solves the mass conservation law where the gas velocity is replaced by Darcy's law. The perfect gas law is used to remove the density and to solve the equation with pressure being the only unknown

$$\frac{\partial}{\partial t}\left(\frac{\epsilon_g W_g P}{RT}\right) = \frac{\partial}{\partial x}\left(\frac{\kappa W_g}{\mu RT} P \cdot \frac{\partial P}{\partial x}\right) + \Pi. \tag{6.22}$$

However, solving this equation is too expensive to be treated explicitly even using an STS scheme because of the stiffness introduced by the reaction term. Therefore, a backward Euler scheme coupled with a Newton-Raphson algorithm is used to solve the non-linear differential equation.

6.3.3 Recession modeling

Several techniques to account for the recession of the computational domain exist. As explained in Section 3.4, these can be roughly divided into *interface tracking* and *interface capturing* techniques. Most material codes use methods among the first category which can be separated in several types. The first type of method keeps the mesh size constant in the interior domain and modifies it accordingly close to a boundary. Either the position of the first node can be changed [36] or the mesh can be tied to the receding surface and the last node is removed once the recession length is sufficient [155]. Removing nodes at the back wall has proved to be more efficient since it removes oscillatory behavior which can occur in the first numerical scheme. Within the first category, another method consists in using the Landau coordinate and therefore keeping the number of nodes constant and adjusting the length of the domain. The same conclusions compared to Section 3.4 hold and *interface capturing* methods are more advantageous than *interface tracking*. The deformation of the mesh due to recession can deteriorate the mesh quality and remeshing can be time consuming and complex depending on the shape of the interface for multidimensional cases.

The *interface capturing* technique does not require the mesh to follow the interface. A preliminary work, using eXtended Finite Element Method (XFEM) was presented in [195] but due to the complexity of implementation for a system of equations, the results presented here were obtained using the moving mesh method proposed by Rindall [155]. This implies the transformation of the system of equations presented in Section 6.2 to a moving coordinate system. For example, the energy equation becomes

$$\frac{\partial(\rho_a e_a)}{\partial t} + \frac{\partial(\epsilon_g v_g \rho_g h_g)}{\partial x} - \dot{S}\frac{\partial(\rho_a e_a)}{\partial x} = \frac{\partial}{\partial x}(\lambda\frac{\partial T}{\partial x}), \tag{6.23}$$

where $\dot{S}$ is the recession velocity. During the simulation, once the recession length is larger than an element, the last element (closest to the adiabatic wall) is removed from the mesh.

6.4 Results

To verify the development of the one dimensional material code, a series of test cases are carried out. First, the implementation of the high-order method is verified using a mesh convergence study. The moving mesh technique is also verified. A series of test cases proposed by Lachaud et al. [121, 122] are used to compare the results with state-of-the art codes. Finally, the results of an experiment are compared to experimental data to validate the code.

6.4.1 Convergence study

Because a material code is essentially a thermal conduction code [143] , it has been validated for a particular thermal conduction problem with variable conductivity. The energy equation, assuming constant density and heat capacity, reduces to

$$\frac{\partial T}{\partial t} = \frac{\partial}{\partial x}\left(\alpha\frac{\partial T}{\partial x}\right), \tag{6.24}$$

where α is the heat diffusivity. The *method of manufactured solutions* is used to verify the implementation and to perform a convergence analysis. For this method, the solution is chosen and inserted in the equation to find out an adequate source term that compensates the effect of the diffusion. In this case, the stationary solution is chosen to be

$$\frac{T}{T_0} = 1e^{-3} \cdot \sin\left(\pi\frac{x}{L}\right), \tag{6.25}$$

and the diffusivity is chosen to be $\alpha = \frac{\alpha_0 x}{L}$. Therefore, the source term can be expressed as

$$S = T_0 \alpha_0 \frac{x}{L} \left(\frac{\pi}{L}\right)^2 1e^{-3} \sin\left(\pi \frac{x}{L}\right) - T_0 \alpha_0 \frac{\pi}{L^2} 1e^{-3} \cos\left(\pi \frac{x}{L}\right), \tag{6.26}$$

where T_0, L and α_0 are reference temperature, length, and diffusivity taken as one in this case. The DG solution matches the analytical solution and the results shown in Fig. 6.6 are in agreement with the theory which implies for DGM a convergence order of $p+1$.

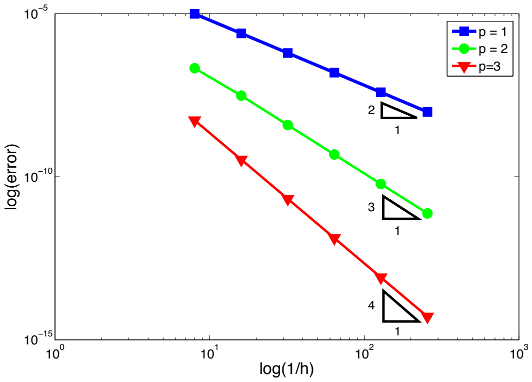

Figure 6.6: Spatial convergence study for a variable diffusivity case and different approximation order.

6.4.2 Mesh movement

In order to verify the implementation of the moving mesh technique, we consider a test case where the temperature as well as the recession rate are imposed [155]. The analytical solution for the recession of a semi-infinite plate was used to verify the implementation. Figure 6.7 shows the comparison between the analytical temperature profile and the results of the present analysis.

6.4.3 Comparison with other codes

To verify the algorithm implemented, the results have been compared to other codes for a series of test cases proposed by Lachaud et al. [121]. The material used is a Theoretical Ablative Composite for Open Testing (TACOT) with publicly available properties. The code results are compared for each test cases with the Pyrolysis and Ablation Toolbox based on OpenFOAM (PATO) developed at NASA Ames Research Center by Lachaud et al. [119]. This code possesses different modules and one is solving the same model as presented in Section 6.2. The results of Echion are compared with this particular module, i.e. we compare the numerical solution of the same equations. For every case,

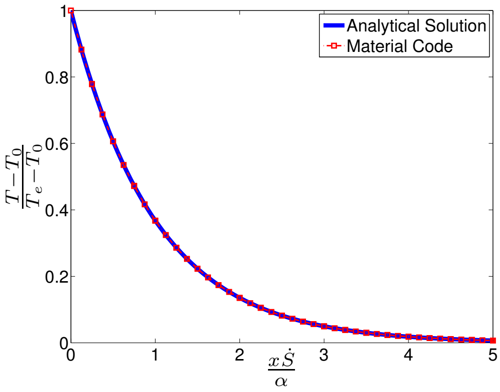

Figure 6.7: Steady state thermal response of a semi-infinite receding solid: comparison between Echion computation and analytical solution.

the temperature field, the mass blowing rate (pyrolysis and char) and the position of different zones within the material are compared. The char and virgin fronts are defined using fractions of the virgin solid density. The thresholds for the solid fractions are

$$\rho_{v,t} = \rho_c + 0.98\left(\rho_v - \rho_c\right), \tag{6.27}$$

$$\rho_{c,t} = \rho_c + 0.02\left(\rho_v - \rho_c\right), \tag{6.28}$$

where subscripts v and c stand for virgin and char material and t is the threshold value.

Ablation test case 1

For the first test case, the sample of TACOT is heated on one side for 1 minute at atmospheric pressure while the back wall is assumed adiabatic. The temperature at the wall is specified and no recession is assumed. Figure 6.8 shows that the results are in good agreements with PATO. A difference in temperature of less than 1% for each of the thermocouples at 60s is observed. The difference for the remaining virgin and char thickness at 60s is respectively of 1.1% and 1.3%. The mass blowing rate computed is also close to PATO's results with a difference of 2.3%. Differences with the same order of magnitude could be observed for most participants of the ablation workshop [121].

Ablation test case 2

For the second test case, three simulations are proposed to verify the implementation of the ablative boundary conditions and response to a high enthalpy flux. The first step was to verify the implementation of the energy balance at the wall without the complexity of a moving mesh (the recession is assumed null). The convective heat flux is given and after 60 seconds, the problem becomes purely re-radiative. The second part of the test case assesses

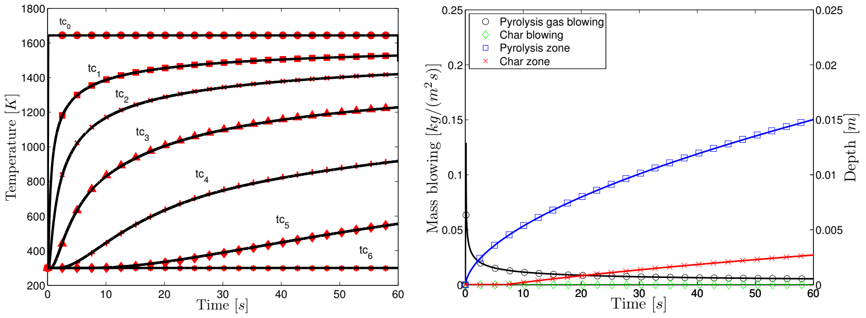

(a) Temperature field for TACOT (b) Mass blowing rate and char-virgin zones

Figure 6.8: In depth thermal response of TACOT to an imposed step of temperature without recession (Ablation Workshop test case 1): comparison with PATO results [121]. The temperatures are measured at different positions corresponding to $\{0, 1, 2, 4, 8, 16, 50\}$ mm from the surface for tc_0 to tc_6 respectively. Solid lines are PATO results, symbols are Echion results.

the recession and the blowing of char material at the surface. Finally, the last simulation shows the response of TACOT to a higher heat flux. Figures 6.9, 6.10 and 6.11 show the results for test cases 2.1, 2.2 and 2.3. Vertical lines in the temperature field indicate the failure of the numerical thermocouples because the recession is higher than this depth. The results for the three cases are very close to the one obtained with PATO. It should be noted that the mesh has to be sufficiently fine to capture the very stiff gradient at the boundary of the material. If the mesh is not sufficiently fine, the high order interpolation may lead to overshoots in the temperature which cause problems in the properties lookup and eventually cause the simulation to stop prematurely.

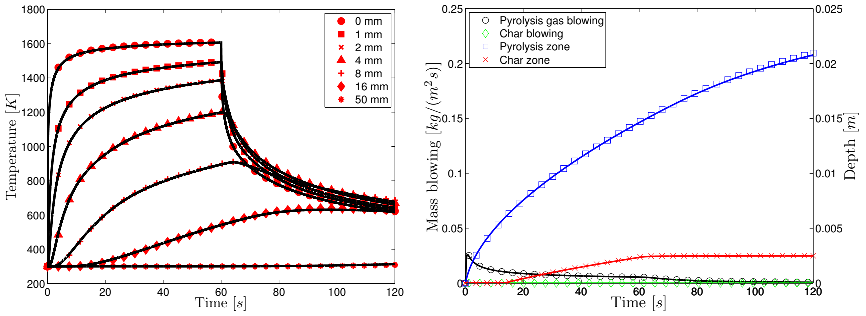

(a) Temperature field for TACOT (b) Mass blowing rate and char-virgin zones

Figure 6.9: In-depth thermal response of TACOT to a convective boundary condition without recession (test case 2.1): comparison with PATO results (solid lines) [122]. The symbols are results obtained with Echion.

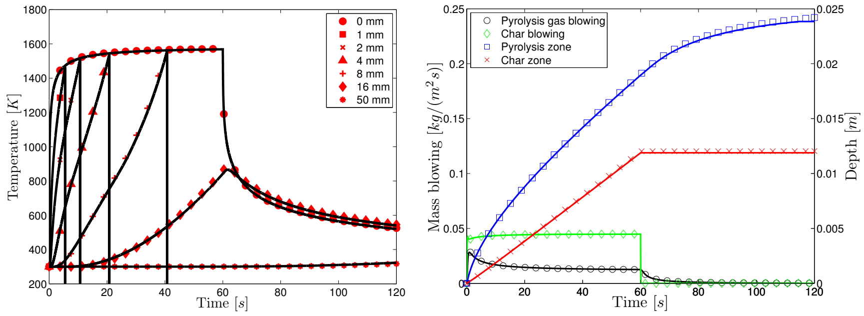

(a) Temperature field for TACOT (b) Mass blowing rate and char-virgin zones

Figure 6.10: In-depth thermal response of TACOT to a high enthalpy convective boundary condition with recession (test case 2.2): comparison with PATO results (solid lines) [122]. The symbols are results obtained with Echion.

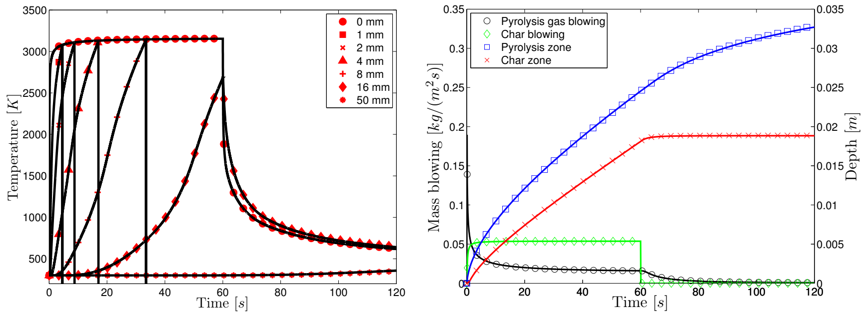

(a) Temperature field for TACOT (b) Mass blowing rate and char-virgin zones

Figure 6.11: In-depth thermal response of TACOT to a high enthalpy convective boundary condition with recession (test case 2.3): comparison with PATO results (solid lines)[122]. The symbols are results obtained with Echion.

6.4.4 Validation

The rebuilding of the experiments conducted by Helber in the VKI Plasmatron [99] is considered as a suitable test to validate the physical model equations and the implemented algorithms. The Plasmatron facility creates a high-enthalpy, highly dissociated subsonic gas flow which can be used to reproduce aero-thermodynamic environment of re-entry plasma flows [31]. The experimental test conditions of Helber [99], used as input for the computation, are summarized in Table 6.1. The free-stream conditions for the simulations were obtained from the test measurements through the standard procedure used at the VKI to rebuild the boundary-layer edge conditions by means of the VKI Rebuilding code [12]. The tables with the B' values (see Section 6.2.4) are generated using Mutation++ [205]. The mixture used to generate the B′ table is composed of 11 air species (e^-, N, N^+, O, O^+, NO, N_2, N_2^+, O_2, O_2^+, NO^+), the solid carbon, and ablation products (CO, $CO2$, CN). Sublimation of the solid carbon is neglected considering the range of temperature. The hemispherical sample of 2.5 $[cm]$ radius was made of Calcarb, a short fibers carbon preform [149] with a nominal density of 180 kg/m^3. In this case, since the material is only composed of carbon fibers, it does not decompose by pyrolysis. During the Plasmatron experiments, data on surface quantities are provided by a two-color pyrometer (surface temperature) and by a high speed camera (recession).

Table 6.1: Plasmatron test conditions [99].

Test ID	Working gas	Cold wall heat flux MW/m^2	Pressure Pa	Duration s
P1	air	1.5	1500	90
P5	air	3.0	1500	30

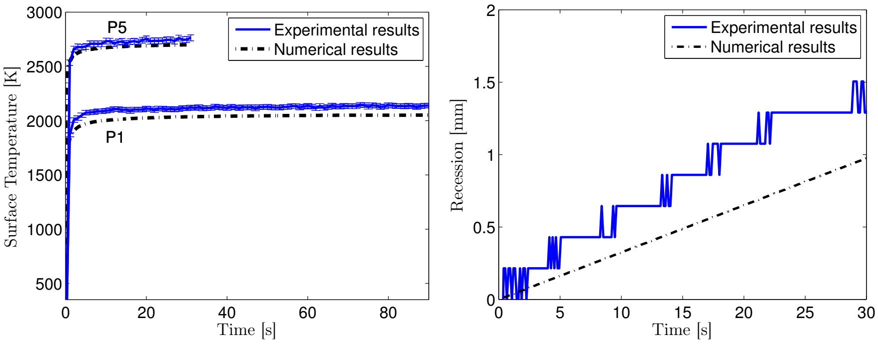

(a) Surface temperature (b) Total recession

Figure 6.12: Comparison between experimental data, material code only solution, CFD only solution and explicit coupling.

Figures 6.12 shows the comparison between experimental data and numerical results using the one dimensional DG code. The surface temperature predicted by the 1D numerical tool underestimates the temperature measured experimentally. This difference in the surface temperature for both tests might be explained by the uncertainty of some parameters such as the emissivity or the catalicity at the wall. This will be further investigated in the next chapter. The computation of the recession rate under-estimates the value measured experimentally. This can be directly linked to the computation of the B' tables and shows the limits of such transfer coefficients approach in this case. Additional experimental data, such as thermocouples measurements, would be useful in the future to compare the in-depth temperature profile.

6.5 Conclusions

The development of a one-dimensional numerical tool to solve in-depth thermal response has demonstrated the implementation challenges and the capability of a discontinuous Galerkin method to simulate this type of problem. The splitting of the equation, the use of super time stepping and implicit schemes have proved to be efficient and robust. The code has been verified on several test cases and the reproduction of an experiment has shown the limits of the model implemented. The code can be loosely coupled to a CFD solver to remove the hypothesis made at the ablative wall. This will be presented in Chapter 7.

CHAPTER 7

LOOSELY COUPLED APPROACH

This chapter is an extended version of the proceeding done for the NASA Ames summer program [194]. The chapter presents a loosely coupled approach to simulate the material response of a high enthalpy flow. It describes the coupling procedure between the material code presented in Chapter 6 and a CFD solver. This chapter investigates also the rebuilding of a Plasmatron experiment. The coupling work was done in close collaboration with A. Turchi during the NASA summer program 2014. The author would like to thank especially N. Mansour for hosting him at NASA during summer 2014 as well as the FNRS for the travel funds.

7.1 Introduction

As explained in the literature review conducted in Chapter 1, the macroscopic modeling of a TPS response to a high enthalpy environment can be divided in four main categories that are recalled here for convenience; i) flow solver approach using ablative boundary conditions; ii) material response code using simplified boundary conditions; iii) loose coupling procedure using a material and a flow solver; iv) strong coupling procedure where both material and flow are solved together. When solving the flow and the material, the coupling can be performed by using two distinct solvers designed to compute the solid and the gas-side of the problem [27, 50] (weak coupling) or by directly developing a unified numerical tool capable of computing the flow through the material accounting also for in-depth ablation of the material fibers (strong coupling). The integrated approach (also referred as fully coupled approach) has been investigated in Chapters 2, 4 and 5. The advantages of developing the last methodology have been demonstrated but a weak coupling procedure can also present some benefits. Indeed, separating the solution of the material and the flow allows for a more efficient development for each part of the problem; for example taking advantages of the different time scale for the problem.

This chapter shows the development of two coupling procedures and the investigation of a validation test case. The loosely coupled approach is based on two separate solvers. The first tool is the material response code developed within this thesis and described in Chapter 6. The second code is a CFD tool using a quasi one dimensional approach to solve the steady state of the flow along the stagnation line. The flow solver has been developed first by Munafò [158] and extended by Turchi [225].

7.2 Loose coupled approach

7.2.1 Numerical tools

The stagnation line code is a pseudo one dimensional code developed originally at the von Karman Institute by Munafò [158]. The solver has been extended by Turchi [225] to treat ablative wall boundary conditions. The development state of this tool allows for CFD steady-state simulations of the flow along the stagnation-line of a pyrolyzing carbon-based material. The boundary conditions account for the injection of both the products of the heterogeneous surface reaction (ablation) and the in-depth material decomposition (pyrolysis). As for the one dimensional code described in Chapter 6, the stagnation line code is a stand alone tool with simplified boundary conditions at the gas-material interface. The model is based on the following hypotheses:

- the interaction between the material and the impinging flow takes place only on the surface (no volumetric ablation);
- surface mass and energy balances are applied to compute the mass blowing rate and the material surface temperature;
- the steady-state ablation approximation is considered to approximate the conductive heat flux through the TPS in order to close the surface energy balance.
- the steady-state ablation approximation allows the evaluation of the pyrolysis mass flow rate as a fixed portion of the mass blowing rate (i.e., at steady state the recession of the surface and that of the char line proceed at the same speed, so the char layer thickness is a constant value);
- the pyrolysis gas has a pre-fixed elemental composition and it is injected in equilibrium at the actual surface condition (pressure and temperature).

The surface balances over the pyrolyzing ablative material are as follows:

$$\left(\rho_i\, u\right)_w + \left(\rho_i\, u_i^d\right)_w = \dot{\omega}_{i_w} + \dot{\omega}_{i_g}, \tag{7.1}$$

$$\underbrace{\lambda_w \left.\frac{\partial T}{\partial r}\right|_w - \sum_i^{N_s} \left(h_i\, \rho_i\, u_i^d\right)_w}_{q_{conv}} + \dot{m}_c\,(h_c - h_w) + \dot{m}_g\,(h_g - h_w)$$

$$- \underbrace{\sigma \xi_w \left(T_w^4 - T_\infty^4\right)}_{q_{rad}} = q_{cond}, \qquad (7.2)$$

where the subscripts g, c, and w indicate the terms that belong to the pyrolysis gas, the char material and the gas-surface interface, respectively. Equation (7.1) is the species surface mass balance ($i = 1, N_s$). This mass balance is equivalent to the one described in Chapter 6 and Fig. 6.2 represents a sketch of it. In Eq. (7.1), the species convective flux ($\rho_i\, u$) due to the non-zero surface velocity is caused by the material recession that injects mass in the system (blowing). The other terms are the diffusive flux generated by the concentration gradient ($\rho_i\, u_i^d$), the source term due to all the surface reactions involving the i^{th} species ($\dot{\omega}_{i_w} = \sum_i^{N_r} \dot{\omega}_{i_w}^r$) and the pyrolysis gas injection ($\dot{\omega}_{i_g}$).

In the surface energy balance, Eq. (7.2), q_{conv} is the convective heat flux, q_{cond} is the solid heat conduction in the material, h is the enthalpy, and the last term of the left hand side is the radiative heat flux. Note that the radiative heat flux accounts only for the re-radiation from the hot surface. Again the sketch of the energy balance is shown in Chapter 6 (see Fig. 6.3). To close the surface balances the computation of the surface source terms due to the heterogeneous surface reactions have to be computed ($\dot{m}_c$). The stagnation line code uses a finite rate chemistry model to compute the heterogeneous production terms. Data from Park [173] are used and the considered reactions are the following: two oxidation reactions ($\mathrm{C_s} + \mathrm{O} \rightarrow \mathrm{CO}$, and $2\mathrm{C_s} + \mathrm{O_2} \rightarrow 2\mathrm{CO}$), one nitridation reaction ($\mathrm{C_s} + \mathrm{N} \rightarrow \mathrm{CN}$), and one sublimation reaction ($3\mathrm{C_s} \rightarrow \mathrm{C_3}$).

7.2.2 Coupling procedures

The transfer coefficient approach described in Chapter 6 is the most used approach to compute the material transient heating in the absence of more accurate boundary conditions computed by a CFD solver. Similarly, when running the stagnation-line code alone, one has to assume simplifying hypotheses and consider the heat conduction through material to be at steady state in order to close the surface energy balance (Eq. (7.2)). Using both tools together, the approximations needed in these two decoupled approaches can be eliminated. The solution computed by the stagnation-line code can be used to feed the material boundary conditions and vice versa.

Several techniques have already been proposed to couple the solution of the flow field and the material response. These are usually distinguished in two categories depending on whether or not the solid and the fluid side of the problem are solved simultaneously. The integrated approach presented in Chapter 2 is part of the first category. In these methods, the transients of both the flow field and the material are solved by marching together in time. With this type of approach, the different time scales of the solid- and fluid-phase phenomena will force the material time steps to be smaller than effectively needed. In the loosely coupled approach, two separate tools can be used independently to solve the two sides of the problem and the exchange of the boundary information can be performed only at defined time steps. Typically, thanks to the difference in the time scales, the CFD solver is run to compute a steady-state solution, whereas the material solver performs a transient simulation to track the evolution of the temperature field inside the solid phase. The loose coupling approach is more flexible than the integrated approach and it is largely used in the open literature [49, 5]. Throughout the years, several implementation choices have been presented. The difference in between loose coupling strategies, lies in the parameters that are exchanged between the codes and in the coupling algorithm definition. A handler script, responsible for running the two codes and ensuring the data exchange between them, has been conceived and implemented. Details on the coupling algorithm are given in the following.

Explicit Coupling

The technique proposed by Chen and Gökçen in [49] was chosen for its ease of implementation considering the discretization scheme of each code. The total test time is divided in a serie of macro time steps and the general logic that applies to each of these steps is as follows:

1. the material code solves the transient simulation during a defined macro time step;
2. the temperature of the wall and the total recession are given to the stagnation line code which updates the CFD domain size and computes the steady state solution for these conditions;
3. the computed convective heat flux and mass blowing rate are exchanged with the material code for the next step.

In short, the mass balance, Eq. (7.1), is solved by the CFD solver while the energy balance, Eq. (7.2), is solved by the material code at every internal time step. Figure 7.1 summarizes the different steps. In such a coupling algorithm, each macro time advancement is performed through a full material-code simulation that is run assuming a constant convective heat flux and mass blowing rate. The boundary conditions of the material code are therefore assigned piecewise constantly over time. The first material code simulation is the only exception in this procedure and it is run assuming cold wall conditions and no ablation. Obviously, attention should be paid in the definition of these macro time steps in order to avoid the onset of instabilities in the procedure.

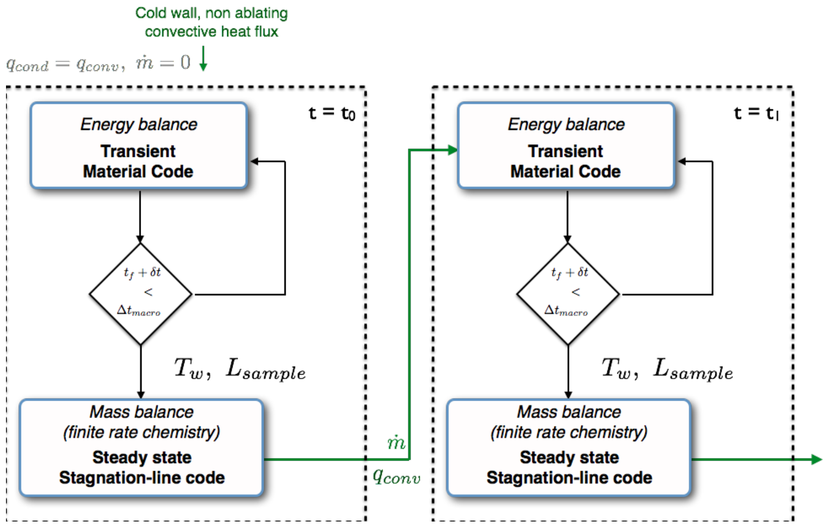

Figure 7.1: Explicit coupling strategy.

Implicit Coupling

A natural evolution of the previous approach is to upgrade the piecewise constant boundary values exchange between the two codes to a piecewise linear one. This approach follows the idea of Chen and Gökçen [50] to improve the standard explicit coupling. The information-passing sequence and the exchanged parameters are unaltered with respect to the previous algorithm, but a loop is added to account for a time varying convective heat flux. At each macro time step, the stagnation-line code is run a first time to compute the initial guess of mass blowing rate and convective heat flux (as it is done in the explicit coupling). Then, instead of directly using these values as boundary conditions for the next macro time step, they are linearly interpolated with those computed at the end of the previous macro time step. The time varying boundary condition is assigned to the current material simulation. After, the new computed wall temperature is compared with the previous guess and the loop is repeated until convergence is reached. This convergence criterium is defined such as the temperature difference between two subsequent iterations is less than a predefined value (see Fig. 7.2). This technique should improve the accuracy and the stability of the coupled simulation for a defined set of macro time steps, in particular when dealing with time-varying free stream conditions (e.g., full trajectory calculation).

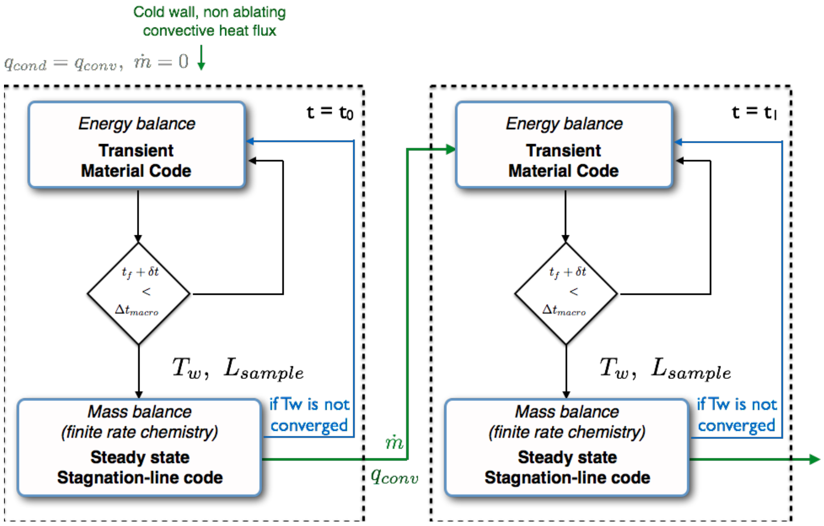

Figure 7.2: Implicit coupling strategy.

7.3 Rebuilding of Plasmatron experiments

The replication of an experiment conducted by Helber [99] in the VKI Plasmatron is considered. The test conditions are identical to the one proposed in Chapter 6 and summarized in Table 6.1.

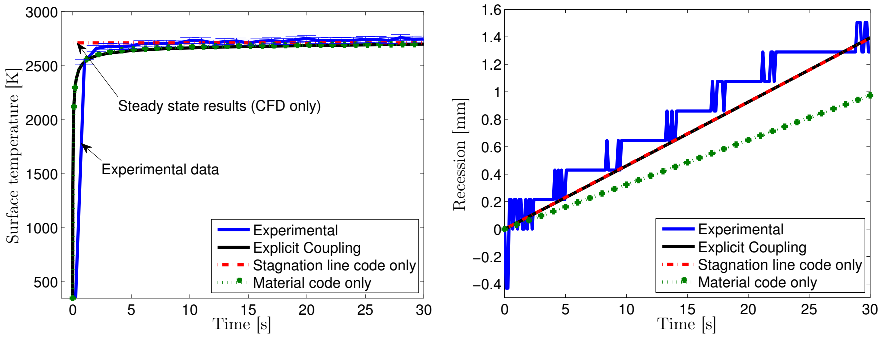

(a) Surface temperature (b) Total recession

Figure 7.3: Comparison between experimental data, material code only solution, CFD only solution and explicit coupling.

Test P5 is used as the baseline test case. Figure 7.3 shows the comparison between the three different methods to rebuild the experiment: using the CFD code only, using the material code only, or performing the explicit coupling. The two transient solutions were computed either by using only the material code with the transfer coefficient approach or running a coupled

CFD/material simulation. The steady-state solution was obtained by using the lone stagnation-line code with the steady-state ablation approximation. As seen, the wall temperature evolution computed by the material code using the transfer coefficient approach agrees well with that obtained using the coupled strategy. In Fig. 7.3(b), the total recession computed by the material code alone differs from the other two, which are closer to experimental data. Also, it is worth noting that, for this particular test case, the stagnation line code alone gives already satisfactory results. However, the critical drawback of this approach is that the transient or the material in-depth temperature field are not captured.

7.3.1 Comparison between explicit and implicit coupling

The test case presented in Section 7.3 is used to compare the explicit and implicit schemes. Figure 7.4 shows the difference between the two schemes in terms of wall temperature and temperature field inside the material. The advantages of the implicit scheme in terms of accuracy are negligible in this case. The two simulations show a difference of 4 K on the wall temperature at the end of the transient. As a matter of fact, the piecewise linear boundary condition assigned to the material code did not improve the solution obtained with the computationally cheaper explicit approach. However, it is worth noting that the free-stream conditions of the Plasmatron test are constant over the test duration. Therefore, the perfect agreement between the two coupling strategy cannot be considered more than a direct consequence of the test conditions. As a proof of that, when applying the implicit coupling algorithm, two steady-state CFD simulations were always sufficient to satisfy the chosen convergence criteria of 5 K difference between two subsequent iterations. With this in mind, only the cheaper explicit coupling is used for the following sensitivity analysis. It is proposed in the perspectives of this work to run other tests with pyrolysing materials. The unsteady effects for pyrolysing material can help showing the need for a coupling strategy.

7.3.2 Sensitivity analysis

The differences observed in Fig. 7.3 between the numerical results and the experimental data might be explained by the uncertainty on several parameters. Within this section, the effect of four different material properties are investigated. The first two are in depth properties: thermal conductivity and density. The last two influence mostly the surface energy and mass balance: emissivity and catalycity. Their influence on the wall temperature, total recession, and temperature field within the material is studied.

Thermal Conductivity

Thermal conductivity has a strong impact on the heat transfer through the solid material in the transient phase. This, together with its objectively difficult characterization due to the complex porous structure of light ablators,

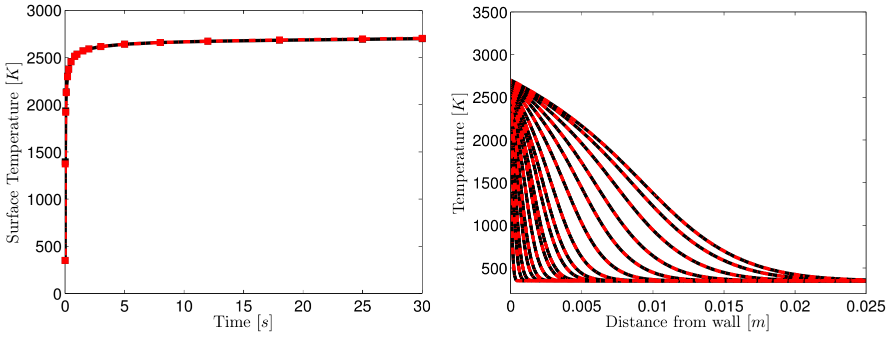

(a) Surface temperature (b) Temperature field for different time

Figure 7.4: Comparison between implicit (dashed) and explicit (solid) coupling. The internal temperature is shown for increasing time in second {0.01, 0.05, 0.1, 0.2, 0.3, 0.5, 0.8, 1.0, 1.5, 3.0, 5.0, 8.0, 12.0, 18.0, 25.0, 30.0} corresponding to the exchange time in between the two codes.

justifies it as an interesting uncertainty to investigate in the sensitivity analysis. The thermal conductivity provided by the manufacturer of Calcarb [149] varies by a factor of two, depending on the type of measurements (laser diffusivity measurement or hot plate technique). Moreover, the range of temperature given is not sufficient to cover the experimental temperature range for the Plasmatron experiment and required data to be extrapolated in the baseline analysis. A simulation using TACOT conductivity is run to investigate the effect of this parameter on the final results. The evolution of the different thermal conductivities with respect to the temperature is shown in in Fig. 7.5. The influence on wall temperature, recession and in-depth thermal response

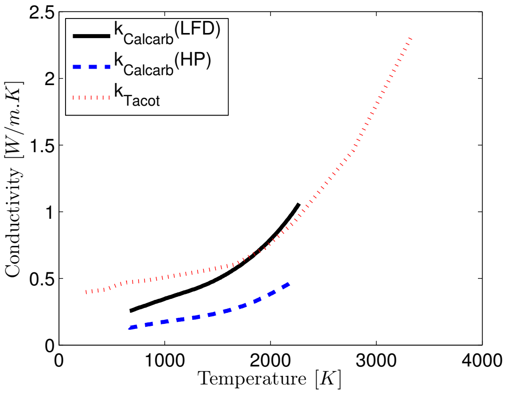

Figure 7.5: Thermal conductivity with respect to temperature. Measured data [149] (two different measurement techniques) and charred TACOT thermal conductivity from [122] are compared.

are shown in Figs. 7.6-7.7. As expected, the conductivity influences mainly the temperature field inside the material without really impacting the surface quantities. It is worth reminding that, theoretically, the thermal conductivity value can have an impact on the surface values during the transient, however the strong heating rate of the present test case seems to nullify this effect. In the future, it would be interesting to have thermocouple data inside the material to compare with the computed temperature field as well as analyzing test cases with less steep heating rates.

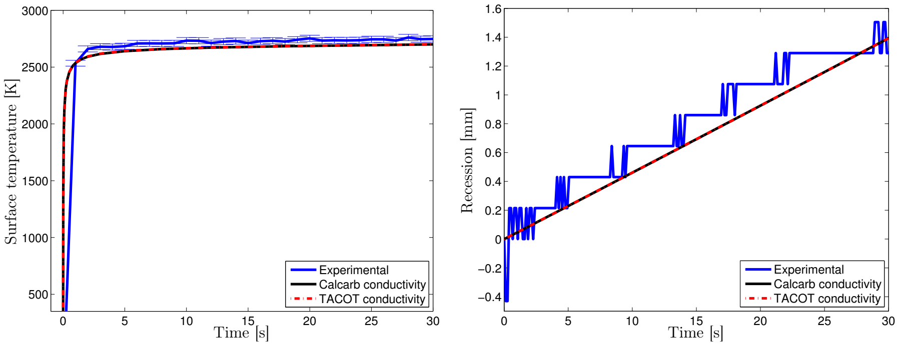

(a) Surface temperature

(b) Total recession

Figure 7.6: Surface temperature and total recession for different thermal conductivities.

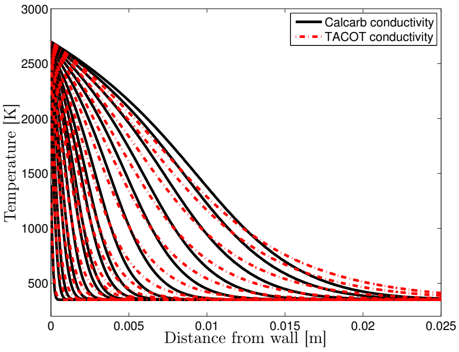

Figure 7.7: Temperature field for different time. Solid lines are the reference results, dashed lines are the results with different conductivity.

Density

The nominal density of the material, as reported in the manufacturer brochure [149], is $180\,\mathrm{kg/m^3}$. However, analysis performed at the VKI by Helber [99] showed substantial variations of this material characteristic for the analyzed samples. The material density has a strong impact on the quantities of interest of the present analysis mainly for two reasons. First, the ablative boundary condition of the stagnation-line code returns the value of the mass blowing rate that has to be "post processed" by the material code, using the material density, to compute the surface recession rate. Secondly, the density has a direct impact on the thermal diffusivity of the material, which affects the in-depth temperature field development. According to Helber [99] a density value of $215\,\mathrm{kg/m^3}$ was chosen for the sensitivity analysis. Figures 7.8-7.9 show the impact of this property on both the surface quantities and the internal temperature field. As shown, the wall temperature is not dependent on this parameter; however, the recession is directly related to the density for the reason explained above. The change in the thermal diffusivity affects the temperature field inside the material by delaying its heating. Interestingly, the effect of the density, through the thermal diffusivity, looks qualitatively different than the effect of the thermal conductivity shown in Fig. 7.7. The latter appears as a modification of the conductive heat flux because of the induced slope change of the temperature profile, whereas the former really looks like a delay in the thermal wave evolution represented by a shift in the temperature profiles.

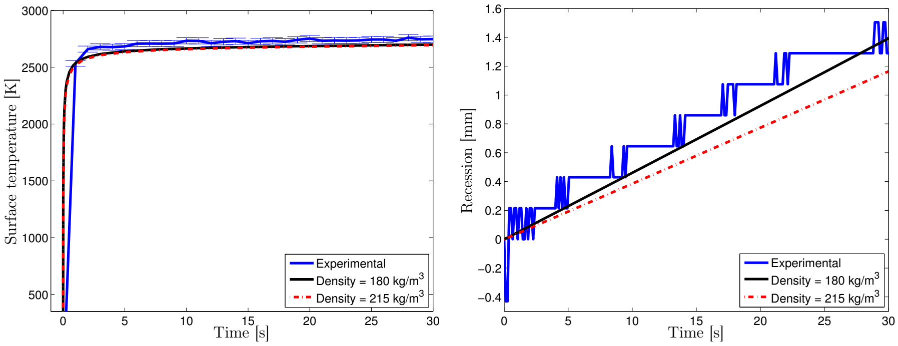

(a) Surface temperature (b) Recession

Figure 7.8: Surface temperature and total recession for different material densities.

Emissivity

An important parameter in Eq. (6.14) is the integral emissivity of the surface. This parameter is necessary to compute the heat lost by the surface because of the re-radiation towards the surrounding environment. A single value, independent on the surface temperature, is considered in the model. In the baseline analysis, Section 7.3, the value of $\xi = 0.86$ was used. This value,

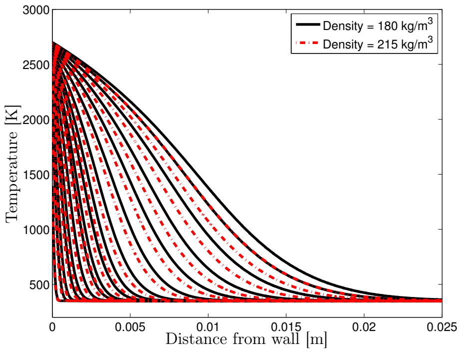

Figure 7.9: Temperature field for different time. Solid lines are the reference results, dashed lines are the results with different density.

given by Helber [99] for the material under investigation, was obtained by combining the independent emissivity measurement of the surface temperature, made through the two-color pyrometer, with an additional temperature measurement performed using an infrared radiometer. However, in Ref. [99] a non-negligible spread in the computed emissivity values is shown for the material with values down to 0.8. Furthermore, other studies pointed out that the roughness of the surface generated and enhanced by ablation will strongly affect the emissivity measurement [231]. Although very low values were measured in Ref. [231] for surface with different polishing levels, it is believed that for the high surface temperature range of the present test and the rough surface of the test specimen, the measured range 0.80-0.86 can be considered the most probable for the emissivity. Therefore, an additional emissivity of 0.8 is tested and Fig. 7.10 and 7.11 show the surface quantities and the in-depth temperature field, respectively. The effect of the reduced emissivity is evident in the surface quantities. The emissivity value of 0.8 causes a slight increase in the surface temperature giving excellent agreement with the experimental data and a negligible variation in the recession. Note that experimental results presented in [194] were not calibrated properly showing a significant difference with numerical results even with a reduced emissivity.

Catalytic Reactions at the Surface

When dealing with ablative materials, the heterogeneous reactions produce the mass loss that has been extensively analyzed throughout the present work. However, when a non-equilibrium mixture impinges on a surface, ablative or not, heterogeneous atomic recombinations can take place because of the catalyzing effect of surface active sites. Although these surface reactions are normally neglected when ablative surface are considered, there is no evidence that they cannot take place. Driver et al. [73] tested a range of catalytic recombination efficiencies with values as high as 0.5 to match arc-jet data. Moreover, values different than zero for the recombination probability of atomic nitrogen are included in the most updated gas-surface interaction models [50]. A reac-

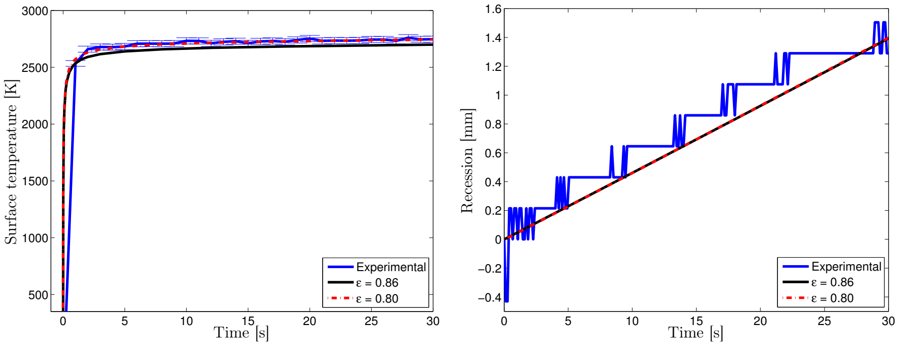

(a) Surface temperature (b) Total recession

Figure 7.10: Surface temperature and total recession for different emissivities.

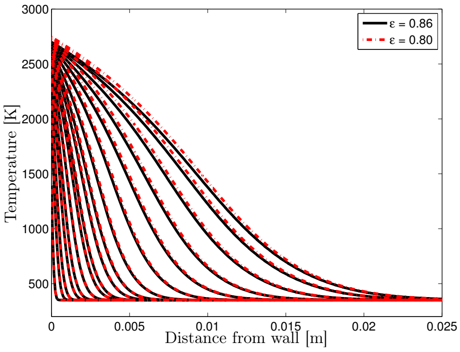

Figure 7.11: Temperature field for different time. Solid lines are the reference results, dashed lines are the results with different emissivities.

tion probability value of 0.05 was selected for the present analysis. Figure 7.12 shows the influence of the enabled surface catalycity on the surface temperature and recession rate. The exothermic process implies a rise of the surface temperature which over predicts the experimental profile. Despite the temperature rise of around 200 K, the surface recession is only slightly increased as a consequence of the diffusion-limited regime of the surface oxidation in the present condition. This small increase in the recession gives a better agreement with the measured one. Figure 7.13 shows the in-depth temperature field. The higher surface temperature produces a sensible change in the internal temperature profile. However, the differences seem to reduce more in depth and the obtained back-wall temperature are still comparable. In previous study [194], the catalicity was flagged to be the most sensible parameter to match experimental data. Using the calibrated data, the emissivity plays a more important role but the sensitivity of catalicity shows that this parameter deserves further investigation.

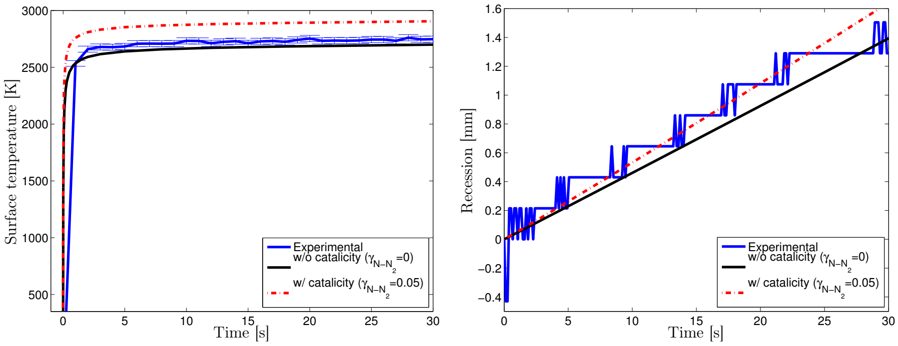

(a) Surface temperature (b) Total recession

Figure 7.12: Surface temperature and total recession for different catalycities.

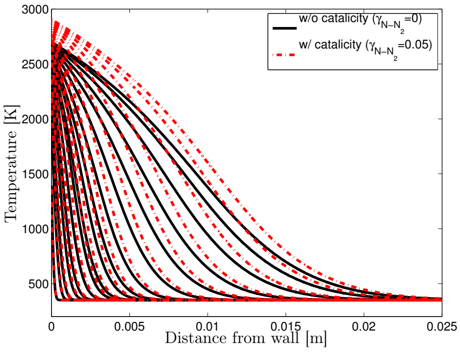

Figure 7.13: Temperature field for different time. Solid lines are the reference results, dashed lines are the results with catalicity.

7.4 Conclusions

The computation of the transient behavior of ablative thermal protections when exposed to reentry-like conditions by coupling two separate tools was completed. These solve the flow and the material side of the problem respectively and have been coupled together by means of a boundary value information passing procedure. Particular attention was paid in the selection of the best coupling algorithm, and two different procedures have been selected and implemented. The selected validation test case was the rebuilding of Plasmatron experiments performed at the von Karman Institute. The computations have shown the advantages of using a coupled approach to reproduce such experiments. Among the two analyzed coupling procedures, the explicit coupling has proven to be more efficient for the analyzed cases, while conserving the same accuracy of the more complex implicit coupling. A sensitivity analysis on the most probable uncertain parameters of the model was also performed. The sensitivity analysis highlight two surface characteristic parameters to be the most influent on quantity of interest such as the wall temperature, the recession, and the in-depth temperature distribution. The first of these parameters, the surface integral emissivity of the material, has shown to have a strong impact on the wall temperature if lower values are considered. It gives very good agreement with experimental data. In addition, the surface catalytic efficiency has shown a non-negligible influence on the wall temperature and the recession rate. Additional experimental data, such as thermocouples measurements, would be useful in the future to identify and quantify the exact role of these parameters. Rebuilding of other plasma wind tunnel test cases would help in both rigorously validating the coupled tools and seeing the expected advantages of the implicit coupling.

CHAPTER 8

CONCLUSIONS AND PERSPECTIVES

8.1 Achievements

The present work constitutes, with some recent publications [145, 64], one of the first methods capable of solving the complex response of an ablative material and the flow field through and around the TPS in a strongly coupled approach. The methodology is based on the volume averaging theory applied to the reactive Navier-Stokes equations. This leads to a single set of conservation laws valid in the entire domain. The material porosity is itself a variable smoothed on the grid during initialization and then computed to track the evolution of the reactive porous medium. The classical Navier-Stokes equations are extended to treat several species as well as non-calorically perfect gases. The thermochemical and transport properties are obtained either through a simplified treatment implemented in an internal library or through a coupling with Mutation^{++}[205]. The code accounts for homogeneous reactions in the flow and heterogeneous reactions within the low density porous material by adequate source terms. Figure 8.1 summarizes the methodology followed in this work by showing the ablation of a carbon preform slab by air.

The integrated numerical tool is based on a multi-physics platform, Argo, in which a separate module has been developed to treat this kind of problem. The Argo solver is based on a high order discontinuous Galerkin discretization which combines the advantages of finite volume and finite element methods. The implementation of new Riemann solvers gives the opportunity to treat low Mach number flows which are typical of the applications targeted in this work. In addition, a fully implicit solver allows to deal with the stiff source terms introduced in particular by the chemical reactions and the pres-

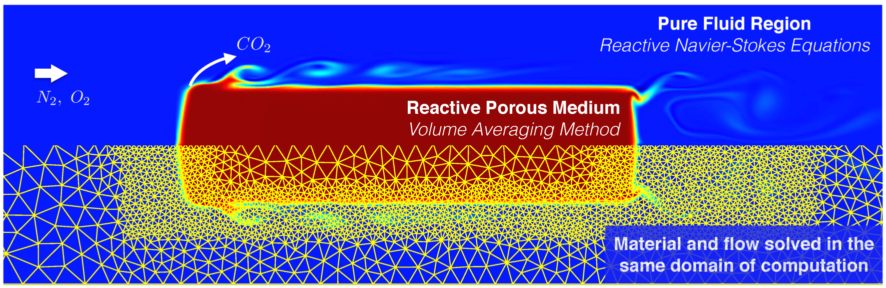

Figure 8.1: Ablation of a carbon perform slab by an air flow at Re = 200, and description of the approach developed.

ence of a porous medium. No particular treatment is required to track the position of the fluid/material interface. The initial high gradient of porosity is regularized on the mesh. The evolution of the porosity can then be used to determine a posteriori the position of this interface. The Argo platform has been proved to be highly flexible and robust to implement complex conservation laws.

The various verification test cases have demonstrated the ability of the code and the approach proposed to handle multicomponent reactive flows, non-calorically perfect gases and the presence of a reactive porous medium. The existing approaches which decouple the solution in the fluid region and in the material are limitative as they simulate the complex gas-solid interactions along an interface. These limitations are waived using the unified description. The fully coupled methodology allows for example to account for volume ablation which can be important for low density ablative material depending on flow conditions. The competition between the surface and volume ablation phenomena has been studied in details with the Argo code by replicating an experiment conducted in the NASA sidearm facility. The numerical results have proved the need for more microstructure information and more adequate models for the ablation of carbon fibers. Indeed, the numerical results computed with the cylindrical model proposed by Lachaud et al. [120] have shown discrepancies with the experimental data in the surface and volume ablation balance at these experimental conditions. A simplified model has been proposed to treat the fibers oxidation in event of pitting, for which the existing models were shown to be inappropriate. The sinusoidal model which treats the formation of holes at the micro-scale level has shown better agreement with experimental results. It is a first step in the right direction to investigate the competition between surface and volume ablation.

The development of a one dimensional thermal response code (Echion) for a pyrolysing material using a discontinuous Galerkin scheme is the first step towards improving the model fidelity of the multidimensional module. The 1D tool has shown very good agreement with state-of-the-art codes for a series of test cases, demonstrating the capability of a discontinuous Galerkin method to simulate this problem. In addition, the investigation of interface capturing techniques using Echion have highlighted the complexity of implementing a sharp interface method within Argo and oriented the choice of a diffuse approach to treat the solid-gas interface. Finally, the coupling of Echion with the stagnation line code developed at VKI has shown the challenges and benefits of developing a loosely coupled approach. The validation of the weak coupling procedure was done by the replication of an experiment conducted in the VKI plasmatron. The sensitivity analysis conducted with the loosely coupled tools has shown the main important parameters to be measured in order to compare numerical and experimental results. The weak coupling offers a fast approach in order to increase the model fidelity in the interface region without the complexity of developing a fully coupled approach.

The set of tools developed in this work allows to clearly identify the main influencing physical parameters to study in order to predict accurately the thermal response of an ablative material. In particular, the unified approach developed has demonstrated the importance of computing the specific surface of the fibers and its evolution in order to predict volume ablation in highly diffusive regime.

8.2 Perspectives

The fully integrated numerical approach can be considered as a first brick to better characterize the interactions between the flow and the ablative material. The code has been used mainly to study the volume ablation phenomenon for carbon preform materials. Other gas-surface interactions or different types of material can be studied with the unified tool. This section briefly reviews the main prospects of this work. We describe the improvements on the modeling and numerical aspects that are required to enhance the predictive capability of the code and to increase the range of applications that can be studied. First, we present the perspectives to improve the high fidelity models used to simulate the thermal response of low density ablative material. Then, we review several other applications which can be investigated with the developed numerical tool provided some implementations.

The use of the integrated tool together with the development of new models for fiber oxidation has lead to good predictive capabilities in the reproduction of the experiments conducted in NASA sidearm facility. The lessons learnt from the numerical replications demonstrated the need for additional experimental data to correctly model the oxidation of carbon fibers. Some suggestions are provided here to increase the fidelity of the models implemented.

First, tomography and SEM images of oxidized carbon fibers in several regimes [169] can be used to feed or improve the sinusoidal model developed (e.g. geometric data on the size and distribution of the pits on a fiber). The computation of the specific surface for the porous matrices at different degradation stages using tomography data can be compared with the value predicted by the models developed to correct these. The numerical results in this work suggest that this evolution will be different depending on flow conditions. Therefore, it is proposed to compare the change of the specific surface measured using micro-tomography for several flow regimes. For example, as suggested in Chapter 5, the replication of the plug experiment at several pressure conditions could help investigating the pressure effect on the competition between surface and volume ablation. The current implementation implies the choice of the fiber oxidation model (cylindrical or sinusoidal) beforehand. For now, the two models are tested and compared with experimental data to study the most appropriate to be used but no guidelines are provided for specific conditions. If experimental data at different conditions are available, simulations using Argo can be performed to study the limits of each model and to give recommendations on which is the most appropriate.

Secondly, uncertainty quantification is proposed to account for example on the stochastic effects of the porous material. The propagation of the uncertainties on material parameters would help assess the predictive capability of such a tool. Furthermore, this work already provides the key parameters (specific surface, intrinsic reactivity, permeability, surface emissivity, solid density) to be investigated first.

The unified tool has mainly been used to reproduce experiments conducted in the NASA sidearm facility. The experimental conditions are at relatively low temperatures and low velocities and the geometry of the test cases is rather simple (ring or plug in a tube). It is proposed to investigate the ablation of carbon preform in other test conditions. In particular, we suggest to simulate Plasmatron test cases such as presented in Chapter 6 and 7 with the integrated tool. Figure 8.2 shows preliminary results using Argo for the ablation of a carbon preform sphere in conditions similar to the Plasmatron. The effect on the streamlines of the blowing of char material in the boundary layer can clearly be observed. The solution of the strongly coupled approach could then be compared with other numerical strategies (flow solver with ablative boundary conditions, material code, loose coupling). This could help identifying conditions and material properties for which an accurate reproduction of the flow/material interaction is needed to match numerical predictions with experimental measurements.

The 2D numerical code is not yet able to account for the thermal degradation (pyrolysis) of the ablative thermal protection material. Implementing the presence of multiple solid species will enable the code to track the decomposition of phenol content for PICA-like material. To simulate pyrolysing material, the model proposed by Lachaud et al. [117] can be used. In this model, the fibers are protected by the presence of several solid species which protect the carbon fibers. Once these layers depleted, the fibers will start to react with the flow as described in Chapter 2. In terms of implementation, it implies to add several solid equations and correct the computation of the

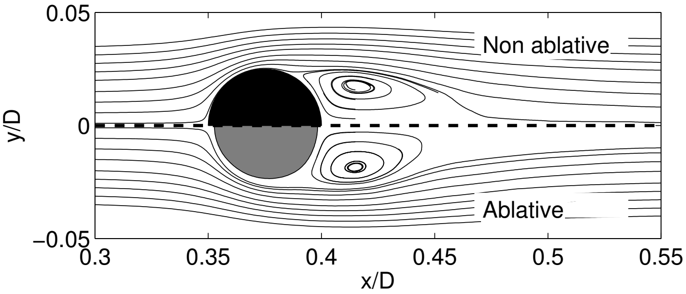

Figure 8.2: Streamlines of the flow past a porous non-ablative sphere (on top) and ablative sphere (below).

medium properties (porosity, conduction, tortuosity, etc). The test cases proposed to validate the one dimensional code and the comparison with the latter is a good start to verify such implementation. A code featuring this model together with the strongly coupled approach will be, to the author's knowledge, the first strongly coupled tool able to treat the flow and a pyrolysing material in the same domain of computation.

Finally, as explained in the introduction, the transition from laminar to turbulent flow can be triggered by the ablation process. This strong dynamic interaction between a turbulent eroding flow and an eroded surface can -in theory- be investigated using the approach developed. The study of ablation under different flow regime has been studied experimentally by Vignoles [229]. Its numerical reproduction can be investigated to study if the same erosion pattern can be observed. The computational cost of this simulation can be extremely high if one wants to capture roughness details on the surface of the ablative material in 3D. The work of Cabrit et al. [37], Velghe [228] and Crocker and Dubief [63] can be used as references to start studying this dynamic interaction between turbulence and erosion. In addition, the complex interaction between turbulence and reactive flows is a topic in itself and requires a lot of efforts to accurately model the effects of small turbulent scales on reactions [177]. Finally, one should review the hypotheses made on the development of the VANS equations if the flow inside the porous medium becomes turbulent [34].

Several numerical improvements are also proposed as perspectives of this work. First, a strong effort should be dedicated to enhance the computational performances of solving multi-species reactive flows. The computational cost associated to solving many species considerably reduces the numerical test cases which can be simulated. Obviously, increasing the number of species adds considerably more DOF $N_{elem} \times N_{nodes}$ but, also, enhances the complexity of the linear system to solve. The investigation of efficient parallel implementation has to be considered in order to simulate test cases with a large number of species and fine meshes. As suggested in Chapter 3, a splitting method to treat the reactions terms can also help decreasing the CPU time.

Another direction to investigate is to find a proper preconditioning of the matrix to enhance the convergence of the solution for the linear system at each time step. Finally, the solution of the Newton-Raphson algorithm can also be helped by the derivation of an analytical Jacobian for the convective fluxes. Colonia et al. [60] have shown a factor two in the computational time by developing an analytical Jacobian for the single component AUSM^+up scheme.

The numerical tool developed here is not yet able to deal with shocks; therefore, the simulation of supersonic and hypersonic test cases cannot be reproduced. A separate PhD thesis has been dedicated to deal with shock capturing technique in high order methods (research conducted by Verheylewegen at Cenaero). The method is based on the artificial viscosity and adds dissipation close to discontinuous regions in order to capture the shock without spurious oscillations. Figure 8.3 shows the supersonic flow around a cylinder with the shock capturing method. The extension of this approach to the multi-component reactive flows will enable the simulation of the whole problem including the shock. A large variety of test cases simulating hypersonic flows with ablative materials can be found in the literature to compare with the extended approach (see for example [51, 6, 154, 138]).

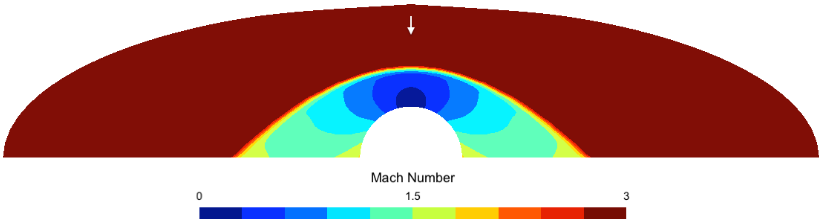

Figure 8.3: Inviscid supersonic flow of N_2 around a cylinder ($Ma = 3$). The numerical results are obtained using the artificial viscosity approach implemented in Argo by Verheylewegen and Cagnone.

Finally, the implementation of the approach developed in this work inside the Argo platform, opens avenues for other types of applications which can be simulated using this software. First, the variable thermodynamic and transport properties allows to account for non-calorically perfect gases which can be important for some applications. The internal library developed was already used by Cagnone [38] inside the *DGFluid* module of Argo. The treatment of multi-species flows and chemical reactions has shown that it is possible to use DGM for this type of applications. It is, for example, a first step to simulate combustion problems with Argo. In addition, the presence of a (reactive) porous medium is frequent in industrial or environmental applications. Among these, one can cite the erosion of the soil by a river flow, the wind over a forest canopy but also the design of a biomass reactor which has a behavior similar to that of a TPS. Another interesting application is the study of meteor ablation during atmospheric entry for which Dias et al. [71] propose to use the Argo code as a basis to investigate this problem. Finally, the treatment of the moving boundary can be useful for other types of application such as the erosion of airfoils in turbo machinery. Obviously, some of these applications constitute long term perspectives of this work; nevertheless, this thesis has paved the way in several of the challenges posed by these problems to the simulation framework of Argo.

APPENDIX A

JACOBIAN MATRICES

The time integration chosen is based on a fully implicit solver for which a Newton-Raphson algorithm has to be solved at every time step. The Jacobians of the system of equations with respect to the variables have to be derived to ensure convergence of the NR algorithm. This section shows the development of the Jacobians for the convective and diffusive fluxes. First, it can be observed that the non-linear dependence of the internal energy with respect to the temperature implies that deriving the energy with respect to the temperature is trivial while the inverse does not exist analytically. In addition, the presence of the temperature and the pressure in the Navier-Stokes equations makes the use of primitive variables very attractive. Therefore, the change from primitive ($\mathbf{Q} = \{P_i,\ \mathbf{u},\ T\}$) to conservative ($\mathbf{U} = \{\rho_i,\ \rho\mathbf{u},\ \rho E\}$) should be defined. It is written considering the perfect gas law and the definition of total energy

$$P_i = \frac{\rho_i R T}{W_i},\ \forall\, i \in 1, N_s \tag{A.1}$$

$$\rho E = \rho e + \frac{1}{2}\rho(\mathbf{u}^2). \tag{A.2}$$

where N_s is the number of species and $\mathbf{u}$ is the velocity vector which size depends on the dimension of the problem. The conversion matrix can be written

$$\frac{\partial \mathbf{U}}{\partial \mathbf{Q}} = \begin{pmatrix} \dfrac{\partial \rho_i}{\partial P_j} & 0 & \dfrac{\partial \rho_i}{\partial T} \\ \\ \dfrac{\partial \rho \mathbf{u}}{\partial P_j} & \dfrac{\partial \rho \mathbf{u}}{\partial \mathbf{u}} & \dfrac{\partial \rho \mathbf{u}}{\partial T} \\ \\ \dfrac{\partial \rho E}{\partial P_j} & \dfrac{\partial \rho E}{\partial \mathbf{u}} & \dfrac{\partial \rho E}{\partial T} \end{pmatrix}, \tag{A.3}$$

with the terms

$$\frac{\partial \rho_i}{\partial P_j} = \delta_{ij}\frac{W_i}{RT}, \tag{A.4}$$

$$\frac{\partial \rho_i}{\partial T} = -\frac{P_i W_i}{RT^2}, \tag{A.5}$$

$$\frac{\partial \rho \mathbf{u}}{\partial P_j} = \frac{W_j}{RT}\mathbf{u}, \tag{A.6}$$

$$\frac{\partial \rho \mathbf{u}}{\partial \mathbf{u}} = \sum_{i=1}^{N_s} \frac{P_i W_i}{RT}, \tag{A.7}$$

$$\frac{\partial \rho \mathbf{u}}{\partial T} = \sum_{i=1}^{N_s} -\frac{P_i W_i}{RT^2}\mathbf{u}, \tag{A.8}$$

$$\frac{\partial \rho E}{\partial P_j} = \frac{W_j}{RT}e_j(T) + \frac{W_j}{RT}\frac{\mathbf{u}^2}{2}, \tag{A.9}$$

$$\frac{\partial \rho E}{\partial \mathbf{u}} = \sum_{i=1}^{N_s} \frac{P_i W_i}{RT}\mathbf{u}, \tag{A.10}$$

$$\frac{\partial \rho E}{\partial T} = \sum_{i=1}^{N_s} \frac{P_i W_i}{RT}\frac{de_i(T)}{dT} + \sum_{i=1}^{N_s} -\frac{P_i W_i}{RT^2}\left(e_i(T) + \frac{\mathbf{u}^2}{2}\right). \tag{A.11}$$

For the derivation of the Jacobians for convective and diffusive fluxes, the expressions are given without limiting the general scope for one-dimensional cases. The extension to multi-dimensions is direct from the following expressions. The inviscid flux F^c and diffusive fluxes F^d are written as

$$\mathbf{F}^c = \begin{pmatrix} \rho_i u \\ \rho u u + P \\ \rho H u \end{pmatrix} \tag{A.12}$$

$$\mathbf{F}^d = \begin{pmatrix} D_{i,m} W_i \dfrac{P}{RT}\nabla X_i - Y_i \sum_{k=1}^{Ns} D_{k,m}\frac{W_k}{W}\dfrac{P}{RT}\nabla X_k \\ \\ \mu \tau^{\mu} \\ \\ (\mu \tau^{\mu}) \cdot u + \lambda \nabla T - \rho \sum_{i=1}^{Ns} h_i Y_i V_i \end{pmatrix} \tag{A.13}$$

where $\tau^{\mu} = \big((\nabla u + \nabla u^t) - \frac{2}{3}\nabla \cdot uI\big)$ and the diffusion flux is

$$J_i \;=\; \rho Y_i V_i \;=\; -\,D_{i,m} W_i \frac{P}{RT} \nabla X_i. \tag{A.14}$$

The Jacobians of Eq. (A.12) and (A.13) are derived in Eq. (A.16) and (A.17). The implementation inside the Argo code has been verified against a finite difference method. Note that the expression for the Jacobian of the mass diffusive flux in Eq. (A.17) is given without the Ramshaw correction which can be easily derived since it is the weighted sum of the J_i. In the Jacobian of the diffusive flux, the derivative of the species diffusion flux is given as

$$\frac{\partial J_i}{\partial \mathbf{Q}} = \begin{pmatrix} -\dfrac{\partial D_{i,m}}{\partial P_j} \left(\dfrac{W_i}{RT}\right) \dfrac{P \nabla P_k - P_k \nabla P}{P} + D_{i,m} \dfrac{W_i}{RT} \left(\dfrac{\delta_{i,j} P \nabla P - P_i \nabla P}{P^2}\right) \\ 0 \\ \left(-\dfrac{\partial D_{i,m}}{\partial T} \dfrac{PW_i}{RT} + D_{i,m} \dfrac{PW_i}{RT^2}\right) \nabla X_i \end{pmatrix} \tag{A.15}$$

Note that the transport properties (mass diffusivity coefficient, viscosity and conductivity) are dependent on the mixture composition and the temperature. Currently, the derivative of the transport properties is computed by finite difference. An analytical evaluation of these terms can improve both the convergence and the computational cost of the method.

$$\frac{\partial \mathbf{F}^c}{\partial \mathbf{Q}} = \begin{pmatrix} \frac{W_i u}{RT} & \frac{P_i W_i}{RT} & \frac{-P_i W_i u}{RT^2} \\ \frac{W_i}{RT} uu + 1 & \sum_{i=1}^{N_s} \frac{P_i W_i}{RT} 2u & -\sum_{i=1}^{N_s} \frac{P_i W_i}{RT^2} uu \\ u\left(\frac{W_i}{RT}\left(e_i(T) + \frac{u^2}{2}\right) + 1\right) & \rho H + u\left(u \sum_{i=1}^{N_s} \frac{P_i W_i}{RT}\right) & u\left(\sum_{i=1}^{N_s}\left(\frac{P_i W_i}{RT}\frac{de_i(T)}{dT}\right) - \sum_{i=1}^{N_s} \frac{P_i W_i}{RT^2}\left(e_i(T) + \frac{u^2}{2}\right)\right) \end{pmatrix} \tag{A.16}$$

$$\frac{\partial \mathbf{F}^d}{\partial \mathbf{Q}} = \begin{pmatrix} -\frac{\partial J_i}{\partial P_j} & 0 & -\frac{\partial J_i}{\partial T} \\ \frac{\partial \mu}{\partial P_j}\tau^{\mu} & 0 & \frac{\partial \mu}{\partial T}\tau^{\mu} \\ \left(\frac{\partial \mu}{\partial p_j}\tau^{\mu}\mathbf{u}\right) + \frac{\partial \lambda}{\partial P_j}\nabla T - \sum_{i=1}^{N_s} \frac{\partial J_i}{\partial P_j} h_i & \mu\tau^{\mu} & \left(\frac{\partial \mu}{\partial T}\tau^{\mu} u\right) + \frac{\partial \lambda}{\partial T}\nabla T - \sum_{i=1}^{N_s}\left(\frac{\partial J_i}{\partial T} h_i + \frac{dh_i}{dT} J_i\right) \end{pmatrix}, \tag{A.17}$$

APPENDIX B

SHARP INTERFACE METHODS FOR DGM

Using a one domain approach to treat the bulk flow and the ablative (porous or non-porous) material requires the numerical treatment of an immersed moving boundary problem. This appendix reviews the efforts and investigates several techniques to treat the high gradients/discontinuities at an immersed interface. The investigations have been focused on the study of one dimensional problems with concerns about extending this to multi dimensions.

To treat the moving boundary problem, two main categories of methods exist represented in Fig. B.1. On one hand, the *interface tracking* technique uses a body fitted mesh that should be updated with the solution and on the other hand an *interface capturing* method does not require the internal boundary to conform with the mesh (embedded geometry).

A body fitted mesh technique presents many limitations for multidimensional problems, since the mesh movement can seriously degrade mesh quality in cases of non-uniform material recession. Furthermore, remeshing can be time consuming and quite complex depending on the shape of the interface. Therefore, the effort focuses on *interface capturing* techniques which do not require the meshes to follow the interface. The next section reviews several methods to solve embedded geometries. A detailed investigation about a family of methods thought to be a good candidate is proposed in Section B.2. The challenges of implementing this kind of approach within a DG framework are studied.

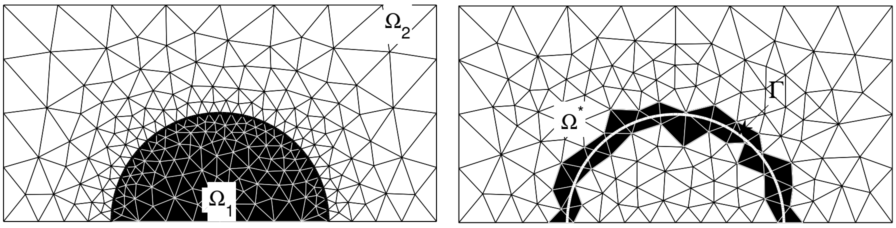

(a) Interface tracking

(b) Interface capturing

Figure B.1: Comparison between interface tracking and interface capturing techniques. The notations used throughout the text are shown.

B.1 Review of main embedded approaches

A large number of physical problems involves moving boundaries: crack propagation in solid mechanics, conduction in composite layers, fluid-structure interactions, non-miscible flows simulations, etc. The treatment of this kind of problem with unfitted grids has gathered the attention of the CFD community leading to numerous and various techniques to handle the presence of an immersed interface.

First, the representation of the embedded geometry should be tackled. The main methods are

1. **Lagrangian**: these methods use particles to explicitly track the movement of the interface and localize it. The interface is therefore discretized by the set of markers [97].
2. **Eulerian** : this approach uses the advection of a scalar to describe implicitly the position of the interface. The latter is reconstructed based on this scalar field. Volume of Fluid (VOF) [103] and level-set methods are the most popular approaches within this category [208].

Secondly, the boundary conditions at the interface can be implemented differently. Several classifications can be done on these methods and the reader is referred to the thesis of Quan [182] for an example based on whether the mathematical model, the discretization scheme or the grid is modified. However, all these techniques can be roughly divided in *diffuse* and *sharp interface* methods with respect to the numerical evaluation of the discretized equations.

1. **Diffuse techniques**, such as the *immersed boundary method* proposed by Peskin [174] or the Continuum Surface Force (CSF) model developed by Brackbill [32] , smooth the discontinuity over a transition region. Due to this regularization, the method obviously is easy to implement, but on the other hand, it implies a loss of accuracy near the surface.
2. **Sharp interface methods** modify the stencil of the numerical scheme locally, and can thereby - in theory - keep the convergence order of the

method even in the vicinity of the interface. Of the several variants in this last category, both the *immersed interface finite element (IFEM)* technique [132] and the *eXtended Finite Element Method (XFEM)* [19] were investigated.

Because of the attractive advantages of keeping the high-order convergence near the interface, sharp interface methods were first investigated to be implemented within the DG framework. This is described in the next section.

B.2 Description of two sharp interface approaches

The idea of a sharp treatment of discontinuities inside an element seemed to be very promising to conserve the high order accuracy of DGM. This section summarizes the effort undertaken to evaluate the challenges of implementing this kind of approach within DGM. In particular, the IFEM technique and the XFEM were implemented and compared in the 1D Echion code.

B.2.1 Immersed Finite Element Method

Immersed interface methods were first proposed by Li and Ito [133] for finite difference discretization and extended after for finite element schemes [132]. The IFEM technique consists in modifying the shape functions associated to the elements crossed by the interface. The solution can therefore be approximated as

$$u(x) = \sum_{i=0,\text{ if } \Omega_e \notin \Omega^*}^{p} U_i \zeta_i(x) + \sum_{i=0,\text{ if } \Omega_e \in \Omega^*}^{p} U_i \lambda_i(x), \tag{B.1}$$

where λ_i are the modified shape functions built considering the jump conditions of the solution. The set of elements (Ω_e) that are cut by the interface are noted Ω^* (see Fig. B.1). The major advantage of IFEM is that no additional unknowns are introduced. For a first order approximation, the new basis functions can be easily computed in one or two dimensions (see Fig. B.2). However, despite recent efforts conducted by Adjerid et al. [2] to extend this method to high-order approximation in 1D cases, the main drawback of IFEM remains that it seems difficult to find high-order basis functions for multidimensional problems.

B.2.2 Extended finite element Method

The extended finite element method developed by Belytschko [19] extends the basis functions and enriches the nodes disturbed by an interface.

$$u(x) = \sum_{i=0\,,\,\forall \Omega_e}^{p} U_i \zeta_i(x) + \sum_{i=0,\text{ if } \Omega_e \in \Omega^*}^{p} A_i \left(\zeta_i(x) \cdot \Psi(x) \right), \tag{B.2}$$

where $\zeta_i(x)$ are the standard shape functions and $\Psi(x)$ is the enrichment function that depends on the type of discontinuity to be represented (a priori

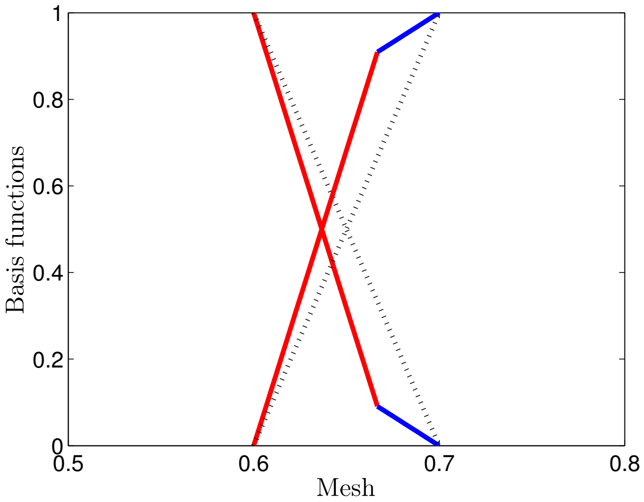

Figure B.2: Modification of the first order basis functions in IFEM to account for the discontinuity inside an element in 1D. Dashed lines are the usual first order Lagrange polynomial functions, solid lines are the modified shape functions accounting for the discontinuity.

known). The A_i are the additional unknowns to be computed. This method was proposed initially to solve crack propagation problems but was applied successfully to other problems with discontinuities such as multi-phase problems, shocks, fluid-structure interaction, etc [1, 20, 56, 87]. Readers are referred to Fries and Belytschko [82] for a comprehensive review on XFEM. The main disadvantage of this method lies in the variable number of degrees of freedom per node which may lead to important problems of implementation due to data structure changes. However, the extension to high order is simple even for multidimensional cases and therefore XFEM was coupled with the DG code to model a non-smooth solution independently of the mesh.

B.3 Challenges of sharp interface methods

Applying sharp interface approaches to DG raises different issues mainly related to the discontinuous character of this kind of methodology (enrichment strategy, numerical integration, temporal integration and extension to multidimensional problems). Although the challenges are faced by the two methods discussed (IFEM, XFEM), this section is focused on XFEM which seemed to be the most appropriate approach. The following section describes briefly these issues and how they were addressed in the one dimensional code.

B.3.1 Enrichment

The nodes and the shape functions space associated to the elements crossed by an interface need to be enriched for XFEM. The enrichment function is chosen according to the type of discontinuity to be represented and is therefore dependent on the location of the discontinuity. Usually, a level-set function is used to track the position of the interface and to build implicitly the enrichment function. The type of discontinuity to model can be categorized as weak or strong, depending on whether the solution presents a kink or a jump across the interface. A typical example of a weak discontinuity is the heat conduction through a multi-material sample with different heat diffusivity. While a heaviside or a sign function of the level-set can be chosen to represent a jump in the solution, the absolute value of the level-set is often used to model a weak discontinuity

$$\Psi_{strong} = H(\phi(x)) = \left\{ \begin{array}{ll} 0 & : \phi(x) \leq 0 \\ 1 & : \phi(x) > 0 \end{array} \right. \tag{B.3}$$

$$\Psi_{weak} = \left| \phi(x) \right|, \tag{B.4}$$

where $\phi(x)$ is the level-set function. For convenience, the solution in the enriched element can be written

$$u(x) = \sum_{i=0}^{2p+1} \bar{U}_i \bar{\zeta}_i(x), \tag{B.5}$$

where $\bar{\zeta}_i(x)$ is the enriched basis composed of $\{\zeta_i, \zeta_i \cdot \Psi\}$. To extend this to high-order, a simple strategy consists in using higher order shape functions (ζ_i). However, to ensure high order accuracy, the numerical integration must be defined carefully to account for the interface position (see discussion below). Finally, it is worth mentioning that for a classical finite element method coupled with XFEM, an element can be categorized in three sets depending whether all, none or part of its nodes are enriched. The last category is called *blending elements* which need special treatment to ensure convergence. However, in a DG framework each element is separated and therefore this avoids partial enrichment.

B.3.2 Numerical integration challenges

For a sharp interface technique, the basis functions are no longer continuous inside some elements. Therefore, the numerical integration has to be adapted to compute volume integral in the variational formulation. For a one dimensional case, the element crossed by the interface is divided in several segments where Gauss-quadrature are defined. For multidimensional cases, the shape of the interface has to be taken into account. This problem for curved interface is common for both IFEM and XFEM and several papers addressed this challenge (Cheng and Fries [55] ,Legrain et al [130]) and it will be briefly discussed when dealing with the multidimensional extension.

B.3.3 Time integration challenges

The time advancement strategy requires special consideration in XFEM [83] due to the time dependance of the enrichment function. Indeed, the Ψ function depends on the location of the discontinuity and when implementing time stepping schemes the shape functions have to be evaluated at different time levels. For a backward Euler scheme, the weak form can be written,

$$\int_\Omega u^{n+1}\bar{\zeta}^{n+1} - \int_\Omega u^n\bar{\zeta}^{n+1} = \Delta t \int_\Omega \frac{\partial}{\partial x}\left(\mu \frac{\partial u^{n+1}}{\partial x}\right)\bar{\zeta}^{n+1}, \tag{B.6}$$

where the right hand side should be discretized using the interior penalty method described in Section 3.2. According to Fries and Zilian [83] , the test and trial functions have to be chosen at the same time levels to be consistent with the nodes enriched and the associated functions. Consequently, the second term in equation (B.6) is the integral of functions at different time steps. The quadrature must consider the location of the two discontinuities to keep the convergence properties of the method. The numerical integration is therefore more complex for moving interface problems especially for multidimensional cases (see Fig. B.3).

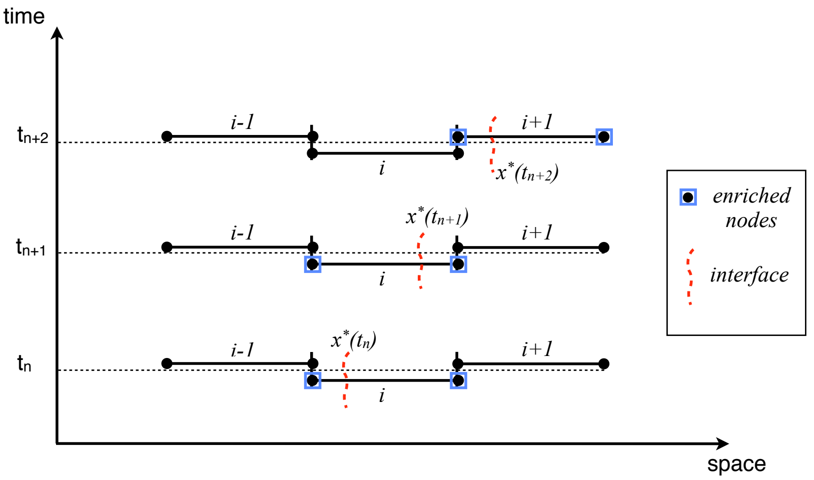

Figure B.3: Enrichment of the node belonging to the element crossed by an interface. Due to the dependance of the enrichment function to the interface location, integrands might have a double discontinuity inside one element

B.3.4 Extension to multidimensional problem

The challenges discussed previously are enhanced when dealing with multidimensional problem. Indeed, in 2D(3D) the interface is a curve(surface) and its curvature should be accounted for in the numerical integration. The challenges for the time discretization scheme are even more complex. Figure B.4

summarizes the major techniques that can be found in the literature to integrate on a 2D triangular element. Four main methods are briefly discussed: the piecewise reconstruction of the interface, the regularized method, the high order reconstruction and moment fitting method.

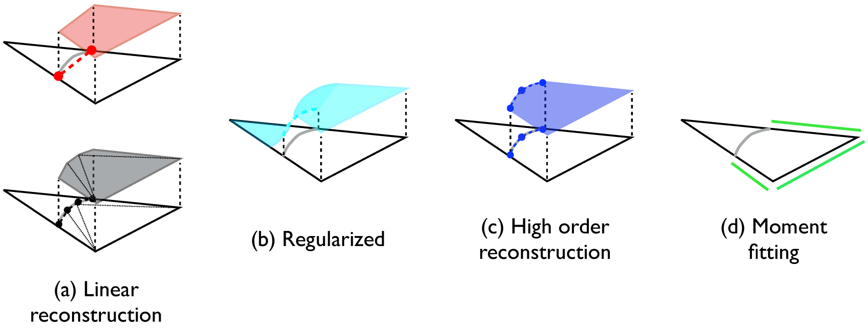
(a) Linear reconstruction
(b) Regularized
(c) High order reconstruction
(d) Moment fitting

Figure B.4: Major numerical integration techniques for a discontinuous solution on a 2D mesh. The integration on the quadrangle part is shown.

Piecewise linear approach

It is the easiest approach for which the interface is reconstructed linearly. To increase the accuracy, the element can be subdivided using tree algorithms [215] leading to a piecewise linear representation of the interface. This method is robust and easy to implement but needs the definition of a quadrature on sub-elements with refinement algorithms. In addition, at most second order convergence can be reached. Figure B.5 taken from [130] shows the description of the interface using a (piecewise) linear approximation.

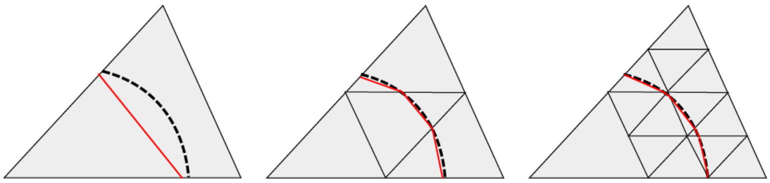

Figure B.5: Piecewise linear reconstruction of the interface. Efficient and robust tree algorithms can be developed to divide the polytope in subelements and increase the accuracy of the interface representation. Figure taken from Legrain et al. [130]

Regularized approach

The regularized approach uses the definition of a smooth function to represent the discontinuity on the interface. Figure B.6 shows an example using a Heavyside function. The value of this function is one in part of the element and zero in the other region. The regularized method uses a standard quadrature rule and is very easy to implement however, only low order convergence can be reached and the accuracy is highly dependent on the smeering region defined.

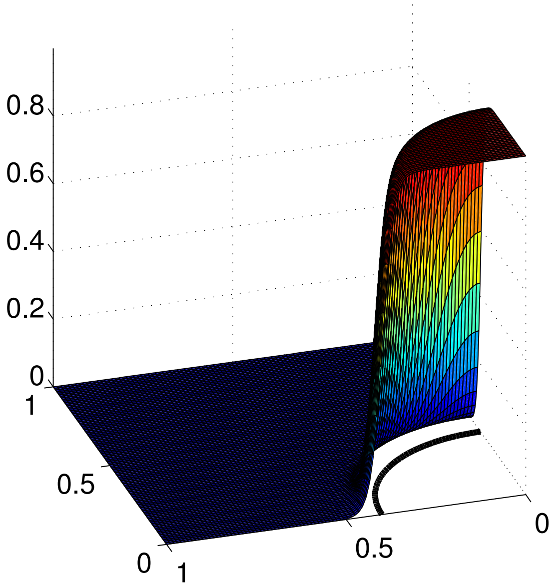

Figure B.6: Regularized approach, a color function is defined on the quadrangle element in this case. The function is zero everywhere except in the region to be integrated. A smooth transition region is defined across the interface.

High order reconstruction

In this technique (see Fig. B.4(c)) proposed by Cheng and Fries [55] , the interface is approximated by a high order polynomial function. Therefore, the element is divided, as for the piecewise linear approach, in sub-elements but in this case, the subelements are sharing a curved edge. The quadrature is defined on these degenerated sub-elements. For a triangular mesh for example, the element can always be cut in a triangle and a quadrangle with one curved edge (see Fig. B.7). A degenerated reference element with an edge of the same order as the representation of the level-set function is defined. The volume integral can therefore be computed using the projection of Gauss Legendre points on the element using the mapping defined previously. Figure B.7 shows the reference element used for the integration on the triangle and quadrangle part respectively. To define this mapping, the approach requires the knowledge of the location of the nodes on the interface and some efficient techniques proposed by Huerta et al.[106] are proposed in the literature. This high order reconstruction seems to have interesting properties regarding the accuracy and convergence of the method. However, generalizing this method to 3D requires to identify all sub-elements that appear when cutting a reference element which may become quite complex.

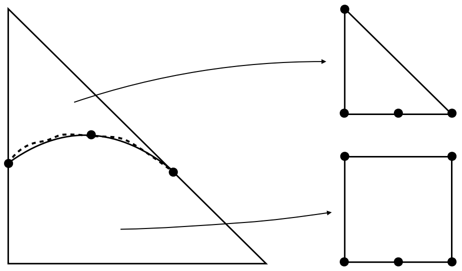

Figure B.7: High-order reconstruction for curved interface. The interface is approximated by a second order polynomial and the quadrature points are defined on degenerated reference elements.

Moment fitting

The moment fitting method is proposed by Muller [157] and keeps the same quadrature points but reevaluates the weights. In short, the method is based on the generic strategy to define quadrature rules where the system

$$\begin{pmatrix} f_1(x_1) & . \quad . \quad . & f_1(x_N) \\ . \quad . & & \\ . & \quad . & \\ . & \quad\quad . & \\ f_N(x_1) & & f_N(x_N) \end{pmatrix} \begin{pmatrix} w_1 \\ . \\ . \\ . \\ w_N \end{pmatrix} = \begin{pmatrix} \int_\Omega f_1 d\Omega \\ . \\ . \\ . \\ \int_\Omega f_N d\Omega \end{pmatrix}, \tag{B.7}$$

is solved to define the weights w_i and the nodes x_i. The method proposed by Muller [157] keeps the traditional Gauss-Legendre points x_i but redefine the weights solving Eq. (B.7) by approximating the right hand side. For an element crossed by the interface and divided in two polytopes $\mathcal{A}$ and $\mathcal{B}$, Muller has shown that the domain integral in Eq. (B.7) of a sub-element can be expressed based on the integral of the edge of this polytope if one chooses appropriate f_i. Therefore, this hierarchical approach approximates an integral of the polytope $\mathcal{A}$ by computing the integral on the edge $\partial\mathcal{A}$. This elegant methodology is very easy to implement and it can be applied to any type of element. However, this method requires the solution of a system at each time step to redefine the weights.

Comparison

The integration methods were implemented in a Matlab code and compared on a simple test case. For this test case, the surface of an embedded circle in 2D is computed using the several methods. A level-set function defines the circle boundary which does not conform with the mesh (see Fig. B.8). The convergence error on the computation of the inner area is shown in Fig. B.9 for each method. It was found that, although the technique of Cheng and Fries [55] gives the lowest errors, the convergence of the moment fitting technique was comparable. In addition, this last method is way easier to implement and the extension to 3D cases is straightforward. Therefore, this numerical integration method seems the most promising for a multidimensional implementation.

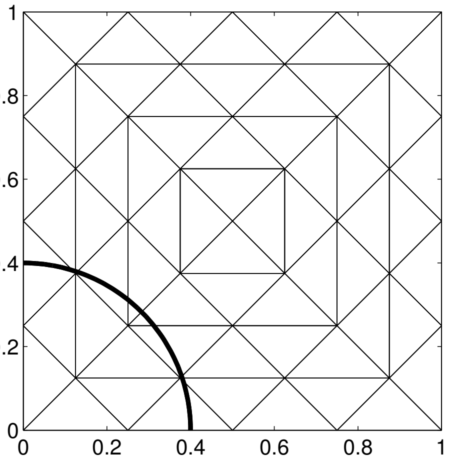

Figure B.8: Test case used to compare the accuracy of the four integration methods presented. The inner surface of a quarter of a circle is computed and compared with the exact area.

B.4 One dimensional implementation

To evaluate the challenges of implementing this kind of technique within the multidimensional tool Argo, XFEM was first implemented in the one dimensional DG code and simple test cases have proved the validity of the method. Two test cases are described. First, a non-moving interface case is used to verify the convergence order of the method. Secondly, a moving interface problem is treated and compared with a finite difference code using a regularization method.

B.4.1 Steady interface

The first test case is the diffusion of a sine function with a discontinuous diffusivity not conforming with the mesh. The stationary solution can be evaluated analytically and used as reference solution. Figure B.10(a) shows that

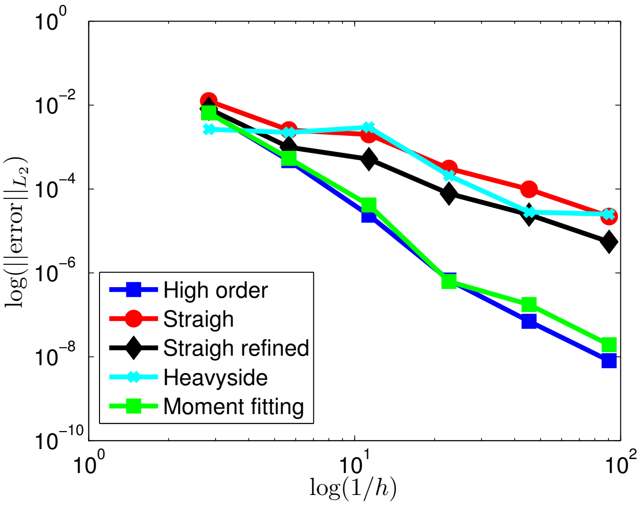

Figure B.9: Convergence of the error on the computation of a circle area. Comparison between integration techniques on a triangular multidimensional mesh.

DG solution matches the analytical expression for a diffusivity ratio of 10. The convergence analysis in the L^2 error is shown in Fig. B.10(b) for $p = 1$. The solution presents a kink (weak discontinuity), hence the absolute value of the level-set function is used to build the enrichment function. Here, the alternative proposed by Moes et al. [151] to keep the Lagrange properties of the enriched basis is implemented

$$\Psi_{weak} = \sum_i |\phi_i|\zeta_i(x) - \left|\sum_i \phi_i\zeta_i(x)\right|. \tag{B.8}$$

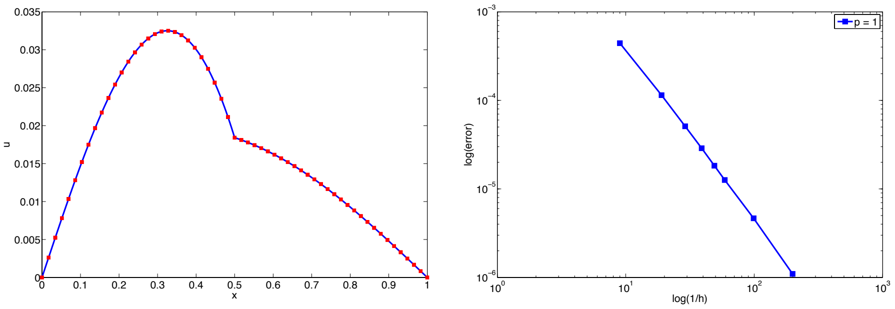

(a) Stationary solution

(b) Convergence study

Figure B.10: Diffusion of a sine function with discontinuous diffusivity at x = 0.5. The mesh is defined so it does not conform with the interface. The results of Echion are the solid lines, the analytical solution shown by the squares.

B.4.2 Moving interface

The second test case deals with a moving interface to verify the time-stepping method implemented. This example was proposed by Fries and Zilian [83] , and consists of the diffusion of a C_∞ function defined as

$$u_0(q(x)) = \begin{cases} \exp\left(5 + \frac{5}{q^2-1}\right) & \text{for } q \leq 1 \\ 0 & \text{otherwise}\,, \end{cases} \tag{B.9}$$

where $q(x) = |x - 0.5|/0.2$. The test case is run for different diffusivity ratios and different velocities of the interface. The interface position is defined by the level-set function

$$\phi(x,t) = (x_A + (x_B - x_A)t)) - x, \tag{B.10}$$

where x_A and x_B are the initial and final positions of the discontinuity. The results are compared with a finite difference code which uses a smoothing technique to represent the jump in diffusivity and a highly refined mesh to capture the discontinuity. The results for different speed and diffusivity ratio are shown in Fig. B.11.

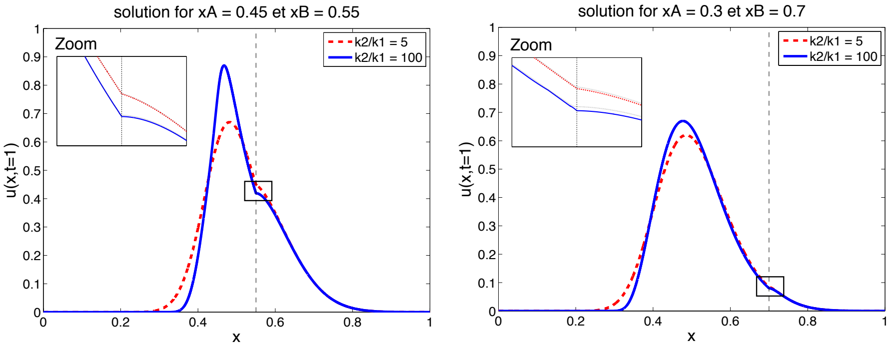

(a) Solution for $x_A = 0.45$ and $x_B = 0.55$ (b) Solution for $x_A = 0.3$ and $x_B = 0.7$

Figure B.11: Moving interface problem for different velocities and different diffusivity ratios. The solution is shown at time $t = 1$, the zoom window shows the weak discontinuity and the comparison with the finite difference solution (black lines).

B.5 Conclusion

The effort to treat a sharp interface method within the discontinuous Galerkin discretization has proved the advantages of keeping a high order convergence near a discontinuous region although it has also shown the complexity and the numerical issues regarding the implementation of this methodology inside the Argo code. In order to avoid this complexity, a diffuse interface method has finally been selected. The last approach is also more adequate with respect to the physical modeling of the transition region chosen (variable porosity/permeability).

APPENDIX C

DEVELOPMENT OF A 1D SHOCKING CODE

The 1D shocking^{++} code solves the stationary 1D Euler equations for reactive flows using a one temperature model. This section summarizes the development of such system of equations, describes the code developed and presents some verification test cases. The 1D flow solver is based on a model proposed by Magin et al. [139] modified to account for only one temperature. Assuming steady state the system can be written

$$\frac{\partial \mathbf{F}^c}{\partial x} = \mathbf{S}, \tag{C.1}$$

with **F** and **S**

$$\mathbf{F} = \begin{pmatrix} \rho_i u \\ \rho u^2 + P \\ \rho H u \end{pmatrix}, \text{ and } \mathbf{S} = \begin{pmatrix} \dot{\omega}_i^{hom} \\ 0 \\ 0 \end{pmatrix}. \tag{C.2}$$

Manipulating the system of equation, it is possible to find an equivalent system of ODE which can be easily solved. The mathematical development is shown hereafter.

C.1 Mass conservation law

The sum of all source terms is equal to zero therefore, $\dot{m} = \rho u$ is constant. The mass conservation law can be rewritten such as

$$\frac{\partial \frac{\rho_i}{\rho}}{\partial x} = \frac{\partial Y_i}{\partial x} = \frac{\omega_i^{hom}}{\rho u}. \tag{C.3}$$

C.2 Momentum conservation law

Using the perfect gas law assumption and the mass conservation law, the momentum conservation can be rewritten

$$dP = \sum_{i=1}^{N_s} \frac{Y_i}{W_i} \rho R dT + \frac{P}{\rho} d\rho + \rho R T \sum_{i=1}^{N_s}, \frac{dY_i}{W_i} \tag{C.4}$$

$$\left(\frac{\rho \boldsymbol{u}^2}{RT} - \frac{P}{RT} \right) \frac{\partial u}{\partial x} + \frac{\rho u}{T} \sum_{i=1}^{N_s} \frac{Y_i}{W_i} \frac{\partial T}{\partial x} = - \sum_{i=1}^{N_s} \frac{\omega_i^{hom}}{W_i}. \tag{C.5}$$

C.3 Energy conservation law

Doing the same tricks for the energy equation,

$$\sum_{i=1}^{N_s} Y_i c_{v,i} \frac{\partial T}{\partial x} + \sum_{i=1}^{N_s} h_i \frac{\dot{\omega}_i}{.} \rho u + u \frac{\partial u}{\partial x} \tag{C.6}$$

Isolating $\frac{\partial u}{\partial x}$ and $\frac{\partial T}{\partial x}$, the last two equations can be expressed as

$$\begin{pmatrix} a & b \\ d & e \end{pmatrix} \cdot \frac{\partial}{\partial x} \left(\begin{array}{c} u \\ T \end{array} \right) = \left(\begin{array}{c} c \\ f \end{array} \right) \tag{C.7}$$

with each terms defined as

$$\begin{array}{ccc} a = \frac{\rho u^2}{RT} - \frac{P}{RT} & b = \frac{\rho u}{T} \sum_{i=1}^{N_s} \frac{Y_i}{W_i} & c = - \sum_{i=1}^{N_s} \frac{\dot{\omega}_i^{hom}}{W_i} \\ d = \rho u^2 & e = \rho u . \left(\sum_{i=1}^{N_s} Y_i c_{v,i} \right) & f = - \sum_{i=1}^{N_s} h_i \dot{\omega}_i \end{array} \tag{C.8}$$

The system can finally be expressed as

$$\frac{\partial}{\partial x} \left(\begin{array}{c} Y_i \\ u \\ T \end{array} \right) = \left(\begin{array}{c} \frac{\dot{\omega}_i^{hom}}{\dot{m}} \\ \frac{(ec - bf)}{\det_A} \\ \frac{(af - cd)}{\det_A} \end{array} \right). \tag{C.9}$$

The shocking^{++} code is written in C^{++} and linked to Mutation^{++}. It was verified against the old shocking code developed by T.E. Magin and written in Fortran [139, 142]. It takes as input the pressure, temperature composition before the shock and the shock speed. It computes the post-shock values assuming first calorically perfect gas and then iterating to find the correct values for a non-calorically perfect gas. The chemical composition is frozen through the shock. The chemical relaxation behind the shock is computed solving the system C.9 using an existing ODE solver provided by the Boost library [1]. A variant of the shocking^{++} code also provides the values at chemical equilibrium. The relaxation is not solved anymore but an additional loop is implemented to find the post-shock values corresponding to this equilibrium. The quantities can be compared to the one obtained at the end of the relaxation.

---

[1] http://www.boost.org

C.4 Verification test cases

The test case compares the values after the relaxation for the shocking^{++} code developed, the shocking^{++} code assuming chemical equilibrium and the fortran code developed by Magin et al. [139, 142]. The chemical relaxation of air with 11 species after a typical shock during an atmospheric entry specified in Table C.1 is studied. Table C.2 shows the comparison between the three solutions, note that the history will depend on the reaction mechanism chosen hence the relaxation profile are not shown here. Since the thermochemical library in the shocking code [139] and in shocking^{++} are different, slight discrepancies can be observed.

Table C.1: Freestream shock characteristic quantities.

X [-]	P [Pa]	T [K]	v_s [m/s]
N_2/O_2	5.0	300	12300
$0.79/0.21$			

Table C.2: Temperature, pressure and velocity at the end of the chemical relaxation behind the shock. Codes comparison for shock conditions given in Table C.1.

Code	$T\ [K]$	$P\ [Pa]$	$v_s - u_e\ [m/s]$
shocking [139]	11307.8	8256.9	699.1
shocking^{++}	11303.7	8257.4	698.5
shockingEq^{++}	11303.6	8257.4	698.5

APPENDIX D

ANALYTICAL SOLUTION FOR A TWO DOMAIN APPROACH

The Beaver and Joseph problem of a fluid flow on top of a permeable wall has a steady analytical solution if we assume that the flow is fully developed. For this analytical solution, we consider a two domain approach where the domain is composed of two distinct homogeneous regions separated by a sharp interface. The equations inside the porous medium and the flow are solved separately and appropriate boundary conditions are used at the interface. In addition, we assume that the porous domain is semi-infinite. This problem is depicted in Fig. D.1.

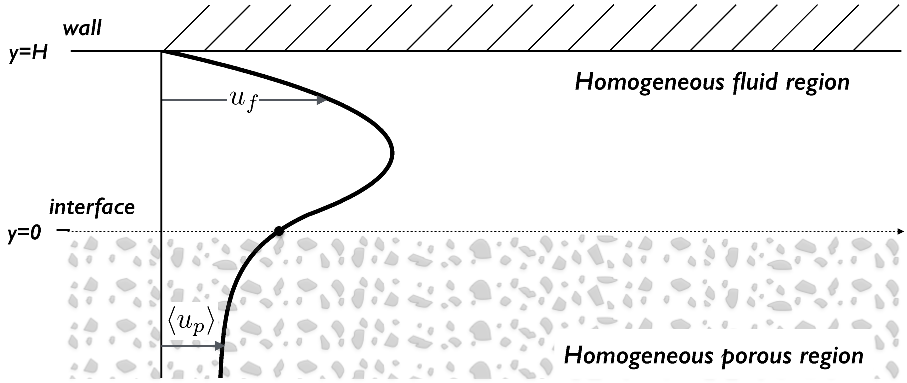

Figure D.1: Two domain approach with interface conditions to reconcile the solutions in each part.

Assuming incompressible flows, the equations for each phase are

$$0 = -\frac{1}{\rho}\frac{d\langle P\rangle_g}{dx} + \frac{\mu}{\rho}\frac{d^2\langle u_f\rangle}{dy^2}, \text{ for } y > 0, \tag{D.1}$$

$$0 = -\frac{\epsilon_g}{\rho}\frac{d\langle P\rangle_g}{dx} + \frac{\mu}{\rho}\frac{d^2\langle u_p\rangle}{dy^2} - \frac{\mu}{\rho\kappa}\epsilon_g\langle u_p\rangle, \text{ for } y < 0, \tag{D.2}$$

where $\langle u_p\rangle$ is the superficial average velocity of the gas flow in the porous medium ($\langle u_p\rangle = \epsilon_g\langle u_p\rangle_g$) and $\langle u_f\rangle$ is the superficial average in the fluid region. Note that, in the homogeneous fluid region, there is no distinction between the superficial and intrinsic average since the porosity is unity. The boundary conditions are simple, we impose a non-slip velocity on the top of the channel ($y = H$) and that the solution exists and is bounded in the porous medium ($\lim_{y\to-\infty}$). The conditions at the interface are more challenging to be specified. In this case, we are using the one proposed by Ochoa-Tapia-Whitaker [165]

$$\left.\langle u_p\rangle\right|_{y=0^-} = \left.\langle u_f\rangle\right|_{y=0^+}, \tag{D.3}$$

$$\frac{1}{\epsilon_g}\mu\left.\frac{\partial\langle u_p\rangle}{\partial x}\right|_{y=0^-} - \mu\left.\frac{\partial\langle u_f\rangle}{\partial x}\right|_{y=0^+} = \frac{\mu\beta_{OTW}}{\sqrt{\kappa}}\left.\langle u_p\rangle\right|_{y=0}. \tag{D.4}$$

The first boundary condition implies the continuity of the superficial volume averaged velocity at the interface. This implies that the intrinsic average will be discontinuous at the interface. While it is obvious for flows perpendicular through porous medium, this condition is less intuitive for parallel flows but it is justifyied by various authors [160, 94, 164]. The development of the second condition is theoretically described in details by Ochoa-Tapia and Whitaker [164] and is used by several authors [21, 62, 34, 152]. This jump condition is built on the effective shear stress. As explained in Section 2.4, the determination of the closure parameter β_{OTW} remains an open challenge. In Goyeau et al. [92], they provide a first analytical attempt to compute an expression for the jump parameter by introducing a heterogeneous continuous transition zone in the interface region. This approach is also used by Chandesris and Jamet [43]. In addition, in Ref. [43], the authors provide a rigorous development of the interface boundary conditions and a comparison between every model. The discussion on which interface conditions to use is beyond the scope of this thesis. In this appendix, we will develop the analytical solution for a general case and use the Ochoa-Tapia-Whitaker conditions. We will assume that β_{OTW} is given. It can be considered to be zero as in [21], it can be computed through direct numerical simulations as in Ref. [34], it can be fitted on experimental data [165] or an explicit relation can be used as proposed in Ref. [92, 44].

Porous medium

To solve the ordinary differential equation of second order, the particular solution is

$$\langle u_p\rangle^{\text{part}} = -\frac{\kappa}{\nu}\frac{d\mathcal{P}}{dx}, \tag{D.5}$$

where $\mathcal{P} = \frac{\langle P \rangle_g}{\rho}$ and ν is the kinematic viscosity. The homogeneous solution can be written

$$\langle u_p \rangle^{\text{hom}} = A \exp\left(\sqrt{\frac{\epsilon_g}{\kappa}} y\right) + B \exp\left(-\sqrt{\frac{\epsilon_g}{\kappa}} y\right). \tag{D.6}$$

The existence of a bounded solution in $\lim_{y \to -\infty}$ implies $B = 0$ leaving one parameter to be determined based on the interface conditions. Therefore, the solution in the porous medium is

$$\langle u_p \rangle = A \exp\left(\sqrt{\frac{\epsilon_g}{\kappa}} y\right) - \frac{\kappa}{\nu}\frac{d\mathcal{P}}{dx}. \tag{D.7}$$

Pure fluid region

Inside the pure fluid region, we integrate twice the Eq. (D.1) leading to

$$\langle u_f \rangle = \frac{1}{\nu}\frac{d\mathcal{P}}{dx}\left(\frac{y^2}{2} + by + c\right) \tag{D.8}$$

where b, c are unknowns to be determined based on the boundary and interface conditions. The non-slip velocity at the top implies that $c = -\left(\frac{H^2}{2} + bH\right)$.

Interface conditions

The solution obtain for the pure fluid region and the homogeneous porous medium is not dependent on the interface conditions chosen. To compute the unknowns A and b in Eq. (D.7) and (D.8), we need to choose two interface conditions. Here, using the one proposed in Eq. (D.3)-(D.4), we can find

$$A = \frac{1}{\nu}\frac{d\mathcal{P}}{dx}\epsilon_g\sqrt{\frac{\kappa}{\epsilon}}\left[b\left(1 - \frac{H\beta_{OTW}}{\sqrt{\kappa}}\right) - \frac{\beta_{OTW}}{\sqrt{\kappa}\frac{H^2}{2}}\right], \tag{D.9}$$

using the second interface conditions and the second parameter is determined using this result in Eq. (D.3)

$$b = \frac{\kappa - \dfrac{H^2}{2} + \sqrt{\epsilon}\beta_{OTW}\dfrac{H^2}{2}}{\epsilon\sqrt{\dfrac{\kappa}{\epsilon}}\left(1 - \dfrac{H\beta_{OTW}}{\sqrt{\kappa}}\right) + H}, \tag{D.10}$$

Non-dimensionalizing the expressions, we obtain for each region

$$\frac{\langle u_p \rangle}{-\frac{1}{\nu}\frac{d\mathcal{P}}{dx}H^2} =$$

$$Da - \epsilon_g\sqrt{\frac{Da}{\epsilon}}\left[\frac{b}{H}\left(1 - \frac{\beta_{OTW}}{\sqrt{Da}}\right) - \frac{\beta_{OTW}}{2\sqrt{Da}}\right] \exp\sqrt{\frac{\epsilon_g}{Da}}\frac{y}{H}, \tag{D.11}$$

$$\frac{\langle u_f \rangle}{-\frac{1}{\nu}\frac{d\mathcal{P}}{dx}H^2} = -\frac{1}{2}\left(\frac{y}{H}\right)^2 - \frac{b}{H}\frac{y}{H} + \left(\frac{1}{2} + \frac{b}{H}\right), \tag{D.12}$$

where $Da = \frac{\kappa}{H^2}$ is the Darcy number, and the factor b/H is written

$$\frac{b}{H} = \frac{Da - \frac{1}{2} + \frac{\sqrt{\epsilon_g}\beta_{OTW}}{2}}{\epsilon_g\sqrt{\frac{Da}{\epsilon}}\left(1 - \frac{\beta_{OTW}}{\sqrt{Da}}\right) + 1}. \tag{D.13}$$

The only parameters involved in the analytical solution are the Darcy number, the porosity and the closure parameter β_{OTW}. Figure D.2 shows the average velocity profile for several porosities and Darcy numbers considering $\beta_{OTW} = 0$. We can observe that, as discussed in Chapter 4, the permeability is the most important parameter for the velocity profile. A close-up view for several porosities at constant permeability can be observed in Fig. D.3(b) and for constant porosity with various permeability values in Fig. D.3(a). The lowest permeability ($Da = 1e^{-6}$) for Fig. D.3(b) and highest value for the porosity ($\epsilon_g = 0.8$) for Fig. D.3(a) are chosen because carbon preform samples of interest here have low permeability with high porosity. This shows that the porosity has still a small influence in the interface region but negligible with respect to the permeability parameter.

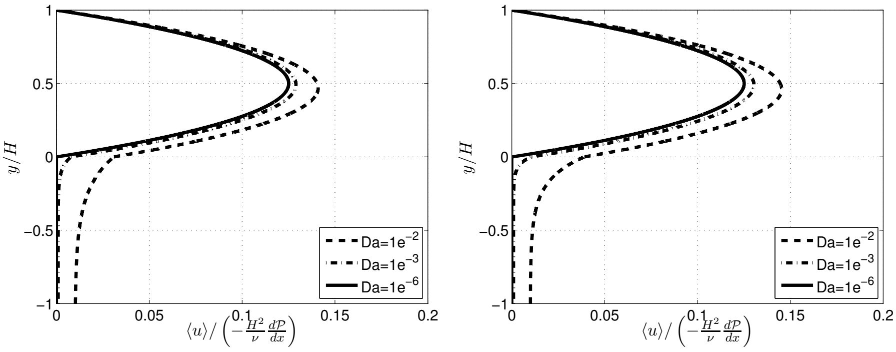

(a) $\epsilon_g = 0.2$

(b) $\epsilon_g = 0.4$

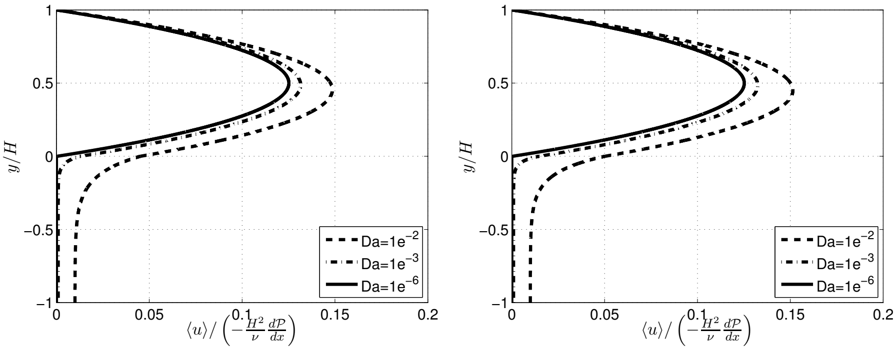

(c) $\epsilon_g = 0.6$

(d) $\epsilon_g = 0.8$

Figure D.2: Analytical solutions for a flow on top of an infinite porous medium using a two domain approach. The solutions are computed for several values of the porosity and Darcy number.

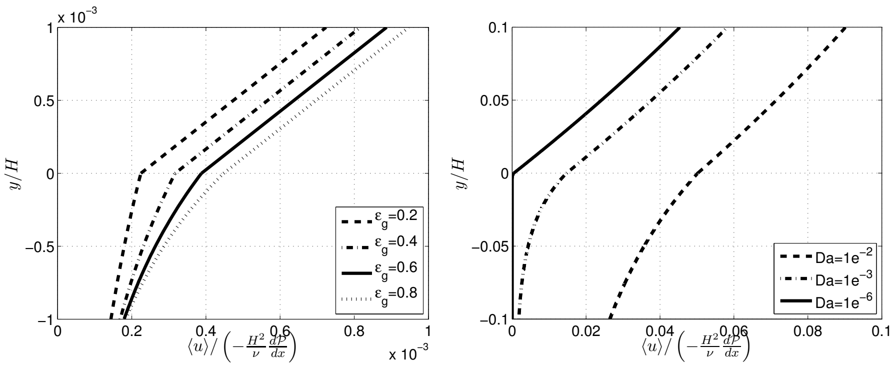

(a) Solution for constant $Da = 1e^{-6}$

(b) Solution for constant $\epsilon_g = 0.8$

Figure D.3: Close-up view in the interface region of the analytical solutions for a flow on top of an infinite porous medium using a two domain approach.

APPENDIX E

CODES COMPARISON

This appendix summarizes and compares the fidelity level of several codes. The same classification as in Ref. [118] is used and the codes are divided in three types depending on the level of fidelity used. The comparison is shown in Fig. E.1 which details the conservation laws implemented in each ablation code. The Table is a modified version of the one proposed in Lachaud et al. [118] where the two developed codes (Argo and Echion) have been added and some properties have been updated for other codes. The original version of the table proposed by Lachaud et al. [118] compare 25 codes. In this appendix, only three design codes (Amaryllis, CMA and FIAT3D) and four analysis research tools are proposed in the table. The references used to update the recent developments are given in the table. It is important to notice that most codes are still of type II and only few (PATO, CAT, NIDA) feature higher fidelity models [118]. The Argo code has been added to this list even if it is not strictly a material code. Indeed, Argo has not been used to study only the material side but nothing prevents to fill the entire domain of computation with a porous medium. As observed in the table, Argo is not yet able to treat the thermal decomposition of phenolic content. With the treatment of pyrolysis gases, Argo will be capable of simulating complex in-depth material response with the highest fidelity (type III). This is discussed in the perspectives.

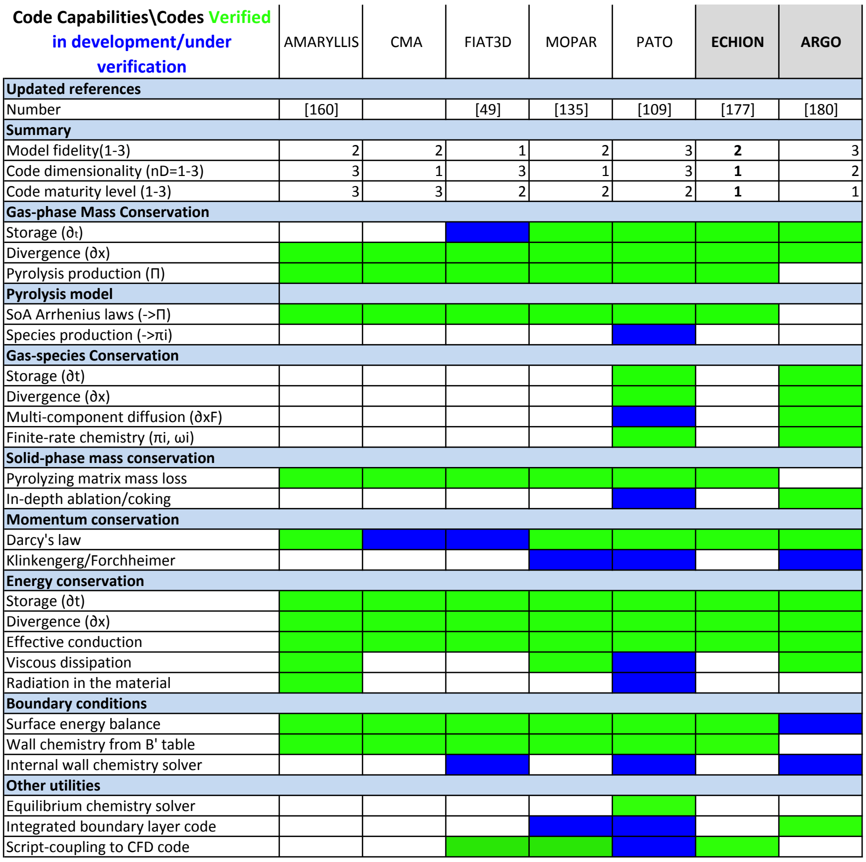

Code Capabilities\Codes Verified in development/under verification	AMARYLLIS	CMA	FIAT3D	MOPAR	PATO	**ECHION**	**ARGO**
Updated references							
Number	[160]		[49]	[135]	[109]	[177]	[180]
Summary							
Model fidelity(1-3)	2	2	1	2	3	**2**	3
Code dimensionality (nD=1-3)	3	1	3	1	3	**1**	2
Code maturity level (1-3)	3	3	2	2	2	**1**	1
Gas-phase Mass Conservation							
Storage (∂_t)			🟦	🟩	🟩	🟩	🟩
Divergence (∂x)	🟩	🟩	🟩	🟩	🟩	🟩	🟩
Pyrolysis production (Π)	🟩	🟩	🟩	🟩	🟩	🟩	
Pyrolysis model							
SoA Arrhenius laws (->Π)	🟩	🟩	🟩	🟩	🟩	🟩	
Species production (->πi)					🟦		
Gas-species Conservation							
Storage (∂t)					🟩		🟩
Divergence (∂x)					🟩		🟩
Multi-component diffusion (∂xF)					🟦		🟩
Finite-rate chemistry (πi, ωi)					🟩		🟩
Solid-phase mass conservation							
Pyrolyzing matrix mass loss	🟩	🟩	🟩	🟩	🟩	🟩	
In-depth ablation/coking					🟦		🟩
Momentum conservation							
Darcy's law	🟩	🟦	🟦	🟩	🟩	🟩	🟩
Klinkengerg/Forchheimer				🟦	🟦		🟦
Energy conservation							
Storage (∂t)	🟩	🟩	🟩	🟩	🟩	🟩	🟩
Divergence (∂x)	🟩	🟩	🟩	🟩	🟩	🟩	🟩
Effective conduction	🟩	🟩	🟩	🟩	🟩	🟩	🟩
Viscous dissipation	🟩			🟩	🟦		🟩
Radiation in the material	🟩				🟦		
Boundary conditions							
Surface energy balance	🟩	🟩	🟩	🟩	🟩	🟩	🟦
Wall chemistry from B' table	🟩	🟩	🟩	🟩	🟩	🟩	
Internal wall chemistry solver			🟦		🟦		🟦
Other utilities							
Equilibrium chemistry solver					🟩		
Integrated boundary layer code				🟦	🟦		🟩
Script-coupling to CFD code			🟩	🟩	🟦	🟩	

Figure E.1: State-of-the art material response codes with their properties and comparison with Argo and Echion. Table adapted and updated from Lachaud et al. [118]

APPENDIX F

PARK MODEL TO ACCOUNT FOR ROUGHNESS OF CARBON FIBERS

The numerical results using the cylindrical model (see Section 2.3.2) have shown that, for some cases, the competition between surface and volume ablation is not correctly predicted. In reaction limited regime, as in the flow tube experiment [170], the fibers will exhibit pitting and not accounting for it implies an underestimation of surface ablation. The hypothesis is based on the fact that eroded fibers are more reactive than virgin fibers leading to an increase of reactivity at the surface of the sample. This has lead to the development of the sinusoidal model (see Section 2.3.2). Another model based on Park [172] considerations for the roughness has been developed and is presented in this appendix.

To account for the TPS roughness of an aerospace vehicle, Park introduced the surface roughness ratio Ψ[172]. For simulation at the scale of the vehicle, the reaction rate is therefore expressed using this parameter,

$$k_{eff} = 1 - \exp\left(-k_f \Psi\right), \text{ if } k_f \; << 1. \tag{F.1}$$

If Ψ is unity, the effective reaction rate is $k_{eff} \approx k_f$ but for high surface roughness ratio, the effective reaction rate is increased. According to Park [172], the roughness can explain the large spread of experimental data for the reaction rate values of graphite ablation. At the micro scale level, the same observation holds with the fibers [95]. Therefore, instead of modifying the surface function to treat the holes as in the sinusoidal model, the effective reaction rate can be computed using Eq. (F.1). This model has the advantage of having only one parameter to be tuned. In addition, a threshold on the reaction rate is easily defined such that in diffusion limited regime where pitting phenomenon is absent, the effective reaction rate is not dependent of the surface roughness. The evolution of Ψ with respect to the porosity has to be described to model the history of the surface roughness ratio. Figure F.1 shows the three phases model proposed here, the curve is $C1$ to ensure a definite Jacobian. First the evolution of the roughness factor is described by a second order polynomial relation from the initial radius to r_1 (phase I). The value of r_1 is based on experimental observation (depth of the holes in the fibers). Then, Ψ is supposed constant (phase II) until the transition towards total depletion of the fibers (phase III).

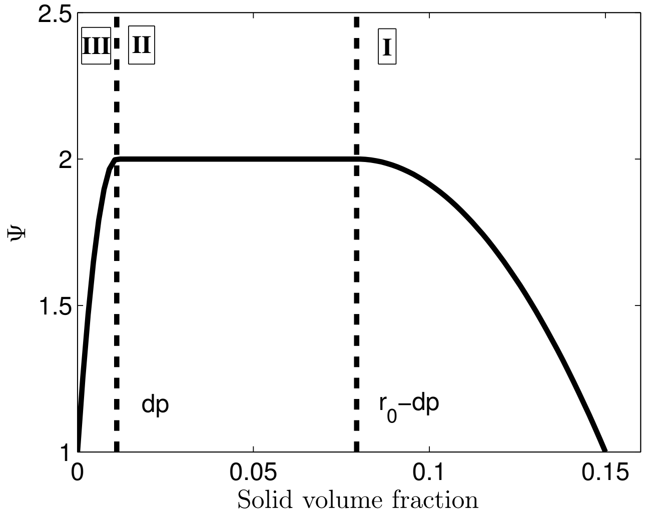

Figure F.1: Surface roughness ratio (Ψ) with respect to the solid volume fraction.

Despite some advantages of this model, the sinusoidal model was preferred because of its flexibility to account for more microstructure information. The effective reactive surface function specified in this model can be changed to account for more precise evolution of the fibers recession or geometrical information. In addition, using Park's model, the evolution of the mass loss and volume loss is strongly non-linear. This leads to difficulties to predict and optimize the correct roughness ratio to adopt.

APPENDIX G

REPLICATION OF THE RING EXPERIMENT

Preliminary runs investigated the ablation of a ring of carbon Preform inside the NASA side arm facility [171]. This appendix presents the results and the conclusions of this study. Table G.1 summarizes the experimental conditions and Table G.2 the properties used for the numerical simulations. A diagram of the side arm facility can be found in Fig. 5.3.

Table G.1: Summary of the flow tube test conditions [171].

Test ID	Temperature $[K]$	Pressure $[kPa]$	Density $[kg/m^3]$	$\dot{m}$ $[mg/s]$	Initial Solid Density $[kg/m^3]$
b2	800	10.0	0.0433737	2.19	165.6
b3	900	10.0	0.0385544	2.19	174.5
b4	1000	10.0	0.0346989	2.18	173.1
b5	1100	10.0	0.0315445	2.19	164.8
b6	1200	10.0	0.0289158	2.21	167.3

In this preliminary study on the ring experiment, only the forward heterogeneous reaction $C_{(s)} + O_2 \rightarrow CO_2$ was considered on the whole range of temperature. The reference forward reaction rate is taken from by Panerai et al. [171].

$$k_f = 0.087 \exp\left(\frac{-42400}{RT}\right). \tag{G.1}$$

Table G.2: Summary of material properties used in the numerical simulation.

Test ID	ϵ $[-]$	κ $[m^2]$	η $[-]$	Initial Fiber Radius $[\mu m]$	Emmissivity $[-]$
b	0.9	$1.367e^{-10}$	1.15	5.5	0.9

Figures G.1(a) and G.1(b) show respectively the mass loss after an hour of exposition and the evolution with time. The surface recession is compared in Fig. G.2 showing the oxidized profiles for the test in Table G.2.

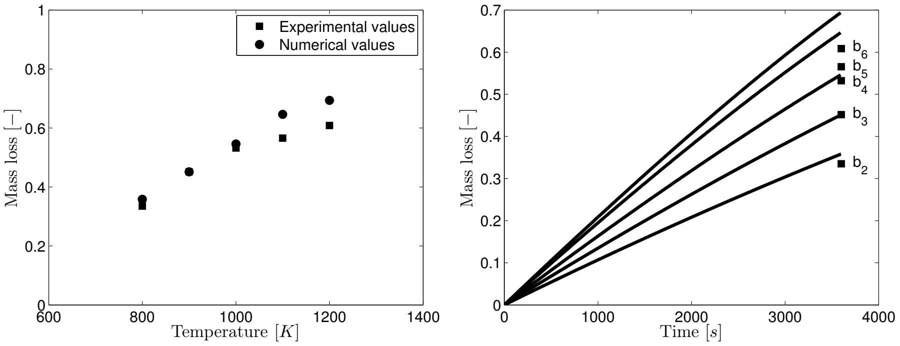

(a) Mass Loss for different temperature (b) Mass loss evolution with respect to time

Figure G.1: Mass loss for the ablation of a ring with conditions given by Table G.1 and computed with Argo and the cylindrical model.

The conclusion is the same as for the first run on the plug geometry; the mass loss is quite well predicted (especially at low temperature) but the surface recession is always underestimated. Indeed, the volume of the oxidized ring computed numerically is higher for every test temperature than the experimental one. A closer match of the ring profile can be observed at higher temperature but, in this case, the mass loss is over predicted. The conclusion of this investigation is that some surface phenomena not captured by the cylindrical model enhance the reactivity of the fibers close to the gas-porous medium interface. This has lead to the development of the sinusoidal model.

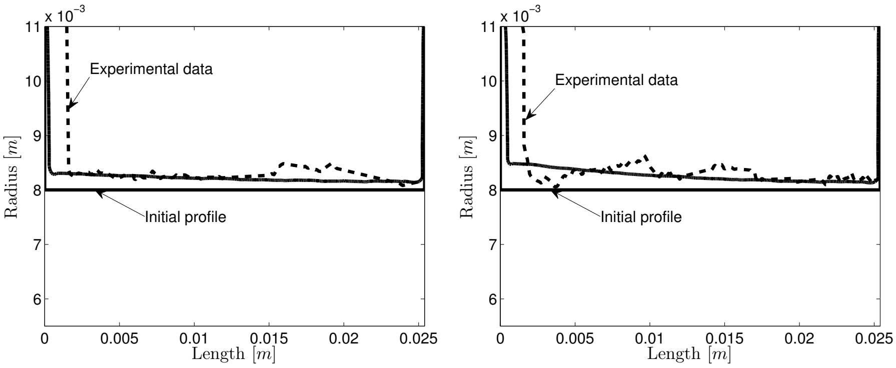

(a) b2 (b) b3

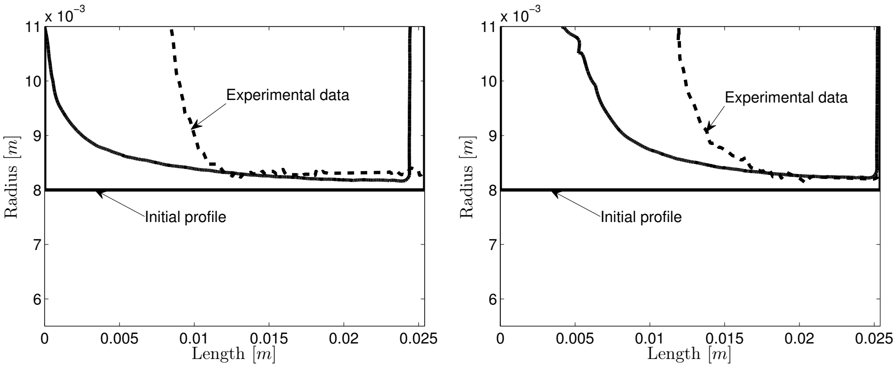

(c) b4 (d) b5

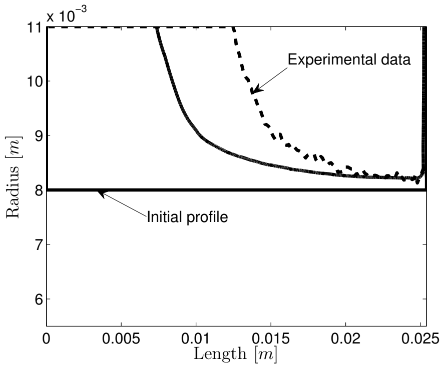

(e) b6

Figure G.2: Solid density profile of oxidized samples of carbon preform rings. Dashed lines are the experimental profiles (digitized from [171]), solid lines are the numerical results computed with Argo.

BIBLIOGRAPHY

[1] S. Abbas, A. Alizada, and T.-P. Fries. The XFEM for high gradient solutions in convection-dominated problems. *International Journal for Numerical Methods in Engineering*, 82(8):1044–1072, 2010.

[2] S. Adjerid and T. Lin. A p-th degree immersed finite element for boundary value problems with discontinuous coefficients. *Applied Numerical Mathematics*, 59(6):1303–1321, 2009.

[3] V. Alexiades, G. Amiez, and P.A. Gremaud. Super-time-stepping acceleration explicit schemes for parabolic problems. *Communications in Numerical Methods in Engineering*, 12:12–31, 1996.

[4] H. Alkandry, I.D. Boyd, and A. Martin. Comparison of models for mixture transport properties for numerical simulations of ablative heatshields. In *51st AIAA Aerospace Sciences Meeting including the New Horizons Forum and Aerospace Exposition*, number AIAA 2013-0303, Grapevine, TX, 7-10 January 2013. American Institute of Aeronautics and Astronautics.

[5] H. Alkandry, I.D. Boyd, and A. Martin. Coupled flow field simulations of charring ablators with nonequilibrium surface chemistry. In *44th AIAA Thermophysics Conference*, number AIAA 2013-2634, San Diego, CA, 24-27 June 2013. American Institute of Aeronautics and Astronautics.

[6] H. Alkandry, E.D. Farbar, and I.D. Boyd. Evaluation of finite-rate surface chemistry models for simulation of the Stardust reentry capsule. In *43rd AIAA Thermophysics Conference*, number AIAA 2012-2874, New Orleans, LA, 25-28 June 2012. American Institute of Aeronautics and Astronautics.

[7] P.D. Antoniadis. *Modeling and numerical simulation of transient flows in superposed porous and pure fluid layers*. PhD thesis, Université catholique de Louvain, 2015.

[8] P.D. Antoniadis and M.V. Papalexandris. Dynamics of shear layers at the interface of a highly porous medium and a pure fluid. *Physics of Fluids*, 27(1):1–26, 2015.

[9] D.N. Arnold, F. Brezzi, B. Cockburn, and Marini L.D. Unified analysis of discontinuous Galerkin methods for elliptic problems. *SIAM Journal Numerical Analysis*, 39(5):1749–1779, 2001.

[10] H.L. Atkins. Continued development of the discontinuous Galerkin method for computational aeroacoustic applications. In *3rd AIAA/CEAS Aeroacoustics Conference*, number AIAA 1997-1581, Atlanta, GA, 12 May 1997. American Institute of Aeronautics and Astronautics.

[11] P.F. Barbante. *Accurate and efficient modeling of high temperature nonequilibrium air flows*. PhD thesis, Université Libre de Bruxelles, 2001.

[12] P.F. Barbante and O. Chazot. Flight extrapolation of plasma wind tunnel stagnation region flowfield. *Journal of Thermophysics and Heat Transfer*, 20(3):493–499, 2006.

[13] E. P. Bartlett and R. M. Kendall. An analysis of the coupled chemically reacting boundary layer and charring ablator. Part 3 - nonsimilar solution of the multicomponent laminar boundary layer by an integral matrix method. Contractor Report CR-1062, NASA, June 1968.

[14] E. P. Bartlett, R. M. Kendall, C. B. Moyer, and R. A. Rindal. An analysis of the coupled chemically reacting boundary layer and charring ablator, Part 1 summary report. Contractor Report CR-1060, NASA, June 1968.

[15] F. Bassi and S. Rebay. A high-order accurate discontinuous finite element method for the numerical solution of the compressible Navier-Stokes equations. *Journal of Computational Physics*, 131:267–279, 1997.

[16] G.S. Beavers and D.D. Joseph. Boundary conditions at a naturally permeable wall. *Journal of Fluid Mechanics*, 30:197–207, 1967.

[17] G.S. Beavers, E.M. Sparrow, and B.A. Masha. Boundary conditions at a porous surface which bounds a fluid flow. *AIChE Journal*, 20:596–597, 1974.

[18] G. Bellas-Chatzigeorgis, P.F. Barbante, and T.E. Magin. Development of detailed chemistry models for boundary layer catalytic recombination. In *8th European Conference on Aerothermodynamics for Space Vehicles*, 2-5 March 2015.

[19] T. Belytschko and T. Black. Elastic crack growth in finite elements with minimal remeshing. *International Journal for Numerical Methods in Engineering*, 45:601–620, 1999.

[20] M.K. Bernauer and Herzog R. Implementation of an X-FEM solver for the classical two-phase Stefan problem. *Journal of Scientific Computing*, 52(2):271–293, 2011.

[21] L. Betchen, A.G. Straatman, and B. E. Thompson. A nonequilibrium finite-volume model for conjugate fluid/porous/solid domains. *Numerical Heat Transfer*, 49(A):543–565, 2006.

[22] A. Bhatia and S. Roy. Pyrolysis gas flow in thermally ablating media using time-implicit discontinuous Galerkin methods. In *49th AIAA Aerospace Sciences Meeting including the New Horizons Forum and Aerospace Exposition*, number AIAA 2011-145, Orlando, FL, 4-7 January 2011. American Institute of Aeronautics and Astronautics.

[23] A. Bhattacharyya, S. Dhinakaran, and A. Khalili. Fluid motion around and through a porous cylinder. *Chemical Engineering Science*, 61:4451–4461, 2006.

[24] D. Bianchi. *Modeling of ablation phenomena in space applications*. PhD thesis, Universita degli Studi di Roma, 2007.

[25] D. Bianchi, F. Nasuti, and E. Martelli. Navier-Stokes simulations of hypersonic flows with coupled graphite ablation. *Journal of Spacecraft and Rockets*, 47(4):554–562, 2010.

[26] D. Bianchi, F. Nasuti, and E. Martelli. Thermochemical erosion analysis for graphite/carbon-carbon rocket nozzles. *Journal of Propulsion and Power*, 27(1):197–205, 2011.

[27] D. Bianchi, A. Turchi, and M. Onofri F. Nasuti. Coupled CFD analysis of thermochemical erosion and unsteady heat conduction in solid rocket nozzles. In *48th AIAA/ASME/SAE/ASEE Joint Propulsion Conference and Exhibit*, number AIAA 2012–4318. American Institute of Aeronautics and Astronautics, 29 July - 1 August 2012.

[28] D. Bianchi, A. Turchi, and M. Nasuti, F.and Onofri. Chemical erosion of carbon-phenolic rocket nozzles with finite-rate surface chemistry. *Journal of Propulsion and Power*, 29(5):1220–1230, 2013.

[29] G. Billet and J. Ryan. A Runge-Kutta discontinuous Galerkin approach to solve reactive flows: the hyperbolic operator. *Journal of Computational Physics*, 230:1064–1083, 2011.

[30] D. Bose, T. White, J.A. Santos, Feldman J., M. Mahzari, M. Olson, and B. Laub. Initial assessment of Mars Science Laboratory heatshield instrumentation and flight data. In *51st AIAA Aerospace Sciences Meeting including New Horizons Forum and Aerospace Exposition*, number AIAA 2013-0908. American Institute of Aeronautics and Astronautics, 7-10 January 2013.

[31] B. Bottin, O. Chazot, M. Carbonaro, V. van der Haegen, and S. Paris. The VKI Plasmatron characteristics and performance. Contractor Report RTO EN-8, Los Alamos Scientific Laboratory, June 1999.

[32] J.-U. Brackbill, D.-B. Kothe, and C. Zemach. A continuum method for modeling surface tension. *Journal of Computational Physics*, 100:335–354, 1992.

[33] J-P. Braeunig, J.F. Bourgat, P. Charrier, F. Coatena, B. Dubroca, G. Duffa, P. Tallec, L. Mieussens, and B. Perthame. Comparison of discrete velocity and random particle methods for rarefied reentry flows. In *11th AIAA/AAAF Congress, Space Planes and Hypersonic Systems and Technologies*, number AIAA 2002-5180. American Institute of Aeronautics and Astronautics, 30 September - 3 October 2002.

[34] W.P. Breugem. *The influence of wall permeability on laminar and turbulent flows*. PhD thesis, Technische Universiteit Delft, 2005.

[35] W.P. Breugem, B.J. Boersma, and Uittenbogaard R.E. Direct numerical simulations of plane channel flow over a 3D cartesian grid of cubes. *Computer Methods in Applied Mechanics and Engineering*, 192:3163–3177, 2003.

[36] J.J. Brogan. A numerical method of solution for heat conduction in composite slabs with a receding surface. Technical Report LMSD 288204, Lockheed Aircraft Corp, April 1960.

[37] O. Cabrit, L. Artal, and F. Nicoud. Direct numerical simulation of turbulent multispecies channel flow with wall ablation. In *39th AIAA Thermophysics Conference*, number AIAA 2007-4401, Miami, FL, 25-28 June 2007. American Institute of Aeronautics and Astronautics.

[38] J.-S. Cagnone. Argo development advancement meeting. Cenaero, Private Communication.

[39] J.-S. Cagnone, K. Hillewaert, and N. Poletz. A discontinuous galerkin method for multiphysics welding simulations. *Key Engineering Materials*, 611-612:1319–1326, 2014.

[40] C. Carton de Wiart. *Towards a discontinuous Galerkin solver for scale-resolving simulations of moderate Reynolds number flows, and application to industrial cases*. PhD thesis, Université catholique de Louvain, 2014.

[41] C. Carton de Wiart, K. Hillewaert, L. Bricteux, and G. Winckelmans. Implicit les of free and wall-bounded turbulent flows based on the discontinuous galerkin/symmetric interior penalty method. *International Journal for Numerical Methods in Fluids*, 78(6):335–354, 2015.

[42] D.L. Cauchon. Radiative heating results from the FIRE II flight experiment at a re-entry velocity of 11.km/s. Tech. Report TM X-1402, NASA, 1973.

[43] M. Chandesris and D. Jamet. Boundary conditions at a planar fluid-porous interface for a poiseuille flow. *International Journal of Heat and Mass Transfer*, 49:2137–2150, 2006.

[44] M. Chandesris and D. Jamet. Boundary conditions at a fluid-porous interface: An a priori estimation of the stress jump coefficients. *International Journal of Heat and Mass Transfer*, 50:3422–3436, 2007.

[45] M.W. Chase. NIST-JANAF thermochemical tables (part I and II). *Journal of Physical and Chemical Reference Data Monographs*, 9:550–551, 1998.

[46] O. Chazot and F. Panerai. High-enthalpy facilities and plasma wind tunnels for aerothermodynamics ground testing. In E. Josyula, editor, *Hypersonic nonequilibrium flows: fundamentals and recent advances (Progress in Astronautics and Aeronautics Series)*. American Institute of Aeronautics and Astronautics, Oxford, 2015.

[47] H. K. Chelliah, A. Makino, I. Kato, N. Araki, and C.K. Law. Modeling of graphite oxidation in a stagnation-point flow field using detailed homogeneous and semiglobal heterogeneous mechanisms with comparisons to experiments. *Combustion and Flame*, 104(4):469–480, 1996.

[48] X. Chen and T.D. Papathanasiou. On the variability of the Kozeny constant for saturated flow across unidirectional disordered fiber arrays. *Composites: Part A*, 37:836–846, 2006.

[49] Y.-K. Chen and T. Gökçen. Effect of non-equilibrium surface thermochemistry in simulation of carbon based ablators. *Journal of Spacecraft and Rockets*, 50(5):917–926, 2013.

[50] Y.-K. Chen and T. Gökçen. Implicit coupling approach for simulation of charring carbon ablators. *Journal of Spacecraft and Rockets*, 51(3):779–788, 2014.

[51] Y.-K. Chen and F.S. Milos. Finite-rate ablation boundary conditions for carbon-phenolic heat-shield. In *37th AIAA Thermophysics Conference*, number AIAA 2004-2270. American Institute of Aeronautics and Astronautics, 28 June-1 July 2004.

[52] Y.-K. Chen and F.S. Milos. Navier-Stokes solutions with finite rate ablation for planetary mission earth reentries. *Journal of Spacecraft and Rockets*, 42(6):961–970, 2005.

[53] Y.-K. Chen, F.S. Milos, and T. Gökçen. Loosely coupled simulation for two-dimensional ablation and shape change. *Journal of Spacecraft and Rockets*, 47(5):775–785, 2010.

[54] Y.-K. Chen, F.S. Milos, and T. Gökcen. Validation of a three-dimensional ablation and thermal response code. In *10th AIAA/ASME Joint Thermophysics and Heat Transfer Conference*, number AIAA 2010-4645. American Institute of Aeronautics and Astronautics, 28-30 June 2010.

[55] K.W. Cheng and T. Fries. Higher-order XFEM for curved strong and weak discontinuities. *International Journal for Numerical Methods in Engineering*, 82:564–590, 2009.

[56] J. Chessa, P. Smolinski, and T. Belytschko. The extended finite element method (XFEM) for solidification problems. *International Journal for Numerical Methods in Engineering*, 53:1959–1977, 2002.

[57] B. Cockburn. Discontinuous Galerkin methods. School of mathematics, University of Minnesota, 2003.

[58] B. Cockburn, G.E. Karniadakis, and C.-W. Shu. *The development of discontinuous Galerkin methods*. Springer, New York, 1999.

[59] B. Cockburn, G.E. Karniadakis, and C.-W. Shu. The development of discontinuous Galerkin methods. In B. Cockburn, G. E. Karniadakis, and C.-W. Shu, editors, *Discontinuous Galerkin Methods*, pages 3–50. Springer, 2000.

[60] S. Colonia, R. Steijl, and G.N. Barakos. Implicit implementation of the AUSM$^+$ and AUSM^+up schemes. *International Journal for Numerical Methods in Fluids*, 75(10):687–712, 2014.

[61] R.J. Conti, R. W. MacCormack, L.S. Groener, and J.M. Fryer. Practical Navier-Stokes computation of axisymmetric reentry flow fields with coupled ablation and shape change. In *30th Aerospace Sciences Meeting and Exhibit*, number AIAA 1992-0752, Reno, NV, 6-9 January 1992. American Institute of Aeronautics and Astronautics.

[62] V.A.F. Costa, L.A. Oliveira, B. R. Baliga, and A. C. M. Sousa. Simulation of coupled flows in adjacent porous and open domains using control-volume finite-element method. *Numerical Heat Transfer*, 45(A):675–697, 2004.

[63] R. Crocker and Y. Dubief. Numerical study of turbulence over a receding wall by controlled and thermal ablation. In *Proceedings of the Summer Program 2010*, Center for Turbulence Research, Stanford, USA, 2010.

[64] A. Dal Bianco, D. D'ambrosio, and V. Mareschi. A fully implicit material response code with ablation and pyrolysis for simulation of thermal protection systems. In *8th European Conference on Aerothermodynamics for Space Vehicles*, 2- 5 March 2015.

[65] R. Davuluri, H. Zhang, and A. Martin. Numerical study of spallation phenomenon in an arc-jet environment. In *11th AIAA/ASME Joint Thermophysics and Heat Transfer Conference*, number AIAA 2014-2249, Atlanta, GA, 16-20 June 2014. American Institute of Aeronautics and Astronautics.

[66] M.J.S. de Lemos. *Turbulence in porous media modeling and applications*. Elsevier, 2006.

[67] J.A. Dec. *Three dimensional finite element ablative thermal response analysis applied to heat shield penetration design*. PhD thesis, Georgia Institute of Technology, 2010.

[68] J.A. Dec, R.D. Braun, and B. Laub. Ablative thermal response analysis using the finite element method. *Journal of thermophysics and heat transfer*, 26(2):201–212, 2012.

[69] G.Z. Dennis, S.C.Z. ad Chang. Numerical solutions for steady flow past a circular cylinder at reynolds numbers up to 100. *Journal of Fluid Mechanics*, 42:471–490, 1970.

[70] A. D'Hueppe. *Heat transfer modeling at an interface between a porous medium and a free region*. PhD thesis, Ecole Centrale Paris, 2011.

[71] B. Dias, A. Turchi, and T.E. Magin. Stagnation-line simulations of meteor ablation. In *45th AIAA Thermophysics Conference*, number AIAA 2015-2349. American Institute of Aeronautics and Astronautics, 22-26 June 2015.

[72] A. D. Drew and S.L. Passman. *Theory of multicomponent fluids*. Springer-Verlag, New York, 1998.

[73] D. Driver, M. Olson, M. Barnhardt, and M. MacLean. Understanding high recession rates of carbon ablators seen in shear tests in an arc jet. In *48th AIAA Aerospace Sciences Meeting including the New Horizons Forum and Aerospace Exposition*, number AIAA 2010-1177, Orlando, FL, 4-7 January 2010.

[74] G. Duffa. *Ablative thermal protection systems modeling*. American Institute of Aeronautics and Astronautics, Inc., Reston,Virginia, 2013.

[75] G. Duffa, G.L. Vignoles, J.-M. Goyheneche, and Y. Aspa. Ablation of carbon-based materials: Investigation of roughness set-up from heterogeneous reactions. *International Journal of Heat and Mass transfer*, 48:3387–3401, 2005.

[76] F.A.L. Dullien. *Porous media: fluid transport and pore structure*. Academic Press, San Diego, 1991.

[77] H.J.T. Ellingham. Reducibility of oxides and sulfides in metallurgical processes. *Journal of the Society of Chemical Industry*, 63(5):125, 1944.

[78] A. Ern and V. Giovangigli. *Multicomponent transport algorithms*. Springer-Verlag, Berlin, 1994.

[79] J. Ferguson, F. Panerai, T. Sandstrom, J. Lachaud, A. Martin, and N.N. Mansour. Modeling of the fiber-scale oxidation of highly-porous carbon fiber materials based on synchrotron X-ray microtomography. In *NASA Ames Research Center, Applied Modeling and Simulation Seminar Series*, Mountain View, CA, 31 July 2014.

[80] J. Florio, J. Henderson, F. Test, and R. Hariharan. A study of the effects of the assumption of local-thermal equilibrium on the overall thermally induced response of a decomposing, glass-filed polymer composite. *Heat and Mass Transfer*, 34(4):135–147, 1991.

[81] B. Fornberg. A numerical study of steady viscous flow past a circular cylinder. *Journal of Fluid Mechanics*, 98:819–855, 1980.

[82] T. Fries and T. Belytschko. The extended/generalized finite element method: An overview of the method and its applications. *International Journal for Numerical Methods in Engineering*, 84(3):253–304, 2010.

[83] T. Fries and A. Zilian. On time integration in the XFEM. *International Journal for Numerical Methods in Engineering*, 79:69–93, 2009.

[84] S. Ganesan and D.R. Poirier. Conservation of mass and momentum for the flow of interdendritic liquid during solidification. *Metallurgical transactions*, 21(B):173–181, 1990.

[85] D. K. Gartling, C.E. Hickox, and R.C. Givler. Simulation of coupled viscous and porous flow problems. *Computational Fluid Dynamics*, 7:23–48, 1996.

[86] G.J. Gassner and D. A. Kopriva. A comparison of the dispersion and dissipation errors of Gauss and Gauss-Lobatto discontinuous Galerkin spectral element methods. *SIAM Journal of Scientific Computing*, 33(5):2560–2579, 2011.

[87] A. Gerstenberger and W.-A. Wall. An embedded Dirichlet formulation for 3D continua. *International Journal for Numerical Methods in Engineering*, 82:537–563, 2008.

[88] V. Giovangigli. *Multicomponent flow modeling*. Birkhauser, Boston, 1999.

[89] H.E. Goldstein. Kinetics of nylon and phenolic pyrolysis. Contractor report, Lockheed Missiles and Space Compagny, October 1965.

[90] B. Gorissen. 1d code for discontinuous Galerkin methods. Cenaero, Private Communication.

[91] R. Gosse and G. Candler. Ablation modeling of electro-magnetic launched projectile for access to Space. In *45th AIAA Aerospace Sciences Meeting and Exhibit*, number AIAA 2007-1210. American Institute of Aeronautics and Astronautics, 8-11 January 2007.

[92] B. Goyeau, D. Lhuillier, D. Gobin, and M.G. Verlade. Momentum transport at a fluid-porous interface. *International Journal of Heat and Mass Transfer*, 46:4071–4081, 2003.

[93] W.G. Gray and P.C.Y. Lee. On the theorems for local volume averaging of multiphase systems. *International Journal of Multiphase Flow*, 3:333–342, 1977.

[94] S. Haber and R. Mauri. Boundary conditions for darcy's flow through porous media. *International Journal of Multiphase flow*, 9:561–574, 1983.

[95] J.R. Hahn. Kinetic study of graphite oxidation along two lattice directions. *Carbon*, 43:1506–1511, 2005.

[96] J.R. Hahn and H. Kang. Vacancy and interstitial defects at graphite surfaces. scanning tunneling microscopic study of the structure, electronic property, and yield for ion-induced defect creation. *Physical Review B*, 60(8):6007–6017, 1999.

[97] F. Harlow and J. Welch. Numerical calculation of time dependent viscous incompressible flow of fluid with free surface. *Physics of Fluids*, 8:2182–2189, 1965.

[98] B. Helber, O. Chazot, T.E. Magin, and A. Hubin. Ablation of carbon preform in the VKI Plasmatron. In *43rd AIAA Thermophysics Conference*, number AIAA 2012-2876, New Orleans, LA, 25-28 June 2012. American Institute of Aeronautics and Astronautics.

[99] B. Helber, A. Turchi, O. Chazot, T.E. Magin, and A. Hubin. Gas/Surface interaction study of low-density ablators in sub-and supersonic plasmas. In *11th AIAA/ASME Joint Thermophysics and Heat Transfer Conference*, number AIAA 2014-2122, Atlanta, GA, 16-20 June 2014. American Institute of Aeronautics and Astronautics.

[100] K. Hillewaert. *Development of the discontinuous Galerkin method for large scale/high-resolution CFD and acoustics in industrial geometries*. PhD thesis, Université catholique de Louvain, 2013.

[101] K. Hillewaert, N. Chevaugeon, P. Geuzaine, and J.-F. Remacle. Hierarchic multigrid iteration strategy for the discontinuous Galerkin solution of the steady Euler equations. *International Journal for Numerical Methods in Fluids*, 59(9):1157–1176, 2006.

[102] K. Hillewaert, J.-F. Remacle, N. Chevaugeon, and P. Geuzaine. Discontinuous Galerkin methods implementation issues. In *VKI 35th CFD/ADIGMA course on very high order discretization methods*. Sint-Genesius-Rode, 13-17 October 2008.

[103] C.W. Hirt and B.D. Nichols. Volume of fluid (VOF) method for the dynamics of free boundaries. *Journal of Computational Physics*, 39(1):201–225, 1981.

[104] J.R. Howell, M.P. Menguc, and R. Siegel. *Radiation heat transfer*. CRC Press Taylor and Francis Group, 2001.

[105] F.Q. Hu. On absorbing boundary conditions for linearized euler equations by perfectly matched layer. Tech. Report CR-198224, NASA, 1995.

[106] A. Huerta, E. Casoni, E. Sala-Lardies, S. Fernadez-Mendez, and J. Peraire. Modeling discontinuities with high-order elements. In *ECCM 2010, IV European Conference on Computational Mechanics*. Paris, 16-21 May 2010.

[107] M.F. Irfan, M.R. Usman, and K. Kusakabe. Coal gasification in co2 atmosphere and its kinetics since 1948: A brief review. *Energy*, 36:12–40, 2011.

[108] D. Jamet, M. Chandresis, and B. Goyeau. On the equivalence of the discontinuous one-and two domain approaches for the modeling of transport phenomena at a fluis/porous interface. *Transport in Porous Medium*, 17(2):232–239, 2003.

[109] G. Jiang and C.-W. Shu. On cell entropy inequality for discontinuous galerkin method. *Mathematics of Computation*, 62(206):531–538, 1994.

[110] C.O. Johnson, P.A. Gnoffo, and K. Sutton. The influence of ablation on radiative heating for Earth entry. *Journal of Spacecraft and Rockets*, 46(3):481–491, 2009.

[111] T.C. Jue. Numerical analysis of vortex shading behind a porous cylinder. *International Journal of Numerical Methods Heat Fluid flow*, 14:649–663, 2004.

[112] M. Kaviany. *Principles of heat transfer in porous media*. Springer-Verlag, New York, 1995.

[113] J. Keenan and G. Candler. Simulation of ablation in Earth atmospheric entry. In *28th AIAA Thermophysics conference*, number AIAA 1994-2083. American Institute of Aeronautics and Astronautics, June 1994.

[114] R. M. Kendall. An analysis of the coupled chemically reacting boundary layer and charring ablator. Part 3 -a general approach to the thermochemical solution of mixed equilibrium-nonequilibrium homogeneous or heterogeneous systems. Contractor Report CR-1064, NASA, June 1968.

[115] K. Khadra, P. Angot, S. Parneix, and J.-P. Caltagirone. Fictitious domain approach for numerical modeling of Navier-Stokes equations. *International Journal for Numerical Method in Fluids*, 34:651–684, 2000.

[116] D.W. Kuntz, B. Hassan, and D.L. Potter. Prediction of ablating hypersonic vehicles using an iterative coupled fluid/thermal approach. *Journal of Thermophysics and Heat Transfer*, 15(2):129–139, 2001.

[117] J. Lachaud, I. Cozmuta, and N.N. Mansour. Multiscale approach to ablation modeling of phenolic impregnated carbon ablators. *Journal of Spacecraft and Rockets*, 47(6):910–921, 2010.

[118] J. Lachaud, T. Magin, I. Cozmuta, and N.N. Mansour. A short review of ablative material response models and simulation tools. In *7th European Aerothermodynamics Symposium*, Brugge, 9-12 May 2011.

[119] J. Lachaud and N.N. Mansour. Porous-material analysis toolbox based on openfoam and applications. *Journal of Thermophysics and Heat Transfer*, 28(2):191–202, 2014.

[120] J. Lachaud, N.N. Mansour, A. Ceballos, D. Pejakovic, L. Zhang, and J. Marschall. Validation of a volume-averaged fiber-scale model for the

oxidation of a carbon-fiber preform. In *42nd AIAA Thermophysics Conference*, number AIAA 2011-3640, Honolulu, HA, 27-30 June 2011. American Institute of Aeronautics and Astronautics.

[121] J. Lachaud, A. Martin, I. Cozmuta, and B. Laub. Ablation workshop test case. In *4th Ablation Workshop*, Albuquerque, New Mexico, 1-3 March 2011.

[122] J. Lachaud, A. Martin, T. Van Eekelen, and I. Cozmuta. Ablation test-case series # 2. In *5th Ablation Workshop*, Lexington, Kentucky, 28 March 2012.

[123] J. Lachaud, T. van Eekelen, J.B. Scoggins, T.E. Magin, and N.N. Mansour. Detailed chemical equilibrium model for porous ablative materials. *International Journal of Heat and Mass Transfer*, 90:1034–1045, 2015.

[124] A. Lani. *An object oriented and high performance platform for aerothermodynamics simulation*. PhD thesis, Université Libre de Bruxelles, 2008.

[125] B. Laub and E. Venkatapathy. Thermal protection system technology and facility needs for demanding future planetary missions. In *International Workshop on Planetary Probe Atmospheric Entry and Descent Trajectory Analysis and Science*. Lisbon, Portugal, 6-9 October 2003.

[126] R.D. Launius and D.R. Jenkins. *Coming home: reentry and recovery from space*. Library of Congress Cataloging-in-Publication Data, 2012.

[127] J.W. Lawson, M.M. Stackpoole, and V. Shklover. Examination of scanning electron microscope and computed tomography images of PICA. Tech. Report ARC-E-DAA-TN1167, NASA, 2010.

[128] M. Le Bars and M.G. Worster. Interfacial conditions between a pure fluid and a porous medium implications for binary alloy solidification. *Journal of Fluid Mechanics*, 550:149–173, 2006.

[129] K.H. Lee, H. M. Lee, H.M. Eun, W. R. Lee, S. Kim, and D. Kim. The electronic structure of lattice vacancies on the STM image of a graphite surface. *Surface Science*, 321(3):267–275, 1994.

[130] G. Legrain, N. Chevaugeon, and K. Dreau. High order XFEM and level sets for complex microstructures: uncoupling geometry and approximation. *Computer Methods in Apllied Mechanics and Engineering*, pages 172–189, 2012.

[131] R.J. Leveque. Numerical methods for conservation laws. Lectures in mathematics, ETH Zurich, 1992.

[132] Z. Li. The immersed interface method using a finite element formulation. *Applied Numerical Mathematics*, 27:253–267, 1998.

[133] Z. Li and K. Ito. *The immersed interface method: numerical solutions of PDEs involving interfaces and irregular domains*. SIAM Frontiers in Applied Mathematics, 2006.

[134] M.S. Liou. A sequel to AUSM, part II: AUSM$^+$-up for all speeds. *Journal of Computational Physics*, 214:137–170, 2006.

[135] Q. Liu and O.V. Vasilyev. A Brinkman penalization method for compressible flows in complex geometries. *Journal of Computational Physics*, 227:946–966, 2007.

[136] F.K. Lu and D.E. Marren. *Advanced hypersonic test facilities, Progress in Astronautics and aeronautics*. American Institute of Aeronautics and Astronautics, Reston, 2002.

[137] Y. Lv and M. Ihme. Discontinuous galerkin method for multicomponent chemically reacting flows and combustion. *Journal of Computational Physics*, 270:105–137, 2014.

[138] M. MacLean. An equilibrium ablation boundary condition for the data-parallel line-relaxation code. In *51st AIAA Aerospace Sciences Meeting Including the New Horizon Forum and Aerospace Exposition*, number AIAA 2013–0304. American Institute of Aeronautics and Astronautics, 7-10 January 2013.

[139] T. E. Magin, L. Caillault, A. Bourdon, and C. O. Laux. Nonequilibrium radiative heat flux modeling for the Huygens entry probe. *Journal of Geophysical Research - Planets*, 111(E07S12):1–11, 2006.

[140] T. E. Magin and G. Degrez. Transport of parti ally ionized and unmagnetized plasmas. *Journal of Computational Physics*, 198(2):424–449, 2004.

[141] T.E. Magin. *A Model for Inductive Plasma Wind Tunnels*. PhD thesis, Université Libre de Bruxelles, 2004.

[142] T.E. Magin, M. Panesi, A. Bourdon, and A. Bultel. Analysis of the FIRE II flight experiment by means of a collisional radiative model. Annual research briefs 2008, Center for Turbulence Research, 2008.

[143] N.N. Mansour, J. Lachaud, T.E. Magin, J. de Muelenaere, and Y.-K. Chen. High-fidelity charring ablator thermal response model. In *42nd AIAA Thermophysics Conference*, number AIAA 2011-3124, Honolulu, Hawaii, 27 -30 June 2011. American Institute of Aeronautics and Astronautics.

[144] N.N. Mansour, F. Panerai, A. Martin, D.Y. Parkinson, A.A. MacDowell, A. Haboub, T.A. Sandstorm, T. Fast, G.L. Vignoles, and J. Lachaud. A new approach to light-weight ablators analysis: from micro-tomography measurements to statistical analysis and modeling. In *44th AIAA Thermophysics Conference*, number AIAA 2013-2768, San Diego, CA, 24-27 June 2013. American Institute of Aeronautics and Astronautics.

[145] A. Martin. Volume averaged modeling of the oxidation of porous carbon fiber material. In *44th AIAA Thermophysics Conference*, number AIAA

2013-2635, San Diego, CA, 24-27 June 2013. American Institute of Aeronautics and Astronautics.

[146] A. Martin and I.D. Boyd. Strongly coupled computation of material response and nonequilibrium flow for hypersonic ablation. In *41st AIAA Thermophysics Conference*, number AIAA 2009-3597, San Antonio, TX, 22-25 June 2009.

[147] A. Martin, I.D. Boyd, I. Cozmuta, and M.J. Wright. Chemistry model for ablating carbon-phenolic material during atmospheric re-entry. In *48th Aeropsace Science Meeting Including the New Horizons Forum and Aerospace Exposition*, number AIAA 2010-1175, Orlando, FL, 4-7 January 2010.

[148] B.J. McBride, S. Gordon, and M.A. Reno. Coefficients for calculating thermodynamic and transport properties of individual species. Tech. Report NASA Technical Memorandum 4513, NASA, October 1993.

[149] Mersen. Calcarb rigid carbon thermal insulation. Technical guide HT 29 GB 0121, Mersen, 2011.

[150] F.S. Milos and D. J. Rasky. Review of numerical procedures for computational surface thermochemistry. *Journal of Thermophysics and Heat Transfer*, 8(1):24–34, 1994.

[151] N. Moes, M. Cloirec, P. Cartraud, and J.F. Remacle. A computational approach to handle complex microstructure geometries. *Computer Methods in Applied Mechanics and Engineering*, 192:3163–3177, 2003.

[152] M. Moesner and R. Radespiel. Numerical simulation of turbulent flow over porous media. In *21st AIAA Computational Fluid Dynamics Conference.*, number AIAA 2013-2963, San Diego, CA, 24-27 June 2013. American Institute of Aeronautics and Astronautics.

[153] J.A. Moore. *Chemical equilibrium to viscous flows*. PhD thesis, State University of New York at Buffalo, 1967.

[154] C.H. Mortensen and X. Zhong. High-order shock fitting method for hypersonic flow with graphite ablation and boundary layer stability. In *42nd AIAA FLuid Dynamics Conference and Exhibit*, number AIAA 2012-3150, New Orleans, LA, 25-28 June 2012. American Institute of Aeronautics and Astronautics.

[155] C. B. Moyer and R. A. Rindal. An analysis of the coupled chemically reacting boundary layer and charring ablator. Part 2 - finite difference solution for the in-depth response of charring materials considering surface chemical and energy balances. Contractor Report CR-1061, NASA, June 1968.

[156] C. B. Moyer and M.R. Wool. Aerotherm equilibrium surface thermochemistry computer program version 3. Technical Report AD875385, Aerotherm, April 1970.

[157] B. Muller, F. Kummer, and M. Oberlack. Highly accurate surface and volume integration on implicit domains by means of moment-fitting. *International Journal for Numerical Methods in Engineering*, 96(8):512–528, 2013.

[158] A. Munafò. *Multi-Scale models and computational methods for aerothermodynamics*. PhD thesis, Ecole Centrale Paris, 2014.

[159] G. Neale and W. Nader. Practical significance of Brinkman's extension of darcy's law: coupled parallel flows within a channel and a bounding porous medium. *Canadian Journal of Chemical Engineering*, 52:475–478, 1974.

[160] D.A. Nield and A. Bejan. *Convection in porous media*. Springer, New York, 1992.

[161] I. Nompelis, G. Candler, and R. Conti. A parallel implicit CFD code for the simulation of ablating re-entry vehicles. In *47th AIAA Aerospace Sciences Meeting Including The New Horizons Forum and Aerospace Exposition*, number AIAA 2009–1562. American Institute of Aeronautics and Astronautics, 5-8 January 2009.

[162] P.D. Noymer, L.R. Glicksman, and A. Devendran. Drag on a permeable cylinder in steady flow at moderate reynolds number. *Chemical Engineering Science*, 53:2859–2869, 1998.

[163] J.A. Ochoa-Tapia, P. Stroeve, and S. Whitaker. Diffusive transport in two-phase media: Spatially periodic models and maxwell's theory for isotropic and anisotropic systems. *Chemical Engineering Science*, 49:709–726, 1994.

[164] J.A. Ochoa-Tapia and S. Whitaker. Momentum transfer at the boundary between a porous medium and a homogeneous fluid-I. Theoretical development. *International Journal of Heat and Mass Transfer*, 38:2635–2646, 1995.

[165] J.A. Ochoa-Tapia and S. Whitaker. Momentum transfer at the boundary between a porous medium and a homogeneous fluid-II. Comparison with experiment. *International Journal of Heat and Mass Transfer*, 38:2647–2655, 1995.

[166] S. Osher. Riemann solvers, the entropy condition, and difference approximations. *SIAM Journal Numerical Analysis*, 21:217–235, 1984.

[167] G. Palmer, M. Barnhardt, B. Kirk, A. Amar, Y.-K. Chen, and N.N. Mansour. Coupled CFD-ablation response model simulations using the libMesh framework. In *11th AIAA/ASME Joint Thermophysics and Heat Transfer*, number AIAA 2014-2123, Atlanta, GA, 16-20 June 2014. American Institute of Aeronautics and Astronautics.

[168] G.E. Palmer and M.J. Wright. Comparison of methods to compute high-temperature gas viscosity. *Journal of Thermophysics and Heat Transfer*, 17(2):232–239, 2003.

[169] F. Panerai, A. Martin, J. Lachaud, N.N. Mansour, and M.J. Gasch. Analysis of fibrous felts for flexible ablators using synchrotron hard x-ray micro-tomography. In *8th European Conference on Aerothermodynamics for Space Vehicles*, 2-5 March 2015.

[170] F. Panerai, A. Martin, and N.N. Mansour. Numerical and experimental study of carbon fiber oxidation. In *52nd Aerospace Sciences Meeting*, number AIAA 2014-1208. American Institute of Aeronautics and Astronautics, 13 - 17 January 2014.

[171] F. Panerai, A. Martin, N.N. Mansour, S. A. Sepka, and J. Lachaud. Flow-tube oxidation experiments on the carbon preform of a phenolic-impregnated carbon ablator. *Journal of Thermophysics and Heat Transfer*, 28(2):181–190, 2014.

[172] C. Park. *Nonequilibrium hypersonic aerothermodynamics*. Wiley inter science publication, New York, 1990.

[173] C. Park, R. L. Jaffe, and H. Partridge. Chemical-kinetic parameters of hyperbolic earth entry. *Journal of Thermophysics and Heat Transfer*, 15(1):76–90, 2001.

[174] C. Peskin. Numerical analysis of blood flow in the heart. *Journal of Computational Physics*, 25:220–252, 1977.

[175] G. Pinaud and T. van Eekelen. A numerical comparison of high- and low fidelity radiation models for conduction-radiation coupling in (charring) ablators. In *7th European Workshop on Thermal Protection Systems and Hot Structures*, 8-10 April 2013.

[176] F. Pochet, K. Hillewaert, P. Geuzaine, J.F. Remacle, and E. Marchandise. A 3D strongly coupled implicit discontinuous Galerkin level-set based method for modeling two-phase flows. *Computers and Fluids*, 87(25):144–155, 2013.

[177] T. Poinsot and D. Veynante. *Theoretical and numerical combustion: Third Edition*. Poinsot, T. and Veynante, D., 2011.

[178] D. Potter. *Modelling of radiating shock layers for atmospheric entry at Earth and Mars*. PhD thesis, University of Queensland, 2011.

[179] D. Poulikakos and M. Kazmirczak. Forced convection in a duct partially filled with a porous material. *Journal of Heat Transfer*, 109:653–662, 1987.

[180] J. Proft and B. Rivière. Discontinuous galerkin methods for convection-diffusion equations for varying and vanishing diffusivity. *International Journal of Numerical Analysis and Modeling*, 6(4):533–561, 2009.

[181] N. Puiroux, M. Prat, and M. Quintard. Non-equilibrium theories for macro scale heat transfer: ablative composite layer systems. *International Journal of Thermal Sciences*, 43:541–554, 2004.

[182] D.L. Quan. *A mesh-based technique for solving CFD problems with embedded geometries: Anisotropic adaptive "nearly" body-fitted mesh approach*. PhD thesis, Université catholique de Louvain, 2014.

[183] M. Quintard and S. Whitaker. Transport in ordered and disordered porous media: Volume averaged equations, closure problems and comparison with experiment. *Chemical Engineering Science*, 48:2537–2564, 1993.

[184] M. Quintard and S. Whitaker. Transport in ordered and disordered porous media II: Generalized volume averaging. *Transport in Porous Media*, 14:179–206, 1994.

[185] W.H. Reed and T.R. Hill. Triangular mesh methods for the neutron transport equation. Contractor Report LA-UR-73-479, Los Alamos Scientific Laboratory, 1973.

[186] D.O. Revelle and W.N. Edwards. Stardust- an artificial, low velocity "meteor" fall and recovery: 15 january 2006. *Meteorics and Planetary Science*, 42(3):271–299, 2007.

[187] S. Richardson. A model for the boundary condition of a porous material. part II. *Journal of Fluid Mechanics*, 49(2):327–336, 1971.

[188] B. Rivière. *Discontinuous Galerkin methods for solving elliptic and parabolic equations - theory and implementation*. Society for Industrial and Applied Mathematics, 2008.

[189] B. Rivière, M.F. Wheeler, and K. Banas. Part II. discontinuous Galerkin method applied to single phase flow in porous media. *Computational Geosciences*, 4(4):337–341, 2012.

[190] L. Romagnosi, N. Gascoin, E. El-Tabach, I. Fedioun, M. Bouchez, and J. Steelant. Pyrolysis in porous media: Part 1. numerical model and parametric study. *Energy Conversion and Management*, 68:63–73, 2013.

[191] M. Sahraoui and M. Kaviany. Slip and no-slip velocity boundary conditions at interface of porous, plain media. *International Journal of Heat and Mass Transfer*, 35:927–943, 1992.

[192] I. Sakraker, E. Umit, V. Van der Haegen, T. Scholz, P. Testani, and G. Baillet. Qarman: An atmospheric entry experiment on cubesat platform. In *8th European Conference on Aerothermodynamics for Space Vehicles*, 2-5 March 2015.

[193] J.A. Schetz and A.E. Fuhs. *Fundamentals of fluid mechanics*. John Wiley and Sons, New York, 1999.

[194] P. Schrooyen, Turchi A., K. Hillewaert, T.E. Magin, and P. Chatelain. Loose-coupled simulations of stagnation-point ablation with material transient response. In *Proceeding of the Heliophysics Research Institute Summer Program 2014*, NASA AMES RESEARCH CENTER, California, 2014.

[195] P. Schrooyen, K. Hillewaert, T.E. Magin, and P. Chatelain. Discontinuous Galerkin discretization coupled with sharp interface method for ablative materials. In *21st AIAA Computational Fluid Dynamics Conference*, number AIAA 2013-2457, San Diego, CA, 24-27 June 2013. American Institute of Aeronautics and Astronautics.

[196] P. Schrooyen, K. Hillewaert, T.E. Magin, and P. Chatelain. Discontinuous Galerkin discretization for one-dimensional in-depth thermal response of ablative materials. In *Gordon Research conference on Atmospheric Reentry Physics*, Ventura, CA, 3-8 February 2013.

[197] P. Schrooyen, K. Hillewaert, T.E. Magin, and P. Chatelain. Continuum approach for aerothermal flow through ablative porous material using discontinuous Galerkin discretization. In *DFD14 Meeting of the American Physical Society*, San Francisco, CA, 22-24 November 2014. American Physical Society.

[198] P. Schrooyen, K. Hillewaert, T.E. Magin, and P. Chatelain. Fully implicit discontinuous galerkin solver to study surface and volume ablation competition in atmospheric entry flows. *[submitted for publication]*, 2015.

[199] P. Schrooyen, K. Hillewaert, T.E. Magin, and P. Chatelain. Fully implicit integrated approach for the numerical simulation of aerothermal flows through and around ablative thermal protection systems. In *8th European Conference on Aerothermodynamics for Space Vehicles*, 2-5 March 2015.

[200] P. Schrooyen, T.E. Magin, and P. Chatelain. Development of a numerical simulation tool for the aerothermal flow through an ablative thermal protection system for atmospheric entry. In *3rd VKI PhD Symposium*, Sint-Genesius Rode, Belgium, 5-7 March 2012.

[201] P. Schrooyen, T.E. Magin, and P. Chatelain. Development of a numerical simulation tool for the aerothermal flow through an ablative thermal protection system for atmospheric entry. In *4th VKI PhD Symposium*, Sint-Genesius Rode, Belgium, 4-6 March 2013.

[202] P. Schrooyen, T.E. Magin, and P. Chatelain. Development of a numerical simulation tool for the aerothermal flow through an ablative thermal protection system for atmospheric entry. In *5th VKI PhD Symposium*, Sint-Genesius Rode, Belgium, 10-12 March 2014.

[203] P. Schrooyen, T.E. Magin, and P. Chatelain. Development of a numerical simulation tool for the aerothermal flow through an ablative thermal

protection system for atmospheric entry. In *6th VKI PhD Symposium*, Sint-Genesius Rode, Belgium, 11-13 March 2015.

[204] T.E. Schwartzentruber, S. Poovathingal, and E. Stern. Molecular simulation of oxygen reactions with realistic silica and carbon surfaces at high temperature. In *8th European Conference on Aerothermodynamics for Space Vehicles*, 2-5 March 2015.

[205] J. B. Scoggins and T. E. Magin. Development of Mutation^{++}: Multicomponent Thermodynamic and Transport Properties for Ionized Plasmas written in C++. In *11th AIAA/ASME Joint Thermophysics and Heat Transfer Conference.*, number AIAA 2014-2966. American Institute of Aeronautics and Astronautics, 16-20 June 2014.

[206] J.B. Scoggins. The development of a thermochemical nonequilibrium ablation and pyrolysis model for carbon-phenolic thermal protection systems. Master's thesis, North Carolina State University, 2011.

[207] J.B. Scoggins, L. Soucasse, P. Rivière, A. Soufiani, and T.E. Magin. An adaptive hybrid statistical narrow band model for coupled radiative transfer in atmospheric entry flows. In *8th European Conference on Aerothermodynamics for Space Vehicles*, 2-5 March 2015.

[208] J.A. Sethian and S. Osher. Front propagating with curvature-dependent speed: algorithms based on hamilton-jacobi formulations. *Journal of Computational Physics*, 79:12–49, 1988.

[209] K. Shahbazi. An explicit expression for the penalty parameter of the interior penalty method. *Journal of Computational Physics*, 205:401–407, 2004.

[210] L.F. Shampine and M.W. Reichelt. The matlab ode suite. *SIAM Journal on Scientific and Statistical Computing*, 18:1–22, 1997.

[211] E. Shima and K. Kitamura. Parameter-free simple low-dissipation AUSM-family scheme for all speeds. *AIAA Journal*, 49(8):1693–1709, 2011.

[212] R.D. Skeel and M. Berzins. A method for the spatial discretization of parabolic equations in one space variable. *SIAM Journal on Scientific and Statistical Computing*, 11:1–32, 1990.

[213] J.C. Slattery. Flow of viscoelastic fluids through porous media. *AIChE Journal*, 13:1066–1071, 1967.

[214] M. Stackpoole, S. Sepka, and I. Cozmuta. Post-flight evaluation of Stardust sample return capsule forebody heatshield material. In *46th AIAA Aerospace Sciences Meeting and Exhibit*, number AIAA 2008-1202. American Institute of Aeronautics and Astronautics, 7-10 January 2008.

[215] J. Strain. Tree methods for moving interfaces. *Journal of Computational Physics*, 151(2):616–648, 1997.

[216] K. Sutton and P. Gnoffo. Multi-component diffusion with application to computational aerothermodynamics. In *7th AIAA/ASME Joint Thermophysics and Heat Transfer Conference*, number AIAA 98-2575. American Institute of Aeronautics and Astronautics, 15-18 June 1998.

[217] R.A. Svehla. Transport coefficients for the NASA Lewis chemical equilibrium program. Tech. Report NASA Technical Memorandum 4647, NASA, April 1995.

[218] K. Tao, J. Yao, and Z. Huang. Analysis of the laminar flow in a transition layer with variable permeability between a free-fluid and a porous medium. *Acta Mechanica*, 224(9):1943–1955, 2013.

[219] G.I. Taylor. A model for the boundary condition of a porous material. part i. *Journal of Fluid Mechanics*, 49(2):319–326, 1971.

[220] P. Thakre and V. Yang. Chemical erosion of carbon-carbon/graphite nozzles in solid-propellant rocket motors. *Journal of Propulsion and Power*, 24(4):822–833, 2008.

[221] K.W. Thompson. Time dependent boundary conditions for hyperbolic systems. *Journal of Computational Physics*, 68:1–24, 1986.

[222] M.M. Tomadakis and S.V. Sotirchos. Ordinary and transition regime diffusion in random fiber structures. *AIChE Journal*, 39(3):397–412, 1993.

[223] H. K. Tran, C. E. Johnson, D. J. Rasky, F. C. L. Hui, M. T. Hsu, T. Chen, Y. K. Chen, D. Paragas, and L. Kobayashi. Phenolic impregnated carbon ablators (PICA) as thermal protection systems for discovery missions. Technical Report TM 110440, NASA Ames Research Center., 1997.

[224] A. Turchi, D. Bianchi, F. Nasuti, and M. Onofri. A numerical approach for the study of the gas-surface interaction in carbon-phenolic solid rocket nozzles. *Aerospace Science and Technology*, 27:25–31, 2013.

[225] A. Turchi, B. Helber, A. Munafò, and T.E. Magin. Development and testing of an ablation model based on plasma wind tunnel experiments. In *11th AIAA/ASME Joint Thermophysics and Heat Transfer Conference*, number AIAA 2014-2125, Atlanta, GA, 16-20 June 2014.

[226] K. Vafai and S.J. Kim. Fluid mechanics of the interface region between a porous medium and a fluid layer- an exact solution. *International Journal of Heat and Fluid Flow*, 11:254–256, 1990.

[227] F.V. van Zeggeren and S.H. Storey. *The computation of chemical equilibria*. Cambridge University Press, New York, 1970.

[228] A. Velghe. *Modélisation de l'interaction entre un écoulement turbulent et une paroi ablatable*. PhD thesis, Institut National Polytechnique de Toulouse, 2007.

[229] G. Vignoles, J. Lachaud, Y. Aspa, and J.M. Goyhénèche. Ablation of carbon-based materials: Multiscale roughness modelling. *Composites Science and Technology*, 69:1470–1477, 2008.

[230] N. Wakao and J.M. Smith. Diffusion in catalyst pellets. *Chemical Engineering Science*, 17:825–834, 1962.

[231] F. Wang, L. Cheng, H. Mei, Zhang Q., and Zhang L. Effect of surface microstructures on the infrared emissivity of graphite. *International Journal of Thermophysics*, 35:62–75, 2014.

[232] S. Weisberg. Effective diffusion coefficient in porous media. *Journal of Applied Physics*, 34:2636–2639, 1963.

[233] S. Whitaker. The species mass jump condition at a singular surface. *Chemical Engineering Science*, 47:1677–1685, 1992.

[234] S. Whitaker. *The method of volume averaging*. Kluwer Academic Publishers, Dordrecht, The Netherlands, 1999.

[235] C.R. Wilke. A viscosity equation for gas mixtures. *Journal of Chemical-Physics*, 18(4):517–519, 1950.

[236] P. Yu, T.S. Lee, Y. Zeng, and H.T. Low. A numerical method for flows in porous and homogenous fluid domains coupled at the interface by stress jump. *International journal for Numerical Methods in Fluids*, 53(11):1755–1775, 2007.

[237] P. Yu, Y. Zeng, T.S. Lee, X.B. Chen, and H.T. Low. Steady flow around and through a permeable circular cylinder. *Computers and Fluids*, 42:1–12, 2010.